Engineering genetically encoded FRET sensors

Engineering genetically encoded FRET sensors

PROEFSCHRIFT

ter verkrijging van de graad van doctor aan de Technische Universiteit Eindhoven, op gezag van de rector magnificus prof.dr.ir. C.J. van Duijn, voor een commissie aangewezen door het College voor Promoties, in het openbaar te verdedigen op woensdag 23 april 2014 om 16:00 uur

door

Laurens Herman Lindenburg

geboren te Groningen

Dit proefschrift is goedgekeurd door de promotoren en de samenstelling van de promotiecommissie is als volgt:

voorzitter:	prof.dr. P.A.J. Hilbers
1e promotor:	prof.dr.ir. L. Brunsveld
copromotor(en):	dr. M. Merkx
leden:	prof.dr. T.W.J. Gadella Jr. (UvA)
	prof.dr. W.T.S. Huck (RU)
	dr.rer.nat. C. Ottmann
adviseur(s):	dr.ing. J.W. Borst (WU)

Printed by CPI Koninklijke Wöhrmann, Zutphen
A catalogue record is available from the Eindhoven University of Technology Library
ISBN: 978-90-386-3594-1

Contents

Chapter 1

Engineering genetically encoded FRET sensors

Abstract. Förster Resonance Energy Transfer (FRET) between two fluorescent proteins can be exploited to create fully genetically encoded and thus subcellularly targetable sensors. FRET sensors report changes in energy transfer between a donor and an acceptor fluorescent protein that occur when an attached sensor domain undergoes a change in conformation in response to ligand binding. The design of sensitive FRET sensors remains challenging as there are few generally applicable design rules and each sensor must be optimized anew. In this introductory chapter, we discuss various strategies to efficiently generate robust FRET sensors, including approaches that exploit ligand-induced domain-domain interactions and systematic screening of large numbers of FRET sensors. The challenges involved in multiparameter imaging, where more than one FRET sensor is used in the same cell, are also reviewed. Finally, we present an outlook of this thesis.

Intracellular fluorescent sensors

Until two decades ago, tools to localize and quantify proteins and small molecules inside cells were limited. Protein trafficking could be tracked in time by the radiolabel pulse chase and in space through fractionation but these techniques did not allow measurements on single cells. Moreover, the spatiotemporal resolution was limited by the number of fractions that could feasibly be obtained. All of this changed with the use of the Green Fluorescent Protein (GFP) as a genetically encoded fluorescent tag. First appearing as a footnote to the paper describing the discovery of aequorin in the jellyfish *Aequoria victoria* in 1962 (1), GFP was first cloned (2) and recombinantly expressed (3, 4) in the early 1990s. GFP has the remarkable property of becoming fluorescent in an entirely autocatalytic process. The fluorescent protein (FP) resembles a barrel formed of beta strands with at its centre a solvent-excluded helix containing a tri-residue fluorophore (5, 6) (Figure 1.1). This fluorophore is formed through cyclization of the polypeptide backbone between S65 and G67, elimination of water and oxidation by O_2 (5). Another important development was the generation of blue and yellow-shifted FPs, achieved through mutagenesis of the chromophore and of beta-barrel residues interacting with the chromophore (6). In addition to its application as a marker of gene expression (4), it was soon shown that genetic fusions of GFP to a protein of interest readily allowed protein trafficking to be monitored under the fluorescence microscope (7). Techniques such as fluorescence recovery after photobleaching (FRAP) (8), as well as photoactivatable FPs (9), have since rendered the radiolabel pulse chase largely obsolete for proteins.

Similar to protein trafficking, there was initially a lack of tools with which to monitor small molecules with high spatiotemporal resolution at the single cell level. Metal ions could be detected by atomic absorption spectroscopy but this could not distinguish between bound and freely available metal and could not report concentrations at the single cell level. An example of such a metal is Ca^{2+}, which as a second messenger plays an important role in transmitting the information provided by extracellular stimulation of membrane receptors (10). Its concentration can fluctuate more than 10-fold, making it one of the easiest transients to detect. As early as 1968,

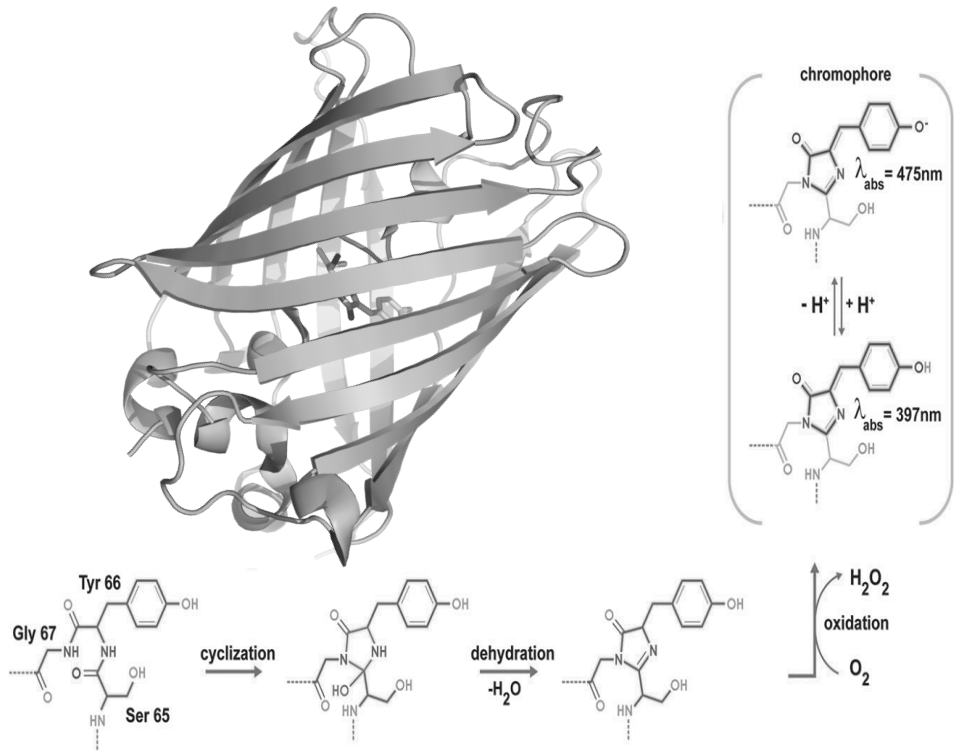

Figure 1.1: Fluorescent protein tertiary structure and formation of the GFP chromophore. *The β-barrel, within which the chromophore is located, is conserved across FPs. The cartoon represents the EGFP crystal structure (PDB code 3EUL). In GFP, the chromophore is formed when tortional rearrangements bring the carboxyl carbon of S65 in close proximity of the amide nitrogen of G67 (bottom left structure), allowing the latter to nucleophilically attack the former, resulting in an imidazolin-5-one heterocycle. This heterocycle is then dehydrated, followed by oxidation of the alpha-beta carbon bond of Y66, yielding the functional chromophore, resulting from conjugation of the heterocycle's electron system with that of the phenyl ring of Y66. Deprotonation at the latter's para oxygen substituent results in a dramatic shift of the chromophore's absorption spectrum (11). Chromophore formation scheme obtained from (12) .*

the Ca^{2+}-sensitive bioluminescent protein aequorin had been microinjected into single muscle fibres and used to follow Ca^{2+} transients (11). The 1980s saw the development of a series of synthetic fluorescent Ca^{2+} dyes that greatly advanced the Ca^{2+} imaging field. Three key innovations that were introduced were the development of Ca^{2+}-specific chelator BAPTA (12), linking of BAPTA to a fluorescent dye (12) and the

development of a strategy allowing cells to be irreversibly loaded with this Ca^{2+} reporter dye (13).

A disadvantage of small molecule synthetic dyes is the limited repertoire of binding specificities available, contrasting with the vast diversity of binding specificities found amongst proteins in nature. One of the first examples of the use of a natural protein domain for an intracellular fluorescent sensor was provided by the FlCRhR sensor for cAMP (Figure 1.2). The two catalytic subunits of the cAMP-dependent protein kinase (PKA) were labeled with fluorescein, while the two regulatory subunits were labeled with a rhodamine dye. Förster Resonance Energy Transfer (FRET) from the fluorescein donor to the rhodamine acceptor in the holoenzyme complex was disrupted when cAMP binding at the regulatory subunits induced dissociation of the protein subunits (13).

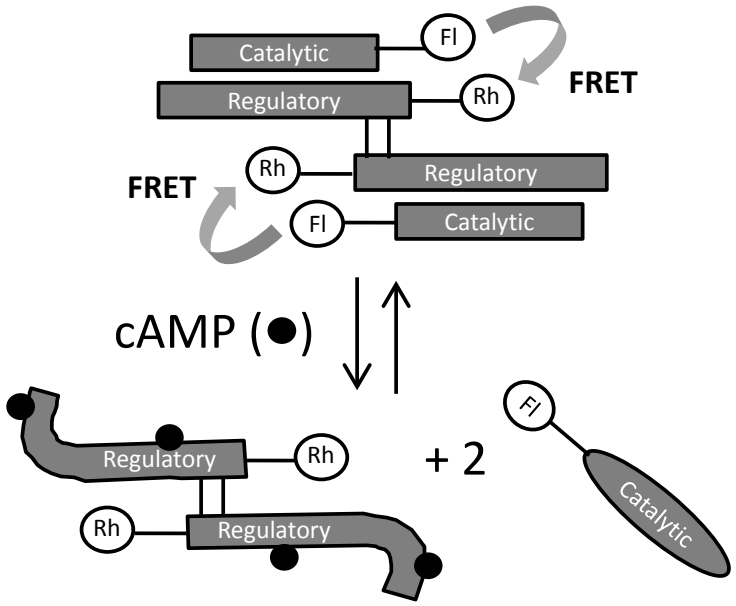

Figure 1.2: Schematic representation of FlCRhR, a semi-synthetic FRET sensor for cAMP. *The purified catalytic and regulatory subunits were first labeled separately with a fluorescein and a rhodamine dye. The subunits were then mixed and allowed to form a holoenzyme complex. Fluorescein's emission (peak at 519 nm) and rhodamine's absorption (peak at 555 nm) overlap, resulting in non-radiative energy transfer from fluorescein to rhodamine in the holoenzyme complex. The binding of cAMP at the regulatory subunits results in disruption of the complex. Picture adapted from (13).*

Although FlCRhR allowed single cell measurements of cAMP for the first time, it still suffered the disadvantage of needing microinjection to enter the cell. The next step, the development of fully genetically encoded sensors, is the subject matter of this introductory chapter. In the following, various aspects of FRET sensor development will be considered, including general strategies to allow optimization of sensor dynamic range (DR), rational protein engineering approaches and strategies that permit more than one parameter to be measured in the same single cell. While the focus is on the development of FRET sensors, throughout the chapter, we will use work on single FP sensors as a source of inspiration for the FRET sensor field.

Genetically encoded fluorescent sensors

Genetically encoded fluorescent sensors can be divided into two categories: those that modulate the fluorescence of a single FP and those that display changes in FRET between a donor and acceptor FP.

The single FP sensors rely on modulation of the degree of exposure of the FP chromophore to the solvent, which has a large effect on its fluorescent properties. Some of the first sensors developed along this principle were sensitive to pH (14) and to redox state (15). With the development of circular permutants of GFP it became possible to graft protein domains onto the β-barrel (16) such that these domains' conformation directly modulated the chromophore's access to solvent. For example, Calmodulin and M13, which undergo a Ca^{2+}-dependent interaction, were fused to the new N- and C-termini of circularly permutated GFP, generating the GCaMP probe (17), whose fluorescence is quenched in absence of Ca^{2+} (Figure 1.3A). GCaMP has since spawned a series of ever improving Ca^{2+} dyes (18-20). Other useful single FP sensors developed since include the ATP to ADP ratio sensor Percival (21, 22), the dual pH and Cl^- sensor ClopHensorN (23), the membrane potential sensor ArcLight (24, 25), the H_2O_2 sensor HyPer (26) and the glutamate sensor iGluSnFR (27). Most single FP-based sensors are intensiometric which makes them less robust as fluctuations in sensor concentration may be mistaken for actual signal change.

However, a few single FP-based sensors have been developed that are excitation-ratiometric, changing their relative excitation at two different wavelengths as a function of ligand concentration (28, 29). In the single FP sensors, the necessity for allosteric coupling of ligand binding to modulation of the chromophore environment introduces a serious protein engineering challenge. Nevertheless, several single FP-based sensors have been developed that showed excellent signal to noise ratios (20, 27).

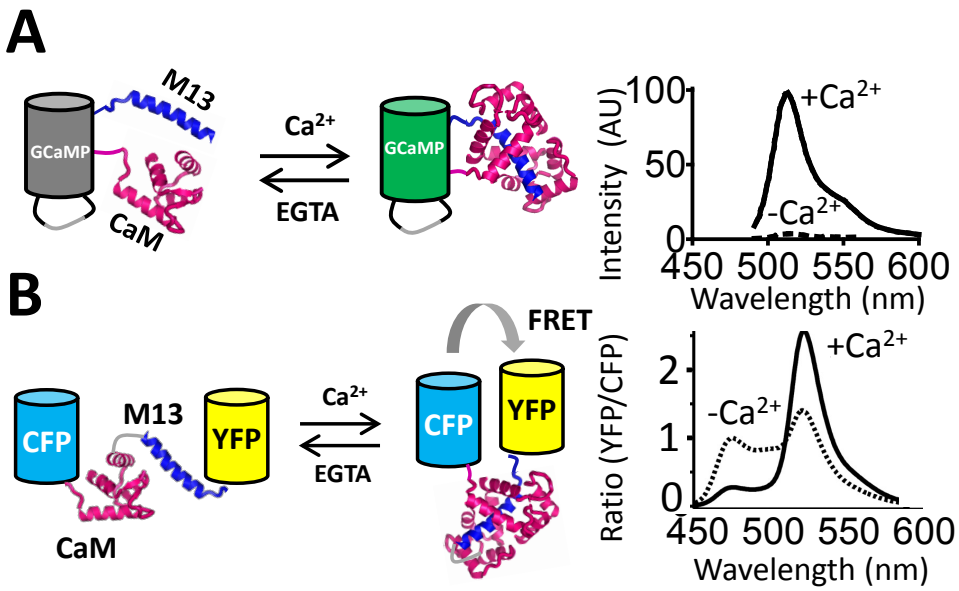

Figure 1.3: Comparison of a single FP-based sensor with a FRET-based sensor. *(A) GCamP consists of a circularly permutated GFP in which Calmodulin (CaM) and M13 are grafted into the beta-barrel using the newly available N- and C-termini. In absence of Ca^{2+}, the FP is only dimly fluorescent, due to solvent quenching of the fluorophore. Ca^{2+} binding and the concomitantly induced M13-Calmodulin interaction excludes solvent from the chromophore, dramatically increasing fluorescence intensity. Graph on the right shows the change in intensity for the highly optimized GCaMP5 (30). (B) The Cameleon FRET sensor for Ca^{2+} also uses CaM and M13, but now sandwiched between ECFP and EYFP. The Ca^{2+}-binding-induced intramolecular CaM-M13 interaction results in an increase in FRET. The graph on the right shows the emission spectra in presence and absence of Ca^{2+} for the highly optimized Cameleon variant YC3.60 (31).*

Genetically encoded FRET sensors (recently reviewed by Goedhart and colleagues (32)) consist of two fluorescent domains flanking a recognition domain and forming a

single polypeptide chain. Ligand binding to the recognition domain changes its conformation, resulting in a change in the relative orientation of the FP-FP geometry, and thus a change in FRET. FRET is defined as radiationless energy transfer between two chromophores as a result of long-range dipole-dipole interactions (33). The FRET efficiency depends not only on the distance and the relative orientation (κ^2) of those two dipoles, but also on their intrinsic fluorescent properties. These factors are the overlap (J) between the donor's emission and the acceptor's absorption spectra, normalized to the acceptor's extinction coefficient and the quantum yield of the donor. The refractive index of the medium through which the radiationless energy transfer takes place also affects the FRET efficiency (E). The intrinsic fluorescent properties of both fluorophores can be used to calculate the distance between the dipoles at which energy transfer is 0.5 (i.e. where the donor's emission intensity is reduced to 50% of its value in absence of acceptor), a convenient measure of a FRET pair's suitability, and known as R_0 (equation 1.1).

$$R_0 = 0.211 \cdot [n^{-4} \cdot \kappa^2 \cdot \phi \cdot J]^{\frac{1}{6}} \quad (1.1)$$

The refractive index is usually assumed to be 1.5, while κ^2 is assumed to be 2/3, a value representing freely rotating dipoles. The actual efficiency of energy transfer (E) will depend on the distance (r) between the fluorophores, as given by equation 1.2

$$E = \frac{{R_0}^6}{{R_0}^6 + r^6} \quad (1.2)$$

Typical values for FP pairs' R_0 range between 40 and 60 Å (34, 35). For fluorescent proteins, a lower limit in *r* of about 30 Å is set by the width of the beta-barrel protein shell surrounding the fluorophore.

A FRET sensor for Ca^{2+}, Cameleon, was one of the first sensors to be constructed using the principle of FRET between two fluorescent domains (Figure 1.3B). This construct is a single polypeptide chain consisting of ECFP, Calmodulin (CaM), M13 and EYFP. Upon binding of Ca^{2+} to CaM, M13's affinity for CaM was increased, resulting in the wrapping of the M13 around CaM, changing the relative geometry of the FPs, leading to an increase in FRET (36). The dynamic range (DR) ($\Delta R/R_{min}$) of this sensor was a very reasonable 70%. As Cameleon's output signal was emission

ratiometric, measurements were not sensitive to fluctuations in sensor concentration, optical path length or excitation intensity (36).

The goal in FRET sensor development is to make the *change* in *r i)* as large as possible and *ii)* centered around R_0 as closely as possible. An additional means of modulating the efficiency of energy transfer is achieved through a change in R_0 resulting from a change in dipole-dipole orientation. The next section will deal with strategies undertaken to increase the ligand-dependent change in energy transfer in FRET sensors.

Design of FRET sensors based on single recognition domains

Since the Cameleon Ca^{2+} sensor described above, many genetically encoded FRET sensors have been developed and further improved. These probes, of which a selection (not intended to be exhaustive) is given in Table 1.1, are often the end products of significant protein engineering efforts. Researchers chose protein domains known to change conformation upon ligand binding and fuse FPs to either end of that domain, in the hope that the change of conformation in the recognition domain is transduced to a change in FP relative distance and/or orientation. However, initial designs typically yield sensors with poor DR, necessitating laborious and time-consuming rounds of trial and error based improvement.

For example, a number of FRET sensors have been constructed using the bacterial periplasmic binding proteins (PBPs) as sensing module. PBPs, despite possessing seemingly ideal properties such as solubility, a well-understood venus flytrap-like motion of two lobes upon ligand binding and a large selection of binding specificities for many small molecules of interest (37), often make poor FRET sensor recognition domains in simple fusion constructs. As the N and C-termini of the PBP are located on the same lobe, they show little change in their relative orientation and distance upon ligand binding (Figure 1.4A, B). In a series of papers (38-42), Frommer and colleagues introduced generally applicable strategies to improve the poor performance of such fusion constructs for a wide selection of small molecule ligands (see Table 1.1). For

example, the DR of a FRET sensor based on MglB (39), a glucose binding PBP, was initially just 10% (Figure 1.4C). The sensor was improved by truncating the linkers between MglB and the fluorescent domains, yielding a glucose sensors with a 20% DR (38). Also, improvements were noted when the ECFP donor fluorescent domain was inserted at rationally selected sites of the MglB domain (38). The improvements were ascribed to a tighter allosteric coupling of the ligand-induced conformational change of MglB with a change of the FP-FP orientation. In particular, the linker truncation and

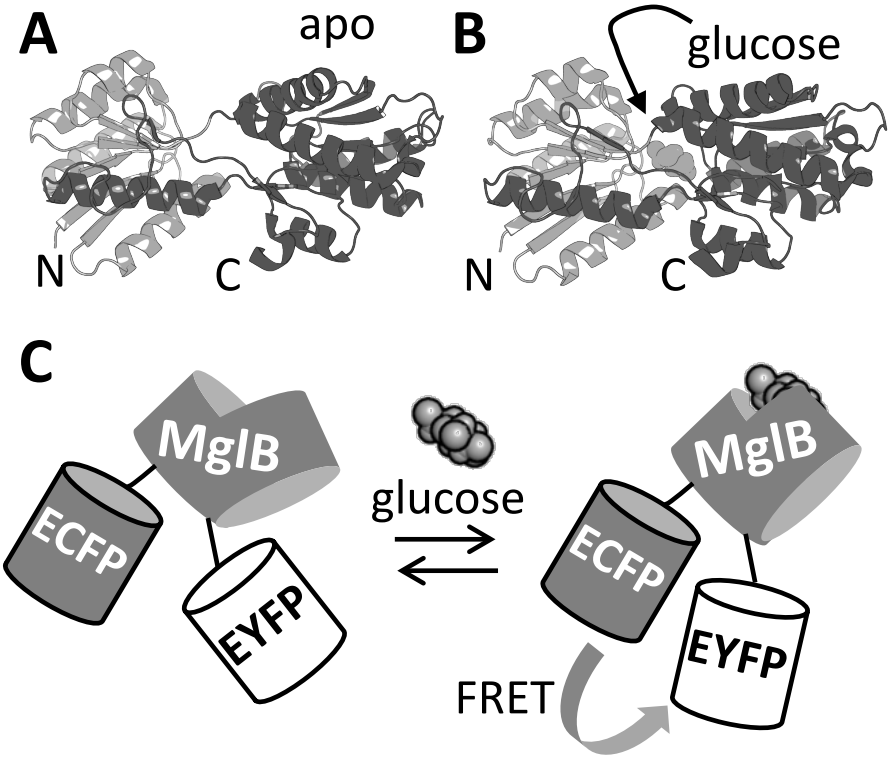

Figure 1.4: A genetically encoded FRET sensor for glucose based on the periplasmic binding protein MglB. *(A) Crystal structure of apo-MglB (PDB 2FW0,(43)). The N-terminal lobe is colored in white while the C-terminal lobe is colored dark gray. Note the C-terminal extension of the C-terminal lobe into and back out from the N-terminal lobe. (B) Crystal structure of glucose-bound MglB (PDB 2FVY), using the same color scheme. Note the lack of any large change in orientation or distance of the N and C-termini relative to the situation in the apo-form in A. (C) Schematic representation of the mechanism of action of a glucose FRET sensor based on MglB. Although in this figure a FRET increase is depicted upon glucose binding, a decrease in FRET was also observed in some other variants (38).*

recognition domain insertion should reduce the fluorescent domains' degrees of freedom for rotation. A further improvement in sensor DR (10 times better than the original sensor) was achieved by combining both strategies of linker truncation and domain insertion into a single sensor, FLII^{12}Pglu-700μδ6 (40). Another "trick" that can be used to improve the response of PBP-based sensors is circular permutation of the recognition domain with the aim of having the new PBP N and C –termini reside on different lobes of the PBP. It was shown that FRET sensors using six different PBPs could be improved this way, including two that were non-functional in absence of the PBP circular permutation (44).

Another example of a FRET sensor based on the conformational change of a single domain is the GEBRA FRET sensor for retinoic acid (RA), developed on the basis of the ligand binding domain (LBD) of the Retinoic Acid nuclear Receptor (RAR) (45). Different combinations of several different circular permutants of CFP and YFP derivatives were tested, with some displaying a much better response than others. The sensor GEBRA-G displayed a DR in the HeLa cell of 93%. A range of sensors with different RA affinities (2, 4 and 50 nM) was generated by mutations in the RAR domain, or by exchanging RAR subtypes. The sensors yielded novel insights into the role of RA as a primordial morphogen determining the body plan in early embryogenic development of zebrafish (45).

FRET sensors based on ligand-induced domain-domain interactions

A disadvantage of the single recognition domain-based FRET probes described above is that they rely on the subtle internal rearrangements of an individual domain's tertiary structure to change the relative distance and orientation between two FPs. Sensors that are based on multiple domains that undergo ligand-dependent intramolecular protein-protein interactions often yield better results as these sensors exploit the movement of large globular domains relative to one another.

One of the early examples of such a sensor is provided by the first genetically encoded FRET sensor for Ca^{2+}, Cameleon, mentioned above (Figure 1.3B). Miyawaki *et al.* found that a combination of deletions, insertions and substitutions at linker sites between CaM-M13 and the FPs was crucial to achieve sufficient DR, although at the time they provided little detail on their strategy or the number of constructs tested. Their best effort at this time had a DR of 70% (36). In the years that followed, improved Ca^{2+} FRET sensors were developed. Replacement of the photolabile and pH sensitive EYFP with Citrine (46) or Venus (47) improved the sensors' *in situ* performance. Replacement of the CaM-M13 sensing module by the protein Troponin C from chicken helped to improve DR and served to avoid undesirable interactions that might otherwise occur with a FRET sensor employing a human-derived recognition domain (48). Also of importance were mutations, both in Troponin C (49) and CaM (50), that increased the specificity for Ca^{2+} over Mg^{2+}. A significant ~4-fold improvement in the DR of these Ca^{2+} sensors was achieved by replacing the acceptor with a circular permutant acceptor (cpAcceptor), either cpVenus (31) or cpCitrine (49). How the cpAcceptor strategy improved the sensors remained unclear. It has been argued that introduction of a cpAcceptor results in a greater difference in orientation of the FP pair between the Ca^{2+}-loaded and the apo state, modulating R_0 itself (31). However, an alternative hypothesis is that with a cpAcceptor, a hydrophobic face of this protein becomes available for complex formation with the donor FP, resulting in a higher level of FRET in the Ca^{2+}-loaded state of the sensor (51).

Another important second messenger for which FRET sensors have been developed is cAMP, which is synthesized from ATP upon extracellular stimulation of G-protein-coupled receptors (GPCRs). While early efforts in the field focused on using the cAMP-dependent protein kinase (PKA) as a recognition domain in sensors, this protein had the disadvantage of possessing multiple cAMP binding sites and an affinity that was too high (13, 52). Jalink and coworkers realized that the "Exchange protein directly activated by cAMP" (Epac1) had the fortuitous property of a large change in

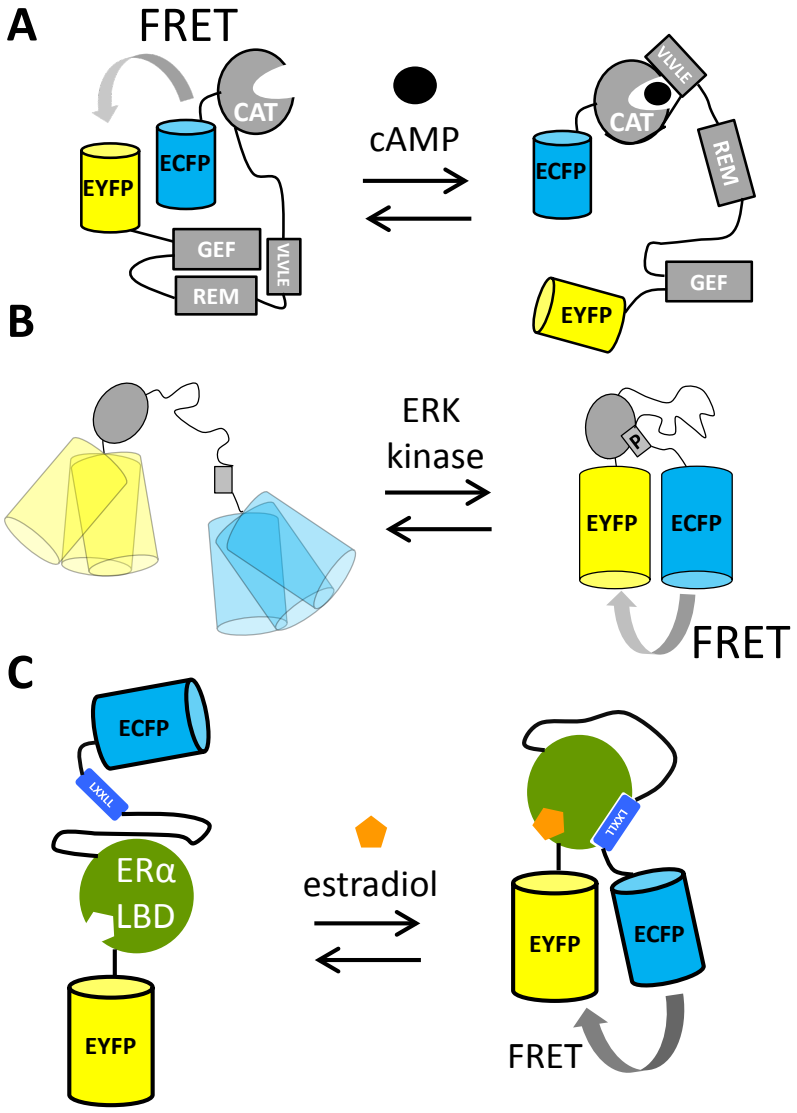

Figure 1.5: Ligand-dependent protein-protein interactions of recognition domains often yield good FRET sensors. *(A) A FRET sensor for cAMP exploiting the multidomain Epac1 cAMP-binding protein. The large conformational rearrangement of Epac1 upon binding cAMP results in a large change in FRET between fluorescent proteins fused to the termini of Epac1(53). (B) In kinase sensors, interaction between a phosphobinding domain and a phosphorylated substrate peptide typically results in an increase in FRET (54). (C) A FRET sensor for agonists of the estrogen receptor uses the ligand binding domain of ERα, together with a co-activator peptide, to bring about a large increase in FRET between ECFP and EYFP upon an estradiol-binding induced co-activator-LBD interaction (55).*

conformation upon cAMP binding. Simply fusing ECPF and EYFP to either end of EPAC1 yielded a functional sensor, which was further improved by deleting a membrane anchoring sequence and introducing mutations that rendered EPAC catalytically dead (Figure 1.5A). This sensor, named CFP–Epac(δDEP-CD)–YFP, had a DR of 45% and an *in vitro* K_d for cAMP of 14 μM (53), two orders of magnitude higher than that of the FlChR sensor (13). Upon binding of cAMP to an N-terminal catalytic domain (CAT), a protein-protein interaction between CAT and a VLVLE motif resulted in an extended conformation of the protein, as the regulatory domain (REM) and the guanine nucleotide exchange factor (GEF) domain no longer interacted (53). The importance of the intramolecular, interdomain interactions seen in the CFP–Epac(δDEP-CD)–YFP mechanism of action is illustrated by the fact that a cAMP sensor that employed only the catalytic domain, Epac2-camps, displayed a significantly reduced DR (56). Further attempts to improve the cAMP sensor included the use of a double acceptor (57) (cpVenus and Venus) and introduction of the brighter donor mTurquoise (58), finally resulting in $^{T}Epac^{VV}$, a bright sensor with a DR of 100% (59).

FRET sensors for another critical component in cell signaling, kinase activity, have been reported for the activities of a number of kinases such as PKA (60), tyrosine kinases such as the insulin receptor (61), Src (62), extracellular signal-regulated kinase (ERK) (54, 63, 64) and protein kinase C (PKC) (65). All these reporters of kinase activity share a common mechanism of action: a kinase "substrate" peptide that becomes phosphorylated and then is recognized by and becomes bound to a binding domain (Figure 1.5B). An important factor that affects the DR of FRET sensors for kinase activity is the basal (i.e. prestimulation) level of phosphorylated sensors. Recently, a strategy was introduced to minimize this level. Komatsu *et al.* reasoned that by increasing the length of the linker connecting the phosphobinding domain with the substrate peptide, the reduced effective concentrations of these interactants would encourage faster dissociation (54). Faster dissociation of the phosphobinding domain from the phosphorylated peptide would allow phosphatases to act on the peptide and return the sensor to the non-phosphorylated off-state. An added benefit of the longer

linker was a reduced level of FRET in the off state. Impressively, the authors demonstrated the benefit of their approach by improving the DR of sensors for the activities of four different kinases, as well as introducing several novel functional kinase sensors (54). For example, EKAR, a FRET sensor for ERK activity (63), was improved 4-fold (54).

Nuclear Receptors (NRs) are transcription factors whose activity can be modulated by small molecule ligands. A large number of NRs are known, with each NR binding specific signaling molecules such as hormones, intracellularly. Upon binding ligand, the NR ligand binding domain (LBD) increases its affinity for co-activator proteins, binding these co-activators *via* their canonical LXXLL motif. This ligand-dependent protein-protein interaction was exploited in FRET sensors consisting of ECFP, LBD, an LXXLL containing peptide and EYFP (Figure 1.5C). For example, a FRET sensor responsive to 17β-estradiol (E2) and other Estrogen Receptor (ER) agonists was constructed using the LBD from ERα. The sensor displayed a 40% DR, binding E2 with an EC_{50} of 80 nM (55). Similar FRET sensors based on the LBDs of the androgen receptor (66) and the glucocorticoid receptor (67) have also been successfully constructed.

Table 1.1: Overview of genetically encoded FRET sensors for small molecules.

ligand	sensor name	donor	acceptor	recognition domain	DR[1]	Ref.
Ca^{2+}	Yellow cameleon 2	ECFP	EYFP	CaM/M13	52%	(36)
	D3cpv	ECFP	cpVenus		273%	(50)
	CaYin1	cpmAm	tdTom		105%	(68)
	CaYang1	mTFP	cpVenus		152%	
	YC3.60	ECFP	cpVenus		1400%	(69)
	YC-Nano15	ECFP	cpVenus		1450%	
	TN-XL	ECFP	cpCit	Troponin C	400%	(49)
	Twitch-2	ECFP	cpCit		1000%	(70)
Zn^{2+}	eCALWY	Cerulean	Citrine	ATOX1/WD4	122%	(71)
	Cys_2His_2	ECFP	Citrine	Zif268	390%	(72)
	ZF12-FRET	ECFP	EYFP	Zap1	30%	(73)
	ZapCmR1	Clover	mRuby2	Zap1	55%	(74)
	redCALWY	mOr	mCherry	ATOX1/WD4	60%	(75)
Mg^{2+}	MagFRET	Cerulean	Citrine	HsCen3	50%	(76)
Cu^{+}	Amt1-FRET	ECFP	EYFP	Amt1	16%	(77)
	eCALWY-C2M/C3M	Cerulean	Citrine	ATOX1/WD4	60%	(78)

Table 1.1 continued

ligand	sensor name	donor	acceptor	recognition domain	DR[1]	Ref.
Cd^{2+}	cdFRET-1	Cerulean	Citrine	FP surface mutations	120%	(79)
	Met-cad 1.57	ECFP	cpVenus	CadR	35%	(80)
PO_4^-/PO_4^{2-}	FLIPPi	ECFP	Venus	PiBP	82%	(81)
citrate	FLIP-CIT8μ	ECFP	Venus	CitA	63%	(82)
glucose	$FLII^{12}Pglu$-600μ	ECFP	EYFP	MglB	42%	(38)
	$FLII^{12}Pglu$-700μδ6	ECFP	Citrine		70%	(40)
	GIP	GFPuv	EYFP		N.R.	(83)
		ECFP	Venus		N.R.	(84)
		acGFP1	mCherry		3.6%	(85)
arabinose	Flip-ara-200n	ECFP	Venus	AraF	20%	(41)
maltose	FLIPmal-2μ	ECFP	EYFP	MBP	13%	(42)
ribose	Fliprib	ECFP	EYFP	RBP	20%	(86)
sucrose	FLIPsuc-90μΔ1	ECFP	EYFP	AtThuE	57%	(87)
lactate	Laconic	mTFP	Venus	LLDR	12%	(88)
histidine	FlIP-cpHisJ194	ECFP	Venus	HisJ	63%	(44)
glutamate	FLII 81PE-1μ	ECFP	Venus	GltI	95%	(38)
	GluSnFR	ECFP	Citrine		7%	(89)
	SuperGluSnFR	ECFP	Citrine		46%	
glutamine	No name provided	ECFP	Citrine	Glutamine BP	56%	(90)
	FLIPQ-TV3.0	mTFP1	Venus	GlnH	25%	(91)
arginine	No name provided	ECFP	Citrine	Glutamine BP	34%	(92)
	FLIP-cpArtJ185	ECFP	Venus	ArtJ	57%	(44)
ATP	Ateam	mseCFP	Venus	ε of FoF1-ATPase	150%	(93)
peptide	Clamp sensor	CyPET	YPet	PDZ/FN3	133%	(94)
bile acids	BAS-1	Cerulean	Citrine	FXR LBD	100%	(95)
retinoic acid	GEPRA-G	ECFP	EYFP	RAR LBD	93%	(45)
molybdate	MolyProbe	Cerulean	cpVenus	MoBD	109%	(96)
cGMP	CGY-del	ECFP	EYFP	cGKI	21%	(97)
	Cygnet-1				55%	(98)
	cGES-DE5			PDE5A/ GAF	16%	(99)
	cGi-500	ECFP	EYFP	cNMP-BD of cGKI	77%	(100)
cAMP	$^{T}Epac^{VV}$	Turq	CP Venus*2	Epac	100%	(59)
	Epac2-camps	ECFP	EYFP	Epac	16%	(56)
	ICUE1	ECFP	Citrine	Epac1	30%	(101)
	CFP–Epac(δDEP-CD)–YFP	ECFP	EYFP	Epac1	45%	(53)
IP_3	LIBRAv	ECFP	Venus	rat IP_3R_3	15%	(102)
testosterone	ficaro	ECFP	EYFP	AR	22%	(66)
glucocorticoids	GLUCOCOR	ECFP	EYFP	GR LBD	45%	(67)
estradiol	SCCoR	ECFP	EYFP	ER LBD	37%	(55)
H_2O_2	OxyFRET	Cerulean	cpVenus	YAP1 and ORP1	10%	(103)
	PerFRET				25%	

*FP abbreviations: mOr (mOrange), cpmAm (circularly permutated mAmetrine), tdTom (tandem dimer Tomato), cpCit (circularly permutated Citrine), CP Venus*2 (tandem heterodimer of a circularly permutated Venus and Venus), Turq (mTurquoise). [1]Where available, the dynamic range measured in vitro for purified FRET sensor protein is reported. If in vitro data is unavailable, the dynamic range measured in mammalian cells is given.*

FRET sensors based on interacting fluorescent domains

Although the strategies described above have delivered many useful and robust FRET sensors, their development required a high level of labor input. The "classical" approaches do not yield generically applicable sensor designs and lack modularity. For example, despite their homology, exchanging of one PBP for another in a FRET sensor requires a whole new round of sensor optimization (38). Similarly, FPs typically cannot be easily exchanged without perturbing the sensor's performance (49, 65).

Our group recently introduced a novel strategy for engineering FRET sensors that use two mutually exclusive interactions within the sensor. In this approach, a ligand-induced protein-protein interaction is mutually exclusive with an interaction between the two fluorescent proteins. Mutations that allow this intramolecular interaction of the fluorescent domains were first discovered in a FACS-based screening of a CFP-YFP containing caspase sensor by Daugherty and colleagues (104). The original aim of that study was to discover mutations that improved the intrinsic fluorescent properties of the fluorescent domains for FRET (104). The authors discovered a FRET pair (CyPet-YPet) that yielded a dramatically improved caspase sensor that underwent a 20-fold change in emission ratio upon caspase cleavage, compared to a 3-fold change in an ECFP-EYFP-based sensor. Although both FPs were somewhat brighter than their ECFP and EYFP parent proteins, we and others subsequently showed that this enhancement could be attributed mainly to an intramolecular dimerization of CyPET with YPet, a conformation that brings the fluorophores in the smallest possible distance of one another (105, 106). We showed, through a systematic study of a system consisting of ECFP and EYFP connected by a long, flexible GGSGGS linker, that it was the mutation S208F on both ECFP and EYFP that was responsible for a

hydrophobic interaction between the domains (105). V224L, another mutation discovered in the original CyPET-YPet FACS-based screening, was found to enhance the FRET efficiency in the dimerized state, likely through a subtle effect on the dimer orientation, but was not capable of mediating the interaction on its own. Crucially, upon enzymatic cleavage of the linker between ECFP and EYFP, the interaction was disrupted (Figure 1.6A). Thus, the interaction only operated at the mM effective concentration provided by the tethering of ECFP and EYFP to one another. Although the interaction was not directly quantified, the K_d should be well above the 1 μM protein concentration used in this study (105).

One of the first applications of these "sticky" fluorescent domain interactions was in the improvement of the CALWY FRET sensor for Zn^{2+}, previously developed in our group (107). In this sensor, Zn^{2+} coordination was provided by two pairs of cysteines, each one located on a separate domain, thereby bringing these domains (ATOX1 and WD4) in fixed orientation to one another upon Zn^{2+} binding, resulting in a reduction of FRET upon Zn^{2+} binding, with a DR of about 21% (107). Introduction of the hydrophobic mutations S208F/V224L resulted in a 6-fold improvement of the DR. This improvement is due to the increase in FRET in the Zn^{2+}-free state, where the hydrophobic FP mutations bring the FPs in close proximity (Figure 1.6B). Upon addition of Zn^{2+}, the FP-FP interaction in eCALWY-1 is disrupted as this state is mutually exclusive with the state in which Zn^{2+} is coordinated between the metal binding domains (Figure 1.6B). Interestingly, the S208F/V224L mutations resulted in a 10-fold attenuation of the sensor's affinity for Zn^{2+}, an observation that is best explained by a thermodynamic coupling between the two mutually exclusive states. As it was found that the resulting 2 pM affinity for Zn^{2+} was still too high, a combined strategy of ATOX1-WD4 linker truncations (107) together with a cysteine to serine mutation of WD4, allowed the generation of series of sensor with attenuated affinities ranging from 2 pM to 3 nM (71). The series of sensors helped to accurately determine the free Zn^{2+} concentration in the mammalian cytosol (~400 pM) for the first time (71).

In a second example, the sticky mutations were applied to the design of a FRET sensor based on the LBD of FXR, the nuclear receptor for bile acids. Like the NR-

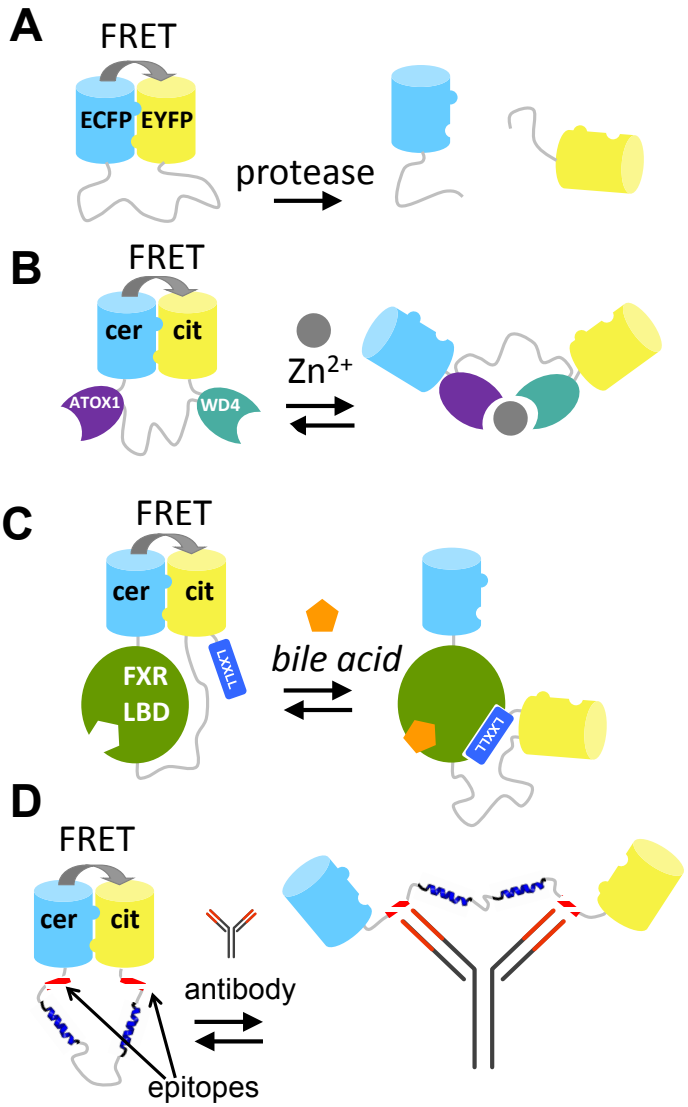

Figure 1.6: FRET sensors based on self-associating fluorescent domains. *These FRET sensors employ the S208F/V224L (A, B) or Q204F/V224L (C, D) hydrophobic mutations on the ECFP-EYFP (A) or Cerulean (cer)-Citrine (cit) (B-D) FRET pairs, ensuring an initial self-association and thus a high level of starting FRET. (A) Protease sensor, cleavage of the intervening linker sequence disrupts the fluorescent domain complex. (B) eCALWY Zn^{2+} sensor, ATOX1-WD4-Zn^{2+} complex disrupts fluorescent domain complex. (C) Bile acid sensor, bile acid-dependent binding of LXXLL to FXR-LBD results in disruption of the fluorescent domain complex. (D) Antibody sensor, binding of antibody to the epitopes adjacent to Cerulean and Citrine disrupts the fluorescent domain complex. Picture from (108).*

based FRET sensors discussed above (Figure 1.5D), the bile acid sensor (BAS) exploited a ligand-induced LBD-cofactor peptide interaction. In this case this interaction served to disrupt the "sticky" FP intramolecular interaction, creating a molecular switch triggered by bile acid binding (95). In the bile acid FRET sensor, the LBD was tightly fused to Cerulean at the LBD's N-terminus, while the LBD's C-terminus was connected via a long flexible linker to Citrine. Finally, a co-activator peptide, containing the LXXLL motif, was fused to Citrine's C-terminus (Figure 1.6C). In the absence of bile acid, the Q204F mutations (equivalent to S208F) on Cerulean and Citrine ensured a high level of FRET due to the intramolecular complex formation of these fluorescent domains. Addition of bile acids resulted in a large reduction of FRET (DR = 100%), due to the induced LBD-co-activator interaction, which was sterically incompatible with the fluorescent domain complex (95).

The "sticky" FPs were also used to design FRET sensors for antibody detection (109). In these sensors, two epitopes, short peptide sequences that are recognized by an antibody, are connected by a semi-flexible linker and are flanked by the Cerulean and Citrine fluorescent domains bearing the Q204F mutation (Figure 1.6D). The epitope binding sites of an antibody are separated by ~100 Å so that binding of a single antibody to both epitopes results in disruption of the FP-FP complex. An initial design, using a fully flexible linker consisting of 9 repeats of GGSGGS, was not functional. This is probably because bridging the 100 Å distance required a full extension of the linker and conformations bringing the linker in the fully extended state occupy just a small proportion of the entire distribution of possible linker conformations. Another way of putting this is that the effective concentration of the second epitope and the second paratopes occurring once the first paratope had bound the first epitope, was very low. Insertion of two alpha-helical blocks within the linker solved the problem and a sensor was produced that displayed a large reduction in its Citrine/Cerulean emission ratio, from 10.5 to 2 (109).

Koide and colleagues recently established a novel protein engineering technique, affinity clamping, whereby a Fibronectin type III domain is evolved by phage display to form a complex with a peptide sequence of choice and a natural peptide binding

domain (PDZ) (110). These domains, which are connected by a short linker, could be converted to FRET sensors of specific peptides, by fusing CyPet and Ypet to either end of the construct. In absence of peptide, CyPet and YPet were intramolecularly dimerized, resulting in a high level of FRET. Addition of a specific peptide resulted in complex formation between Fibronectin type III, peptide and PDZ, resulting in disruption of Cypet-Ypet complex (94) with a DR of 130%.

It is important to realize that many of the classically designed FRET sensors, such as Cameleon and its derivatives have been carefully optimized to exploit subtle changes in the conformation of the recognition domain, so that introduction of dimerizing mutations is unlikely to improve them. Kotera *et al.* reported that introduction of S208F and V224L into the fluorescent domains of Ca^{2+} sensors YC3.60 or TN-XL reduced these FRET sensors' DR more than 5-fold (51). GFP derivatives have a known tendency to dimerize, with a ~100 μM K_d (111). Interestingly, the same sensors required a subtle level of interaction between the fluorescent domains in the Ca^{2+}-bound state of the sensor, as introduction of monomerizing mutation A206K (111) also attenuated the DR of YC3.60 and TN-XL (51) . The KCP-1 and KCP-2 FRET sensors of PKC kinase activity are another example of sensors that require FPs' weak dimerization tendency for their mechanism of action. Introduction of A206K into these sensors' fluorescent domains completely attenuated the sensors' ratiometric response. A control experiment ruled out intermolecular FRET, indicating intramolecular dimerization was the dominant factor (65).

Apart from the detection of small molecules and enzyme activity, FRET between fluorescent proteins may also be used to detect protein-protein interactions (PPI), by tagging one interactant with a FRET donor and the other with an acceptor FP. To achieve sufficient FRET in the PPI state, it is necessary to tightly couple the fluorescent tag to the protein of interest, yet this may cause steric hindrance of the PPI. Longer linkers, while minimizing interference of the PPI, result in only a very weak FRET signal due to the distance dependence of FRET. Recently, Serrano and colleagues provided a solution to this problem, by using a peptide-domain interaction as a secondary interaction for the fluorescent domains. The peptide (Wp2) was fused

adjacent to one FP, while a small domain (WW) with affinity for the peptide was fused adjacent to the other fluorescent domain (Figure 1.7A). The peptide-domain interaction (from a set of previously characterized pairs) was chosen so that the interaction occurred only in the presence of a primary PPI. This "helper" interaction, with a K_d of around 170 μM, improved the detection of PPIs by fluorescence lifetime imaging, by increasing FRET efficiencies about two-fold, from ~20% efficiency of transfer to ~40% (112).

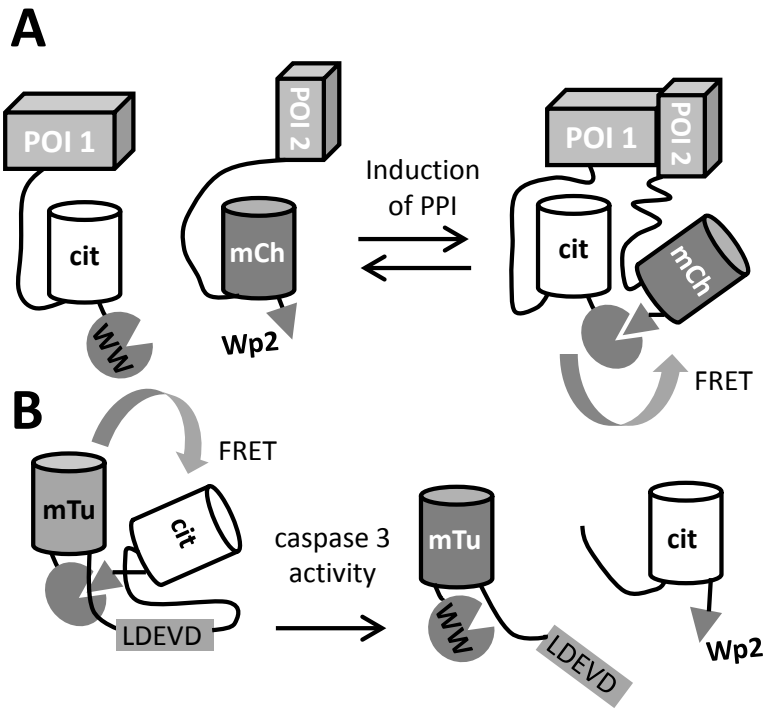

Figure 1.7: "Weak helper interaction" strategy for the generation of efficient FRET probes. *(A) The FRET-based detection of a protein-protein interaction (PPI) between one protein of interest (POI1) and a second POI (POI2) is improved through the use of helper interactions that allow lengthening of the POI-FP linkers. Induction of a PPI leads to efficient FRET from mCitrine (cit) to mCherry (mCh). (B) The helper interactions also improved the dynamic range of intracellular caspase sensors that use mTurquoise2 (mTu) and Citrine (cit) (112).*

A single polypeptide chain caspase sensor was also constructed by fusing the WW domain to the N-terminus of mTurquoise2, the Wp2 peptide to the C-terminus of mCitrine, with a DEVD-containing linker connecting both fluorescent domains (Figure

1.7B). The strategy allowed interactions to be mediated between evolutionarily unrelated mCitrine and mCherry, which would not currently be possible using the hydrophobic mutation strategy discussed above. The authors reported an improvement in the DR of this caspase sensor from about 125% to 150%. The suitability of this strategy for the development of FRET sensors based on mutually exclusive interactions remains to be established.

Development of FRET sensors using high throughput screening

Screening of improved variants by rational, variant-by-variant approaches can be laborious and time-consuming. A more efficient method may be systematically screening a large number of variants for ratiometric response to ligand addition. An early example of the use of high throughput screening for improving such sensors was provided by Hires *et al.* (89). GluSnFr is a sensor of neurotransmitter glutamate and employs the periplasmic binding protein (PBP) GltI, but displayed a poor DR of less than 10% (89). GluSnFr was improved through screening of 175 linker truncation variants, creating SuperGluSnfr, with a 46% DR (89). The poorly responsive EKAR FRET sensor for ERK kinase activity (63), also improved upon by Komatsu *et al.* (54) (see section FRET sensors based on interacting fluorescent domains), was also subjected to a systematic screening. The effects of different combinations of donor FP (wt mTFP1 or 4 different cp variants thereof) and acceptor FP (wt Venus or different cp variants thereof), were tested in the context of four different topologies of the two FPs, substrate peptide and phosphobinding domain (64). A total of 100 different variants were screened directly in mammalian cells using a fluorescence plate reader. Notably, Pertz and coworkers discovered a variant displaying a 2-fold improvement in DR over the original EKAR sensor (64).

With the goal of establishing a rapidly implementable, universal strategy for FRET sensor optimization, Schulz and colleagues created a set of 36 vectors carrying FRET sensor backbones with different combinations of donor (ECFP, mTurquoise and mTurquoise carrying a C-terminal deletion) and acceptor (Venus and 4 different

cpVenus variants) fluorescent domains, together with different linker lengths, between which a kinase of interest was to be cloned (113). Particularly innovative was the use of reverse transfection, where DNA is spotted onto glass microslides, before transfection is achieved by culturing mammalian cells over this DNA. The authors generated FRET sensors for the activities of two different calcium/calmodulin associated kinases. The DR of sensors based on death-associated protein kinase 1 (DAPK1), varied from 10% for the worst variant to 55% for the best variant, proving the value of this systematic screening strategy (113).

Library sizes in FRET sensor development are relatively small when compared to the sizes typically encountered in the development of fluorescent proteins. The screening of sensors is a more complex operation than that of FPs, as sensors need to be screened under two different conditions, in the on and in the off state. In screening for FRET sensors of enzyme activity, one can exploit the fact that sensor variants can be imaged both before and after induction of the enzyme-of-interest. In one particularly innovative effort, Campbell and colleagues discovered improved FRET sensors for the activity of histone methylating enzymes by screening bacterial colonies under two expression regimes: expression of a sensor variant alone or in presence of a co-expressed methylating enzyme. Two libraries with variation in the linker sequences were screened in succession, the first with 392 possible members, the second with 640 possible variants. The throughput was limited due to the need to manually spot each colony on a co-expression and a repression plate. Only 270 colonies for the first library and 540 colonies for the second library were actually screened, suggesting that many potentially useful variants were missed, especially since some variants would have occurred more than once in the screening. Perhaps as a result of that, improvement in DR was a modest 2.3-fold (114).

The same group also reported the use of high throughput, bacterial colony-based screening to improve FRET sensors for kinase activity (115). Earlier work on a FRET sensor for protein kinase B/Akt (PKB) named BKAR (116) had failed to improve the sensor's small DR. A library of ~400 BKAR variants was created, in which the linker sequence between the peptide substrate and the phosphobinding domain was varied,

and different CFP and YFP variants were tested. Dual expression plasmids were used in which BKAR was under an IPTG-inducible promoter, while a constituively active kinase was under control of an arabinose inducible promoter. Bacterial colonies, grown on an IPTG-containing medium, were first imaged in absence of kinase expression. Subsequently, expression of kinase within the bacterial cells was induced by spraying arabinose on the colonies. After 2 hours, during which time kinase formed and was allowed to phosphorylate the BKAR variants, the colonies were imaged again. The best BKAR variant obtained had a DR that represented a disappointing 1.3-fold improvement over the original sensor. Unfazed, the authors attempted to optimize a second kinase sensor, one that reported the activity of CDK1 in complex with cyclin B1. Using the same approach, the authors discovered a highly responsive variant with a DR of 70%, a 4.5-fold improvement over the original sensor (115).

For the high throughput screening of sensors of small molecules, sensors must somehow be exposed to high and low concentrations of ligand. Manipulating the ligand concentration in the cytosol, where sensor variants would normally be located, can be challenging due to the impermeable cytoplasmic membrane. Campbell and co-workers, seeking to improve single FP-based Ca^{2+} sensors, realized that the cytosolic concentration of Ca^{2+} in *E. coli* is low and cannot easily be manipulated, but that the bacterial outer membrane is permeable to small molecules and metal ions, rendering the periplasmic space far more accessible to external manipulation (29).

Using the twin arginine translocation pathway, a system that transports fully folded proteins across the cytoplasmic membrane, single FP-based Ca^{2+} sensors were brought into the periplasmic space (Figure 1.8A). Once there, the Ca^{2+} concentration could be manipulated by spraying a fine mist of EGTA solution over the bacterial colonies growing on an agar plate (Figure 1.8B). Impressively, the authors managed to screen up to 200,000 colonies. Crucially, this strategy allowed manipulation of the sensors' environmental conditions, while keeping the protein associated with its encoding DNA for later analysis. Not only was the DR of the best performing indicator at that time (GCaMP3) improved 2-fold, the authors also introduced novel red-shifted and blue-

shifted variants, as well as an excitation-ratiometric variant displaying a 110-fold change in excitation ratio (29).

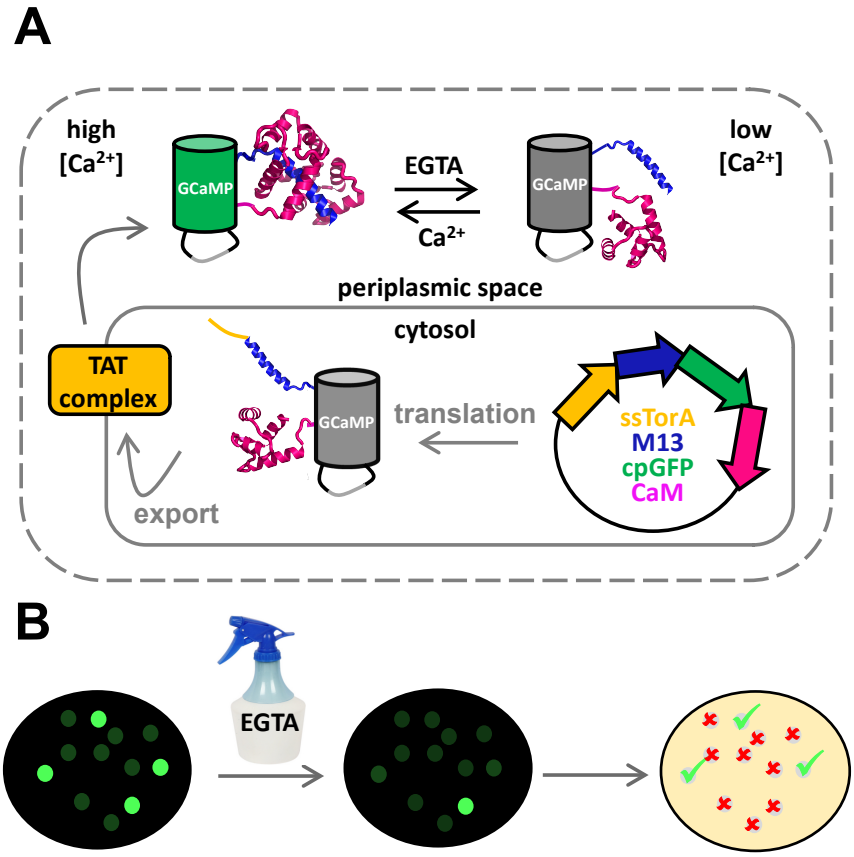

Figure 1.8: Development of GECO-type Ca^{2+} fluorescent sensor proteins. *(A) Fusion of an N-terminal Tat signal sequence targets GCaMP3 to the periplasm, where its fluorescence can be modulated by changing the external [Ca^{2+}] through the addition of EGTA. (B)* E. coli *colonies carrying GCaMP3 variants are screened for EGTA-induced loss of fluorescence. Colonies showing bright fluorescence in the absence and dim fluorescence in the presence of EGTA are selected for further analysis or subsequent rounds of evolution. Figure adapted from (117).*

Recently, Thrustrup *et al.* presented an impressive strategy by which bright Ca^{2+} FRET sensors (called Twitch) were produced with a DR of up to 1000% (70). The initial design, Twitch 1, consisted of a fusion of ECFP, a minimal Ca^{2+}-binding domain (toadfish Troponin C) and EYFP (Figure 1.9A) and yielded, after selection from a 49-member linker library, a sensor with a DR of 400%. Next the authors devised a clever

way to rapidly screen additional variants. Colonies were blotted onto filters, before the filters were sprayed with ionomycin and polylysine, permeabilizing the cells. Using automated image analysis that could recognize the discrete colonies, emission ratios were then detected before and after application of 100 mM $CaCl_2$. In total, two libraries of almost 100,000 colonies each were screened, the first for optimal linkers, the second for optimal mutations at hotspots of the Troponin C domain, selected on the basis of an NMR solution structure (Figure 1.9B). Finally, the ECFP donor was replaced with the much brighter and photostable mCerulean3 (118) or mTurquoise2

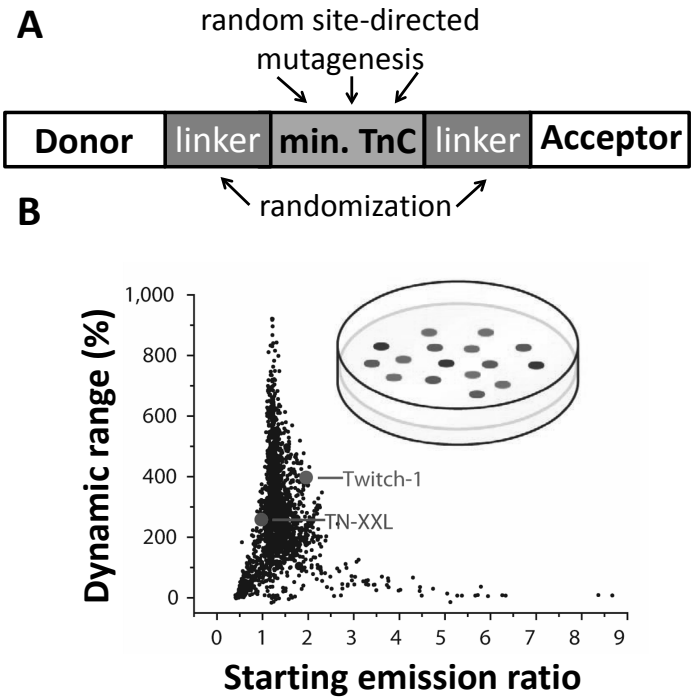

Figure 1.9: High throughput screening of TnC-based Ca^{2+} FRET sensors on bacterial colony basis. *(A) The basic Twitch sensor design consisted of a minimal toadfish TnC domain (min. TnC) flanked by linkers and a donor and acceptor FP. Libraries were created in which the linkers between TnC and the fluorescent domains were randomized and in which certain hotspots within TnC were selected for random site-directed mutagenesis. (B) The graph shows the dynamic range as a function of starting emission ratio measured in >2000 (out of a total of almost 200,000 screened) bacterial colonies. The inset depicts a schematic representation of the screen, which involved imaging the fluorescence from cell-permeabilized bacterial colonies, before and after application of 100 mM $CaCl_2$. Figure adapted from (70).*

(119). Although this initially led to a large reduction in DR, additional screening with extended linkers recovered the sensors' responsiveness.

Several groups have demonstrated the importance of carrying out systematic screening of FRET sensors *in situ* in the cell lines in which the sensor is to be used. Genetically encoded sensors sometimes yield promising results *in vitro* or in mammalian cell cultures yet then fail in more demanding settings such as neurons or mice. For example, it was found that there was a poor correlation between Ca^{2+} sensor GCaMP's DR measured in bacterial lysate and the DR measured in intact HEK293 cells (19). Many of the existing Ca^{2+} sensors are not capable of responding to the rapid neuronal Ca^{2+} switching kinetics. Screening 447 variants in rat hippocampal neurons revealed GCaMP variants with unprecedented sensitivity and fast dynamics (20). GCaMP6f had a two-fold faster rise time and a 1.7-fold faster decay time than the previous generation GCaMP5G (20). Similarly, the Twitch series of Ca^{2+}-FRET sensors was also improved through the screening of 120 variants in rat neurons that were exposed to electrical field stimulation (70).

FRET sensors for multicolor imaging

Signaling pathways in the cell do not operate in isolation but are intricately linked in time and space. The majority of FRET sensors developed to date use derivatives of CFP and YFP (Table 1.1). Determining relationships and their hierarchies is greatly simplified when two or more parameters can be measured in the cell at the same time (120, 121). Red-shifted FRET pairs are therefore needed for co-imaging with these optimized CFP-YFP based FRET sensors. Despite considerable protein engineering efforts, no useful *A. victoria* GFP mutants were found with emissions beyond ~530 nm. It was not until the discovery of red fluorescent proteins DsRed (122) in the coral *Discosoma* and eqFP611 (123) and eqFP578 (124) in the anemone *Entacmaea quadricolor* that this part of the spectrum became accessible (Figure 1.10A). As all three of these RFPs occur as homotetramers, initial efforts focused on monomerizing

them, while maintaining their fluorescent properties. DsRed's hydrophobic AB interface and its more hydrophilic AC interface were successfully broken by 33 mutations resulting in the first monomeric RFP, mRFP1 (125). Further directed evolution on mRFP1 resulted in the mFruit series of differently colored mRFPs, the most notable of which were mOrange and mCherry (126) and later mApple (127). Similar work with eqFP578 led to monomers TagRFP (124) and mKate (128), while mRuby was the product of eqFP611 monomerization (129). The development of FPs with very long Stokes shifts, such as mKeima (130), mAmetrine (131), LSSmOrange (132), LSSmKate2 (133) and mBeRFP (134) has also enabled improved use of the available spectrum.

The reduced spectral footprints of the single FP-based sensors render them useful components in multiparameter imaging strategies. A Ca^{2+}-indicator based on mApple was combined with ATeam, a CFP/YFP-based FRET sensor of ATP (93), allowing simultaneous imaging of cytosolic Ca^{2+} and ATP transients upon stimulation of HeLa cells with histamine (29).

To generate mutually compatible FRET sensors, one strategy has been to avoid CFP/YFP-based FRET sensors altogether and to develop novel sets of orthogonally compatible FRET pairs (135). Multiple FRET pairs can be co-imaged when the donors can be excited separately, even if the pairs' emission spectra partially overlap. An example of such a set of FRET pairs is the combination of Cerulean/mCherry as one pair together with mVenus/mCherry as a second pair, for sensors of cAMP and PKA activity respectively (136). Despite sharing an acceptor, both pairs could be easily excited separately and both sensors displayed excellent *in situ* DRs of ~50%. A second example of mutually compatible FRET pairs is that of mAmetrine/tdTomato ("Yin") & mTFP1/mCitrine ("Yang") (68, 131) reported by Campbell and coworkers. LSS FP mAmetrine's excitation peak is blue-shifted relative to that of mTFP1, again allowing both pairs to be imaged separately, despite the fact that the mAmetrine and mCitrine emission spectra are near-identical (Figure 1.10B). This strategy allowed the imaging of Ca^{2+} and caspase activity in the same cellular compartment (68).

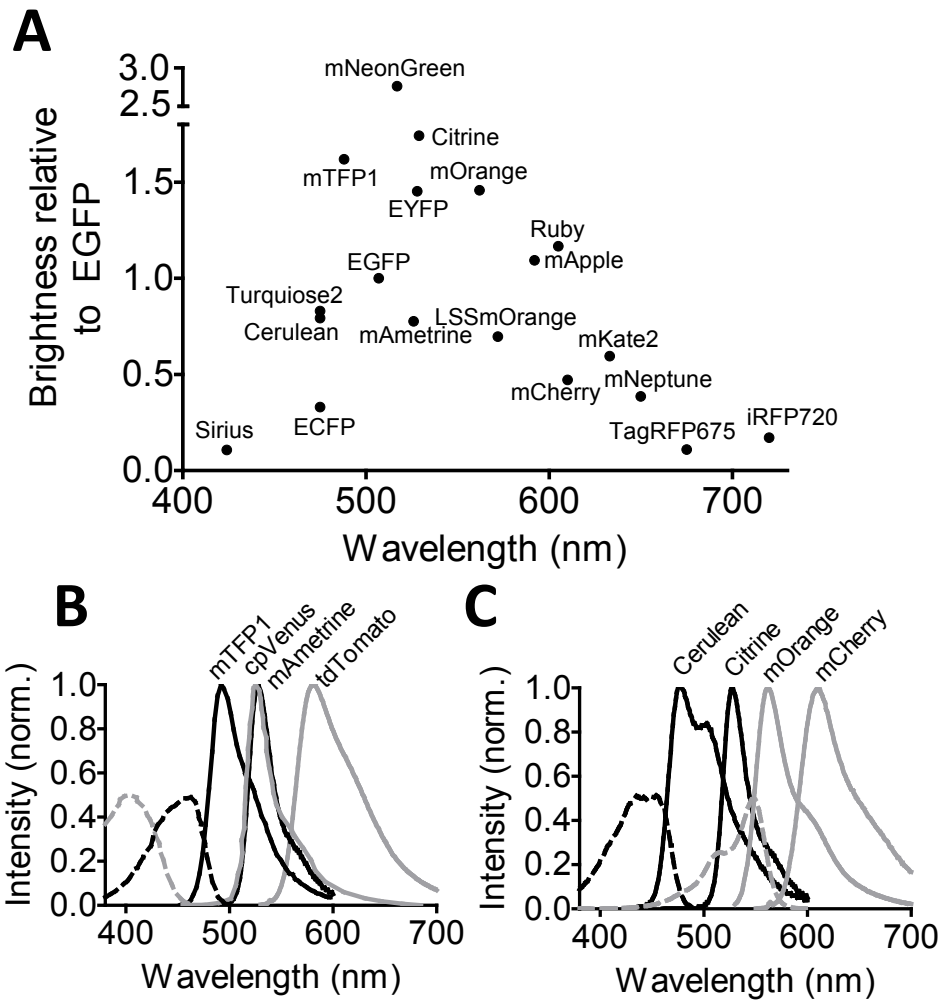

Figure 1.10: Strategies allowing FRET multiplexing. (*A) Overview of important FPs distributed throughout the visible spectrum. Each protein's brightness (a product of its quantum yield and its extinction coefficient at its excitation maximum), relative to the brightness of EGFP, is shown as a function of the emission wavelength peak of that protein. Picture adapted from (137). (B) Donor excitation (dashed traces) and donor and acceptor emission spectra (solid traces) for FRET pairs mAmetrine-tdTomato (Yin, gray) and mTFP1-tdTomato (Yang, black). The separation of the donor excitation spectra allows either FRET pair to be monitored without interference from the other. (C) Same as (B) but with FRET pairs Cerulean-Citrine (black) and mOrange-mCherry (gray). The prevalence of existing CFP-YFP-based FRET sensors makes this combination more attractive than the Yin-Yang pair.*

A major disadvantage of the latter approach is that it is incompatible with the many CFP/YFP-based FRET sensors. The mOrange and mCherry FRET pair is compatible with CFP/YFP-based FRET sensors (Figure 1.10C) and several groups have reported using this red-shifted pair (65, 74, 138-140). However, the DR of sensors using this orange-red FRET pair was typically poor (74, 140) and some even failed to give any response at all (65). For example, a study found that a protease sensor's DR was reduced from 570% to 40% when its CFP/YFP FRET pair was replaced by mOrange and mCherry (140). Despite the poor performance of the mOrange/mCherry FRET pair it played an important part in a seminal paper by Piljic and Schulz, where spatial segregation of sensors into different cellular compartments allowed three parameters to be measured simultaneously (138). A CFP-YFP-based FRET sensor reported protein kinase IIα activity in the cytosol, another CFP-YFP-based sensor tethered to the plasma membrane reported protein kinase C activity while a third sensor (ORNEX4) consisting of mOrange and mCherry fused to annexin A4, a Ca^{2+}-dependent phospholipid-binding protein, was initially in the cytosol and nucleus. When the Ca^{2+} concentration was increased, ORNEX4 translocated to the plasma membrane, where it self-associated, resulting in increased mOrange-mCherry (intermolecular) FRET. The maximal ratiometric change of about 15% seen for ORNEX4 compared poorly to the 150% change previously seen by Piljic and Schulz with CYNEX4, an Annexin A4 sensor based on ECFP and EYFP (141).

The poor performance of the mOrange-mCherry FRET pair is caused by the bleedthrough from the donor emission into the acceptor detection channel, coupled to a low quantum yield of the acceptor (135). As a donor's bleedthrough intensity always changes in the *opposite* direction to the acceptor's sensitized emission in response to a change in FRET, bleedthrough severely attenuates DR. A high acceptor quantum yield can partially compensate for the bleedthrough effect but mCherry's low quantum yield (0.22) results in little compensation (see also Appendix to this thesis).

Aim and outline of this thesis

The work described in this thesis had three main aims: i) to develop improved FRET sensors for intracellular imaging, ii) to increase the efficiency of FRET sensor construction by developing generally applicable sensor design strategies and iii) to gain an improved understanding of the mechanisms behind such improvements.

In **Chapter 2**, the development of the first intracellular FRET sensor for Mg^{2+} is described. This metal ion plays important structural and catalytic roles in the cell. This sensor is based on HsCen3, a protein that binds Mg^{2+} with almost the same high affinity as it does Ca^{2+}. Importantly, upon binding Mg^{2+}, HsCen3 transitions from a molten globule state to a more compact, well-defined, EF-hand-like state. Fusion of Cerulean and Citrine to the N- and C-terminus of HsCen3 resulted in the sensor MagFRET-1, with a 50% increase in emission ratio. Mutations in the metal binding sites yielded MagFRET variants whose Mg^{2+} affinities were attenuated 2- to 100-fold relative to MagFRET-1, thus covering a broad range of Mg^{2+} concentrations. The sensor responded to changes in Mg^{2+} when measured in the cytosol of permeabilized HEK293 cells. The use of intrinsically disordered proteins such as HsCen3 represents a novel strategy for the generation of sensitive FRET sensors.

In **Chapter 3** a generic strategy is reported to enhance the traditionally poor sensitivity of red FRET sensors by developing self-associating variants of mOrange and mCherry that allow sensors to switch between well-defined on- and off states. Similar to our group's recent work on self-association of CFP and YFP derivatives, mutations were discovered that allowed the strength of the mOrange-mCherry interaction to be varied over a 300-fold range. The strategy resulted in a 10-fold improvement of the performance of an mOrange-mCherry-based protease sensor and was essential to generate functional red variants of CFP-YFP-based Zn^{2+} sensors. The large dynamic range afforded by the new red FRET pair allowed simultaneous use of differently colored Zn^{2+} FRET sensors to image Zn^{2+} over a broad concentration range in the same cellular compartment. The strategy developed here should be applicable to many of the recently developed FRET sensors based on mutually exclusive interactions, providing a rapid way of converting these to red-shifted sensors.

In **Chapter 4**, a comprehensive thermodynamic characterization of the stability of a range of self-associating FRET pairs is reported. This stability was quantified by urea titrations, both for the CFP/YFP derivatives and for the newly found mOrange/mCherry interaction. This led to novel insights in the difference between the ECFP and the Cerulean surfaces and their respective ability to form a stable complex with acceptor FPs. Also, novel mutations in mOrange/mCherry were found that allow subtle tuning of the strength of the intramolecular interaction of this FRET pair. Together these findings allow for a better understanding of the subtle effects that determine the performance of existing FRET sensors and help guide the rational design of sensors using modular design strategies.

In **Chapter 5** the application of the newly found self-associating mOrange-mCherry FRET pair is reported for the rapid conversion to a red-shifted probe of another sensor based on mutually exclusive interactions. The Cerulean and Citrine fluorescent domains in the original FXR-based bile acid sensor BAS-1 were replaced by several different self-associating variants of mOrange and mCherry. It was found that a relatively weak mOrange-mCherry interaction was optimal for the sensor. The sensor bound primary bile acids cholic acid and chenodeoxycholic with a 66% change in emission ratio. Multicolor imaging was demonstrated by measuring FRET from the red-shifted sensor and the original sensor targeted to the same cellular compartment.

In **Chapter 6**, a library of genetically encoded FRET-based antibody sensors for the discovery of novel epitope sequences for antibodies of interest is reported. To allow bivalent binding of the antibody to members of the FRET sensor library, a technique was developed that allowed the cloning of a randomly varied, yet perfectly repeated epitope sequence at two separate sites on the DNA encoding the FRET sensor. As a proof of principle, a medium-throughput screening of a small library of FRET sensors carrying variants of epitopes recognized by an anti-HIV antibody is reported. Furthermore, important first steps towards much higher throughput screening of the library using newly developed microfluidics technology is presented. It is demonstrated that the antibody FRET sensors can be expressed by *in vitro* transcription and translation (IVTT) and assayed directly in this IVTT mix.

In the **Appendix** a theoretical background is provided explaining the effects of bleedthrough and acceptor quantum yield on the dynamic range of FRET sensors. Based on this analysis, some FRET pairs are suggested that have not yet been explored but which might be useful in future studies due to increased sensitivity.

Acknowledgements

I am grateful to the members of the Laboratory of Chemical Biology (TU/e) for fruitful discussions. Part of this chapter appeared in:

1) L. Lindenburg, M. Merkx (2012) Colorful calcium sensors, *ChemBioChem* **13**: 349.

2) M. Merkx, M. Golynskiy, L. Lindenburg, J. Vinkenborg (2013) Rational design of FRET sensor proteins based on mutually exclusive domain interactions, *Biochem Soc Trans* **41:** 1201.

References

1. Shimomura O, Johnson FH, & Saiga Y (1962) *J Cell Comp Physiol* **59,** 223-239.
2. Prasher DC, *et al.* (1992) *Gene* **111,** 229-233.
3. Inouye S & Tsuji FI (1994) *FEBS Lett* **341,** 277-280.
4. Chalfie M, *et al.* (1994) *Science* **263,** 802-805.
5. Cody CW, *et al.* (1993) *Biochemistry* **32,** 1212-1218.
6. Heim R & Tsien RY (1996) *Curr Biol* **6,** 178-182.
7. Wang S & Hazelrigg T (1994) *Nature* **369,** 400-403.
8. Presley JF, *et al.* (1997) *Nature* **389,** 81-85.
9. Patterson GH & Lippincott-Schwartz J (2002) *Science* **297,** 1873-1877.
10. Clapham DE (2007) *Cell* **131,** 1047-1058.
11. http://www.olympusconfocal.com/java/fpfluorophores/gfpfluorophore/.
12. Frommer WB, Davidson MW, & Campbell RE (2009) *Chem Soc Rev* **38,** 2833-2841.
13. Adams SR, *et al.* (1991) *Nature* **349,** 694-697.
14. Miesenbock G, De Angelis DA, & Rothman JE (1998) *Nature* **394,** 192-195.
15. Ostergaard H, Henriksen A, Hansen FG, & Winther JR (2001) *EMBO J* **20,** 5853-5862.
16. Baird GS, Zacharias DA, & Tsien RY (1999) *Proc Natl Acad Sci U S A* **96,** 11241-11246.
17. Nakai J, Ohkura M, & Imoto K (2001) *Nat. Biotechnol.* **19,** 137-141.
18. Mank M & Griesbeck O (2008) *Chem. Rev.* **108,** 1550-1564.
19. Tian L, *et al.* (2009) *Nat Methods* **6,** 875-U113.
20. Chen TW, *et al.* (2013) *Nature* **499,** 295-300.
21. Berg J, Hung YP, & Yellen G (2009) *Nat Methods* **6,** 161-166.
22. Tantama M, Martinez-Francois JR, Mongeon R, & Yellen G (2013) *Nat Commun* **4,** 2550.
23. Raimondo JV, *et al.* (2013) *Front Cell Neurosci* **7,** 202.
24. Jin L, *et al.* (2012) *Neuron* **75,** 779-785.
25. Cao G, *et al.* (2013) *Cell* **154,** 904-913.
26. Bilan DS, *et al.* (2013) *ACS Chem Biol* **8,** 535-542.

27. Marvin JS, *et al.* (2013) *Nat Methods* **10,** 162-170.
28. Hanson GT, *et al.* (2004) *J Biol Chem* **279,** 13044-13053.
29. Zhao YX, *et al.* (2011) *Science* **333,** 1888-1891.
30. Akerboom J, *et al.* (2012) *J Neurosci* **32,** 13819-13840.
31. Nagai T, *et al.* (2004) *Proc Natl Acad Sci U S A* **101,** 10554-10559.
32. Hamers D, van Voorst Vader L, Borst JW, & Goedhart J (2013) *Protoplasma* **251,** 333-347.
33. Lakowicz JR (2006) *Principles of fluorescence spectroscopy* (Springer, New York).
34. Patterson GH, Piston DW, & Barisas BG (2000) *Anal Biochem* **284,** 438-440.
35. Akrap N, Seidel T, & Barisas BG (2010) *Anal. Biochem.* **402,** 105-106.
36. Miyawaki A, *et al.* (1997) *Nature* **388,** 882-887.
37. Dwyer MA & Hellinga HW (2004) *Curr Opin Struct Biol* **14,** 495-504.
38. Deuschle K, *et al.* (2005) *Protein Sci* **14,** 2304-2314.
39. Fehr M, *et al.* (2003) *J Biol Chem* **278,** 19127-19133.
40. Takanaga H, Chaudhuri B, & Frommer WB (2008) *Biochim Biophys Acta* **1778,** 1091-1099.
41. Kaper T, *et al.* (2008) *Biotechnol Biofuels* **1,** 11.
42. Fehr M, Frommer WB, & Lalonde S (2002) *Proc Natl Acad Sci U S A* **99,** 9846-9851.
43. Borrok MJ, Kiessling LL, & Forest KT (2007) *Protein Sci* **16,** 1032-1041.
44. Okada S, Ota K, & Ito T (2009) *Protein Sci* **18,** 2518-2527.
45. Shimozono S, *et al.* (2013) *Nature* **496,** 363-366.
46. Griesbeck O, *et al.* (2001) *J Biol Chem* **276,** 29188-29194.
47. Nagai T, *et al.* (2002) *Nat Biotechnol* **20,** 87-90.
48. Heim N & Griesbeck O (2004) *J Biol Chem* **279,** 14280-14286.
49. Mank M, *et al.* (2006) *Biophys J* **90,** 1790-1796.
50. Palmer AE, *et al.* (2006) *Chem Biol* **13,** 521-530.
51. Kotera I, *et al.* (2010) *ACS Chem Biol* **5,** 215-222.
52. Zaccolo M, *et al.* (2000) *Nat Cell Biol* **2,** 25-29.
53. Ponsioen B, *et al.* (2004) *EMBO Rep* **5,** 1176-1180.
54. Komatsu N, *et al.* (2011) *Mol Biol Cell* **22,** 4647-4656.
55. Awais M, Sato M, Sasaki K, & Umezawa Y (2004) *Anal Chem* **76,** 2181-2186.
56. Nikolaev VO, *et al.* (2004) *J Biol Chem* **279,** 37215-37218.
57. van der Krogt GN, Ogink J, Ponsioen B, & Jalink K (2008) *PLoS One* **3,** e1916.
58. Goedhart J, *et al.* (2010) *Nat Methods* **7,** 137-139.
59. Klarenbeek JB, *et al.* (2011) *PLoS One* **6,** e19170.
60. Zhang J, Ma Y, Taylor SS, & Tsien RY (2001) *Proc Natl Acad Sci U S A* **98,** 14997-15002.
61. Sato M, *et al.* (2002) *Nat Biotechnol* **20,** 287-294.
62. Wang Y, *et al.* (2005) *Nature* **434,** 1040-1045.
63. Harvey CD, *et al.* (2008) *Proc Natl Acad Sci U S A* **105,** 19264-19269.
64. Fritz RD, *et al.* (2013) *Sci Signal* **6,** rs12.
65. Jost CA, Reither G, Hoffmann C, & Schultz C (2008) *ChemBioChem* **9,** 1379-1384.
66. Awais M, Sato M, Lee X, & Umezawa Y (2006) *Angew Chem Int Ed Engl* **45,** 2707-2712.
67. Awais M, Sato M, & Umezawa Y (2007) *Steroids* **72,** 949-954.
68. Ding Y, Ai HW, Hoi H, & Campbell RE (2011) *Anal Chem* **83,** 9687-9693.
69. Horikawa K, *et al.* (2010) *Nat Methods* **7,** 729-732.
70. Thestrup T, *et al.* (2014) *Nat Methods* **11,** 175-182.
71. Vinkenborg JL, *et al.* (2009) *Nat Methods* **6,** 737-740.
72. Dittmer PJ, Miranda JG, Gorski JA, & Palmer AE (2009) *J Biol Chem* **284,** 16289-16297.
73. Qiao W, *et al.* (2006) *Proc Natl Acad Sci U S A* **103,** 8674-8679.
74. Miranda JG, *et al.* (2012) *PLoS One* **7,** e49371.
75. Lindenburg LH, *et al.* (2013) *ACS Chem Biol* **8,** 2133–2139.
76. Lindenburg LH, *et al.* (2013) *PLoS One* **8,** e82009.
77. Wegner SV, *et al.* (2010) *J Am Chem Soc* **132,** 2567-2569.
78. Koay MS, Janssen BM, & Merkx M (2013) *Dalton Trans* **42,** 3230-3232.

79. Vinkenborg JL, van Duijnhoven SM, & Merkx M (2011) *Chem Commun (Camb)* **47,** 11879-11881.
80. Chiu TY, Chen PH, Chang CL, & Yang DM (2013) *PLoS One* **8,** e65853.
81. Gu H*, et al.* (2006) *FEBS Lett* **580,** 5885-5893.
82. Ewald JC*, et al.* (2011) *PLoS One* **6,** e28245.
83. Ye K & Schultz JS (2003) *Anal Chem* **75,** 3451-3459.
84. Garrett JR, Wu X, Jin S, & Ye K (2008) *Biotechnol Prog* **24,** 1085-1089.
85. Veetil JV, Jin S, & Ye K (2010) *Biosens Bioelectron* **26,** 1650-1655.
86. Lager I, Fehr M, Frommer WB, & Lalonde S (2003) *FEBS Lett* **553,** 85-89.
87. Lager I*, et al.* (2006) *J Biol Chem* **281,** 30875-30883.
88. San Martin A*, et al.* (2013) *PLoS One* **8,** e57712.
89. Hires SA, Zhu Y, & Tsien RY (2008) *Proc Natl Acad Sci U S A* **105,** 4411-4416.
90. Yang H, Bogner M, Stierhof YD, & Ludewig U (2010) *PLoS One* **5,** e8917.
91. Gruenwald K*, et al.* (2012) *PLoS One* **7,** e38591.
92. Bogner M & Ludewig U (2007) *J Fluoresc* **17,** 350-360.
93. Imamura H*, et al.* (2009) *Proc Natl Acad Sci U S A* **106,** 15651-15656.
94. Huang J & Koide S (2010) *ACS Chem Biol* **5,** 273-277.
95. van der Velden LM*, et al.* (2013) *Hepatology* **57,** 740-752.
96. Nakanishi Y*, et al.* (2013) *PLoS One* **8,** e58175.
97. Sato M, Hida N, Ozawa T, & Umezawa Y (2000) *Anal Chem* **72,** 5918-5924.
98. Honda A*, et al.* (2001) *Proc Natl Acad Sci U S A* **98,** 2437-2442.
99. Nikolaev VO, Gambaryan S, & Lohse MJ (2006) *Nat Methods* **3,** 23-25.
100. Russwurm M*, et al.* (2007) *Biochem J* **407,** 69-77.
101. DiPilato LM, Cheng X, & Zhang J (2004) *Proc Natl Acad Sci U S A* **101,** 16513-16518.
102. Tanimura A*, et al.* (2009) *J Biol Chem* **284,** 8910-8917.
103. Enyedi B, Zana M, Donko A, & Geiszt M (2013) *Antioxid Redox Signal* **19,** 523-534.
104. Nguyen AW & Daugherty PS (2005) *Nat Biotechnol* **23,** 355-360.
105. Vinkenborg JL*, et al.* (2007) *ChemBioChem* **8,** 1119-1121.
106. Ohashi T, Galiacy SD, Briscoe G, & Erickson HP (2007) *Protein Sci* **16,** 1429-1438.
107. van Dongen EM*, et al.* (2007) *J. Am. Chem. Soc.* **129,** 3494-3495.
108. Merkx M, Golynskiy MV, Lindenburg LH, & Vinkenborg JL (2013) *Biochem Soc Trans* **41,** 1201-1205.
109. Golynskiy MV, Rurup WF, & Merkx M (2010) *ChemBioChem* **11,** 2264-2267.
110. Huang J, Koide A, Makabe K, & Koide S (2008) *Proc Natl Acad Sci U S A* **105,** 6578-6583.
111. Zacharias DA, Violin JD, Newton AC, & Tsien RY (2002) *Science* **296,** 913-916.
112. Grünberg R*, et al.* (2013) *Nat Methods* **10,** 1021-1027.
113. Piljic A, de Diego I, Wilmanns M, & Schultz C (2011) *ACS Chem Biol* **6,** 685-691.
114. Ibraheem A, Yap H, Ding Y, & Campbell RE (2011) *BMC Biotechnol* **11,** 105.
115. Belal AS*, et al.* (2013) *Mol Biosyst* **10,** 191-195.
116. Kunkel MT*, et al.* (2005) *J Biol Chem* **280,** 5581-5587.
117. Lindenburg L & Merkx M (2012) *ChemBioChem* **13,** 349-351.
118. Markwardt ML*, et al.* (2011) *PLoS One* **6,** e17896.
119. Goedhart J*, et al.* (2012) *Nat Commun* **3,** 751.
120. Welch CM, Elliott H, Danuser G, & Hahn KM (2011) *Nat Rev Mol Cell Biol* **12,** 749-756.
121. Depry C, Mehta S, & Zhang J (2013) *Pflugers Arch* **465,** 373-381.
122. Matz MV*, et al.* (1999) *Nat Biotechnol* **17,** 969-973.
123. Wiedenmann J*, et al.* (2002) *Proc Natl Acad Sci U S A* **99,** 11646-11651.
124. Merzlyak EM*, et al.* (2007) *Nat Methods* **4,** 555-557.
125. Campbell RE*, et al.* (2002) *Proc Natl Acad Sci U S A* **99,** 7877-7882.
126. Shaner NC*, et al.* (2004) *Nat Biotechnol* **22,** 1567-1572.
127. Shaner NC*, et al.* (2008) *Nat Methods* **5,** 545-551.
128. Shcherbo D*, et al.* (2007) *Nat. Methods* **4,** 741-746.

129. Kredel S, *et al.* (2009) *PLoS One* **4,** e4391.
130. Kogure T, *et al.* (2006) *Nat Biotechnol* **24,** 577-581.
131. Ai HW, Hazelwood KL, Davidson MW, & Campbell RE (2008) *Nat Methods* **5,** 401-403.
132. Shcherbakova DM, *et al.* (2012) *J Am Chem Soc* **134,** 7913-7923.
133. Piatkevich KD, *et al.* (2010) *Proc Natl Acad Sci U S A* **107,** 5369-5374.
134. Yang J, *et al.* (2013) *PLoS One* **8,** e64849.
135. Carlson HJ & Campbell RE (2009) *Curr Opin Biotechnol* **20,** 19-27.
136. Aye-Han NN, Allen MD, Ni Q, & Zhang J (2012) *Molecular Biosystems* **8,** 1435-1440.
137. Dedecker P, De Schryver FC, & Hofkens J (2013) *J Am Chem Soc* **135,** 2387-2402.
138. Piljic A & Schultz C (2008) *ACS Chem Biol* **3,** 156-160.
139. Goedhart J, *et al.* (2007) *PLoS One* **2,** e1011.
140. Ouyang M, *et al.* (2010) *Cancer Res* **70,** 2204-2212.
141. Piljic A & Schultz C (2006) *Mol Biol Cell* **17,** 3318-3328.

Chapter 2

MagFRET: the first genetically encoded fluorescent Mg^{2+} sensor

Abstract. Magnesium has important structural, catalytic and signaling roles in cells, yet few tools exist to image this metal ion in real time and at subcellular resolution. Here we report the first genetically encoded sensor for Mg^{2+}, MagFRET-1. This sensor is based on the high-affinity Mg^{2+}-binding domain of human centrin 3 (HsCen3), which undergoes a transition from a molten-globular apo form to a compactly-folded Mg^{2+}-bound state. Fusion of Cerulean and Citrine fluorescent domains to the ends of HsCen3 yielded MagFRET-1, which combines a physiologically relevant Mg^{2+} affinity (K_d = 148 μM) with a 50% increase in emission ratio upon Mg^{2+} binding due to a change in FRET efficiency between Cerulean and Citrine. Mutations in the metal binding sites yielded MagFRET variants whose Mg^{2+} affinities were attenuated 2- to 100-fold relative to MagFRET-1, thus covering a broad range of Mg^{2+} concentrations. *In situ* experiments in HEK293 cells showed that MagFRET-1 can be targeted to the cytosol and the nucleus. Clear responses to changes in extracellular Mg^{2+} concentration were observed for MagFRET-1-expressing HEK293 cells when they were permeabilized with digitonin, whereas similar changes were not observed for intact cells. Although MagFRET-1 is also sensitive to Ca^{2+}, this affinity is sufficiently attenuated (K_d of 10 μM) to make the sensor insensitive to known Ca^{2+} stimuli in HEK293 cells. While the potential and limitations of the MagFRET sensors for intracellular Mg^{2+} imaging need to be further established, we expect that these genetically encoded and ratiometric fluorescent Mg^{2+} sensors could prove very useful in understanding intracellular Mg^{2+} homeostasis and signaling.

Introduction

Magnesium is the most abundant intracellular divalent cation and is involved in numerous essential cellular processes including replication, transcription, translation and energy metabolism. In addition to its omnipresent role as an essential enzymatic cofactor, Mg^{2+} is also important for chromatin stability and regulates specific ion channels (1, 2). The total cellular Mg^{2+} concentration ranges between 14-20 mM, but the concentration of free Mg^{2+} in the cytosol has been estimated to be between 0.1 and 1.5 mM (3-7). Given its importance to so many different cellular processes, the intracellular Mg^{2+} concentration is generally believed to be strongly buffered and tightly regulated by the combined action of magnesium binding (macro)molecules (proteins, ribonucleic acids, ATP, etc.), storage in organelles and the action of Mg^{2+} channels (8-10). Hereditary disorders related to Mg^{2+} homeostasis have been shown to result in diminished kidney functioning and in severe cases to renal failure, muscle spasms and seizures (11). Magnesium deficiency has also been shown to accelerate cellular senescence (12), providing a potential link between low dietary magnesium intake and the early onset of aging diseases such as diabetes (13), cardiovascular diseases (14) and osteoporosis (15). Recent studies suggested that T cell activation following antigen receptor stimulation was dependent on a transient influx of Mg^{2+} in the cytosol, implicating a novel role for Mg^{2+} as second messenger in intracellular signal transduction (16).

Despite the abundance and importance of Mg^{2+}, the intracellular regulation of Mg^{2+} homeostasis and the putative role of Mg^{2+} in intracellular signal transduction are not well understood. In part this is because of a lack of convenient molecular tools to image the intracellular Mg^{2+} concentration in single living cells in real time (17). Magnesium-selective microelectrodes have been used to determine cytosolic Mg^{2+} levels in different muscle cells, revealing concentrations between 0.7 and 0.9 mM (4). However, these microelectrodes are highly invasive and do not provide spatial information. Another method to probe the intracellular concentration of Mg^{2+} is the measurement of the ratio of Mg^{2+}-bound and Mg^{2+}-free ATP using ^{31}P NMR (18). While non-invasive, ^{31}P NMR measures Mg^{2+} indirectly and averaged over a large

collection of cells (19, 20). Currently, the most commonly applied approach uses synthetic dyes that alter their fluorescent properties upon binding of Mg^{2+} (21-27). However, many of the available dyes show limited specificity for Mg^{2+} and often bind Ca^{2+} with low micromolar affinity (22, 25, 26), which has been shown to interfere in an intracellular setting (28). A notable exception is KMG-104 and related dyes developed by Kuzuki and coworkers, whose affinity for Mg^{2+} is higher than for Ca^{2+} (K_d = 2.1 and 7.5 mM, respectively), rendering these dyes completely insensitive to physiological changes in cytosolic Ca^{2+} concentration (24, 29, 30). Recently a variant of this dye, KMG-103 was reported that showed preferred accumulation in mitochondria (27). Like most synthetic Mg^{2+} dyes, the KMG dyes are intensiometric, making Mg^{2+} quantification challenging and sensitive to changes in sensor concentration. A few ratiometric Mg^{2+} fluorescent dyes (e.g. Mag-Fura and Mag-Indo) exist, yet these have the disadvantage that they require potentially cytotoxic UV excitation (17).

Genetically encoded fluorescent sensor proteins provide an attractive alternative to small-molecule fluorescent sensors, because they do not require cell-invasive procedures, their concentration can be tightly controlled and they can be targeted to different locations in the cell (31). Many of these sensors consist of metal binding domains fused to a donor and an acceptor fluorescent domain capable of Förster Resonance Energy Transfer (FRET). Modulation of the distance and/or orientation of the fluorescent domains following metal binding affects the FRET efficiency, which can be detected as a change in the emission ratio, an output signal that is independent of sensor concentration. In addition, the use of natural metal binding protein domains often ensures a physiologically relevant metal binding affinity and specificity. The wealth of genetically encoded sensors that have been developed for Ca^{2+} (32-35) and more recently also for Zn^{2+} (36-39) and Cu^{+} (40, 41), have made important contributions to the understanding of intracellular metal homeostasis and signaling.

Surprisingly, no genetically encoded sensors have thus far been reported for Mg^{2+}. One of the specific challenges in this case is metal binding specificity. Mg^{2+} and Ca^{2+} show similar coordination chemistry and often bind to the same metal binding proteins, with Ca^{2+} typically showing stronger binding. Here we report the first genetically

encoded fluorescent sensor (MagFRET-1) for Mg^{2+} by taking advantage of the particular metal binding properties of the N-terminal part of the HsCen3 protein, which binds both Ca^{2+} and Mg^{2+} with high affinity (42). We show that Mg^{2+} binding to MagFRET-1 induces folding from a molten-globule state that results in an increase in FRET. Mutagenesis of metal binding site residues allowed further tuning of the metal binding properties, yielding MagFRET variants with K_d values for Mg^{2+} binding ranging between 0.15 and 15 mM. While also responsive to Ca^{2+} *in vitro*, we show that the Ca^{2+} affinities of the MagFRET sensors are sufficiently attenuated that they are not responsive to normal Ca^{2+} fluctuations *in situ*.

Results

Sensor design

The construction of a FRET sensor for Mg^{2+} requires the availability of a metal binding domain that undergoes a large conformational change and displays a relatively high affinity for Mg^{2+} compared to Ca^{2+}. Cox and coworkers previously reported that a truncated version of HsCen3, containing the first two of its four native EF-hand metal binding sites, undergoes a dramatic change in conformation upon metal binding from a molten globular (MG) state to a compact, natively-folded state (42). Unlike most other EF hand-like proteins, which typically bind Ca^{2+} orders of magnitude more strongly than Mg^{2+}, HsCen3's first EF hand is a high-affinity mixed Mg^{2+}/Ca^{2+} binding site, with a reported K_d for Mg^{2+} of 10-28 μM and a K_d for Ca^{2+} of 1.5-8 μM. The second metal binding site was reported to bind only Ca^{2+}, but with a much weaker affinity (K_d = 140 μM). HsCen3 is one of the four isoforms of human Centrin, a family of proteins that is involved in centriole duplication. We based our design on the structure of HsCen2, which shows high homology to HsCen3 and is the only isoform for which an X-ray structure has been determined (Figure 2.1A). The 11 kDa N-terminal fragment studied by Cox and coworkers contained the complete α-helix connecting the 2nd and 3rd EF hand sites. To decrease the distance between the N- and C-termini of the recognition domain in the Mg^{2+}-bound state, we decided to truncate this helix to

approximately half its size (aa 23-98) and fuse it to the fluorescent proteins Cerulean and Citrine (Figure 2.1B). To ensure that a conformational change of the HsCen3 domain in MagFRET-1 was translated to a maximal change in relative orientation of the fluorescent domains, the final 8 amino acids from the flexible C-terminus of Cerulean were removed.

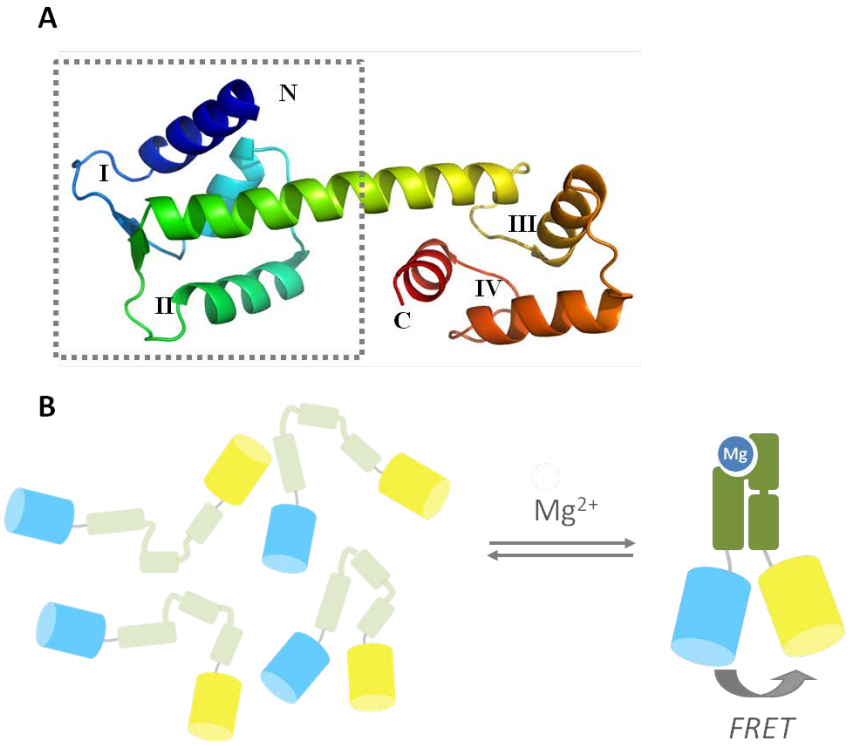

Figure 2.1: Design of the genetically encoded magnesium FRET sensor MagFRET. *(A) Crystal structure (PDB code 2GGM) of HsCen2 in the calcium-bound, compact state. The typical helix-loop-helix structure can be observed, with EF-hands indicated by Roman numerals. The dotted lines indicate the N-terminal truncated part of the domain used in the sensor. In HsCen3, the high-affinity Mg^{2+}/Ca^{2+} binding site is in loop I, and a much weaker Ca^{2+}-binding site is found in loop II. (B) Schematic representation of MagFRET, where the N-terminal truncation of HsCen3 is flanked by Cerulean and Citrine. In absence of Mg^{2+}, the HsCen3 domain is in a molten globule-like state, with little tertiary structure and a relatively large average distance between the fluorescent domains. Mg^{2+}-binding induces a compact, well-defined tertiary structure, resulting in increased energy transfer between Cerulean and Citrine.*

In vitro characterization of MagFRET-1

To allow characterization of MagFRET-1 *in vitro*, a His-tagged sensor construct was expressed in good yield in *E. coli* BL21(DE3) and purified using Ni^{2+}-affinity and size exclusion chromatography. A relatively high ratio of Citrine to Cerulean emission of 3.6 was observed in the absence of Mg^{2+}, indicating that the molten globule state of the metal binding domain is relatively compact bringing the fluorescent domains close together (Figure 2.2A). As expected, a further increase in emission ratio of 50% was observed upon addition of Mg^{2+}, which is consistent with the formation of a more compact metal-bound, native state. The increase in emission ratio could be fitted using a 1:1 binding model, yielding a K_d for Mg^{2+} of 148 ± 23 μM (Figure 2.2B). Fortunately, this affinity is in the (lower) range of the cytosolic $[Mg^{2+}]_{free}$ reported by previous methods, and 10-fold weaker than that reported by Cox *et al.* for their N-terminal variant of HsCen3 (42). Since HsCen3 was reported to not only bind Mg^{2+} but also contain two Ca^{2+} binding sites (42), the Ca^{2+} response of MagFRET-1 was also tested. Addition of Ca^{2+} led to a biphasic increase in emission ratio, which was fitted to a 2:1 binding model. Binding of Ca^{2+} to the high affinity site showed a K_d of 10 ± 4 μM and resulted in a 19% increase in emission ratio. An additional 20% increase in emission ratio was observed at Ca^{2+} concentrations above 1 mM, but the low affinity for this site precluded accurate determination of its K_d (Figure 2.2C). While the absolute affinity of MagFRET-1 for Ca^{2+} is higher than for Mg^{2+}, the sensor would not be expected to be sensitive to normal fluctuations in bulk cytosolic Ca^{2+} concentrations, which range between 0.1 and 1 μM (43). No increase in emission ratio was observed upon addition of 10 μM Ba^{2+}, Ni^{2+}, Cu^{2+} or Fe^{3+}, while only a very small increase was seen for 10 μM Zn^{2+} (Figure 2.2D), a concentration that is 10,000-fold higher than the free Zn^{2+} concentration found in the cytosol (36).

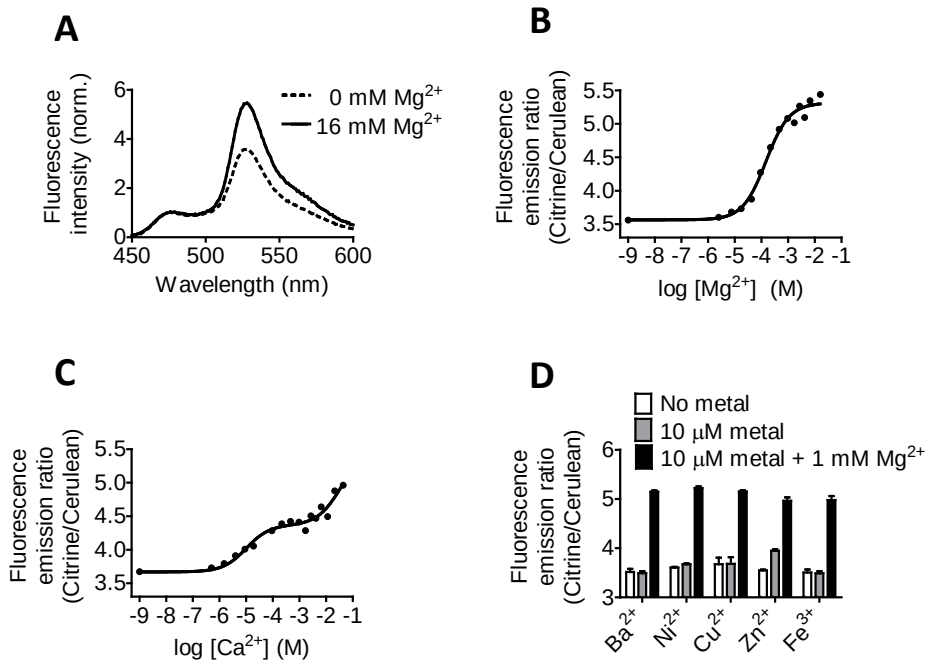

Figure 2.2: Metal binding properties of MagFRET-1. *(A) Normalized fluorescence emission spectra of MagFRET-1 at 0 and at 16 mM Mg^{2+} after excitation at 420 nm. (B, C) Emission ratio (Citrine to Cerulean) of MagFRET-1 as a function of the Mg^{2+} (B) or Ca^{2+} (C) concentration. Solid lines indicate a fit to a single (B) or a double (C) binding event, yielding a K_d of 0.15 ± 0.02 mM for Mg^{2+} and K_ds of 10 ± 4 µM and ~35 mM for Ca^{2+}, respectively. (D) Emission ratios of MagFRET-1 in absence of metal, in the presence of 10 µM Ba^{2+}, Ni^{2+}, Cu^{2+}, Zn^{2+} or Fe^{3+} , and in the presence of the same metals and 1 mM Mg^{2+}. Measurements were performed in triplicate, error bars indicate SEM. All measurements were performed in 150 mM Hepes (pH 7.1), 100 mM NaCl and 10% (v/v) glycerol with 0.2 µM sensor protein.*

Another important aspect of sensor performance is pH sensitivity. Ca^{2+} and Mg^{2+} titrations performed at pH 6 and pH 8 showed that metal binding affinities were unaffected within this pH range (Figure 2.3A-D). As expected, the absolute emission ratios were somewhat lower at pH 6 (Figure 2.3A, C), due to the pH sensitivity of Citrine, which has a pK_a of 5.7 (44). Finally, we noticed that the emission ratio of the apo form of the sensor is dependent on the ionic strength of the buffer (Figure 2.3E). When the Mg^{2+} titration was repeated in a low ionic strength buffer, the emission ratio

of the apo form decreased to 2.2, whereas the emission ratio in the Mg^{2+}-bound state

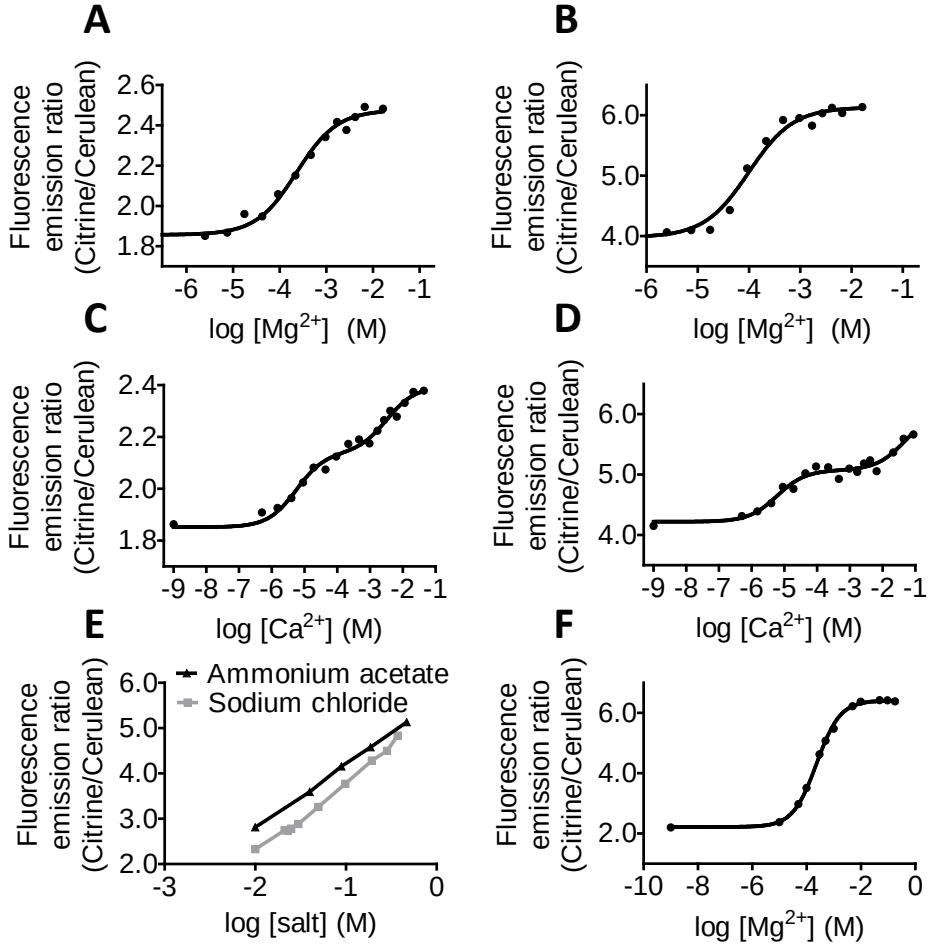

Figure 2.3: Effect of pH and ionic strength on MagFRET-1. *To investigate pH sensitivity, the MagFRET-1 emission ratio was followed as a function of Mg^{2+} (A, B) and Ca^{2+} (C, D) concentration, at pH 6 (A, C) and pH 8 (B, D). Fitting of the data revealed a MagFRET-1 K_d for Mg^{2+} of 230 ±35 µM at pH 6 and 99 ±18 µM at pH 8. The sensor's K_d for Ca^{2+} (first binding event) at pH 6 was found to be 5.6 ±1.7 µM, while at pH 8 it was 5.9 ± 1.9 µM. Buffers used were 150 mM MES (pH 6), 100 mM NaCl and 10% glycerol for pH 6 and 150 mM Tris (pH 8), 100 mM NaCl and 10% glycerol for pH 8. (E) Emission ratio of MagFRET-1 at increasing concentrations of ammonium acetate or NaCl in a buffer with low ionic strength. (F) Emission ratios of MagFRET-1 as a function of Mg^{2+} concentration in a buffer with low ionic strength. The low ionic strength buffer used in (E, F) was 20 mM Hepes (pH 7.1), 10 mM NaCl, 10% (v/v) glycerol. Fitting of the data using a single binding event revealed a K_d for Mg^{2+} of 231 ± 10 µM.*

was the same (Figure 2.3F) and the Mg^{2+} affinity remained mostly unaffected (K_d = 231 ± 10 μM). This ionic strength dependence most likely reflects the influence of ionic strength on the compactness of the molten globule structure of HsCen3. Although the effect is less pronounced at physiologically relevant salt concentrations, it does mean that large changes in ionic strength should be avoided when applying MagFRET-1 *in situ*.

Tuning metal binding affinities

To test whether we could further tune the metal affinity and specificity of the MagFRET sensor we explored several mutations in both metal binding sites. Targeting key residues in the 1st EF hand (D1A, D3E, A7D and D5E/A7E) resulted in a reduction of both the Mg^{2+} and Ca^{2+} affinity to the millimolar regime, indicating that these residues are indeed directly involved in high affinity metal binding (Table 2.1, Figure 2.4C-F). Only a single Ca^{2+}-binding event was observed for these mutants, suggesting that the two EF hands in MagFRET-3-6 have a similar Ca^{2+} affinity, making the two binding events indistinguishable. Interestingly, an E6D substitution (MagFRET-2) did not alter the affinity for Mg^{2+} or Ca^{2+} (Figure 2.4B, Table 2.1), showing that the presence of a glutamic acid at this position is not essential for high affinity metal binding. Although the change in emission ratio for binding Mg^{2+} is attenuated to 33% in this variant, the response to Ca^{2+} binding is almost absent for the high affinity site (3%), rendering this variant effectively Ca^{2+} insensitive. In an effort to abolish Ca^{2+} binding to the weakly Ca^{2+}-binding EF hand II, we replaced aspartic acid 1 (MagFRET-7) and glycine 6 (MagFRET-8) at that site by positively charged lysine residues. Surprisingly, upon titration of Ca^{2+}, both sensor variants still displayed the same biphasic response as seen with MagFRET-1 (Figure 2.4A, G, H), showing that neither of these residues is essential for the low affinity Ca^{2+} binding event in EF hand II. Interestingly, both the D1K and the G6K mutation subtly attenuated the high affinity mixed Ca^{2+}/Mg^{2+} site in EF-hand I, leading to a 6- and 5-fold decrease of the Mg^{2+} affinity and a 6- and 4-fold decrease in Ca^{2+} affinity, respectively (Figure 2.4G,

H). The somewhat weaker affinities for both Mg^{2+} and Ca^{2+} observed for MagFRET-7 and MagFRET-8 could prove beneficial for imaging Mg^{2+} homeostasis under conditions where the intracellular Mg^{2+} concentrations are higher.

Table 2.1. Sensor properties of the different MagFRET variants.

Mutant	1st EF-Hand sequence[1]	2nd EF-Hand sequence[1]	K_d Mg^{2+} / mM ±SE[2]	DR Mg^{2+} binding event[3]	$K_{d,1}$ Ca^{2+} / µM ±SE[2]	D.R. 1st Ca^{2+} binding event[3]
MagFRET-1	DTDKDEAIDYHE	DREATGKITFED	0.15 ±0.02	49%	10 ±3.7	19%
MagFRET-2	DTDKD**D**AIDYHE	DREATGKITFED	0.35 ±0.03	33%	15 ±9.8	3.1%
MagFRET-3	**A**TDKDEAIDYHE	DREATGKITFED	9.2 ±0.7	58%	4500 ±243	66%
MagFRET-4	DT**E**KDEAIDYHE	DREATGKITFED	8.5 ±0.5	62%	4500 ±311	64%
MagFRET-5	DTDKDE**D**IDYHE	DREATGKITFED	7.4 ±0.5	74%	1600 ±116	49%
MagFRET-6	DTDK**E**E**E**IDYHE	DREATGKITFED	15 ±0.8	50%	7900 ±786	55%
MagFRET-7	DTDKDEAIDYHE	**K**REATGKITFED	0.78 ±0.04	38%	57 ±5	23%
MagFRET-8	DTDKDEAIDYHE	DREAT**K**KITFED	0.89 ±0.06	56%	36 ±5	25%

[1]Mutations introduced in the first or second 12-residue metal binding loops of HsCen3 are indicated in bold and are underlined. [2]The dissociation constant (K_d) for each variant's Mg^{2+} and first Ca^{2+} binding event is indicated, together with the standard error (SE). [3]A binding event's dynamic range (DR) is defined as the difference in emission ratio between the unbound and fully metal bound form divided by the emission ratio in the unbound form, multiplied by 100%.

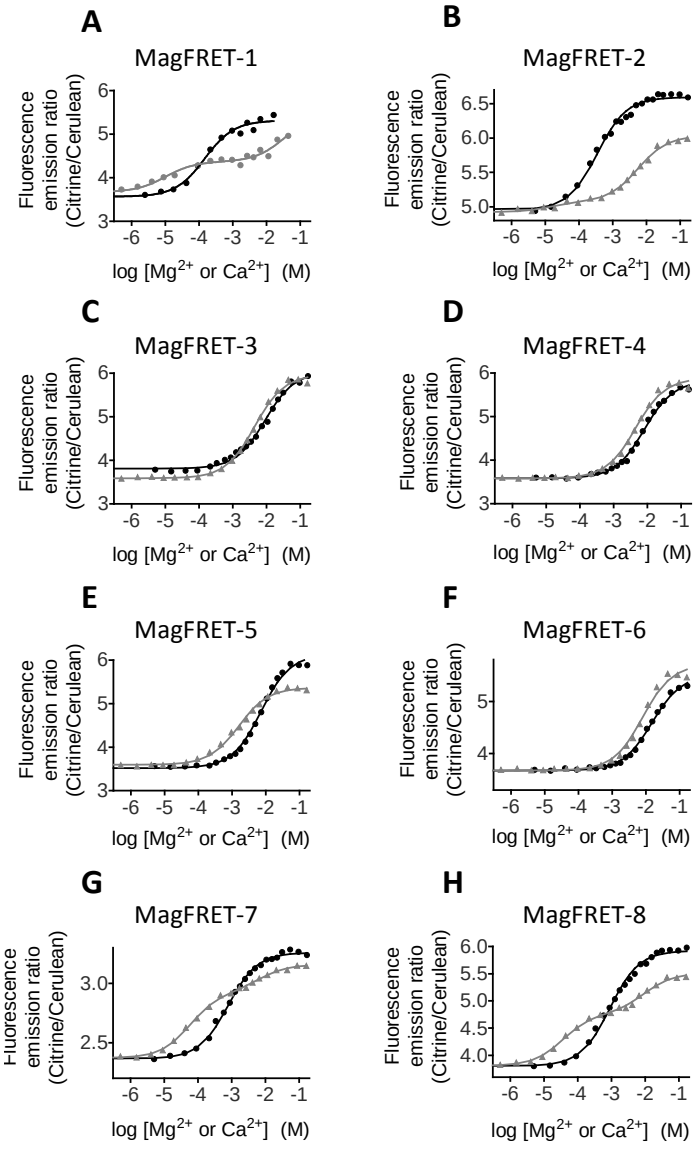

Figure 2.4: Mg^{2+}/Ca^{2+} titrations of MagFRET variants with mutations in metal binding sites. *(A-H) Emission ratio (Citrine to Cerulean) of MagFRET variants as a function of the Mg^{2+} (black circles) or Ca^{2+} (grey triangles) concentration. Solid black traces indicate a fit to a Mg^{2+}-binding event, while grey traces indicate a fit to either double Ca^{2+}-binding events (A, B, G, H) or a single Ca^{2+}-binding event (C-F). Results of the titrations are summarized in Table 2.1. Measurements were performed in 150 mM Hepes (pH 7.1), 100 mM NaCl and 10% (v/v) glycerol and 0.2 (A) or 1 (B-H) μM protein.*

In situ characterization of MagFRET-1 in HEK293 cells

To assess the sensor properties of MagFRET-1 *in situ*, CMV vectors were constructed to allow transient expression of MagFRET-1 in HEK293 cells. Fluorescence microscopy images revealed homogeneous expression of the sensor in the cytosol (Figure 2.5A, B). In addition, transfection of cells with a construct containing three repeats of the nuclear localization sequence PKKKRKV (45, 46) at the C-terminus of the sensor protein (MagFRET-1-NLS), resulted in a clear cyan and yellow emission in the nucleus (Figure 2.5C, D), which demonstrates the ability to target MagFRET-1 to a specific location in the cell.

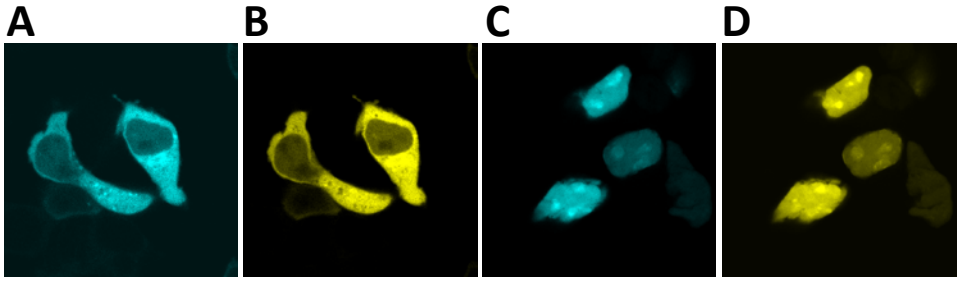

Figure 2.5: Confocal fluorescence microscopy of HEK293 cells expressing MagFRET. *False-colored images showing HEK293 cells expressing MagFRET-1 (A, B) and MagFRET-1-NLS (C, D) with Cerulean (A,C) or Citrine emission (B, D).*

Although the K_d of MagFRET-1 for Ca^{2+} determined *in vitro* is an order of magnitude higher than the maximum Ca^{2+} concentration that is typically observed in the cytosol during signaling, it was still important to verify that the MagFRET-1 sensor does not respond to stimuli that are known to transiently induce increases in cytosolic Ca^{2+} concentrations. Ca^{2+} signaling in HEK293 cells was activated via addition of 50 µM of the protease activated receptor-1 (PAR-1) agonist peptide (*47, 48*). No changes in the emission ratio of MagFRET-1 were observed after addition of this stimulant (Figure 2.6A). Cells loaded with the synthetic Ca^{2+} dye Oregon Green-BAPTA did show a transient increase in fluorescence upon addition of PAR-1 agonist peptide, confirming that the expected increase in intracellular Ca^{2+} concentration was induced under these conditions (Figure 2.6B).

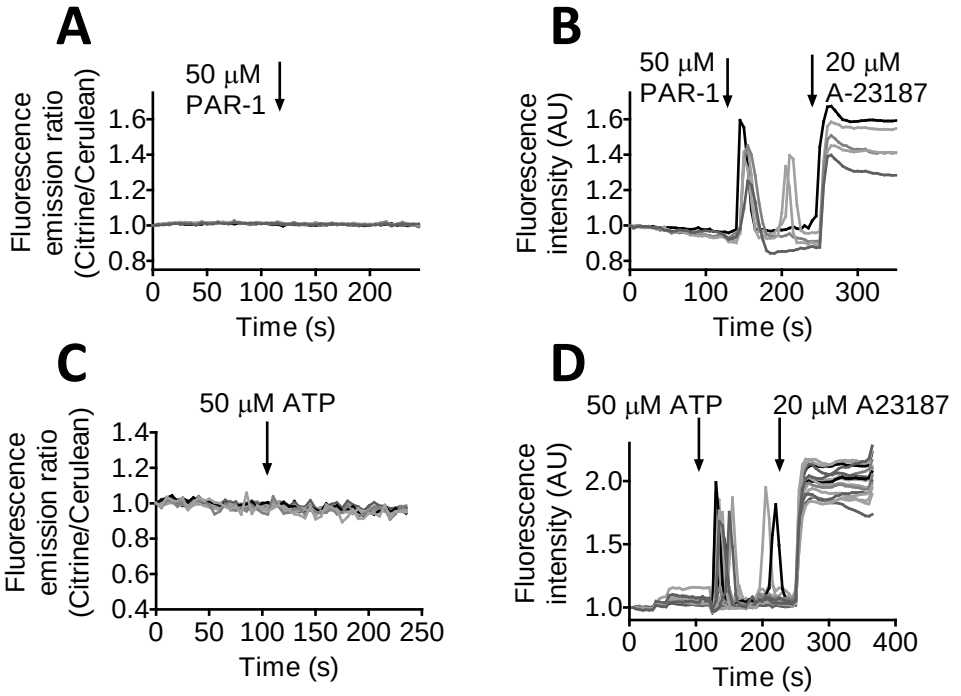

Figure 2.6: Investigation of MagFRET-1's in situ Ca^{2+} sensitivity. *(A) Emission ratio over time of intact HEK293 cells expressing MagFRET-1 measured by widefield fluorescence microscopy. At t = 120 s, 50 μM of PAR-1 agonist peptide was added to activate Ca^{2+} signaling. (B) To confirm Ca^{2+} signaling took place in stimulated cells, the fluorescence intensity of intact HEK293 cells loaded with Ca^{2+}-dye Oregon Green–BAPTA was followed. At t = 120 s, 50 μM of PAR-1 agonist peptide was added to activate Ca^{2+} signaling, and at t = 240 s, 20 μM A23187 was added. (C) Same as A, but with addition of 50 μM ATP at t = 104 s. (D) Same as B but with addition of 50 μM ATP at t = 104 s and of 20 μM A23187 at t = 226 s. Each trace represents the response of an individual cell, with ratio (A, C) or intensity (B, D) normalized to the value at t = 0 s.*

Similar results were obtained with ATP, another commonly used stimulant for Ca^{2+} signaling (49-51). Addition of 50 μM ATP did not affect the emission ratio of MagFRET-1 in HEK293 cells (Figure 2.6C), while cells loaded with Oregon Green-BAPTA showed a clear response to the same treatment (Figure 2.6D).

Having established that MagFRET-1 could be targeted and that it was insensitive to normal cytosolic Ca^{2+} fluctuations, we next characterized MagFRET-1's ability to report on changes in cytosolic $[Mg^{2+}]_{free}$. Surprisingly, attempts to perturb the free concentration of Mg^{2+} in the cytosol of intact HEK293 cells using previously reported

procedures did not induce a significant ratiometric response in HEK293 cells transfected with MagFRET-1 (not shown). These protocols included incubation of the cells in 50 mM $MgCl_2$ (29), exposure to the Mg^{2+} competitor Li^+ (52) and varying of the sodium concentration to affect the Mg^{2+}/Na^+ exchanger (53). To verify that the transiently expressed sensor is still responsive, we permeabilized HEK293 cells transfected with MagFRET-1 using 10 µg/mL digitonin and exposed them to buffers with different Mg^{2+} or EDTA concentrations (Figure 2.7A, B). Addition of 2 mM Mg^{2+}

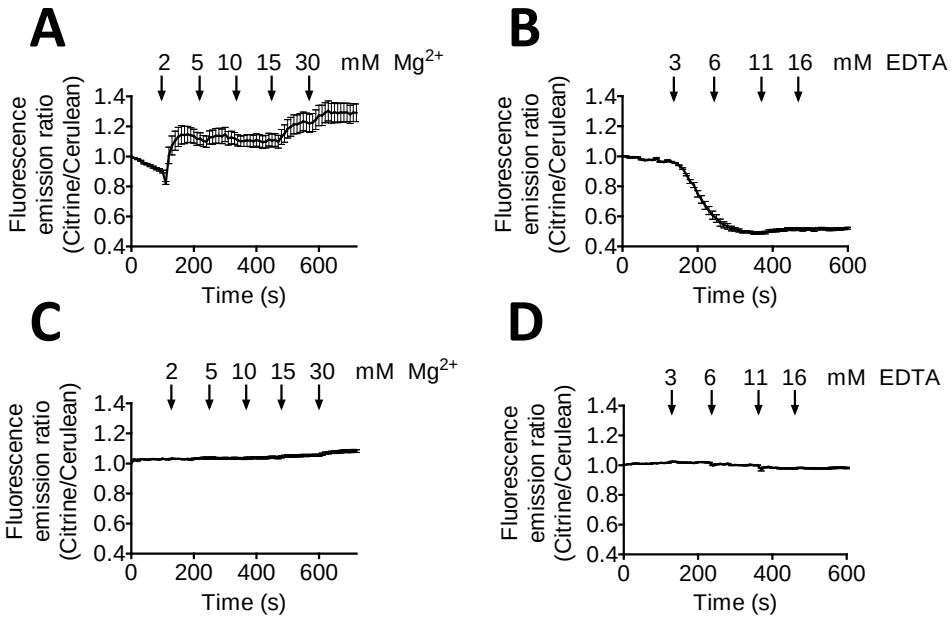

Figure 2.7: Response of MagFRET-1 expressed in permeabilized HEK293 cells to changes in [Mg^{2+}]. *(A, B) MagFRET-1 emission ratio was followed over time as the concentration of $MgCl_2$ (A) or EDTA (B) was increased, as indicated on the panels. (C, D) Response of negative control construct Cerulean-linker-Citrine expressed in permeabilized HEK293 cells to changes in [Mg^{2+}] (C) or [EDTA] (D). Prior to imaging, cells were permeabilized using 10 µg/mL digitonin. To maintain an isotonic solution, the increase in Cl^- concentration due to addition of $MgCl_2$ was compensated for by reducing the KCl concentration in the buffer. Traces represent averages of at least 9 cells, error bars indicate SEM, ratios were normalized to the emission ratio at t = 0.*

resulted in an increase in emission ratio for MagFRET-1, indicating metal binding to this sensor (Figure 2.7A). Subsequent addition of increasing Mg^{2+} concentrations did

not result in a further increase in emission ratio up to 10 mM, while rounding of cells was observed at concentrations of 15 and 30 mM Mg^{2+} (not shown). To verify that the sensor could also monitor a decrease in cytosolic Mg^{2+} levels, the metal chelator EDTA was added to permeabilized cells expressing MagFRET-1. Upon addition of EDTA, cells expressing MagFRET-1 showed a decrease in emission ratio that is consistent with a decrease in cytosolic Mg^{2+} levels (Figure 2.7B). Importantly, no changes in emission ratio were observed upon addition of Mg^{2+} or EDTA to digitonin-treated cells expressing a negative control construct consisting of Cerulean, a flexible linker and Citrine but lacking any metal binding sites (Figure 2.7C, D**).** These results exclude the possibility that changes in emission ratio observed in MagFRET-1-expressing cells may have resulted from changes in the fluorescent domains' properties due to their sensitivity to pH or [Cl^-] and confirm that MagFRET-1 is capable of responding to changes in intracellular Mg^{2+} levels.

Discussion

To the best of our knowledge, this work represents the first report of a genetically encoded fluorescent sensor for Mg^{2+}. The new sensor principle of metal-induced folding of an EF-hand protein was used to create a FRET-based sensor protein that combines a physiologically relevant Mg^{2+} affinity with a 50% increase in emission ratio upon Mg^{2+} binding. Mutations introduced in the metal binding domains yielded sensor variants with different degrees of attenuation in Mg^{2+} affinity, generating a toolbox of MagFRET variants for different applications. Unlike most synthetic fluorescent Mg^{2+} probes reported so far, MagFRET-1 allows emission ratiometric detection of Mg^{2+} and is thus less sensitive to fluctuations in sensor concentration or background fluorescence. A general advantage of genetically encoded sensors is that their subcellular localization can be easily controlled, as we demonstrated by targeting MagFRET-1 to the cytosol and nucleus of HEK293 cells. Importantly, while MagFRET-1 is also sensitive to Ca^{2+}, its Ca^{2+} affinity is sufficiently attenuated to make the sensor effectively unresponsive to the Ca^{2+} levels reached during signaling.

Although MagFRET-1 was clearly responsive to changes in Mg^{2+} in permeabilized HEK293 cells, we did not observe similar changes in emission ratio for intact cells. A lack of selective Mg^{2+} ionophores and chelators is a fundamental problem in the Mg^{2+} imaging field (4) and prevented us from calibrating the sensor's resting emission ratio by depleting and saturating the sensor *in situ*, as is commonly done for genetically encoded Ca^{2+} and Zn^{2+} sensors.

Despite the intrinsically large conformational change associated with protein folding, surprisingly few examples of FRET sensors exist where ligand-induced folding of a partially unfolded recognition domain is employed in FRET sensor design. Most FRET sensors developed so far either use ligand binding domains that are known to undergo significant conformational changes upon ligand binding (e.g. the periplasmic binding proteins (54)), or recognition domains that undergo a ligand-induced interaction with another peptide/protein domain (e.g. Cameleons (32)). Ligand-induced folding is believed to occur for intrinsically-disordered proteins, which may account for 35-51% of all eukaryotic protein domains (55). In addition, ligand binding domains can be intentionally destabilized to turn conformationally silent ligand binding domains into input domains for FRET sensor design (56). This work revealed that ligand-induced folding of intrinsically-disordered proteins is an attractive mechanism for FRET sensor design. However, it also identified a potential disadvantage as we observed that the conformation and thus the amount of energy transfer of the ligand-free state is sensitive to ionic strength. Although this effect is most apparent below physiologically relevant salt concentrations, it is important to be aware of this phenomenon and use these sensors under conditions of constant ionic strength or use appropriate control sensors that have a strongly attenuated Mg^{2+} affinity, such as MagFRET-6.

The Mg^{2+} and Ca^{2+} affinities of MagFRET-1 were found to be attenuated compared to the affinities previously reported for the N-terminal domain of HsCen3 (K_d = 10-28 μM for Mg^{2+}; K_d = 1.5-8 and 140 μM for Ca^{2+}). The difference in metal binding affinity might be explained by the fact that the central α-helix that connects the 2nd and 3rd EF hands in HsCen3 was reduced to half its length in MagFRET-1, possibly further

destabilizing the N-terminal domain, resulting in a net decrease in Mg^{2+} affinity. Fortunately, in this case the attenuation yielded a sensor that is sensitive to physiologically relevant Mg^{2+} concentrations, and insensitive to normal cytosolic Ca^{2+} concentrations. The limited number of metal binding domain mutations that were explored in this study revealed that mutations in the first EF hand typically result in strongly attenuated metal binding affinities. A more subtle, 4-6 fold attenuation of metal binding affinity was obtained after introduction of positively charged amino acids in the 2nd EF hand. These effects could be due to direct allosteric coupling between the two EF hands in the metal-bound state, but alternatively could also result from further stabilization of the molten globule state. An important goal is to develop sensor variants that are less sensitive to Ca^{2+} yet retain affinity for Mg^{2+}, as this would allow targeting to organelles known to have much higher resting levels of Ca^{2+}. The similar coordination chemistries of Ca^{2+} and Mg^{2+} make rational design of such variants challenging, although mutations in an EF-hand-like protein have been reported that decreased the Ca^{2+} affinity 100-fold while simultaneously doubling the Mg^{2+} affinity (57). Further optimization of metal binding affinity and specificity, but also the sensor's dynamic range, may benefit from directed evolution approaches similar to the ones that were recently applied to develop new color variants of the Ca^{2+} sensor GECO (34, 58).

In situ characterization of MagFRET-1 in HEK293 cells revealed that the sensor is readily expressed in the cytosol and can be targeted to the nucleus. Two ligands that are known to induce Ca^{2+} signaling in cells, PAR-1 agonist peptide and ATP, did not affect the emission ratio of the MagFRET-1 sensor in HEK 293 cells. This result was expected based on the affinity of MagFRET-1 that was determined *in vitro* (K_d = 10 µM) and previous reports that show that bulk cytosolic Ca^{2+} concentrations typically reach a maximum of 1 µM during signaling (43). In contrast, synthetic Mg^{2+} dyes with similar affinity to Ca^{2+} as MagFRET-1 have been reported to respond to Ca^{2+}. This may be explained by the fact that MagFRET-1 is exclusively localized in the cytosol, whereas synthetic dyes sometimes partially mislocalize to Ca^{2+}-rich organelles such as the ER or even leak into the external buffer (59). Surprisingly, HEK293 cells

expressing MagFRET-1 did not respond to procedures that were previously reported to affect the intracellular Mg^{2+} concentration. A possible explanation could be that the free concentration of Mg^{2+} in the cytosol is tightly buffered and controlled and not easily changed by external stimuli. The free concentration of Mg^{2+} in the cytosol is at least a 1000-fold higher than that of Ca^{2+} and 10^6 fold higher than that of Zn^{2+}. For this reason and because Mg^{2+} is essential to such a wide variety of biological processes, it would not be surprising that manipulation of intracellular free Mg^{2+} is much more difficult than that of other metals. Nonetheless, it is conceivable that while the overall free Mg^{2+} concentration in cells is relatively constant, substantial and physiologically relevant fluctuations in Mg^{2+} concentration could still occur locally, e.g. at the plasma membrane near Mg^{2+}-specific ion channels. Although MagFRET-1 responded to changes in Mg^{2+} concentration in the order of seconds both *in vitro* and in cells, protein-based sensors often display slower kinetics than small molecule sensors, so that MagFRET-1 might fail to respond to extremely fast Mg^{2+} transients, should they occur. In addition, overall Mg^{2+} levels could change over longer periods of time, e.g. as a function of the cell cycle. These changes may be more reliably monitored using lifetime imaging, which might also be the preferred method to allow quantification of intracellular Mg^{2+} concentrations. Although we confirmed that MagFRET-1 is responsive to changes in Mg^{2+} concentration in permeabilized cells, we cannot completely rule out that for some unknown reason MagFRET-1 is less responsive in intact cells. The potential and limitations of the MagFRET sensors for intracellular Mg^{2+} imaging therefore remain to be further established.

Materials & methods

Cloning of expression plasmids. DNA encoding the N-terminal fragment of HsCen3 (residues 23 to 98 (42)) was obtained as a synthetic pUC57 construct (GenScript, USA). Restriction of this construct with restriction enzymes NheI and NcoI yielded an insert fragment that was compatible with a pET28a acceptor vector encoding for His_6-Cerulean-$(GGS)_{18}$-Citrine (60) that had been treated with restriction enzymes SpeI

(creating an NheI-compatible cohesive overhang) and NcoI. A ligation was carried out at equimolar vector-to-insert ratio using T4 DNA ligase (TaKaRA Mighty Mix, Takara, USA) at 16 °C for 1 hour following the manufacturer's instructions, resulting in pET28a-MagFRET-1. The SpeI restriction site in the pET28a-His_6-Cerulean-$(GGS)_{18}$-Citrine acceptor vector was located 8 residues upstream of the Cerulean C-terminus, such that in the final MagFRET construct, the native flexible C-terminus of Cerulean was deleted, resulting in tighter allosteric coupling between changes in HsCen3 conformation and changes in the fluorescent domains' interchromophore distance. The mammalian expression vector for MagFRET-1 was obtained by digesting pET28a-MagFRET-1 using restriction enzymes AgeI and NotI. Ligation into a peCALWY-1 vector (36) that was digested with the same restriction enzymes resulted in pCMV-MagFRET-1. Mutations in metal binding loop I and II of MagFRET-1 were introduced using site-directed mutagenesis (QuikChange Multi Site-Directed Mutagenesis Kit for mutations in loop I and QuikChange Site-Directed Mutagenesis Kit for mutations in loop II), following the kit manufacturer's (Qiagen) instructions. Primers used to introduce these mutations are listed in Table 2.2. To obtain the mammalian expression vector encoding for a nuclear-targeted MagFRET-1 (MagFRET-1-NLS), a pUC57 vector containing a synthetic gene encoding for the final part of Citrine together with three PKKKRKV repeats was digested using restriction enzymes HindIII and NotI, followed by ligation into a pCMV-MagFRET-1 plasmid that was treated with the same restriction enzymes. The correct open reading frame of each sensor was confirmed by Sanger dideoxy sequencing (Baseclear, Leiden, The Netherlands).

Table 2.2: Primers used for mutagenesis of HsCen3.

MagFRET variant	Site directed mutagenesis primers (5'→3')
MagFRET-2	GCCACCTTCAGTTCATGATAATCTATTGCaTCATCTTTGTCTGTATC
MagFRET-3	GCTTATCTTTGTCTGTtTCAAACAGTTCAAAAGCATC
MagFRET-4	GCCACCTTCAGTTCATGATAATCTATTGCTTCtTCTTTGTCTGTATC
MagFRET-5	GCCACCTTCAGTTCATGATAATCTATgtCTTCATCTTTGTCTGTATC
MagFRET-6	GCCACCTTCAGTTCATGATAATCTATTtCTTCtTCTTTGTCTGTATC
MagFRET-7	Forward: GACAGAGAAGCCACAAAGAAAATCACCTTTGAAG Reverse: CTTCAAAGGTGATTTTCTTTGTGGCTTCTCTGTC
MagFRET-8	Forward: CTGAAGATTCTTAAAGATTATAAGAGAGAAGCCACAGGG Reverse: CCCTGTGGCTTCTCTCTTATAATCTTTAAGAATCTTCAG

Protein expression and purification. *E. coli* BL21(DE3) cells were used for protein expression. A single colony was used to inoculate 5 mL LB medium (10 g/L NaCl, 10 g/L peptone, 5 g/L yeast extract) supplemented with 30 µg/mL kanamycin which was grown overnight at 225 rpm at 37 °C. Overnight cultures were diluted in 500 mL LB medium containing kanamycin (30 µg/mL) and grown until an optical density of 0.6-0.8 was reached at 600 nm wavelength. Protein expression was induced by the addition of 0.1 mM isopropyl β-D-1-thiogalactopyranoside (IPTG, Sigma). Bacteria were cultured overnight at 225 rpm at 25 °C and harvested by centrifugation at 10,000 g for 10 minutes at 4 °C. The cell pellets were lysed using Bugbuster reagent (Novagen) according to the manufacturer's instructions. The resulting soluble protein fraction was used for further purification. The expressed MagFRET proteins contain an N-terminal hexahistidine-tag. Ni^{2+}-NTA resin (His-bind, Novagen) was used for affinity chromatography following the manufacturer's instructions. After elution of the protein using 0.5 M imidazole, the protein was dialyzed overnight against 100 volumes of 20 mM Tris-HCl (pH 8.4), 150 mM NaCl and 2.5 mM $CaCl_2$ using a 12-14 kDa Molecular Weight Cut-Off (MWCO) dialysis membrane (Spectropore) at 4 °C. The hexahistidine-tag was subsequently removed by the addition of 0.3 U thrombin protease (Novagen) per mg protein at a 0.2 mg/mL protein concentration and incubated for 24 hours at 4 °C. His-tags and uncleaved proteins were removed using Ni^{2+} affinity chromatography. The flow-through was further purified using size exclusion chromatography (SEC) on a Sephacryl S-200 High resolution column (GE Healthcare). Fractions containing pure proteins were pooled, concentrated, frozen in liquid nitrogen and stored in aliquots at -80 °C. The purity and correct molecular weight of the obtained proteins was confirmed by SDS-PAGE analysis. The protein concentration was determined using the absorption at 515 nm (ND-1000 Nanodrop) and a molar extinction coefficient of 77,000 $M^{-1}cm^{-1}$ for Citrine (44).

Fluorescence spectroscopy. Unless otherwise mentioned, magnesium and calcium titrations were performed in 150 mM Hepes (pH 7.1), 100 mM NaCl, 10% (v/v) glycerol. Fluorescence emission spectra were recorded between 450 and 600 nm at a 0.2 µM protein concentration on a Varian Cary Eclipse fluorometer with an excitation

wavelength of 420 nm. $MgCl_2$ and $CaCl_2$ (both from Sigma) were added at increasing concentrations from a concentrated stock solution in water. To determine the MagFRET-1 dissociation constant (K_d) for Mg^{2+}, the emission ratio (R) as a function of $MgCl_2$ concentration ($[Mg^{2+}]$) was fit to equation 2.1,

$$R = R_S + \frac{\Delta R[Mg^{2+}]}{K_d + [Mg^{2+}]} \quad (2.1)$$

where R_S is the starting emission ratio in absence of Mg^{2+} and ΔR the difference in emission ratio between the Mg^{2+}-free and Mg^{2+}-saturated form of MagFRET-1. To determine the MagFRET K_{d1} and K_{d2} values associated with the first and second Ca^{2+}-binding events respectively, the emission ratio (R) as a function of $CaCl_2$ concentration ($[Ca^{2+}]$) was fit to a double binding event using equation 2.2,

$$R = R_S + \frac{\Delta R_1[Ca^{2+}]}{K_{d1} + [Ca^{2+}]} + \frac{\Delta R_2[Ca^{2+}]}{K_{d2} + [Ca^{2+}]} \quad (2.2)$$

where R_S is the starting emission ratio in absence of Ca^{2+}, ΔR_1 is the difference between the emission ratio in the Ca^{2+}-free state and the state in which a single Ca^{2+} ion has bound to the first metal binding loop of HsCen3, ΔR_2 the difference between the latter state and the state in which a second Ca^{2+} ion has bound to EF-hand II. For the metal specificity measurements, either $BaCl_2$, $NiSO_4$, $CuSO_4$, $ZnCl_2$ or $FeCl_3$ was added from 1000x concentration stock solutions to a final concentration of 10 µM, followed by addition of 1 mM $MgCl_2$. For titrations testing the effect of ionic strength on the sensor, a low salt buffer was used, consisting of 20 mM Hepes (pH 7.1), 10 mM NaCl and 10% (v/v) glycerol. To test for pH sensitivity of MagFRET-1, $MgCl_2$ and $CaCl_2$ titrations were carried out in buffers where Hepes was replaced with either MES or Tris in the standard measurement buffer. The MES-containing buffer was prepared at pH 6 while the Tris-containing buffer was prepared at pH 8.

Cell culturing and transfection. HEK293 cells were grown in Dulbecco's modified Eagle medium (DMEM, Sigma) containing 10% (vol/vol) fetal bovine serum (FBS, Life Technologies), 3 mM glucose, 2 mM glutamine, 100 units ml^{-1} penicillin and 100 µg ml^{-1} streptomycin at 37 °C and 5% CO_2. Cells were plated on poly-L-lysine (Sigma) treated glass coverslips and transfected with 1.5 µg of plasmid DNA

and 5 µg polyethyleneimine (PEI). Cells were imaged for transient expression 2 days after transfection. In addition to the pCMV-MagFRET-1 and pCMV-MagFRET-1-NLS constructs described above, cells were also transfected with peZinCh-NB (*36*), the Cerulean-linker-Citrine negative control construct mentioned in Figure 2.7.

Fluorescence microscopy. To demonstrate correct localization and subcellular targeting of MagFRET-1, confocal microscopy (Leica TCS SP5 X) was used to image the sensor with high spatial resolution. Samples were excited using a 405 nm laser and emission was detected using a hybrid APD/PMT detector (HyD, Leica). Spectral emission windows were set to 460-490 nm for the Cerulean channel and 510-550 nm for the Citrine channel, using an acousto optical beam splitter (AOBS, Leica). Widefield fluorescence microscopy for FRET measurements was performed on an Axio observer D.1 (Zeiss) equipped with an Axiocam MRm monochrome digital camera (Zeiss) using Axiovision 4.7 software. Samples were excited using a HXP 120 Mercury lamp (Zeiss) and Cerulean and Citrine emission was recorded sequentially using filter set 47 (excitation BP 436/20, dichroic 455, emission BP 480/40) and 48 (excitation BP 436/20, dichroic 455, emission BP 535/30) (Zeiss) in a motorized filter turret. Emission of Oregon Green-BAPTA was recorded using filterset 38 HE (excitation 470/40, dichroic 495, emission BP 525/50) (Zeiss). Images were acquired using an apochromat 40x objective, with an exposure time of 200-300 ms.

Imaging of response to changes in intracellular Mg^{2+}. Prior to addition of Mg^{2+} or EDTA, cells were permeabilized by a 6 minute incubation of HEK293 cells in 400 µL intracellular buffer (IB) containing 10 µg/ml digitonin (Sigma). IB comprised 20 mM Hepes (pH 7.05), 140 mM KCl, 10 mM KH_2PO_4, 100 µM ATP, 2 mM Na^+ succinate and 5.5 mM glucose. After 6 minutes, recordings were started and buffers containing increasing concentrations of EDTA or $MgCl_2$ were added as stated in the main text. When adding $MgCl_2$, KCl concentrations were reduced accordingly to maintain the Cl^- concentration at 140 mM. Imaging frequency was 0.1 Hz.

Intracellular Ca^{2+} specificity. Intracellular calcium specificity measurements were performed on HEK293 cells transfected as described above. Modified Krebs-bicarbonate buffer was used, consisting of 10 mM Hepes (pH 7.4), 140 mM NaCl, 3.6

mM KCl, 0.5 mM NaH_2PO_4, 1.5 mM $CaCl_2$, 25 mM $NaHCO_3$ and 3 mM glucose. Where indicated, PAR-1 agonist peptide (sequence SFLLRN, Genscript, USA) or ATP (Sigma) were added to a final concentration of 50 µM. Control experiments were performed using non-transfected HEK293 cells that were loaded with 10 µM Oregon Green-BAPTA-AM (Life Technologies, Netherlands) in phosphate buffered saline (PBS) with 0.01% (w/v) Pluronic F-127 (Life Technologies) for 30 minutes. At the end of each experiment in which Oregon Green-BAPTA-AM was used, 20 µM of calcium ionophore A23187 (Sigma) was added. Imaging frequency was 0.2 Hz.

Acknowledgments

This work has been published in: L.H. Lindenburg, J.L. Vinkenborg, J. Oortwijn, S.J.A. Aper, M. Merkx (2013), PLoS One 8, e82009. LHL and JLV contributed equally to this article. Part of this work has been previously described in Dr. Jan Vinkenborg's 2010 PhD thesis. Dr. Jan Vinkenborg planned, carried out and analyzed many of the experiments described in this Chapter. In addition, he supervised and guided Jorn Oortwijn and Stijn Aper. Jorn Oortwijn planned, carried out and analyzed experiments concerning the *in vitro* behavior of MagFRET-1. Stijn Aper planned, carried out and analyzed fluorescence microscopy imaging of mammalian cells transfected with MagFRET-1. I am grateful for the use of the fluorescence confocal microscope in the Laboratory of Soft Tissue Biomechanics & Engineering (Eindhoven University of Technology) and appreciate the technical assistance provided by Dr. Ir. M. van Turnhout. I would like to thank Dr. Kees Jalink (Netherlands Cancer Institute, Amsterdam), Dr. Stan van de Graaf (Academic Medical Centre), Dr. Sjoerd Verkaart, Dr. Jenny van der Wijst, Prof. Joost Hoenderop and Prof. René Bindels (Radboud University Nijmegen) for fruitful discussions.

References

1. Shi J, *et al.* (2002) *Nature* **418,** 876-880.
2. Nadler MJ, *et al.* (2001) *Nature* **411,** 590-595.
3. Romani AM (2007) *Front. Biosci.* **12,** 308-331.
4. Grubbs RD (2002) *Biometals* **15,** 251-259.
5. Rutter GA, Osbaldeston NJ, McCormack JG, & Denton RM (1990) *Biochem J* **271,** 627-634.
6. Gunther T (2006) *Magnes Res* **19,** 225-236.
7. Corkey BE, *et al.* (1986) *J Biol Chem* **261,** 2567-2574.
8. Maguire ME (2006) *Curr Opin Struct Biol* **16,** 432-438.
9. Schlingmann KP, *et al.* (2007) *Biochim Biophys Acta, Molecular Basis of Disease* **1772,** 813-821.
10. Hattori M, *et al.* (2007) *Nature* **448,** 1072-1075.
11. Konrad M & Weber S (2003) *J Am Soc Nephrol* **14,** 249-260.
12. Killilea DW & Ames BN (2008) *Proc Natl Acad Sci U S A* **105,** 5768-5773.
13. Chaudhary DP, Sharma R, & Bansal DD (2010) *Biol Trace Elem Res* **134,** 119-129.
14. Bo S & Pisu E (2008) *Curr Opin Lipidol* **19,** 50-56.
15. Rude RK & Gruber HE (2004) *J Nutr Biochem* **15,** 710-716.
16. Li FY, *et al.* (2011) *Nature* **475,** 471-476.
17. Trapani V, *et al.* (2010) *Analyst* **135,** 1855-1866.
18. Cohen SM & Burt CT (1977) *Proc Natl Acad Sci U S A* **74,** 4271-4275.
19. Resnick LM, Gupta RK, & Laragh JH (1984) *Proc Natl Acad Sci U S A* **81,** 6511-6515.
20. Gunther T (2007) *Magnes Res* **20,** 161-167.
21. Kim HM, *et al.* (2007) *J Org Chem* **72,** 2088-2096.
22. Hwan Myung K, *et al.* (2007) *Angew Chem Int Ed Engl* **46,** 3460-3463.
23. Komatsu H, *et al.* (2005) *J Am Chem Soc* **127,** 10798-10799.
24. Komatsu H, *et al.* (2004) *J Am Chem Soc* **126,** 16353-16360.
25. Raju B, *et al.* (1989) *Am J Physiol Cell Physiol* **256,** C540-548.
26. Paredes RM, *et al.* (2008) *Methods* **46,** 143-151.
27. Shindo Y, *et al.* (2011) *PLoS One* **6,** e23684.
28. Hurley TW, Ryan MP, & Brinck RW (1992) *Am J Physiol Cell Physiol* **263,** C300-307.
29. Zhou H & Clapham DE (2009) *Proc Natl Acad Sci U S A* **106,** 15750-15755.
30. Xie J, *et al.* (2011) *Sci Rep* **1,** 146.
31. Palmer AE, Qin Y, Park JG, & McCombs JE (2011) *Trends Biotechnol* **29,** 144-152.
32. Miyawaki A, *et al.* (1997) *Nature* **388,** 882-887.
33. Palmer AE, *et al.* (2006) *Chem Biol* **13,** 521-530.
34. Zhao YX, *et al.* (2011) *Science* **333,** 1888-1891.
35. Tian L, *et al.* (2009) *Nat Methods* **6,** 875-U113.
36. Vinkenborg JL, *et al.* (2009) *Nat Methods* **6,** 737-740.
37. Dittmer PJ, Miranda JG, Gorski JA, & Palmer AE (2009) *J Biol Chem* **284,** 16289-16297.
38. Miranda JG, *et al.* (2012) *PLoS One* **7,** e49371.
39. Qiao W, *et al.* (2006) *Proc Natl Acad Sci U S A* **103,** 8674-8679.
40. Wegner SV, *et al.* (2010) *J Am Chem Soc* **132,** 2567-2569.
41. Koay MS, Janssen BM, & Merkx M (2013) *Dalton Trans* **42,** 3230-3232.
42. Cox JA, *et al.* (2005) *Biochemistry* **44,** 840-850.
43. Bootman MD (2012) *Cold Spring Harb Perspect Biol* **4,** a011171.
44. Griesbeck O, *et al.* (2001) *J Biol Chem* **276,** 29188-29194.
45. Kalderon D, Roberts BL, Richardson WD, & Smith AE (1984) *Cell* **39,** 499-509.
46. Fischer-Fantuzzi L & Vesco C (1988) *Mol. Cell. Biol.* **8,** 5495-5503.
47. Jiang T, Danilo Jr P, & Steinberg SF (1998) *J Mol Cell Cardiol* **30,** 2193-2199.
48. Hui KY, Jakubowski JA, Wyss VL, & Angleton EL (1992) *Biochem Biophys Res Commun* **184,** 790-796.

49. Isshiki M, *et al.* (1998) *Proc Natl Acad Sci U S A* **95,** 5009-5014.
50. Nagai T, *et al.* (2004) *Proc Natl Acad Sci U S A* **101,** 10554-10559.
51. Qi Z, Murase K, Obata S, & Sokabe M (2000) *Br J Pharmacol* **131,** 370-374.
52. Fonseca CP, *et al.* (2000) *Met Based Drugs* **7,** 357-364.
53. Schweigel M, Park HS, Etschmann B, & Martens H (2006) *Am J Physiol Gastrointest Liver Physiol* **290,** G56-65.
54. Okumoto S, *et al.* (2005) *Proc Natl Acad Sci U S A* **102,** 8740-8745.
55. Dunker AK, *et al.* (2002) *Biochemistry* **41,** 6573-6582.
56. Kohn JE & Plaxco KW (2005) *Proc Natl Acad Sci U S A* **102,** 10841-10845.
57. Wang W, *et al.* (2013) *Nat Med* **19,** 305-312.
58. Lindenburg L & Merkx M (2012) *ChemBioChem* **13,** 349-351.
59. Trapani V, Schweigel-Rontgen M, Cittadini A, & Wolf FI (2012) *Methods Enzymol* **505,** 421-444.
60. Golynskiy MV, Rurup WF, & Merkx M (2010) *ChemBioChem* **11,** 2264-2267.

Chapter 3

Robust red FRET sensors using self-associating fluorescent domains

Abstract. Elucidation of sub-cellular signaling networks by multiparameter imaging is hindered by a lack of sensitive FRET pairs spectrally compatible with the classic CFP/YFP pair. Here we present a generic strategy to enhance the traditionally poor sensitivity of red FRET sensors by developing self-associating variants of mOrange and mCherry that allow sensors to switch between well-defined on- and off states. Requiring just a single mutation of the mFruit domain, this new FRET pair improved the dynamic range of protease sensors up to 10-fold and was essential to generate functional red variants of CFP-YFP-based Zn^{2+} sensors. The large dynamic range afforded by the new red FRET pair allowed simultaneous use of differently colored Zn^{2+} FRET sensors to image Zn^{2+} over a broad concentration range in the same cellular compartment.

Introduction

Genetically encoded FRET (Förster Resonance Energy Transfer) sensors allow ratiometric, non-invasive intracellular imaging of small molecules and enzyme activities in single living cells with high spatial and temporal resolution (1-3). These sensors consist of donor and acceptor fluorescent domains that report a conformational change in a native recognition domain through a change in FRET. Elucidation of the spatial and temporal relationships between different biochemical pathways requires the use of spectrally distinct sensors, permitting two or more probes to be used in the same cell at the same time (4, 5).

Several examples of orthogonal FRET pairs have recently been reported, but most of these are incompatible with the classical CFP/YFP pair (6, 7). Attempts to develop spectrally-distinct sensors by simply replacing CFP and YFP by the fully red-shifted mOrange/mCherry pair, resulted in FRET sensors with no or strongly attenuated responses (8-10), often precluding their simultaneous use with CFP-YFP-based sensors in the same cellular compartment (11). Despite a large Förster distance of 63 Å (12), the mOrange- mCherry FRET pair is ill-suited for FRET detected by measuring the fluorescence emission ratio. The large amount of bleedthrough from the donor into the acceptor detection channel results in any change in FRET efficiency being dampened by an *opposite* contribution to the acceptor detection channel's fluorescence intensity. In addition, the low acceptor quantum yield (0.22) in this FRET pair further dampens ratiometric changes (for a thorough discussion, see Appendix).

The development of new FRET sensors is often a process of trial-and-error that requires laborious optimization of linker lengths, linker positions and domain orientations. We recently introduced an alternative, rational design strategy for FRET sensor proteins based on the principle of mutually exclusive domain interactions. These sensors, which include probes for protease activity, Zn^{2+}, bile acids, and antibodies, rely on CFP and YFP variants that interact in one state of the sensor, but whose interaction is readily disrupted upon a ligand-induced interaction at the input domains (13-17). This modular design not only ensures robust changes in energy transfer

efficiency, but should also allow easy exchange of the traditional CFP- and YFP output domains by alternative pairs of self-associating FPs.

Results & discussion

To identify mutations that promote intramolecular association of mOrange and mCherry, we constructed a test protein consisting of mOrange and mCherry fused by a long and flexible glycine-serine linker (Figure 3.1A). Cleavage of the linker by

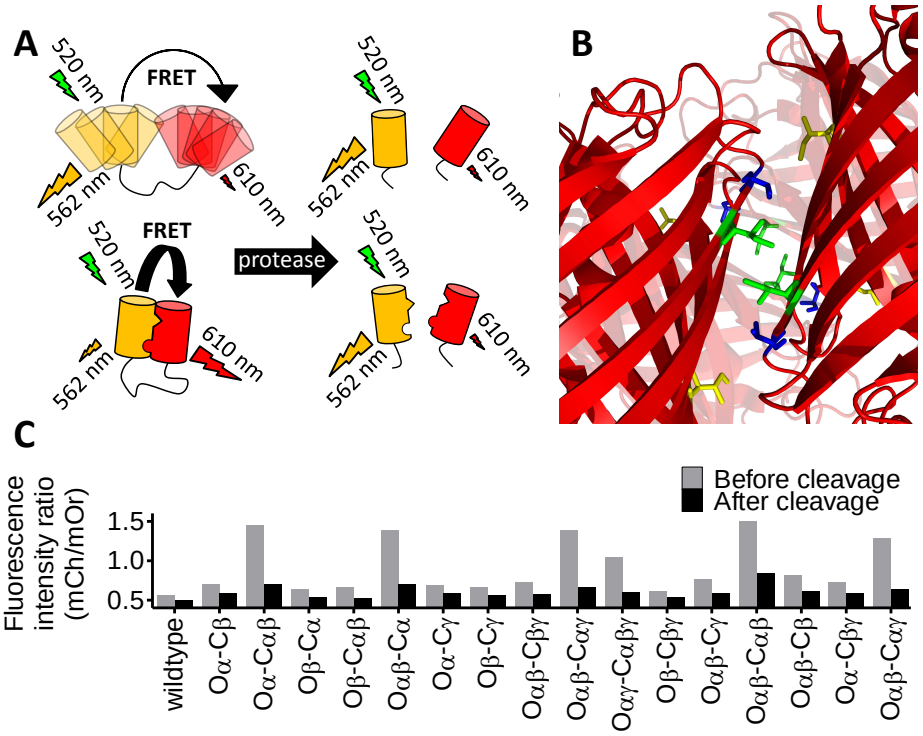

Figure 3.1: Development of self-associating mOrange and mCherry variants for improved performance in red-shifted FRET sensors. *(A) Promoting intramolecular domain interactions increases FRET before proteolytic cleavage. (B) Structure showing the key residues I125 (green), V127 (blue) and I180 (yellow) at the A-B hydrophobic dimer interface in DsRed (PDB 1G7K). (C) A library of mOrange(O)-mCherry(C) fusion proteins carrying reversions R125I (α), T127V (β) and/or T180I (γ) was screened for increased change in FRET after proteolytic cleavage of the linker. Proteins were measured at 10 µM in 50 mM Tris-HCl (pH 8), 100 mM NaCl using a fluorescence plate reader.*

proteinase K resulted in a relatively modest reduction of emission ratio from 0.58 to 0.47 (Figure 3.2A). This poor dynamic range (ΔR/Rmin) of 23% is attributable to the low quantum yield of the acceptor, a critical factor in sensitized emission FRET. Since mOrange and mCherry are both derived from the obligate tetramer DsRed, we reasoned that reversion of one or more of the mutations originally carried out to break the hydrophobic A-B dimeric interface, I125R, V127T and I180T (Figure 3.1B) (18), might be used to promote intramolecular self-association of these fluorescent domains (Figure 3.1A).

Screening of a small library of sensor variants in which one or more of these mutations were reversed revealed a subset of mutants with a large increase in emission ratio (Figure 3.1C). Significantly, all these variants carried the R125I reversion on both fluorescent domains, suggesting that this mutation is crucial for promoting intramolecular association between the donor and acceptor domain. In all cases, protease addition reduced the emission ratio to that of the sensors with the monomeric fluorescent domains (Figure 3.1C). The emission spectra before and after proteolytic cleavage for several of these variants show that the increased dynamic range is caused

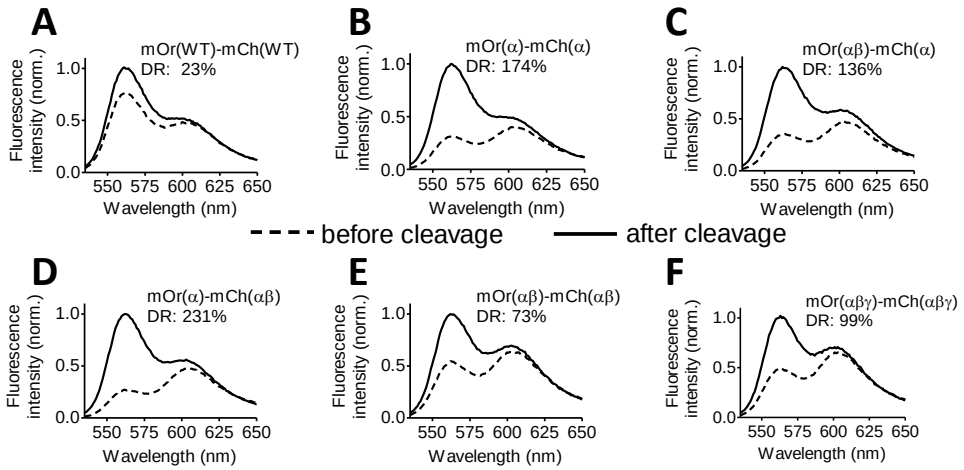

Figure 3.2: Emission spectra of purified red protease sensor variants before and after cleavage. *Dynamic range (DR), calculated as the difference in ratios before and after cleavage, divided by the ratio after proteinase K cleavage, is indicated for each variant. Proteins were measured at 1 µM in 50 mM Tris-HCl (pH 8), 100 mM NaCl at 25 °C.*

by a large change of the mOrange emission, resulting in a three to ten-fold increase in dynamic range (Figure 3.2B- F).

To quantify the strength of the protein-protein interaction brought about by the reversions, we used fluorescence polarization to monitor homodimerization of mCherry variants as a function of protein concentration (Figure 3.3A) (19). Fitting these titration data yielded a K_d for dimerization of 35 ± 4 μM for the R125I reversion, while a 250-fold stronger interaction was observed for the R125I/T127V double

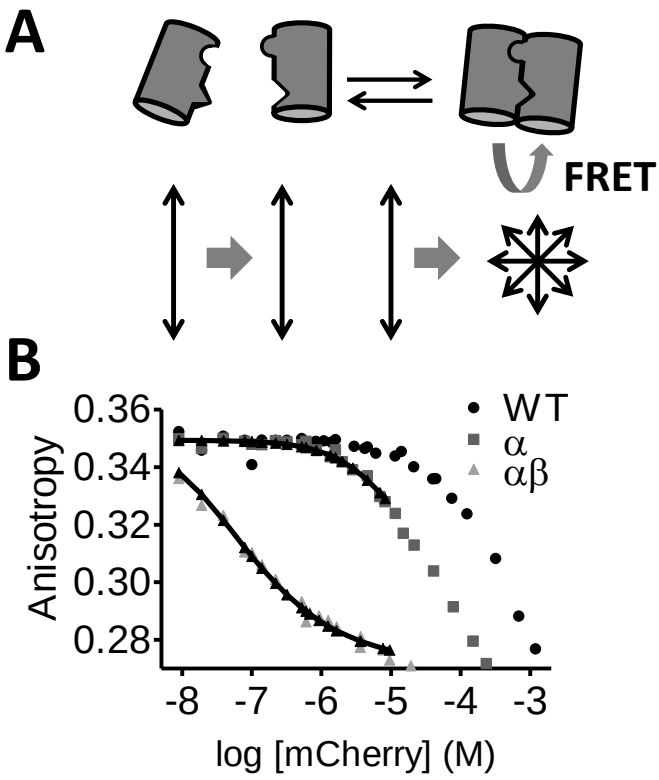

Figure 3.3: Use of fluorescence anisotropy to monitor fluorescent protein dimerization. *(A) Schematic representation of the anisotropy assay. Upon homodimerization, the decreased interchromophore distance allows homoFRET to occur, which has a strong depolarizing effect. (B) Fluorescence anisotropy of mCherry variants as a function of mCherry concentration. Data was fitted to equation 2, yielding dimer dissociation constants of 35 ± 4 μM and 91 ± 7 nM for mCherry-R125I (α) and mCherry-R125I/T127V (αβ), respectively. Measurements were performed at 25 °C in 50 mM Tris-HCl (pH 8), 100 mM NaCl and 1 mg/mL BSA.*

mutation (Figure 3.3B). As the effective concentration provided by the linker is in the low mM range (20), the K_d of 35 µM obtained for the R125I mutation is sufficient to promote essentially complete intramolecular association between the FPs in these constructs. The T127V mutation, while not sufficient to induce dimerization on its own, further strengthens the interaction induced by the R125I mutation, providing an additional possibility to tune FRET sensor properties (13). However, the R125I/T127V mutation also increases the chance of additional intermolecular interactions, which could partially counteract the increase in dynamic range, as shown in Figure 3.2E, F.

Since R125 and T127 are present in all mFruit variants, the results obtained here for mOrange and mCherry should be generally applicable to all monomeric derivatives of DsRed. We therefore tested whether R125I would also improve the performance of FRET sensors containing LSSmOrange, a recently described variant of mOrange that has a blue-shifted excitation peak (440 nm) and a long Stokes-shifted emission peak (572 nm) (21). This variant is useful as a FRET donor to a red acceptor since it prevents direct acceptor excitation and allows simultaneous excitation of CFP-YFP-

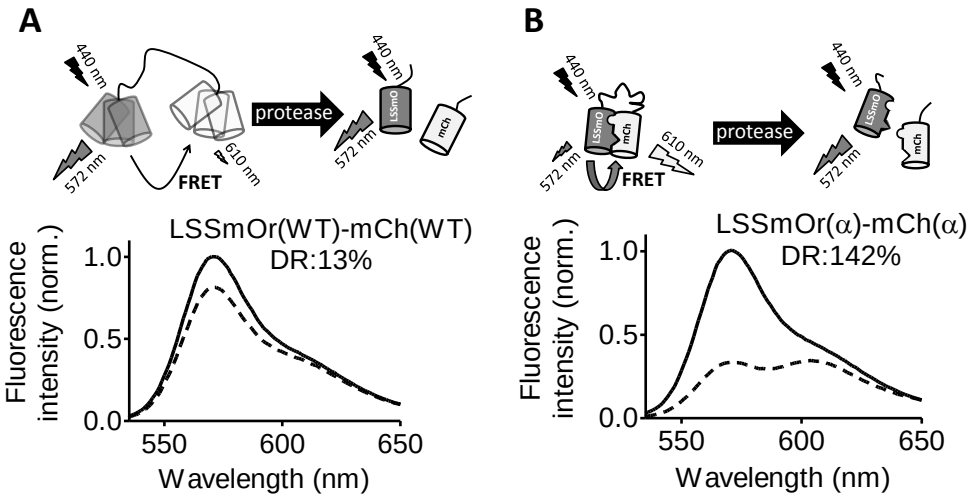

Figure 3.4: LSSmOrange can replace mOrange. *Protease sensors employing LSSmOrange as donor in the absence (A) or presence (B) of the R125I mutation (α) on the fluorescent domains. Emission spectra of LSSmOrange-linker-mCherry sensors are shown before (dashed line) and after protease cleavage (solid line). Proteins were measured at 1 µM in 50 mM Tris-HCl (pH 8), 100 mM NaCl at 25 °C.*

based FRET sensors. Replacement of mOrange by LSSmOrange resulted in a protease sensor that could be excited at 440 nm and detected in the red part of the spectrum, but with a low dynamic range (13%) (Figure 3.4A). Introduction of the R125I reversion on both fluorescent domains again resulted in a 10-fold improvement in dynamic range (Figure 3.4B). Interestingly, these results show that preventing direct acceptor excitation by itself does not significantly improve the sensor's dynamic range, and that intramolecular interaction between the FPs is essential to enhance the sensor's performance. Furthermore, a limit to the (LSS)mOrange-mCherry FRET pairs' sensitivity is caused by the donor to acceptor bleedthrough, which in LSSmOrange-mCherry is exacerbated by the 10 nm red-shift in the LSSmOrange emission spectrum (for a thorough discussion of the effect of bleedthrough on FRET pairs' sensitivity, see Appendix).

We next tested whether the use of self-associating FPs indeed allows straightforward replacement of the fluorescent domains in sensors based on mutually exclusive domain interactions. We previously developed the eCALWY series of Zn^{2+} sensors for intracellular imaging of Zn^{2+} homeostasis and signaling (15, 22). These sensors consist of a fusion of two cysteine-containing metal binding domains (ATOX1 and WD4) connected by a long, flexible glycine-serine linker. Binding of Zn^{2+} between ATOX1 and WD4 is mutually exclusive with the self-association of the FPs, translating to a decrease in emission ratio with increasing $[Zn^{2+}]_{free}$. As expected, replacement of the self-associating Cerulean/Citrine FPs in eCALWY-1 by mOrange and mCherry resulted in a sensor with a low emission ratio (0.55) that did not significantly change upon addition of a saturating concentration of Zn^{2+} (Figure 3.5A). Introduction of the R125I mutation in both fluorescent domains restored the switching capability, however, yielding a genetically encoded red Zn^{2+} FRET sensor (redCALWY-1) with a higher emission ratio in the absence of Zn^{2+} (1.41), a large dynamic range of 62% and a K_d for Zn^{2+} of 12.3 ± 2 pM (Figure 3.5B, C).

The same strategy could also be applied to obtain a red version of eCALWY-4, a variant bearing a mutation on the WD4 domain, yielding redCALWY-4 whose affinity of 234 ± 5 pM is better tuned to monitor increases in cytosolic Zn^{2+} concentrations

(Figure 3.5C). In both cases, the Zn^{2+} affinities of the red variants mirrored those of their CFP-YFP counterparts (15), demonstrating that the fluorescent domains in these sensors can be replaced without affecting their ligand binding properties.

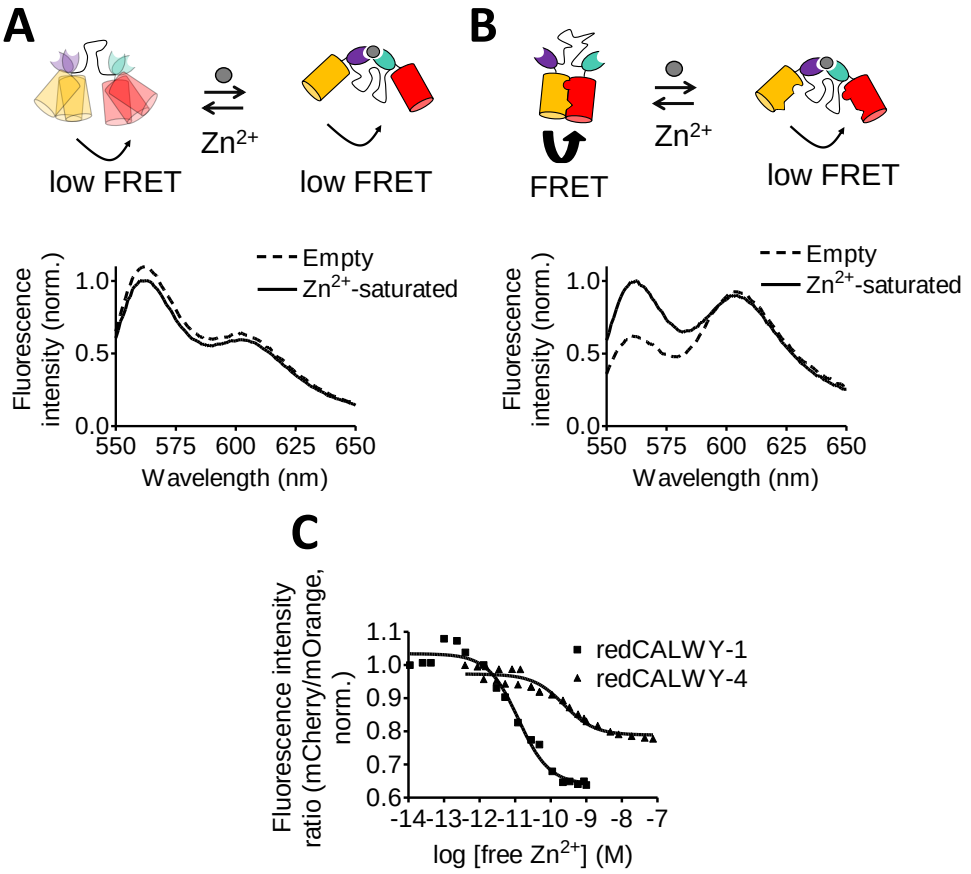

Figure 3.5: Characterization of red-shifted FRET sensor for Zn^{2+}. *(A, B) Emission spectra measured in vitro in the absence and presence of 1.5 nM Zn^{2+}_{free} for redCALWY-1, either without (A) or with (B) the R125I reversions. (C) Emission ratio as a function of $[Zn^{2+}]_{free}$ for redCALWY-1 (K_d = 12.3 ± 2 pM) and redCALWY-4 (K_d = 234 ± 5 pM). Measurements were performed with 0.25 µM FRET sensor protein in 50 mM Tris (pH 7.1), 100 mM NaCl, 10% (v/v) glycerol, 0.5 mM TCEP and 2 µM DTT and 1 mM Zn^{2+} chelator (EDTA, HEDTA, DHPTA, NTA or EGTA).*

To assess the performance of these new red variants for intracellular imaging, we replaced mOrange by the more photostable mOrange2 variant (23) carrying the same R125I mutation and transfected HeLa cells with one or more CALWY variants for cytosolic expression. HeLa cells expressing the high affinity redCALWY-1 showed a

clear increase in emission ratio upon addition of the membrane permeable Zn^{2+}-chelator TPEN, which was completely reversed upon subsequent addition of the Zn^{2+}-specific ionophore pyrithione together with excess Zn^{2+} (Figure 3.6A). This response is similar to that previously reported for the eCALWY-1 sensor (15) and shows that these high affinity sensors are completely saturated with Zn^{2+} under normal physiological conditions. The lower-affinity redCALWY-4 is mostly empty at the start of the experiment, as only a small increase in emission ratio is observed in the presence of

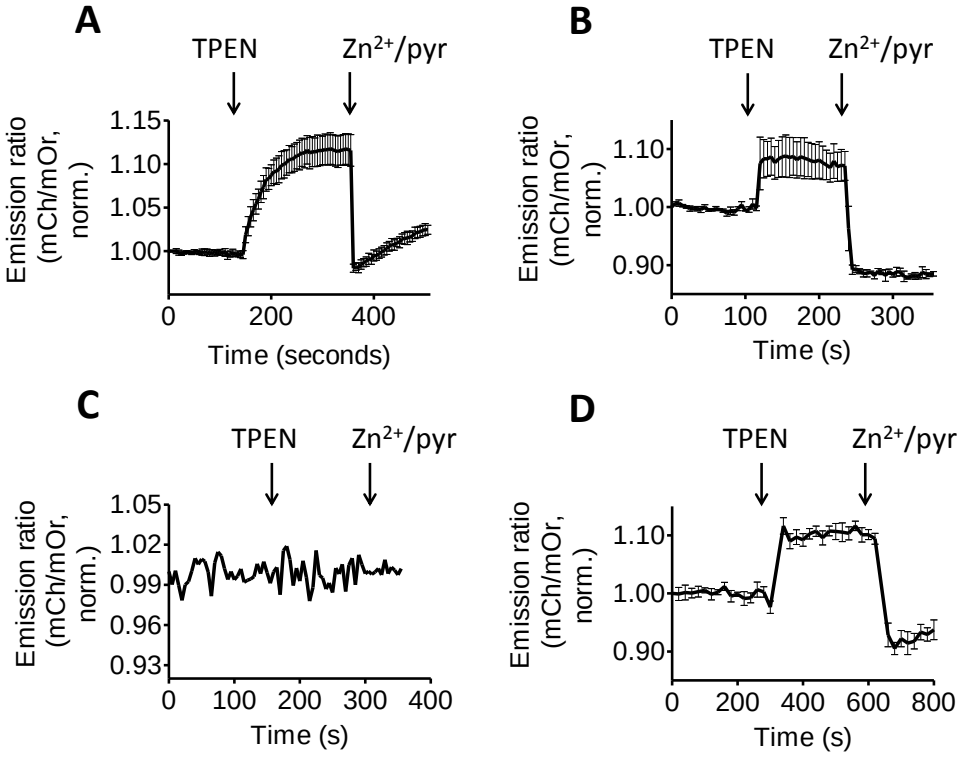

Figure 3.6. Intracellular application of red-shifted FRET sensors for Zn^{2+}. *(A, B) Ratiometric response of HeLa cells expressing redCALWY-1 (A) or redCALWY-4 (B) to the addition of 50 µM TPEN followed by the addition of 100 µM Zn^{2+} and 10 µM pyrithione. (C) HeLa cell transfected with redCALWY-4 with wild-type mOrange and mCherry domains (lacking the R125I mutations) was exposed first to 50 µM TPEN followed by 100 µM $ZnCl_2$ and 10 µM pyrithione. (D) Ratiometric response of redCALWY-4 in HEK293 cells. Cells transfected with redCALWY-4 were exposed first to 50 µM TPEN, followed by 100 µM ZnCl2 and 5 µM pyrithione. All traces in A, B and D represent the average of multiple cells after normalization of the emission ratio at t = 0. The trace in C represents a single cell. Error bars represent SEM.*

TPEN, whereas a large decrease is observed with Zn^{2+}/pyrithione (Figure 3.6B). As expected, the same sensor lacking the R125I reversion on the mFruit domains did not show any response to perturbations in intracellular Zn^{2+}_{free} (Figure 3.6C). Experiments with redCALWY-4 in HEK293 cells showed results similar to those in HeLa (Figure 3.6D). To provide a critical test for the orthogonality of the green and red FRET sensors, we co-expressed eCALWY-1 together with redCALWY-4 in the HeLa

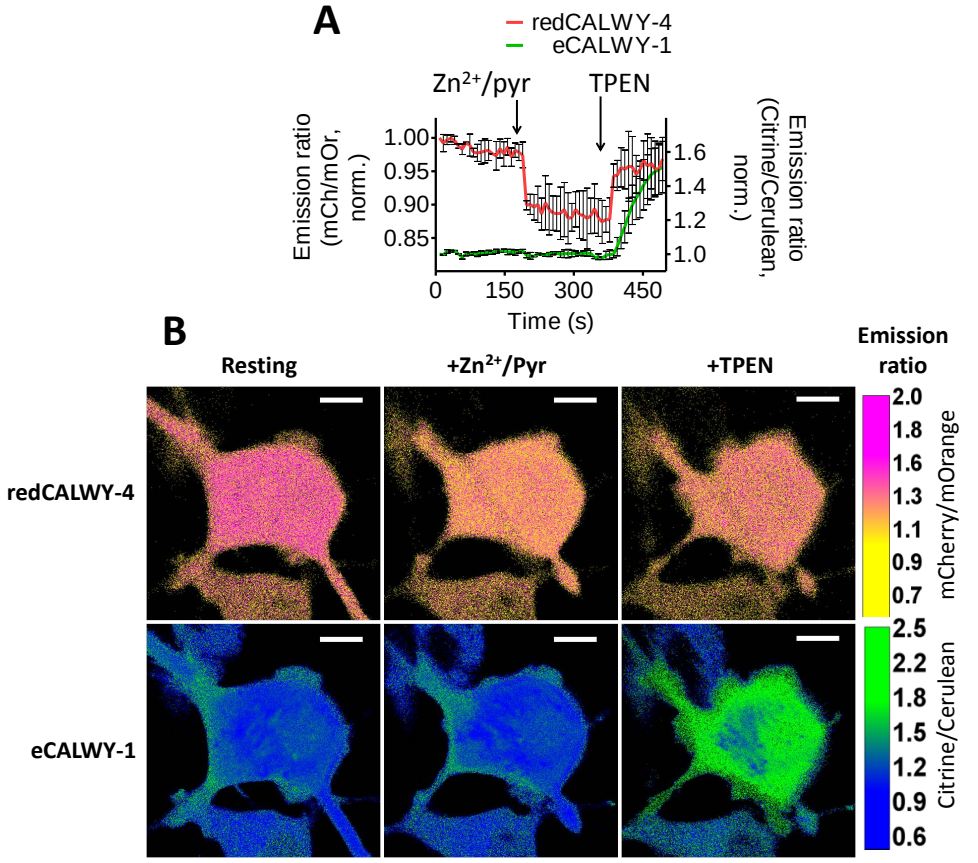

Figure 3.7. Simultaneous imaging of redCALWY-4 and eCALWY-1 Zn^{2+} sensors. *(A) Response of HeLa cells expressing both eCALWY-1 (green) and redCALWY-4 (red) to the addition of Zn^{2+}/pyrithione followed by excess TPEN. Traces in A represent the average of multiple cells after normalization of the emission ratio at t = 0. Error bars represent SEM. (C) False-colored ratiometric images of one of the cells measured in B in the resting state, at high Zn^{2+} concentration (+Zn^{2+}/pyr) and at low Zn^{2+} concentration (+TPEN). White scale bars represent 10 μm.*

cytosol. Since their Zn^{2+} affinities differ by more than an order of magnitude, together these sensors allow measurement of a greatly extended range of cytosolic Zn^{2+} concentrations. First, increasing the intracellular $[Zn^{2+}]_{free}$ led to a decrease in the redCALWY-4 emission ratio without the affecting eCALWY-1 emission ratio (Figure 3.7A). The lack of a response observed for the green eCALWY-1 is consistent with our previous work that showed that this sensor is already fully saturated with Zn^{2+} under normal conditions (15). Subsequent addition of TPEN resulted in an immediate increase in emission ratio for redCALWY-4, followed by a slower increase in emission ratio for the high affinity green eCALWY-1 sensor (Figure 3.7A, B). This result establishes the feasibility of multiparameter imaging using a combination of our newly developed optimized mOrange-mCherry FRET pair with a CFP-YFP based sensor.

In conclusion, we have shown that promoting intramolecular interactions between donor and acceptor fluorescent domains can be an efficient strategy to improve the traditionally poor performance of red FRET sensors. The mutations identified here allowed precise tuning of the intramolecular interaction between mOrange and mCherry, yielding protease and Zn^{2+} sensors with dramatically improved dynamic ranges. It is important to realize that successful application of this new FRET pair in other sensors will critically depend on their design. FRET sensors based on mutually exclusive domain interactions are most likely to benefit, whereas improvement of sensor performance is not guaranteed for sensors based on more subtle allosteric mechanisms, where introduction of these self-associating domains could lead to an increase in FRET in both the on and off states of the sensor (13). In addition to being directly applicable to DsRed-derived fluorescent domains, these design principles should be readily extendable to fluorescent domains from other families, providing a generic method for engineering alternatively colored FRET sensors for use in multiparameter imaging.

Methods

Cloning and mutagenesis. A synthetic construct encoding for mOrange-linker-mCherry inserted in a pUC57 cloning vector was ordered (Genscript, USA). Circular polymerase extension cloning (CPEC) (24) was used to clone the DNA encoding for this construct from pUC57 to the bacterial expression vector pET28a (Novagen), creating pET28a-mOrange-L9-mCherry. Briefly, primers mOrange_F and Streptag_R (Table 3.2) were used to amplify mOrange-linker-mCherry, while primers Strptg_dwnsvec and mOrange_throm were used to amplify and linearize pET28a (Novagen), using high-fidelity DNA polymerase (Phusion, NEB). Primers were designed to incorporate overlapping ends in the PCR fragment, allowing the subsequent CPEC reaction. A CPEC-based mutational strategy was also used to

Table 3.1. Mutational CPEC primers. *Overview of primers used in mutational CPEC to generate a small library of mOrange-linker-mCherry variants. Each primer is designed to introduce a mutation at a location indicated schematically in Figure 3.8.*

Mutation	Position/ Fragment	Primer orientation	Sequence (5'-->3')
mOr R125I	1/D	anti-sense	CGGAAAGTTAGTGCC**AAT**CAGCTTCAC
mOr R125I/T127V	1/D	anti-sense	CGGAAAGTTA**AC**GCC**AAT**CAGCTTCAC
mOr T127V	1/D	anti-sense	GGAAAGTTA**AC**GCCGCGCAGC
none	1/D	anti-sense	GGAAAGTTAGTGCCGCGCAGC
mOr R125I	1/A	sense	GTGAAGCTG**ATT**GGCACTAACTTTCCG
mOr R125I/T127V	1/A	sense	GTGAAGCTG**ATT**GGC**GT**TAACTTTCCG
mOr T127V	1/A	sense	GCTGCGCGGC**GT**TAACTTTCC
none	1/A	sense	GCTGCGCGGCACTAACTTTCC
mOr T180 (WT)	2/A	anti-sense	GGCTTTGTAGGTGGTTTTAACTTCAGAGG
mOr T180I	2/A	anti-sense	GGCTTTGTAG**A**TGGTTTTAACTTCAGAGGTG
none	2/B	sense	CCTCTGAAGTTAAAACCACCTACAAAGCC
mOr T180I	2/B	sense	CACCTCTGAAGTTAAAACCA**T**CTACAAAGCC
mCh R125I	3/B	anti-sense	CAGACGGGAAGTTAGTACC**AAT**CAGTTTTACTTTATAG
mCh R125I/T127V	3/B	anti-sense	CAGACGGGAAGTTA**AC**ACC**AAT**CAGTTTTACTTTATAG
mCh T127V	3/B	anti-sense	CGGGAAGTTA**AC**ACCACGCAGTTTTACTTTATAG
mCh T127V	3/B	anti-sense	CGGGAAGTTAGTACCACGCAGTTTTACTTTATAG
mCh R125I	3/C	sense	CTATAAAGTAAAACTG**ATT**GGTACTAACTTCCCGTCTG
mCh R125I/T127V	3/C	sense	CTATAAAGTAAAACTG**ATT**GGT**GT**TAACTTCCCGTCTG
mCh T127V	3/C	sense	CTATAAAGTAAAACTGCGTGGT**GT**TAACTTCCCG
none	3/C	sense	CTATAAAGTAAAACTGCGTGGTACTAACTTCCCG
none	4/C	anti-sense	CGCTTTGTACGTGGTTTTCACTTCC
mCh T180I	4/C	anti-sense	GCTTTGTA**GA**TGGTTTTCACTTCCGC
none	4/D	sense	GGAAGTGAAAACCACGTACAAAGCG
mCh T180I	4/D	sense	GCGGAAGTGAAAACCA**TC**TACAAAGC

introduce the various combinations of reversions R125I, V127T and T180I (numbering relative to DsRed) in one or both of the fluorescent domains. PCR fragments were generated using primers (Table 3.1) that introduced one or more of the desired reversions at the ends of fragments. Fragments were then combined and circularized

using CPEC (Figure 3.8). To produce single mCherry domains for the intermolecular dimerization studies, site-directed deletion mutagenesis was carried out using a modification of a previously published mutagenesis technique, allowing a one-step 913 bp deletion of DNA encoding mOrange and linker (25). To generate pET28a-mCherry, a primer pair (del_mOrange_R and del_mOrange_F) was designed with complementary 5'- and 3'-ends, ensuring amplification of the entire expression plasmid except the part encoding mOrange and linker. To produce the pET28a-LSSmOrange-L9-mCherry constructs, we introduced LSSmOrange-specific mutations (21) using a mutational CPEC strategy with primer pairs A44V_R & G196D_F, A44V_F & F83L_R, F83L_F & W143M_R, W143M_F & I161D_M163L_R and I161D_M163L_F & G196D.

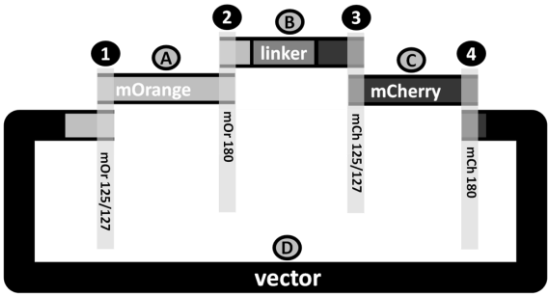

Figure 3.8. Schematic overview of mutational CPEC strategy. *In order to introduce mutations at four different positions in the mOrange-linker-mCherry protease sensor simultaneously, a mutational CPEC strategy was followed. At each of the positions, mOrange 125/127, mOrange 180, mCherry 125/127 and mOrange 180 (labeled 1 to 4 respectively), primers were designed to allow amplification of four different fragments (labeled A, B, C and D). Primers were designed to incorporate different mutations into the ends of PCR fragments in such a way that both ends of each fragment overlapped with the ends of adjacent fragments, with a melting temperature of about 72 °C (calculated using Thermo Scientific's online Tm tool (http://www.thermoscientificbio.com/webtools/tmc/)). These fragments were subsequently recombined in a CPEC reaction, at equimolar concentration and 200 ng of vector fragment D. The primers used at positions 1 to 4, as well as the mutations they were designed to introduce, are listed in Table 3.1.*

To produce the bacterial expression vectors pET28a-redCALWY-1 and pET28a-redCALWY-4, the ATOX-L9-WD4 insert was amplified from pET28a-eCALWY-1 or pET28a-eCALWY-4 using primers Ins_redeCalwy_F and Ins_redeCalwy_R. In

parallel, pET28a-mOrange-L9-mCherry was PCR-linearized using primers Vec_redeCalwy_F and Vec_redeCalwy_R and insert and vector were combined using CPEC. To produce the pGen2.1-redCALWY-4 mammalian expression construct, we took as starting template pGen2.1-mOrange2(R125I)-linker-mCherry(R125I), a vector bearing a synthetic mammalian expression construct (Genscript), restricted it with KpnI and BspEI and ligated it to an insert cut from peCALWY-4 (15) with the same restriction enzymes. pGen2.1-redCALWY-1 was generated by reverting the cysteine-to-serine mutation of the third cysteine of the WD4 domain in pGen2.1-redCALWY-4 back to a cysteine using primers WD4_S _to_C3_F and WD4_S_to_C3_R. Primers RCS_mOr2_I125R_F and RCS_mCh_I125R_F were used to introduce the I125R mutations in pGen2.1-redCALWY-4. All plasmids were confirmed by sequencing prior to use.

Table 3.2. Overview of primers used for cloning and site-directed mutagenesis.

Name	Sequence (5'-->3')
Strptg_dwnsvec	GTCCCATCCGCAGTTCGAGAAATAAGCTGAGCAATAACTAGCATAACCCCTTG
mOrange_F	ATGGTGAGCAAAGGTGAGGAAAAC
Streptag_R	TTATTTCTCGAACTGCGGATGGGAC
mOrange_throm	GTTTTCCTCACCTTTGCTCACCATATGGCTGCCGCGCGG
del_mCherry_F	CGAACTGTATAAATAAGCTGAGCAATAACTAGCATAACCCCTTGGGGCC
del_mOrange_R	GTCCTCTTCGCCCTTAGAAACCATATGGCTGCCGCGCG
del_mOrange_F	GTTTCTAAGGGCGAAGAGGACAATATGGCTATCATCAAAGAGTTCATGCG
del_mCherry_R	GTTATTGCTCAGCTTATTTATACAGTTCGTCCATACCGCCAGTAGAATGACG
A44V_F	TTTCCAGACTGTTAAACTGAAGGTGACCAAAGGCGG
A44V_R	ACCTTCAGTTTAACAGTCTGGAAGCCCTCATACGG
F83L_F	TCCCCGATTATTTAAAACTGTCATTCCCGGAAGGCTTCAAATG
F83L_R	GACAGTTTTAAATAATCGGGGATATCTGCAGGGTGTTTAACATACGCCTTG
W143M_F	ACTATGGGCATGGAAGCTTCCTCTGAACGTATGTATCCG
W143M_R	GAAGCTTCCATGCCCATAGTCTTTTTCTGCATAACCG
I161D&M160L_mOrF	GGTGAGGACAAACTGCGTCTGAAGCTGAAAGATGGC
I163D&M160L_mOrR	GACGCAGTTTGTCCTCACCTTTCAGCGCGCC
G196D_F	TGCTTACATTGTAGATATTAAACTGGATATCACGAGCCATAACGAG
G196D_R	CCAGTTTAATATCTACAATGTAAGCACCCGGCAGTTG
Vec_redeCalwy_F	TTCAGTCTCGGTACCGATGGTTTCTAAGGGCGAAGAGGACA
Vec_redeCalwy_R	GCATTCCGGATTTATACAGTTCGTCCATACCGCCAG
Ins_redeCalwy_F	GGACGAACTGTATAAATCCGGAATGCCGAAGCAC
Ins_redeCalwy_R	TTAGAAACCATCGGTACCGAGACTGAAGCCTCAAATC
WD4_S_to_C3_F	ATGACCTGTGCATCCTGTGTCCATTCCATTG
WD4_S_to_C3_R	CACAGGATGCACAGGTCATGCCGGCAATGG
RCS_mOr2_I125R_F	CTATAAAGTAAAACTGCGTGGTACGAATTTTCCCTCAGATGGACC
RCS_mOr2_I125R_R	CGTACCACGCAGTTTTACTTTATAGATGAACTCCCCATCCTG
RCS_mCh_I125R_F	CAAGGTGAAGCTTAGAGGCACAAACTTTCCAAGCGACG
RCS_mCh_I125R_R	GTGCCTCTAAGCTTCACCTTGTATATAAACTCGCCG

Protein expression and purification. *E. coli* BL21(DE3) transformed with expression plasmid was grown to OD_{600} in 500 mL (for the red protease constructs) or 2 L (for the redCALWY constructs) LB medium containing 50 µg/mL kanamycin in a shaking incubator at 37 °C. Following induction with 0.1 mM IPTG, the bacterial

cultures were grown overnight at 25 °C. Cells were harvested by centrifugation and lysed using 10 mL BugBuster Protein Extraction reagent (Novagen) with 10 µL Benzonase. Proteins were purified by Ni-NTA affinity chromatography and were subsequently loaded onto a size exclusion column (Sephacryl S200, GE Healthcare). The SEC fractions were analyzed by SDS PAGE for correct size and purity, pooled and concentrated using 10 kDa MWCO centrifugation filters. The single domain mCherry constructs used for anisotropy studies were purified by Ni-NTA chromatography only, as SDS-PAGE revealed this single purification step to result in sufficient purity of these constructs. Since His-tags are known to readily bind Zn^{2+} (26), they were removed from all Zn^{2+}-sensor constructs using thrombin cleavage. After elution of the Zn^{2+}-sensor constructs from the Ni-NTA column, the buffer was exchanged to thrombin cleavage buffer (20 mM Tris-HCl (pH 8.4), 150 mM NaCl, 2.5 mM $CaCl_2$) using PD10 desalting columns (GE, Healthcare). Cleavage of the thrombin recognition site between the His-tag and the mOrange N-terminus was initiated by the addition of 0.3 U thrombin protease (Novagen) per mg target protein at a 0.2 mg/mL target protein concentration. Cleavage was carried out at 4 °C for 20 hours, after which proteins were loaded onto Ni-NTA once again. Elution of protein without a His-tag from the Ni-NTA required a buffer containing 30 mM imidazole, presumably due to a weak affinity of the WD4 and/or ATOX1 domain for Ni-NTA, as previously noted for Wilson disease proteins (27). Uncleaved protein remained behind on the Ni-column at this imidazole concentration. The red Zn^{2+} sensor proteins were subsequently further purified by SEC chromatography. The SEC fractions were analyzed by SDS PAGE for correct size and purity, pooled and concentrated using 10 kDa MWCO centrifugation filters.

Library screening. Initial expression, purification and screening of a small library of mOrange-linker-mCherry reversion bearing variants were carried out at small scale. Briefly, protein expression from 100 mL *E. coli* BL21(DE3) cultures was induced with 0.1 mM IPTG overnight at 25 °C. The His-tagged proteins were purified from the soluble fraction of the cell lysate by microfuge-based Ni^{2+}-NTA affinity chromatography (GE). Proteins were salt exchanged to 50 mM Tris-HCl (pH 8), 100

mM NaCl and subsequently incubated at 37 °C overnight to allow complete maturation of the mOrange chromophore. Protein samples were prepared in 200 µL Tris buffer at a 10 µM concentration in a 96-well plate. Fluorescence emission spectra were recorded using a plate reader (TECAN Safire) before and after the addition of 0.006 U proteinase K (Sigma) using 525 nm excitation light. Emission ratios were calculated as emission at 610 nm divided by emission at 565 nm.

Fluorescence spectroscopy and Zn^{2+} titration experiments. Before any measurements, proteins were incubated at room temperature overnight to ensure complete maturation of the mOrange or LSSmOrange chromophore. Red protease sensor fluorescence emission spectra were measured with 1 µM sensor protein in 2 mL buffer (50 mM Tris-HCl (pH 8), 100 mM NaCl) at 25 °C in quartz cuvettes with a 1 cm path length (Hellma) and an excitation wavelength of 525 nm (mOrange) or 440 nm (LSSmOrange), using a Cary Eclipse fluorescence spectrometer (Varian). To cleave the flexible linker, a total of 0.005 units of proteinase K (Sigma) was added. Zn^{2+} titrations were carried out with 0.25 µM redCALWY protein, in buffer consisting of 50 mM Tris (pH 7.1), 100 mM NaCl, 10% (v/v) glycerol, 0.5 mM TCEP and 2 µM DTT, together with different Zn^{2+}-chelators (EDTA, HEDTA, DHPTA, NTA and EGTA) and different concentrations of $ZnCl_2$, as previously described (15). The free Zn^{2+} concentration was calculated using the published critical stability constants of the chelators for Zn^{2+}. To determine the redCALWY variants' dissociation constants (K_d) for Zn^{2+}, the emission ratio (R) was fitted as a function of [Zn^{2+}] using equation 3.1.

$$R = \frac{P_1[Zn^{2+}]}{K_d + [Zn^{2+}]} + P_2 \qquad (3.1)$$

Here R is the ratio of mCherry (at 605 nm) to mOrange (at 562 nm) emission, [Zn^{2+}] the calculated Zn^{2+}_{free} concentration, P_1 the difference in ratio between the Zn^{2+} saturated and Zn^{2+} depleted states and P_2 the ratio in the Zn^{2+} depleted state of the sensor.

Fluorescence anisotropy. To determine the dissociation constant for dimerization of the mCherry mutants, fluorescence anisotropy was used to follow fluorescence emission depolarization induced by homoFRET. This technique was recently described

in detail for variants of CFP (19). Measurements were performed at 25 °C in 50 mM Tris-HCl (pH 8), 100 mM NaCl and 1 mg/mL BSA in a quartz cuvette with a 1x1 cm path length (Hellma), with an excitation wavelength of 560 nm, a 20 nm excitation slit width, a 5 nm emission slit width, while monitoring emission between 595 and 615 nm, using a Cary Eclipse fluorescence spectrophotometer (Varian). At concentrations above 10 µM, a 3x3 mm pathlength cuvette was used instead. The decrease in anisotropy that is observed for mCherry WT at concentrations above 10 µM is most likely not due to formation of a homodimer, as mCherry has been reported to be monomeric up to at least 350 µM (28). Instead this decrease results from homoFRET between molecularly dissolved monomeric proteins and we therefore limited the analysis of the mCherry variants to concentrations no higher than 10 µM. We fitted the data in Figure 3.3B measured at mCherry concentrations below 10 µM to the dimerization model (equation 2) previously derived for CFP (19) to arrive at the K_ds reported here:

$$r = \left(\frac{-K_d + \sqrt{{K_d}^2 + 8 \cdot c \cdot K_d}}{4 \cdot c}\right) \cdot r_m + \left(1 - \left(\frac{-K_d + \sqrt{{K_d}^2 + 8 \cdot c \cdot K_d}}{4 \cdot c}\right)\right) \cdot r_d \qquad (3.2)$$

Here r is the observed anisotropy, K_d the dissociation constant for FP homodimerization, c the FP concentration, r_m the FP anisotropy in the monomeric state and r_d the anisotropy of the FP in the dimeric state. A global fit over both data sets allowed us to exploit the information present in both datasets, with mCherry (R125I/T127V) providing the value for anisotropy in the fully dimerized state and mCherry (R125I) providing the value for anisotropy in the completely monomeric state.

Mammalian cell culture and imaging. HeLa cells were grown in Dulbecco's Modified Eagle Medium (DMEM) supplemented with 25 mM glucose, 10% Fetal Bovine Serum (FBS), 100 U/mL penicillin and 100 µg/mL streptomycin (all from Life Technologies) but lacking sodium pyruvate. Chambered borosilicate cover glass wells (4.2 cm^2 each, Lab-Tek, Nunc) were seeded with 200,000 cells one day before transfection. Transfection was carried out with Lipofectamine 2000 (Life Technologies) according to manufacturer's instructions. Cells were imaged two days

after transfection in a HEPES buffer (Live Cell Imaging Solution, Life Technologies) at 37 °C. Imaging was performed with a confocal microscope (Leica, TCS SP5X) equipped with a 40x water immersion objective, acousto-optical beamsplitters (AOBS), a white light laser and a 405 nm laser. To excite Cerulean, a 405 nm laser was used, while a white light laser set to 550 nm (5% of full power) was used for excitation of mOrange2. Emission was monitored over the following windows using the AOBS and avalanche photo diode/photomultiplier tubes hybrid detectors (HyD, Leica): Cerulean (460-490 nm), Citrine (510-550 nm), mOrange2 (565-600 nm) and mCherry (600-630 nm). Images were acquired at either 8.21 second intervals (two sensor experiments) or at 5 second intervals (single sensor experiments). Cells were first imaged for several minutes with HEPES buffer alone, before HEPES buffer with N,N,N',N'-Tetrakis(2-pyridylmethyl)ethylenediamine (TPEN, TCI Europe) was added to a final concentration of 50 µM TPEN, followed a few minutes later by HEPES buffer containing $ZnCl_2$ and 2-Mercaptopyridine N-oxide (pyrithione, Sigma) with a final concentration of 36 µM TPEN, 100 µM $ZnCl_2$ and 5 µM pyrithione. In other experiments, this order was reversed, and cells were imaged first in their resting state, followed by 10 µM $ZnCl_2$ and 1 µM pyrithion, before the addition of 50 µM TPEN. For ease of comparison, all emission ratios were normalized to the ratio at t = 0. To generate pseudocolored ratiometric images, images corresponding to channels (mOrange, mCherry, Cerulean or Citrine) obtained under three different conditions (in the cell's resting state, at saturating Zn^{2+} levels or in the Zn^{2+}-depleted state) were averaged, after which acceptor averaged images (mCherry or Citrine) were divided by donor averaged images (mOrange or Cerulean respectively), which were then thresholded, removing values above 2 (for mOrange/mCherry images) or 2.5 (for Cerulean/Citrine images).

Acknowledgements

This work was published in: Lindenburg, L. H., Hessels, A. M., Ebberink, E. H., Arts, R., and Merkx, M. (2013) Robust red FRET sensors using self-associating fluorescent

domains, *ACS Chem Biol* **8**, 2133–2139. I am grateful to Eduard Ebberink for planning, carrying out and analyzing crucial experiments revealing the mutations necessary for self-association of mOrange and mCherry. I also appreciate his efforts to first image the mOrange-mCherry-based FRET sensors in mammalian cells. Mark van 't Erve carefully characterized the effect of these mutations on the individual fluorescent domains. Parinaz Goodarzifard carried out initial characterization of the redCALWY Zn^{2+} sensors. Remco Arts planned, carried out and analyzed experiments concerning the *in vitro* behavior of redCALWY and LSSmOrange-L9-mCherry. In addition, he carried out initial successful confocal imaging of redCALWY in mammalian cells. Anne Hessels planned, performed and analyzed all the imaging experiments described in this chapter.

References

1. Campbell RE (2009) *Anal Chem* **81,** 5972-5979.
2. Palmer AE, Qin Y, Park JG, & McCombs JE (2011) *Trends Biotechnol* **29,** 144-152.
3. Hamers D, van Voorst Vader L, Borst JW, & Goedhart J (2013) *Protoplasma* **251,** 333-347.
4. Carlson HJ & Campbell RE (2009) *Curr Opin Biotechnol* **20,** 19-27.
5. Welch CM, Elliott H, Danuser G, & Hahn KM (2011) *Nat Rev Mol Cell Biol* **12,** 749-756.
6. Ai HW, Hazelwood KL, Davidson MW, & Campbell RE (2008) *Nat Methods* **5,** 401-403.
7. Ding Y, Ai HW, Hoi H, & Campbell RE (2011) *Anal Chem* **83,** 9687-9693.
8. Piljic A & Schultz C (2008) *ACS Chem Biol* **3,** 156-160.
9. Ouyang M, *et al.* (2010) *Cancer Res* **70,** 2204-2212.
10. Jost CA, Reither G, Hoffmann C, & Schultz C (2008) *ChemBioChem* **9,** 1379-1384.
11. Miranda JG, *et al.* (2012) *PLoS One* **7,** e49371.
12. Goedhart J, *et al.* (2007) *PLoS One* **2,** e1011.
13. Kotera I, *et al.* (2010) *ACS Chem Biol* **5,** 215-222.
14. Vinkenborg JL, *et al.* (2007) *ChemBioChem* **8,** 1119-1121.
15. Vinkenborg JL, *et al.* (2009) *Nat Methods* **6,** 737-740.
16. van der Velden LM, *et al.* (2013) *Hepatology* **57,** 740-752.
17. Golynskiy MV, Rurup WF, & Merkx M (2010) *ChemBioChem* **11,** 2264-2267.
18. Campbell RE, *et al.* (2002) *Proc Natl Acad Sci U S A* **99,** 7877-7882.
19. Espagne A, *et al.* (2011) *Biochemistry* **50,** 437-439.
20. Evers TH, *et al.* (2007) *J Mol Biol* **374,** 411-425.
21. Shcherbakova DM, *et al.* (2012) *J Am Chem Soc* **134,** 7913-7923.
22. Taylor KM, *et al.* (2012) *Sci Signal* **5,** ra11.
23. Shaner NC, *et al.* (2008) *Nat Methods* **5,** 545-551.
24. Quan J & Tian J (2009) *PLoS One* **4,** e6441.
25. Liu H & Naismith JH (2008) *BMC Biotechnol* **8,** 91.
26. Evers TH, Appelhof MA, Meijer EW, & Merkx M (2008) *Protein Eng Des Sel* **21,** 529-536.
27. Wernimont AK, Yatsunyk LA, & Rosenzweig AC (2004) *J Biol Chem* **279,** 12269-12276.
28. Shemiakina, II, *et al.* (2012) *Nat Commun* **3,** 1204.

Chapter 4

Quantifying stickiness; thermodynamic characterization of intramolecular interactions between fluorescent domains to guide the design of FRET sensors

Abstract. The introduction of a simple hydrophobic ("sticky") interaction between fluorescent proteins (FPs) within a FRET sensor can dramatically enhance the sensors' dynamic range (DR). Quantitative understanding of this interaction would help guide FRET sensor design. Here a comprehensive thermodynamic characterization of the stability of a range of self-associating FRET pairs is reported. A new assay was developed that can directly quantify the stability of weak intramolecular associations by monitoring the high FRET intramolecular complex as a function of urea concentration. It was found that the hydrophobic surface mutation S208F provides an interactional stability of around 1.6 kCal/mol for the intramolecular dimer formed by the commonly used FRET pair ECFP/EYFP, while in the more recently developed Cerulean/Citrine pair it appeared to be significantly weaker (ΔG^0_{o-c} = 0.2 kCal/mol) due to Cerulean's Y145A and H148D mutations. The technique was also used to determine the stability of mOrange-mCherry intramolecular complexes, including a series of new variants with a range of interaction strengths. The relative stabilities found with urea-based analysis for mOrange-mCherry were supported by an assay that determined the K_d for mCherry homodimerization by monitoring the amount of homoFRET using fluorescence anisotropy. Finally, the effect of the intramolecular dimer stability was tested in a red-shifted FRET sensor for Zn^{2+}. Weaker, subtle

interactions were found to be optimal, while stronger interactions unexpectedly resulted in a dampening of the sensor's DR. Together these findings allow for a better understanding of the subtle effects that determine the performance of existing FRET sensors and help guide the rational design of sensors using modular design strategies.

Introduction

FRET-based protein sensors are attractive tools to image changes in small molecule concentrations at subcellular resolution. These genetically encoded sensors typically consist of one or more recognition domains, fused between a donor and acceptor FP. The transfer of energy from a donor, such as Cyan FP (CFP), to an acceptor, such as Yellow FP (YFP), can be modulated through changes in conformation of the recognition domain upon binding of a small molecule of interest and is readily detected through a change in the acceptor to donor fluorescence emission intensity ratio (1). Sensors are now available for many different small molecules, as well as a variety of enzyme activities (2). Most FRET sensors developed to date function by tight coupling of the fluorescent domains to the N and C-termini of the recognition domain, such that changes in conformation are directly transmitted to a change in the FPs' relative distance. Unfortunately, such designs often require time-consuming, trial-and-error based empirical testing to achieve the best possible response from the sensor (3). For example, to produce a Troponin C-based Ca^{2+} FRET sensor with sufficient dynamic range (DR), 70 different protein variants were purified and characterized *in vitro* (4). Furthermore, FRET sensors developed so far lack modularity: replacement of CFP/YFP FRET pairs with red-shifted FRET pairs can significantly dampen the DR (5, 6), and even the exchange of ECFP for the highly similar Cerulean is apparently not always tolerated (7). While directed evolution has been successfully applied in the development of many recent FPs (8-12) and intensity-based fluorescent probes (13-15), similar efforts for FRET sensors remain underdeveloped (16).

In contrast to the classical FRET sensor design, we and others have recently developed an alternative design that relies on intramolecular protein-protein interactions (Figure 4.1). In this strategy, FRET sensors are designed to take on two

mutually exclusive conformations, with a large difference in FRET efficiency between the two. In one conformation, the FP pair forms an intramolecular complex that is mediated by hydrophobic surface mutations, leading to high FRET efficiency. Addition of ligand renders the second conformation energetically favorable, resulting in the disruption of the intramolecular fluorescent domain complex and leading to a dramatic drop in FRET efficiency (Figure 4.1). Several sensors have been explicitly designed to

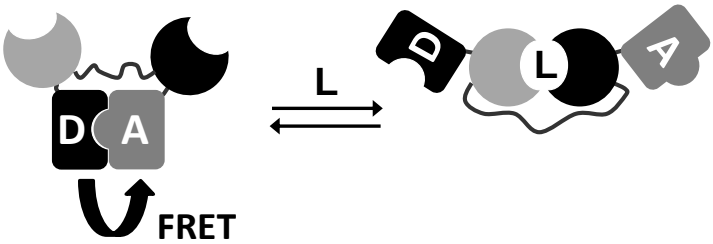

Figure 4.1: Sticky fluorescent domains improve the dynamic range of FRET sensors based on mutually exclusive interactions. *Schematic representation of the ligand-dependent equilibrium that exists between two mutually exclusive conformations of the FRET sensor. In absence of ligand (L), donor (D) and acceptor (A) FPs are in an intramolecular complex, leading to high FRET. The ligand induces an interaction between the ligand binding domains (in grey and black) that is mutually exclusive with the intramolecular FP complex, resulting in a loss of FRET.*

exploit the decrease in FRET efficiency occurring upon a particular intramolecular protein-protein interaction including sensors for Zn^{2+} (17), for peptide (18), for antibody (19) and for bile acids (20). In all of these sensors, "sticky" mutations such as S208F in ECFP and EYFP play a crucial role, and in their absence the sensors show no or only a very weak response to ligand addition. The molecular switch-like FRET sensor design has led to improvements not only in sensor DR, but also in the ease with which sensor parts, such as FPs, recognition domains and linkers can be exchanged. For example, the introduction of hydrophobic surface mutation R125I in both mOrange and mCherry allowed exchange of the CFP/YFP FRET pair with this red-shifted FRET pair without further optimization (Chapter 3).

Although the FRET sensors discussed above greatly benefited from the introduction of interaction-promoting mutations on the fluorescent domains, a sensor's architecture must be carefully considered in deciding whether the probe's response would stand to benefit from this approach. In fact, some highly optimized sensors may already depend on a subtle level of FP self-association even in absence of explicitly introduced sticky mutations. Introduction of both dimerizing (S208F/V224L) and monomerizing (A206K) mutations in highly optimized FRET sensors for Ca^{2+} resulted in attenuation of the DR, indicating that a subtle level of FP complex formation was important for the optimal functioning of these sensors (21). Similarly, introduction of monomerizing mutations in two different FRET sensors for kinase activity had a detrimental effect on DR, indicating the crucial role played by intramolecular FP complex formation in these sensors' mechanism of action (6).

Direct quantification of the weak intramolecular FP domain interaction would help in fully understanding the equilibria at play in these single chain FRET sensors and could guide future FRET sensor design. Here a new approach is introduced in which a urea titration is used to quantitatively probe the stability of the intramolecular CFP-YFP and mOrange-mCherry interactions. The technique is also used to establish the intramolecular dimer stability mediated by several different mutations of the critical 125/127 interface positions of mOrange and mCherry. Pairs of mOrange/mCherry with different stabilities were tested in the context of the redCALWY-1 Zn^{2+} sensor, revealing important insights on the appropriate levels of stability between the FPs for the optimal performance of FRET sensors.

Results

Characterization of the CFP-YFP interaction by urea titration

The S208F and V224L mutations have been reported to improve the DR of CFP/YFP based FRET sensors through introduction of a reversible intramolecular dimerization of the fluorescent domains (22, 23). The presence of S208F was necessary to obtain an intramolecular dimer, while V224L was found to lead to a further improvement in

FRET efficiency, but was not capable of mediating the interaction on its own (23). To quantify the stability of the interaction between ECFP and EYFP mediated by the S208F and V224L mutations (the combination of which is henceforth denoted by *), the amount of FRET was monitored as a function of urea concentration in a fusion construct consisting of the two fluorescent domains, connected by 9x repeat of GGSGGS (ECFP*-L9-EYFP*) (23, 24). This approach is analogous to a classical equilibrium unfolding experiment where single domains are exposed to increasing concentrations of denaturant. It is important to note that FPs are known to be relatively resistant to chemical denaturation (25, 26); indeed EYFP's fluorescence emission intensity was found to change by no more than 20% between 0 and 6 M urea (not shown). As previously observed (23), ECFP*-L9-EYFP* displayed an acceptor to donor emission ratio of ~8 under "native" conditions (pH 8, 20 °C) (Figure 4.2A). Addition of urea resulted in a decrease in emission ratio, indicating a decrease in FRET due to disruption of the intramolecular complex between ECFP* and EYFP*. In contrast, the same fusion construct lacking the S208F/V224L mutations (ECFP-L9-EYFP) displayed a much lower emission ratio under native conditions (Figure 4.2B), consistent with the absence of an interaction between these fluorescent domains (23, 24). The small decrease in emission ratio observed upon addition of urea was not due to a residual interaction between the two fluorescent domains, but results from the effect of urea on the conformational distribution of the long flexible linker. In water, poly-serine/glycine chains form compact, random coil-like structures due to intrachain hydrogen bonds that result in loops within the chain (24, 27). Previous work on isolated poly-serine/glycine peptides has shown that denaturants disrupt those bonds, resulting in an increase of the end-to-end distance distribution (28, 29) and thus a lower efficiency of energy transfer between ECFP and EYFP.

The emission ratio for construct ECFP*-L9-EYFP* displayed a sigmoidal dependence on urea concentration (Figure 4.2A) indicating a two-state equilibrium between sensor in the closed and in the opened state (Figure 4.2A, inset). The sigmoidal curve was fit to a Boltzmann distribution using equation 4.1 (Figure 4.2C),

$$R_x = R_o + \frac{R_c - R_o}{1 + e^{\frac{x - x_0}{dx}}} \tag{4.1}$$

where the emission ratio at each concentration of urea (R_x) depends on the emission ratio in the closed state of the sensor (R_c), the ratio in the opened state (R_o), the urea concentration (*x)*, the point of inflection of the curve where precisely 50% of the sensor remains in the closed state (x_0) and the slope of the curve at the inflection point (*dx)*. Next, the equilibrium constant at each concentration of urea (K_x) was calculated using equation 4.2,

$$K_x = \frac{(R_c - R_x)}{(R_x - R_o)} \tag{4.2}$$

where R_x is the emission ratio observed at a particular concentration of urea. From the equilibrium constants, the Gibbs free energy associated with the transition from closed to opened sensor at any particular concentration of urea (ΔG^x_{o-c}) was calculated using equation 4.3,

$$\Delta G^x_{o-c} = -RTln(K_x) \tag{4.3}$$

where R is the gas constant (1.987 cal/mol/deg) and T the temperature (293.15 K). In analogy to classical domain unfolding studies, changes in ΔG_{o-c} displayed a negative linear correlation to increasing urea concentration (Figure 4.2D). This trend was fit to equation 4.4,

$$\Delta G^x_{o-c} = \Delta G^0_{o-c} + mx \tag{4.4}$$

where ΔG^0_{o-c} represents the extrapolation of ΔG_{o-c} to 0 M urea, indicating the stability of the sticky interaction under native conditions, ΔG^0_{o-c} =1.6 kcal/mol (Figure 4.2D, Table 4.1). The slope of the urea- ΔG_{o-c} relationship, m, was found to be -0.67 kcal/mol/M (Table 4.1). Parameter m is known to correlate with the difference in solvent exposed hydrophobic area between the folded and unfolded state. The small

value of *m* found here is thus consistent with the exposure of a relatively small solvent-excluded contact area (26, 30).

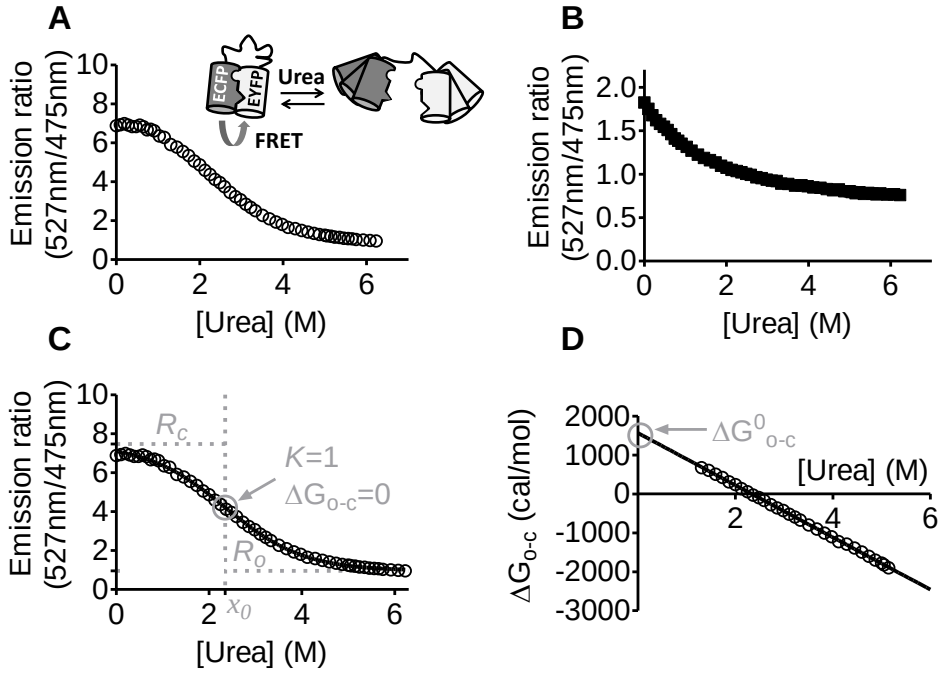

Figure 4.2: Use of urea titrations to establish the stability of the intramolecular dimer interface in ECFP*-L9-EYFP*. *(A) Fluorescence emission ratio of ECFP*-L9-EYFP* monitored as a function of urea concentration. Schematic representation of the two-state equilibrium between protein in the complexed (left) and non-complexed (right) state is included in the inset. (B) As (A) but with ECFP-L9-EYFP. (C) The data for ECFP*-L9-EYFP* was fit to a Boltzmann distribution, assuming a transition between closed and opened sensor. The emission ratio corresponding to completely closed sensor (R_c) and completely opened sensor (R_o) are indicated in grey. Also indicated in grey is the denaturation midpoint (x_0) at which there is an equal amount of closed and opened sensor at equilibrium, so that the equilibrium constant (K) is equal to 1 and the Gibbs free energy (ΔG_{o-c}) is equal to 0. (D) Plot showing the linear correlation between the urea concentration and the Gibbs free energy associated with transition from the closed to opened state. Data was fit to a linear model and extrapolated to 0 M urea, providing the standard Gibbs free energy of the complex under native conditions (ΔG^0_{o-c}), indicated by the grey circle at the intersection of the fit with the Y-axis. Urea titrations were carried out using 1.5 µM protein, in 50 mM Tris-HCl (pH 8), 100 mM NaCl, 10% (v/v) glycerol, at 20 °C.*

Table 4.1: Thermodynamic parameters of urea-induced dissociation of the CFP-YFP intramolecular dimer.

FP pair	R_c	R_o	X_0 (M)	m (kcal/mol/M)	ΔG^0_{o-c} (kcal/mol)
ECFP*-L9-EYFP*	7.5±0.1	0.95±0.02	2.3±0.1	-0.67±0.01	1.6±0.1
Cer*-L9-Cit*	8.9±0.4	0.70±0.02	0.3±0.1	-0.54±0.01	0.17±0.01
Cer*(A145Y/D148H)-L9-Cit*	7.7±0.1	0.82±0.04	2.4±0.1	-0.76±0.01	1.8±0.1

Having established the suitability of urea titrations to determine the stability of the intramolecular donor-acceptor FP complex, we next tested the effect of mutations S208F and V224L on the Cerulean and Citrine donor/acceptor pair. Cerulean and Citrine are frequently used in modern FRET sensors as these FPs have optimized properties relative to parent proteins ECFP and EYFP respectively, including improved brightness, photostability and, for Citrine, decreased pH sensitivity (31, 32). Cer*-L9-Cit* again displayed a high emission ratio under native conditions and showed a clear transition to a low FRET state upon addition of increasing concentrations of urea (Figure 4.3A). However, the transition took place at lower urea concentrations than seen with ECFP*-L9-EYFP* and started immediately upon addition of urea. The data for Cer*-L9-Cit* were fit to a Boltzmann distribution and the resulting parameters were used to determine the free energy barrier between the intramolecularly complexed and uncomplexed form at every concentration of urea (Table 4.1). Under native conditions, Cer*-L9-Cit* displayed a stability of 0.17 kcal/mol, a value that is much lower than that found for the interaction in ECFP*-L9-EYFP*, although it should be noted that the lack of a stable plateau phase at lower urea concentrations increased the uncertainty in the determination of R_c and consequently ΔG^0_{o-c}. The decreased stability seen with the Cerulean-Citrine complex may be due to mutations on either one of these improved FP variants. Mutations Q69M in Citrine and S72A in Cerulean are buried inside the beta-barrel, in the vicinity of the chromophore, and are thus unlikely to affect the FPs' protein-protein interactions. The mutations Y145A and H148D in Cerulean on

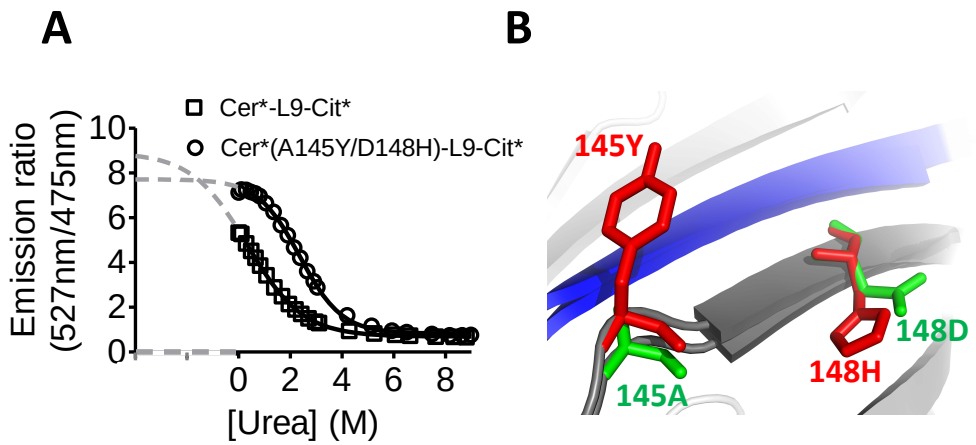

Figure 4.3: The Cerulean-Citrine intramolecular interface is weaker, due to surface mutations on Cerulean. *(A) Fluorescence emission ratio monitored as a function of urea concentration for Cer*-L9-Cit* and Cer*(A145Y/D148H)-L9-Cit*. Curves were fit to a Boltzmann distribution, assuming a transition between closed and opened state. Urea titrations were carried out using 1.5 µM protein, in 50 mM Tris-HCl (pH 8), 100 mM NaCl, 10% (v/v) glycerol, at 20 °C. (B) Detail from an alignment of crystal structures for Cerulean (2WSO) and ECFP (2WSN) showing that residue positions 145 and 148 are in close proximity to positions located along strand 10 (colored blue), mutations of which are known to be crucial in either forming (Q204F, S208F) or disrupting (A206K) a stable dimeric interface. In ECFP, the hydrophobic side group of 145Y (red) clearly points out towards the hydrophobic interface, but in Cerulean the corresponding 145A (green) is buried in the beta-barrel. Also, in ECFP, 148H (red) is oriented parallel to the protein surface, while in Cerulean, 148D (green) points out into the solvent. For clarity, the alternative "B" position of residue 145 is not shown.*

the other hand are located along the seventh beta-strand of Cerulean, adjacent to the 10th strand containing the S208F residue that is responsible for the intramolecular dimerization (Figure 4.3B). In ECFP, H148 is oriented in parallel to the FP surface, but in Cerulean, the D148 side chain is pointing out into the solvent (33) (Figure 4.3B). The presence of the negatively charged side group could lead to destabilization of the intramolecular domain interaction. Furthermore, in ECFP, Y145 points out into the solvent, whereas in Cerulean, A145 has a tendency to point into the protein core (33). The presence of the hydrophobic side group of tyrosine at the surface of ECFP may further stabilize hydrophobic interactions. Indeed, a clear increase in stability was observed (to 1.8 kcal/mol) in the construct Cer*(A145Y/D148H)-L9-Cit* (Figure

4.3A, Table 4.1), confirming the effect of these mutations on the intramolecular dimer stability. Nevertheless, despite the relatively weak interaction between the Cerulean* and Citrine* domains, these FPs have been successfully applied in a range of FRET sensors reported by our group, suggesting that a strong intramolecular interaction is not required to yield FRET sensors with a high DR.

Quantification and tuning of the strength of the mOrange-mCherry interface

Red-shifted FRET pairs such as mOrange/mCherry are useful complements to the existing CFP/YFP-based variants, yet FRET sensors employing this pair tend to suffer from poor DR, hampering their application in multiparameter imaging. We recently discovered that reversion of the I125R mutation, originally carried out to break the mFruits' ancestral DsRed tetramer, was sufficient to bring about intramolecular dimerization between mOrange and mCherry and provided a suitable level of stability to function in the context of a red-shifted FRET sensor for Zn^{2+}, redCALWY-1 (Chapter 3). The presence of the T127V mutation, another reversion to the DsRed original, was found to further enhance the stability of the interaction. To probe the effect of both the R125I and the R125I/T127V mutations, the stability they provided was assessed using urea titrations on an mOrange-linker-mCherry construct (Chapter 3). As expected, a construct bearing the monomeric versions of mOrange and mCherry (mOr(R125/T127)-linker-mCh(R125/T127)) displayed a low starting emission ratio, indicating a lack of intramolecular interaction between the wildtype fluorescent domains (Figure 4.4). Addition of urea led to a small decrease in emission ratio, an observation consistent with the previously noted linker stiffening effect of urea. In contrast, constructs mOr(I125/T127)-linker-mCh(I125/T127) and mOr(I125/V127)-linker-mCh(I125/V127) displayed much higher emission ratios of 1.2 and 1.1, indicating FRET due to intramolecular association of the fluorescent domains (Figure 4.4). Construct mOr(I125/T127)-linker-mCh(I125/T127) responded to urea addition with a rapid decrease in emission ratio, lacking a clear plateau phase, so that by 3 M

urea, the construct appeared to be in the completely opened state (Figure 4.4). Like the Cerulean*-Citrine* interaction studied above, the mOr(I125/T127)-linker-mCh(I125/T127) construct showed a relatively weak intramolecular interaction. In contrast, the mOr(I125/V127)-linker-mCh(I125/V127) construct maintained its high emission ratio even at the highest assayable concentrations of urea (Figure 4.4).

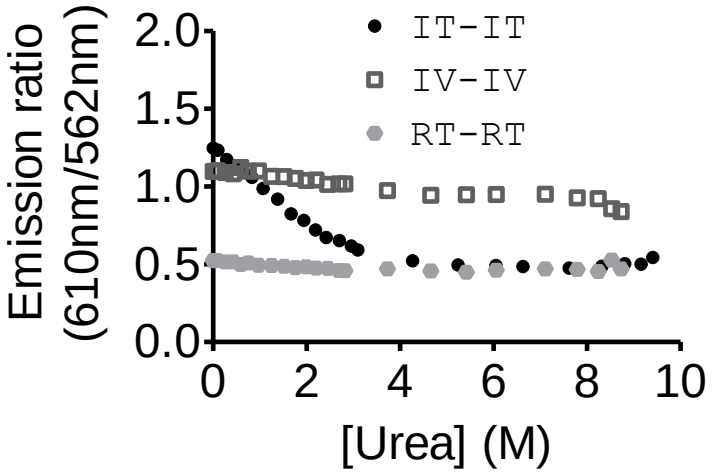

Figure 4.4: Urea-induced dissociation of the intramolecular mOrange-mCherry dimers. *The fluorescence emission ratio was monitored as a function of urea concentration for the wildtype construct (mOr(R125/T127)-linker-mCh(R125/T127)), for mOr(I125/T127)-linker-mCh(I125/T127) and for mOr(I125/V127)-linker-mCh(I125/V127). Urea titrations were carried out using 0.5 µM protein, in 50 mM Tris-HCl (pH 8), 100 mM NaCl, 10% (v/v) glycerol, at 20 °C.*

To allow further tuning of the interaction between the fluorescent domains and to better understand the contribution of individual amino acid mutations, the effect of other mutations at positions 125 and 127 was investigated (Figure 4.5A). Replacement of the positively charged arginine with the hydrophobic isoleucine at the 125 position of both mOrange and mCherry had been found to be sufficient for the formation of an intramolecular association (Chapter 3). However, it was unclear whether this mutation induced interaction due to increased hydrophobic interaction or due to a removal of coulombic repulsion. To test whether removal of coulombic repulsion was mainly at play in allowing complex formation, alanine was introduced at position 125 alone (generating mOr(A125/T127)-linker-mCh(A125/T127)), at both positions 125 and 127

(mOr(A125/A127)-linker-mCh(A125/A127)) or at position 125 in combination with valine at position 127 (mOr(A125/V127)-linker-mCh(A125/V127)). Constructs mOr(A125/T127)-linker-mCh(A125/T127) and (mOr(A125/A127)-linker-mCh(A125/A127) had low emission ratios (0.47 and 0.53 resp., Figure 4.5B), similar to the wildtype construct (0.51, Figure 4.5B, C). Construct (mOr(A125/V127)-linker-mCh(A125/V127), displayed a low, albeit slightly elevated emission ratio relative to wildtype (0.69, Figure 4.5B). Proteolytic cleavage of the linker resulted in a lower ratio (0.50, Figure 4.5D), comparable to mOr(R125/T127)-linker-mCh(R125/T127) after cleavage (0.43, Figure 4.5C). It seemed therefore that removal of coulombic repulsion alone was insufficient to generate a stable intramolecular dimer. Surprisingly, introduction of a tyrosine at position 127 did not result in complex formation; construct mOr(I125/Y127)-linker-mCh(I125/Y127) displayed a low emission ratio (0.46, Figure 4.5B) presumably because the bulky aromatic ring of tyrosine sterically hindered the complex formation otherwise mediated by the isoleucines at position 125. Leucine, with its alternatively branched β-carbon, is often considered slightly less hydrophobic than isoleucine and thus was tested as a subtle way to tune the interaction stability. Interestingly, mOr(L125/T127)-linker-mCh(L125/T127) failed to form a complex (ratio 0.42, Figure 4.5B); only through the introduction of an additional hydrophobic side group, valine at position 127, was the self-association complex restored (mOr(L125/V127)-linker-mCh(L125/V127), ratio 1.7). Upon proteolytic cleavage of the peptide linker, the mOr(L125/V127)-linker-mCh(L125/V127) emission ratio dropped to 0.63 (Figure 4.5E), confirming the high emission ratio was due to intramolecular complex formation. Construct mOr(I125/A127)-linker-mCh(I125/A127) was tested with a view to complementing isoleucine's hydrophobic side chain with a subtle increase in hydrophobicity compared to mOr(I125/T127)-linker-mCh(I125/T127). As expected, mOr(I125/A127)-linker-mCh(I125/A127) formed an intramolecular complex displaying a ratio of 1.7, which again was reduced to a wildtype-like level (0.54) upon cleavage of the linker (Figure 4.5F).

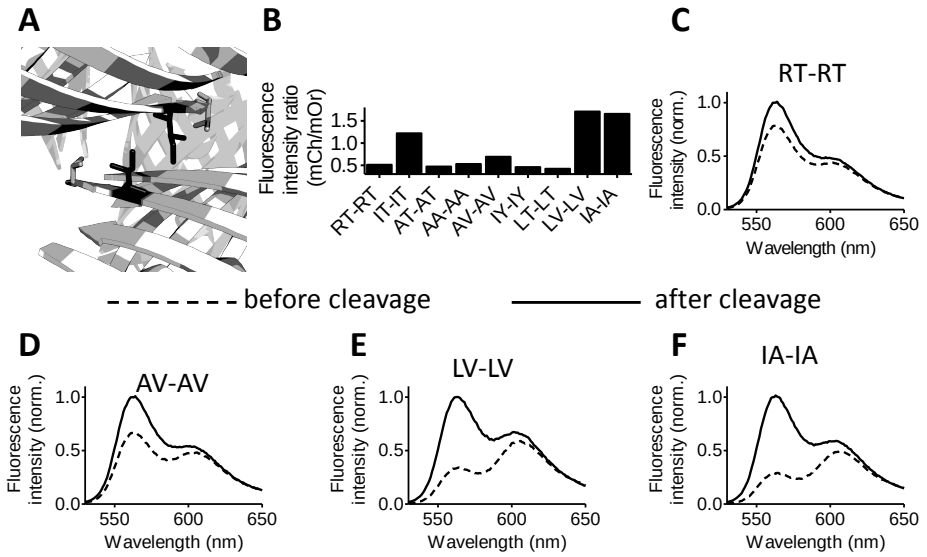

Figure 4.5: Surveying alternative mutations at positions 125 and 127 capable of mediating a hydrophobic intramolecular interaction between mOrange and mCherry. *(A) Detail from the DsRed crystal structure (1G7K), showing the hydrophobic AB interface exploited in this work. Residue I125 is represented in stick form in black, while residue V127 is colored grey. (B) Acceptor to donor emission ratio measured for different combinations of mutations. Labels indicate mutations present at positions 125 and 127 of mOrange and mCherry, using the single-letter amino acid code. (C) Emission spectra measured before and after proteolytic cleavage of wildtype construct mOr(R125/T127)-linker-mCh(R125/T127). (D-F) Emission spectra measured before and after linker cleavage for those variants that appeared to form a complex before cleavage (except mOr(I125/T127)-linker-mCh(I125/T127). Measurements were performed in 50 mM Tris (pH 8), 100 mM NaCl, 25 °C, at a protein concentration of 0.5 µM.*

The stability of the intramolecular complexes in mOr(L125/V127)-linker-mCh(L125/V127), mOr(I125/A127)-linker-mCh(I125/A127) and mOr(A125/V127)-linker-mCh(A125/V127) were probed using a urea titration. In addition, mOr(I125/V127)-linker-mCh(I125/T127) and mOr(I125/T127)-linker-mCh(I125/V127), constructs previously shown to form complexes (Chapter 3), were also probed for their stability (Figure 4.6A). Under native conditions, 3 different emission ratio regimes could be discerned: a high emission ratio of around 1.8 (mOr(L125/V127)-linker-mCh(L125/V127), mOr(I125/A127)-linker-mCh(I125/A127)

and mOr(I125/V127)-linker-mCh(I125/T127) and mOr(I125/T127)-linker-mCh(I125/V127)), an intermediate ratio of around 1.2 (mOr(I125/T127)-linker-mCh(I125/T127)) and a low emission ratio of around 0.7 (mOr(A125/V127)-linker-mCh(A125/V127)) (Figure 4.6A). Addition of urea resulted in the expected reduction of emission ratio with the high-start ratio group displaying a plateau phase at lower urea concentrations, the intermediate ratio construct displaying a relatively steep decline from the lowest urea concentrations, while the low ratio construct displayed a shallow response, resembling the end of an S curve. The three regimes reflected three different levels of interactional stability, with the high emission ratio group possessing an interaction of sufficient strength to ensure completely closed constructs, the intermediate construct possessing a weaker interaction so that a significant fraction of molecules were in the opened state at 0 M urea, and the low ratio construct having such a weak interaction that only a minor fraction of proteins were in the self-associated state at 0 M urea. Due to the lack of a clear plateau phase at low urea concentrations, it would be inaccurate to fit mOr(I125/T127)-linker-mCh(I125/T127) and mOr(A125/V127)-linker-mCh(A125/V127) in isolation. Given that the group of four constructs displaying a high emission ratio all had a plateau at a similar value, the assumption was made that this starting ratio represented the theoretical maximal emission ratio for all constructs. Consequently, the data in Figure 4.6A were fit to a Boltzmann distribution where emission ratios associated with the closed and opened states were shared amongst the entire data set (Table 4.2). These values, together with the experimental data for each individual data set, were then used to calculate K_x and ΔG^x_{o-c}, allowing determination of ΔG^0_{o-c} by extrapolation of the ΔG_{o-c}-urea relation to 0 M urea (Figure 4.6B). The R125I reversion alone (mOr(I125/T127)-linker-mCh(I125/T127)), previously found to be sufficient to induce a molecular switching-like mechanism in redCALWY-1, introduced a relatively weak stability of 0.10 kcal/mol. An increase in stability to 1.2 kcal/mol was achieved by replacement of threonine for alanine at the 127 position (mOr(I125/A127)-linker-mCh(I125/A127). Incorporation of the T127V mutation on either of the fluorescent domains further increased that stability to 1.7 kcal/mol for both mOr(I125/V127)-linker-

mCh(I125/T127) and mOr(I125/T127)-linker-mCh(I125/V127). Constructs mOr(L125/V127)-linker-mCh(L125/V127) displayed a similar stability of 2.1 kcal/mol. A much weaker stability of -1.2 kcal/mol was obtained for mOr(A125/V127)-linker-mCh(A125/V127). Note that this number is uncertain as it is based on the assumption that the ratio in the closed state is the same as for the other variants. Nevertheless, the negative value for ΔG^0_{o-c} confirms that at 0 M urea, a majority of the mOr(A125/V127)-linker-mCh(A125/V127) is in the opened state.

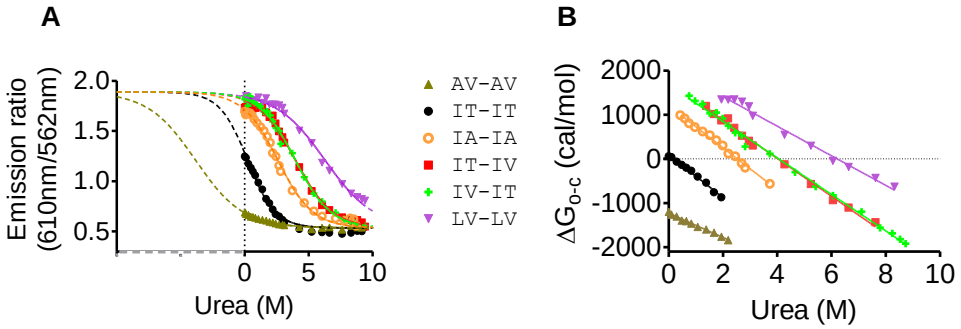

Figure 4.6: Quantification of the stability of the intramolecular dimer in mOrange-linker-mCherry as mediated by combinations of mutations at the 125 and 127 position. *(A) Emission ratio is shown as a function of urea concentration. Data were fit to a Boltzmann distribution. Parameters R_c and R_o were constrained to be shared amongst all data sets. (B) Plot showing the linear correlation between the urea concentration and the Gibbs free energy associated with transition from the closed to opened state. Data were fit to a linear model and extrapolated to 0 M urea, providing the standard Gibbs free energy of the complex under native conditions (ΔG^0_{o-c}). Measurements were performed in 50 mM Tris (pH 8), 100 mM NaCl, 20 °C, at a protein concentration of 0.5 µM.*

Table 4.2: Thermodynamic parameters of urea-induced dissociation of the mOrange-mCherry intramolecular dimer.

FP pair	X_0 (M)	m (kcal/mol/M)	ΔG^0_{o-c} (kcal/mol)
IT-IT	0.23±0.05	-0.48±0.02	0.10±0.02
IT-IV	4.0±0.1	-0.43±0.01	1.7±0.1
IV-IT	4.0±0.1	-0.41±0.01	1.7±0.1
LV-LV	6.3±0.1	-0.34±0.01	2.1±0.1
IA-IA	2.6±0.1	-0.48±0.01	1.2±0.1
AV-AV	-3.8±1	-0.28±0.01	-1.2±0.1

The fitting procedure constrained parameters R_c (1.9 ± 0.1) and R_o (0.53 ± 0.01) to be shared amongst all data sets.

An alternative method to assess the effects of various interface mutants is to study homodimerization of mCherry monomers using fluorescence anisotropy, as previously demonstrated (Chapter 3). Data measured at concentrations below 10 µM, above which homoFRET between molecularly dissolved mCherry monomers starts to play an increasingly important role, were fit to a previously described mCherry dimerization model (Chapter 3). The construct mCherry(I125/T127) had a K_d for homodimerization of 33 ± 3 µM, while mCherry(I125/V127) had a much lower K_d of 99 ± 7 nM (similar to the values found in Chapter 3). Measurement of the mCherry-LV and mCherry-IA mutants revealed intermediate K_ds of 0.87 ± 0.06 µM and 7.9 ± 0.5 µM, respectively (Figure 4.7). The protein mCherry(A125/V127) did not form detectable homodimers, which is consistent with the finding using the urea-based analysis that this variant's intramolecular complex is very weak in nature.

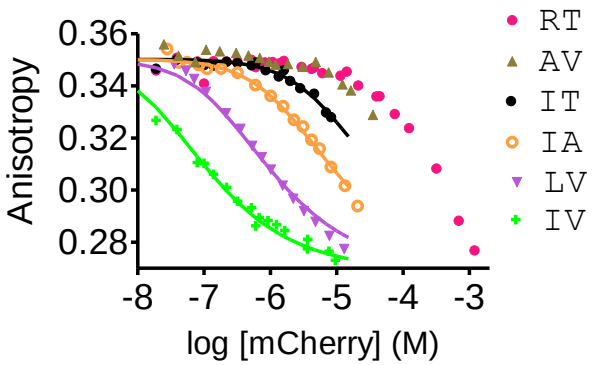

Figure 4.7: Monitoring mCherry dimerization through homoFRET-induced depolarization. *Anistropy was measured as a function of mCherry variant concentration, using 560 nm excitation light, while monitoring emission between 595 and 615 nm, in a buffer consisting of 50 mM Tris-HCl (pH 8), 100 mM NaCl, 1 mg/mL BSA, at 25 °C. Data was fit to the same model as described in Chapter 3, with a high anisotropy level associated with the monomeric state (0.35) and a low anisotropy value associated with the dimeric state (0.27) both constrained in the fitting procedure to be shared amongst all data sets.*

Clearly, the fluorescence anisotropy assay results are consistent with the urea-based measurements in regards to the relative strength of the various mutations, with 125I/127V>125L/127V>125I/127A>125I/127T>125A/127V>125R/127T. In addition, the effects of mutations at positions 125 and 127 seem to be additive at first

approximation, which is most clearly seen from the observation that the interaction strength of the mOr(I125/T127)-linker-mCh(I125/V127) and mOr(I125/V127)-linker-mCh(I125/T127) are similar and in between those of the mOr(I125/T127)-linker-mCh(I125/T127) and mOr(I125/V127)-linker-mCh(I125/V127) constructs. The ΔG^0_{o-c} measured for the intramolecular complex and the K_d determined for the intermolecular dimer are related. If one were to assume that the intermolecular homodimer complex is the same as the intramolecular dimer complex, the ΔG^0_{o-c} for the intramolecular interaction would be related to the intermolecular K_d by an effective concentration term. This effective concentration (C_{eff}) is determined by the linker length, its flexibility, and the distance that the linker bridges in the complexed state (34, 35). Assuming a distance of 30 Å, a linker length of 81 amino acids and a persistence length of 4.5 Å, C_{eff} can be calculated to be 2.6 mM (35). Based on this value for C_{eff} and $K_{d,\ inter}$ = 7.9 µM for mCherry(125I/127A), an intramolecular K_d of 0.003 is calculated, which corresponds to a ΔG^0_{o-c} = 3.4 kcal/mol. This value is significantly higher than the value determined by the urea titration for mOr(I125/A127)-linker-mCh(I125/A127) (1.2 kcal/mol), which may be explained by differences between homo and heterodimer complexes or an influence of the linker on the structure of the protein-protein interaction. This analysis thus highlights the importance of characterizing interactions both in the inter- and intramolecular context.

Effect of FP-FP interface strength on redCALWY Zn^{2+} sensors

Having quantified the intramolecular stability mediated by R125I and a range of other mutations, we next asked whether the stability that had originally been used in the red-shifted Zn^{2+} sensor redCALWY-1 (Chapter 3) was already optimal or whether a stronger or weaker interaction within the sensor might improve its overall properties. An equilibrium exists between the two mutually exclusive conformations of redCALWY-1, with either fluorescent domains self-associated or with both Zn^{2+}-binding domains in complex with Zn^{2+} (Figure 4.8A). Increasing the stability of the fluorescent domain interaction would be predicted to shift the equilibrium to the left,

weakening redCALWY-1's affinity for Zn^{2+}. Furthermore, since in construct mOr(I125/T127)-linker-mCh(I125/T127) a significant fraction of molecules appeared to be in the opened state under native conditions, introduction of a more stable interaction in redCALWY-1 might also be expected to improve the DR of the sensor. First, the affinity between the FP pairs was increased by introduction of T127A mutations, resulting in redCALWY-1-B (Figure 4.8A). Surprisingly, the starting emission ratio for redCALWY-1-B (1.3) was lower than the ratio observed for redCALWY-1 (1.6, Figure 4.8B). Also, addition of Zn^{2+} led to a smaller decrease in emission ratio than that seen in redCALWY-1 (Figure 4.8C), while the variant's K_d for Zn^{2+} (11 ± 2.0 pM) was similar (Figure 4.8D). Next, the FP affinity was increased through addition of a T127V mutation, either on mOrange alone (redCALWY-1-C) or on mCherry alone (redCALWY-1-D). Similarly to redCALWY-1-B, redCALWY-1-C and redCALWY-1-D displayed a dampened DR (both 21%, Figure 4.8C) and largely unaffected K_d (6.1 ± 1 pM and 5.2 ± 0.7 pM for redCALWY-1-C and redCALWY-1-D respectively, Figure 4.8D). Construct redCALWY-1-C also showed an unexpectedly lower starting ratio (1.1), while the starting ratio for redCALWY-1-D (1.8) was more in line with expectations (Figure 4.8B). Further strengthening of the FP-FP interaction, through the introduction of either R125I and T127V or R125L and T127V on both fluorescent domains, resulted in the loss of almost any detectable change in emission ratio: constructs redCALWY-1-E and redCALWY-1-F both displayed emission ratios of 1.0 (Figure 4.8B) that did not respond to Zn^{2+} addition (Figure 4.8C). A possible cause of the lower-than-expected emission ratio and DR might be intermolecular aggregation. However, when redCALWY-1-F was measured at a sensor concentration of 20 nM (40 times lower than the intermolecular mCherry-LV homodimer K_d), the construct continued to display the same low emission ratio and lack of ratiometric response to Zn^{2+} (not shown), while the value found for mCherry anisotropy (0.36) did not support the idea of intermolecular aggregation. In contrast to the mutations described above, introduction of mutations R125A and T127V on both fluorescent domains weakened the FP-FP interaction relative to the interaction seen in redCALWY-1. Construct redCALWY-1-G displayed a low starting emission ratio

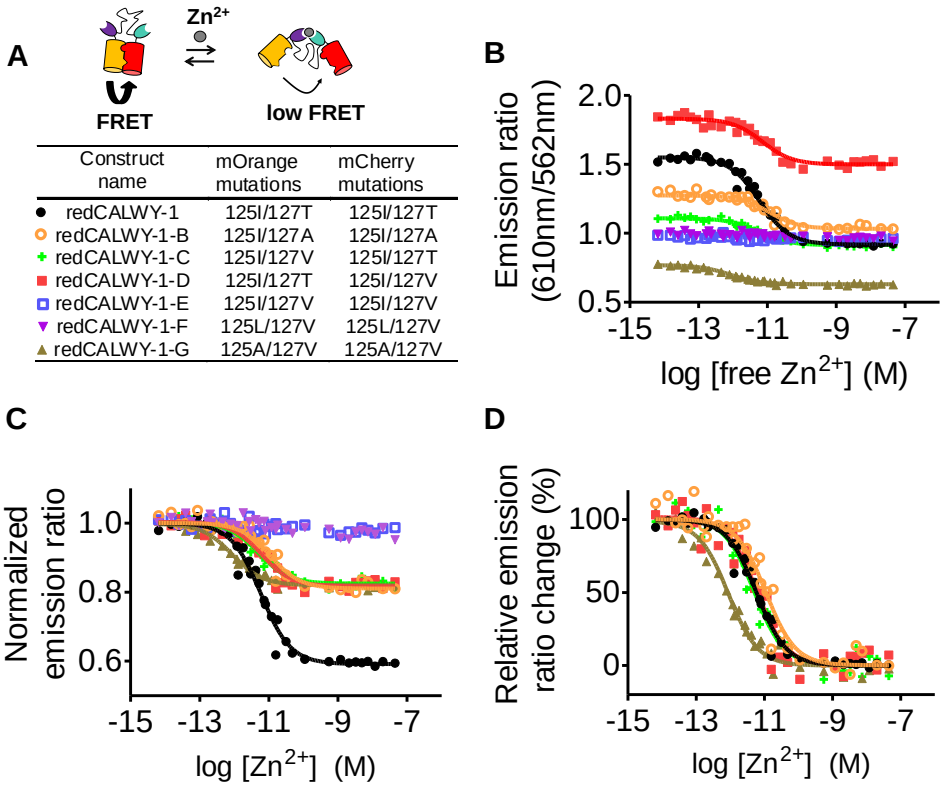

Construct name	mOrange mutations	mCherry mutations
redCALWY-1	125I/127T	125I/127T
redCALWY-1-B	125I/127A	125I/127A
redCALWY-1-C	125I/127V	125I/127T
redCALWY-1-D	125I/127T	125I/127V
redCALWY-1-E	125I/127V	125I/127V
redCALWY-1-F	125L/127V	125L/127V
redCALWY-1-G	125A/127V	125A/127V

Figure 4.8: Effect of the mOrange/mCherry intramolecular complex stability on the properties of the redCALWY-1 Zn^{2+} sensor. *(A) Cartoon depicts the equilibrium that exists between redCALWY-1 with intramolecularly complexed FP domains and sensor bound to Zn^{2+} with disrupted FP complex. Overview of the redCALWY-1 constructs carrying various mutations at the 125 and 127 positions of mOrange and mCherry. (B) Emission ratio as a function of Zn^{2+} concentration for redCALWY-1 variants. (C) The same data set out in (B) normalized to the emission ratio in absence of Zn^{2+}, emphasizing differences in DR amongst the redCALWY-1 variants. (D) The same data as in (B) but scaled from 0 to 100% emission ratio, emphasizing differences in Zn^{2+} affinity amongst the variants. Non-responsive variants redCALWY-1-E and redCALWY-1-F were left out of this panel. Zn^{2+} titrations were carried out at 30 °C in 150 mM Hepes (pH 7.1), 100 mM NaCl, 10% (v/v) glycerol and 1 mg/mL BSA, together with 1 mM of EDTA, HEDTA, DHPTA or EGTA.*

(0.77, Figure 4.8B) and a low DR (22%, Figure 4.8C) that may be explained by the fact that due to the weak AV-mediated interaction, only a fraction of the sensor population was poised to respond to Zn^{2+} addition. Interestingly, the apparent affinity for Zn^{2+} (K_d = 0.90 ± 0.1 pM, Figure 4.8D) was almost 7-fold higher than that measured for

redCALWY-1. This latter observation is consistent with the notion that a weaker intramolecular FP complex would shift the equilibrium (Figure 4.8A) to the right and thus increase the Zn^{2+} affinity relative to the affinity observed for redCALWY-1.

Discussion

In this chapter, a thermodynamic characterization of the intramolecular complexes formed between FP FRET pairs is provided. Using an analysis based on urea-mediated disruption of the intramolecular complex, it was found that hydrophobic surface mutations S208F and V224L mediate an intramolecular complex between ECFP and EYFP with a stability of 1.7 kcal/mol. Surprisingly, the same mutations mediated a much weaker interaction between Cerulean and Citrine (ΔG^0_{o-c} = 0.17 kcal/mol), with a small fraction of the protein apparently in the opened state under native conditions. Two Cerulean-specific mutations, Y145A and H148D, were found to be responsible for destabilizing the Cerulean-Citrine interface. Further mutational screening of the mOrange-mCherry interaction mediated by hydrophobic mutations at positions 125 and 127, revealed that a combination of a lack of coulombic repulsion coupled with a strong hydrophobic effect was necessary for formation of the interaction. Conformational stabilities ranging from -1.2 to 2.1 kcal/mol were found for the various mOrange-mCherry interface mutations. Measurement of the intermolecular mCherry dimer affinities revealed values that indicated the same relative strengths as the intramolecular stabilities established with the urea-based analysis. However, the intramolecular stabilities that were calculated based on the intermolecular K_d were all consistently higher than those experimentally determined with the urea assay. One reason for this may be that the intermolecular dimer and intramolecular dimer are different in structure. All native FPs are known to form antiparallel dimers. In the fusion constructs, the linker might force mOrange and mCherry to assume a parallel complex.

When sticky FRET pairs are used in bimolecular assays, for example to investigate protein-protein interactions (PPIs) or host-guest supramolecular interactions, the

affinity of the fused FPs for one another can affect the apparent affinity measured for the interaction of interest (22, 36). The presence of the sticky mutation S208F has been reported to increase the affinity of ECFP-lithocholic acid for EYFP-β-cyclodextrin ten-fold (37). Interestingly, the latter increase in affinity would indicate the sticky FP interaction contributed ~2 kcal/mol ($\Delta\Delta G = -RT*\ln(K_{d1}/K_{d2}) = -RT*\ln(0.1)$) to the overall binding, close to the value that was obtained for the stability of the ECFP*-L9-EYFP* intramolecular complex (1.6 kcal/mol). Conversely, in single-chain FRET sensors exploiting mutually exclusive conformations, a stabilization of one conformation necessarily entails a free energy penalty for the other. Indeed, several examples in the literature bear out this prediction. The presence of CyPet and YPet in a FRET sensor for peptides weakened the sensor's affinity for peptide 3-fold (18). Introduction of S208F and V224L into the eCALWY-1 Cerulean/Citrine-based FRET sensor for Zn^{2+} resulted in a 10-fold weakening of Zn^{2+} affinity (17). The fact that construct redCALWY-1 has a similarly attenuated affinity for Zn^{2+} confirms that the mOrange(I125/T127)-mCherry(I125I/T127) interaction is comparable in stability to the Cerulean*-Citrine* interaction in eCALWY-1. Weakening of the mOrange-mCherry interaction, in construct redCALWY-1-G, led to an expected 7-fold increase in Zn^{2+} affinity relative to the affinity measured for redCALWY-1.

Surprisingly, introduction into redCALWY-1 of mOrange/mCherry variants with an increased stability did not result in sensors with a higher DR. From the outset, introduction of such stable interactions had been expected to shift the Zn^{2+}-sensor's equilibrium to the left, weakening its affinity for Zn^{2+}, but not to dampen its DR. It is tempting to speculate that an intramolecular interaction between a "sticky" mFruit domain and a hydrophobic patch on one of the Zn^{2+}-binding domains, WD4 and/or ATOX1, was hindering the sensor. Close examination of the ATOX1 crystal structure (38) reveals it to be a relatively hydrophilic domain, with most hydrophobic residues pointing inwards. In contrast, the solution structure for WD4 (39) indicates that this domain is relatively hydrophobic, consistent with this domain's native role involving many protein-protein interactions.

The redCALWY-1 case shows that tuning of the sticky complex stability is important for the optimal functioning of FRET sensors. Similarly, previous work demonstrated that differing levels of FP complex stability were appropriate for different FRET sensors (21). Ca^{2+} FRET sensors YC3.60 and TN-XL had the highest DR when the native CFP/YFP interface was used, and performed more poorly when either dimerizing mutations were introduced or when the interface was disrupted with the A206K mutation (40). Note that the YFP acceptors used here were both of the circularly permutated variety and that it was the use of these acceptors that had originally been reported to improve the sensors' DR (7, 41). Kotera *et al.* speculated that the circular permutation helped juxtapose the FPs in the correct orientation, allowing for an intramolecular interaction in the Ca^{2+}-bound state (21). Remarkably, it was found that replacement of ECFP with Cerulean negated the enhancing effect of a circularly permutated acceptor in the Ca^{2+} sensor TN-XL (7). Our finding that Cerulean contains interface destabilizing mutations helps to explain this initially puzzling observation. The negative charge provided by H148D and the removal of a hydrophobic side group through Y145A likely disrupted the weak interaction otherwise occurring between ECFP and circularly permutated acceptor in the Ca^{2+}-bound state. These findings allow us to predict that third generation CFP variants such as mCerulean3 (with Y145A) (42) and Turquoise2 (with H148D) (12), will not be compatible with Ca^{2+} FRET sensors TN-XL and YC3.60. However, the recently developed FP Aquamarine (ECFP with T65S and H148G) (*43*) might well make an ideal donor to a circularly permutated acceptor, providing an enhanced brightness and photostability without perturbing the intramolecular FP-FP interaction.

Recently, two alternative strategies for the construction of genetically encoded fluorescent sensors were described that are similar in concept to the strategies employing the sticky FPs. In the first, an initially dark protein becomes fluorescent when heterodimerized with another domain, allowing the construction of intensiometric probes (14, 44). In the second strategy, a small domain fused to one FP has moderate affinity for a peptide fused to another FP, resulting in enhanced FRET between FRET pairs. The peptide-domain interaction was tuned to prevent background

binding, with interaction only occurring when two proteins of interest fused to the FPs interacted. The strategy allowed physical decoupling of the fluorescence and interaction modules, and helped to improve FRET efficiency between evolutionarily unrelated Citrine and mCherry (*45*, *46*). The ideal heterodimer K_d value reported in the former strategy, 33 µM, is very similar to the ideal value found for the mOrange/mCherry FRET pair of 33 µM. In the latter strategy, a peptide-domain K_d of 170 µM was reported to be ideal. Both strategies indicate that a thermodynamic "balancing act" is warranted to ensure correct functioning of sensors. The techniques reported here should help future FRET sensor designs to achieve that balance.

In conclusion, the stability of the hydrophobic interaction between various FRET pairs has been quantified. The direct quantification of the intramolecular domain interaction presented here provides for an improved understanding of many FRET sensors' mechanism of action. In addition, we have developed a set of mOrange/mCherry FRET pairs with a broad range of interaction strengths, gaining further understanding of the mOrange-mCherry interface and the mutations tolerated therein. This should help in rapid construction of sensitive FRET sensors for many remaining small molecules of interest and provides a framework for the development of new self-associating FRET pairs, such as derivatives of green and red FPs (11, 47).

Methods

Cloning of protein expression constructs. The pET28a-based bacterial expression constructs for ECFP-L9-EYFP and ECFP*-L9-EYFP* were described previously (23, 24). pET28a-Cer*-L9-Cit* was generated in the course of a previous project. In the latter construct, homology between the DNA sequences encoding Cerulean and Citrine hindered efficient site directed mutagenesis so that a more complex cloning effort to obtain pET28a-Cer*(A145Y/D148H)-L9-Cit* was required. Primers to generate the A145Y and D148H mutations on Cerulean are listed in Table 4.3. To generate mutations at amino acid position 125 and 127 (numbering relative to DsRed) of mOrange and mCherry in the vector encoding the

red-shifted FRET construct, pET28a-mOrange-linker-mCherry (Chapter 3), site-directed mutagenesis was used, together with the primers listed in Table 4.3. The

Table 4.3: Primer sequences used for site directed mutagenesis in this study.

Primer	Sequence (5'-->3')
Cer_A145Y_D148H_F	TACAACTACATCTCCCATAACGTTTACATCACCGCTGATAAGCAG
Cer_A145Y_D148H_R	ATGTAAACGTTATGGGAGATGTAGTTGTATTCCAGTTTGTGGCCCAGG
mOrange_LT_F	GCTGctgGGCacgAACTTTCCGTCTGACGGTCCG
mOrange_LT_R	GTTcgtGCCcagCAGCTTCACTTTGTAAATAAACTCACCGTCC
mCherry_LT_F	GTAAAACTGttgGGTaccAACTTCCCGTCTGATGGCCC
mCherry_LT_R	GGAAGTTggtACCcaaCAGTTTTACTTTATAGATAAATTCGCCGTCCTG
mOrange_IY_F	TGAAGCTGattGGCtatAACTTTCCGTCTGACGGTCCG
mOrange_IY_R	GGAAAGTTataGCCaatCAGCTTCACTTTGTAAATAAACTCACCGTCC
mCherry_IY_F	GTAAAACTGatcGGTtacAACTTCCCGTCTGATGGCCC
mCherry_IY_R	GGGAAGTTgtaACCgatCAGTTTTACTTTATAGATAAATTCGCCGTCCTG
mOrange_IC_F	TGAAGCTGattGGCtgtAACTTTCCGTCTGACGGTCCG
mOrange_IC_R	GAAAGTTacaGCCaatCAGCTTCACTTTGTAAATAAACTCACCGTCC
mCherry_IC_F	AAAACTGatcGGTtgcAACTTCCCGTCTGATGGCCC
mCherry_IC_R	GAAGTTgcaACCgatCAGTTTTACTTTATAGATAAATTCGCCGTCCTG
mOrange_LV_F	AGCTGttgGGCgtgAACTTTCCGTCTGACGGTCCG
mOrange_LV_R	AAGTTcacGCCcaaCAGCTTCACTTTGTAAATAAACTCACCGTCC
mCherry_LV_F	AAAACTGctgGGTgttAACTTCCCGTCTGATGGCCC
mCherry_LV_R	GGAAGTTaacACCcagCAGTTTTACTTTATAGATAAATTCGCCGTCCTG
mOrange_WV_F	GCTGtggGGCgtgAACTTTCCGTCTGACGGTCCG
mOrange_WV_R	GTTcacGCCccaCAGCTTCACTTTGTAAATAAACTCACCGTCC
mCherry_WV_F	TAAAACTGtggGGTgttAACTTCCCGTCTGATGGCCC
mCherry_WV_R	GGAAGTTaacACCccaCAGTTTTACTTTATAGATAAATTCGCCGTCCTG
mOrange_AT_F	AAGCTGgcaGGCACTAACTTTCCGTCTGACGGT
mOrange_AT_R	AAAGTTAGTGCCtgcCAGCTTCACTTTGTAAATAAACTCACCGTCC
mCherry_AT_F	TAAAGTAAAACTGgctGGTACTAACTTCCCGTCTGATGGCC
mCherry_AT_R	GGAAGTTAGTACCagcCAGTTTTACTTTATAGATAAATTCGCCGTCCTG
mOrange_AV_F	GCTGGCAggcGTAAACTTTCCGTCTGACGGTCCG
mOrange_AV_R	AAAGTTTACgccTGCCAGCTTCACTTTGTAAATAAACTCACC
mCherry_AV_F	TAAAGTAAAACTGgctGGTgttAACTTCCCGTCTGATGGCCC
mCherry_AV_R	GGAAGTTaacACCagcCAGTTTTACTTTATAGATAAATTCGCCGTCCTG
mOrange_AA_F	GCTGgcaGGCgctAACTTTCCGTCTGACGGTCCG
mOrange_AA_R	AGTTagcGCCtgcCAGCTTCACTTTGTAAATAAACTCACCGTCC
mCherry_AA_F	AACTGgctGGTgcaAACTTCCCGTCTGATGGCCC
mCherry_AA_R	GAAGTTtgcACCagcCAGTTTTACTTTATAGATAAATTCGCCGTCCTG
mOrange_IA_F	GCTGattGGCgccAACTTTCCGTCTGACGGTCCG
mOrange_IA_R	AGTTggcGCCaatCAGCTTCACTTTGTAAATAAACTCACCGTCC
mCherry_IA_F	AACTGatcGGTgcgAACTTCCCGTCTGATGGCCC
mCherry_IA_R	GAAGTTcgcACCgatCAGTTTTACTTTATAGATAAATTCGCCGTCCTG

same technique was used to introduce mutations at those same positions within the fluorescent domains of the vector encoding the red-shifted FRET sensor for Zn^{2+}, pET28a-redCALWY-1 (Chapter 3), using the same primers. Single domain mCherry constructs were generated through a one-step site-directed deletion mutagenesis of the mOrange and linker domains of the red protease constructs, as

previously described (Chapter 3). All constructs were confirmed by DNA sequencing (Baseclear, Leiden).

Protein expression and purification. *Escherichia coli* BL21(DE3) (Novagen) was transformed with the various pET28a expression constructs and single colonies of the transformants were used to inoculate 5 mL Lysogeny Broth (LB) starter cultures, which in turn were used to inoculate 500 mL (for simple linker constructs) or 2 L (for redCALWY-1 constructs) bacterial cultures. Protein expression was induced at an OD_{600} of 0.6 through addition of 0.1 mM IPTG. Expression was carried out overnight at 25 °C. Cells were harvested by centrifugation, lysed with BugBuster (Novagen) and the soluble fractions, obtained through centrifugation at 40,000g, were loaded onto a Ni-NTA column (HisBind resin, Novagen), washed and eluted following manufacturer's instructions, exploiting the N-terminal polyHis-tag carried by all constructs used in this study. Constructs encoding only a single mCherry domain were buffer exchanged to 50 mM Tris-HCl (pH 8), 100 mM NaCl and stored in aliquots at -80 °C. Size exclusion chromatography (SEC) was used to purify full length ECFP*-L9-EYFP*, Cerulean*-L9-Citrine*, mOr(I125/T127)-linker-mCh(I125/T127), mOr(I125/T127)-linker-mCh(I125/V127), mOr(I125/V127)-linker-mCh(I125/T127) and mOr(I125/V127)-linker-mCh(I125/V127), separating them from undesired C-terminally truncated products. The SEC column (HiPrep 26/60 Sephacryl S-200 HR, GE Healthcare) was equilibrated with 100 mM NaCl, 50 mM Tris-HCl (pH 8). Protein SEC fractions were analyzed for correct size and purity by SDS-PAGE, pooled and concentrated using 10 kDa MWCO centrifugation tubes (Millipore). The mOrange-linker-mCherry constructs not mentioned above, as well as Cer*(A145Y/D148H)-L9-Cit*, were additionally purified through streptactin chromatography instead of by SEC. The proteins carried a C-terminal Strep-tag II, allowing purification of full length protein, following the Streptactin resin manufacturer's instructions (IBA GmbH). Following Ni-NTA affinity chromatography, desalting columns (PD10, GE) were used to exchange the redCALWY-1 constructs' buffer from Ni-NTA elution buffer to thrombin cleavage buffer (20 mM Tris-HCl (pH 8.4), 150 mM NaCl, 2.5 mM $CaCl_2$). The polyHis-tag was cleaved from the N-terminus of the redCALWY-1 constructs to

prevent it from interfering in Zn^{2+}-binding studies (48). Thrombin protease enzyme (Novagen) was added at an enzyme concentration of 0.3 units/mg substrate in the presence of 0.2 mg/mL substrate and incubated at 4 °C for 20 hours. Next, cleavage reactions were loaded onto Ni-NTA columns pre-equilibrated with thrombin buffer and subsequently washed with thrombin buffer, to remove thrombin and cleaved polyHis-tag. To elute cleaved proteins, 30 mM imidazole was added, a concentration at which uncleaved His-tag bearing proteins remained immobilized on the Ni-NTA resin. Finally, redCALWY-1 constructs were also subjected to size exclusion chromatography, using a column (HiPrep 26/60 Sephacryl S-200 HR, GE), pre-equilibrated with 50 mM Tris (pH 8), 100 mM NaCl and 1 mM TCEP. The resulting SEC fractions were analyzed for correct size and purity by SDS-PAGE, pooled, concentrated and stored at -80 °C.

Urea titration experiments. A stock solution of 10 M urea in 50 mM Tris-HCl (pH 8), 100 mM NaCl and 10% (v/v) glycerol was prepared by dissolving urea in preheated buffer in a flask suspended in a bath of hot water that was allowed to cool slowly, with continuous stirring of the urea solution. Due to the known instability of urea in solution, this solution was always prepared on the day of use. Protein variants were dissolved at 1.5 μM (CFP/YFP variants) or 0.5 μM (mOrange/mCherry variants) in a buffer consisting of 50 mM Tris-HCl (pH 8), 100 mM NaCl and 10% (v/v) glycerol in quartz cuvettes with 1 cm pathlength, at 20 °C. The urea concentration was increased by stepwise addition of 10 M urea and an emission spectrum was measured at each concentration of urea, either between 450 and 600 nm (ECFP/EYFP pair and derivatives), or between 550 and 650 (mOrange/mCherry pair) and either through excitation with 420 nm (ECFP/EYFP) or 520 nm (mOrange/mCherry) light. Emission ratios were calculated by dividing the acceptor's intensity by the donor's intensity, at wavelengths corresponding to the published emission intensity peaks for each FP.

HomoFRET-induced depolarization assay. The mCherry variants' anisotropy was monitored at increasing protein concentration, as described previously (Chapter 3). Briefly, measurements were performed in 50 mM Tris-HCl (pH 8), 100 mM NaCl and 1 mg/mL BSA, at 25 °C with an excitation wavelength of 560 nm, a 20 nm excitation

slit width, a 5 nm emission slit width, while monitoring emission between 595 and 615 nm, using a Cary Eclipse fluorescence spectrophotometer (Varian). Data were fit to the same binding model previously described in Chapter 3, with a common high anisotropy value in the monomeric state and a common low anisotropy value in the dimeric state shared amongst data sets. Great care was taken to ensure measurement conditions such as temperature (25 °C) and buffer were kept as constant as possible as even small deviations had a significant effect on absolute anisotropy values measured.

Relating intermolecular dimerization affinity to intramolecular dimer stability. As explained in the Results, the experimentally determined values for the intramolecular stability can be related to the experimentally determined values for the intermolecular dimer K_d by an effective concentration (C_{eff}) term, according to equation 4.5.

$$K_{\mathrm{d,intra}} = \frac{K_{\mathrm{d,inter}}}{C_{eff}} \tag{4.5}$$

The $K_{d,intra}$ can then be used to calculate the Gibbs free energy associated with transition from the closed to opened state, applying equation 4.6.

$$\Delta G^0_{o-c} = -RTln(K_{\mathrm{d,intra}}) \tag{4.6}$$

Zn^{2+} titration with redCALWY-1 FRET sensors. Zn^{2+} titrations with redCALWY-1 constructs were carried out in 384-well plates, at 0.25 µM sensor concentration, 50 µL volume, in Hepes buffer (150 mM Hepes (pH 7.1), 100 mM NaCl, 0.5 mM TCEP, 2 µM DTT, 10% (v/v) glycerol and 1 mg/mL BSA), together with 1 mM of either one of four Zn^{2+} chelators (EDTA, HEDTA, DHPTA or EGTA). By adding $ZnCl_2$ to different concentrations in each well, it was possible to gain precise control over the free Zn^{2+} concentration, which was calculated using the chelators' published critical stability constants for Zn^{2+} in an online calculator tool (http://www.stanford.edu/~cpatton/webmaxcS.htm). Fluorescence emission spectra were obtained in a fluorescence plate reader (Tecan Safire), set to excite at 520 nm and to measure emission from 550 to 650 nm, at a temperature of 30 °C. Data was fit to a Zn^{2+}-binding model as previously described (17).

Acknowledgements

This work is partly based on a manuscript in preparation that is co-authored by M. Malisauskas, T. Sips and M. Merkx. Mantas Malisauskas planned and carried out urea titrations on the ECFP-EYFP constructs and developed a method to analyze the data. Tari Sips carried out many of the experiments involving mOrange-mCherry-based measurements.

References

1. Campbell RE (2009) *Anal Chem* **81,** 5972-5979.
2. Palmer AE, Qin Y, Park JG, & McCombs JE (2011) *Trends Biotechnol* **29,** 144-152.
3. Merkx M, Golynskiy MV, Lindenburg LH, & Vinkenborg JL (2013) *Biochem Soc Trans* **41,** 1201-1205.
4. Heim N & Griesbeck O (2004) *J Biol Chem* **279,** 14280-14286.
5. Ouyang M, *et al.* (2010) *Cancer Res* **70,** 2204-2212.
6. Jost CA, Reither G, Hoffmann C, & Schultz C (2008) *ChemBioChem* **9,** 1379-1384.
7. Mank M, *et al.* (2006) *Biophys J* **90,** 1790-1796.
8. Goedhart J, *et al.* (2010) *Nat Methods* **7,** 137-139.
9. Shaner NC, *et al.* (2004) *Nat Biotechnol* **22,** 1567-1572.
10. Shcherbakova DM, *et al.* (2012) *J Am Chem Soc* **134,** 7913-7923.
11. Lam AJ, *et al.* (2012) *Nat Methods* **9,** 1005-1012.
12. Goedhart J, *et al.* (2012) *Nat Commun* **3,** 751.
13. Zhao YX, *et al.* (2011) *Science* **333,** 1888-1891.
14. Alford SC, Abdelfattah AS, Ding Y, & Campbell RE (2012) *Chem Biol* **19,** 353-360.
15. Hoi H, Matsuda T, Nagai T, & Campbell RE (2013) *J Am Chem Soc* **135,** 46-49.
16. Ibraheem A, Yap H, Ding Y, & Campbell RE (2011) *BMC Biotechnol* **11,** 105.
17. Vinkenborg JL, *et al.* (2009) *Nat Methods* **6,** 737-740.
18. Huang J & Koide S (2010) *ACS Chem Biol* **5,** 273-277.
19. Golynskiy MV, Rurup WF, & Merkx M (2010) *ChemBioChem* **11,** 2264-2267.
20. van der Velden LM, *et al.* (2013) *Hepatology* **57,** 740-752.
21. Kotera I, *et al.* (2010) *ACS Chem Biol* **5,** 215-222.
22. Ohashi T, Galiacy SD, Briscoe G, & Erickson HP (2007) *Protein Sci* **16,** 1429-1438.
23. Vinkenborg JL, *et al.* (2007) *ChemBioChem* **8,** 1119-1121.
24. Evers TH, *et al.* (2006) *Biochemistry* **45,** 13183-13192.
25. Stepanenko OV, Kuznetsova IM, Verkhusha VV, & Turoverov KK (2013) *Int Rev Cell Mol Biol* **302,** 221-278.
26. Stepanenko OV, *et al.* (2010) *Spectroscopy* **24,** 367-373.
27. Zhou HX (2001) *Biochemistry* **40,** 15069-15073.
28. Möglich A, Joder K, & Kiefhaber T (2006) *Proc Natl Acad Sci U S A* **103,** 12394-12399.
29. Soranno A, Longhi R, Bellini T, & Buscaglia M (2009) *Biophys J* **96,** 1515-1528.
30. Pace CN, *et al.* (2010) *Protein Sci* **19,** 929-943.
31. Griesbeck O, *et al.* (2001) *J Biol Chem* **276,** 29188-29194.
32. Rizzo MA, Springer GH, Granada B, & Piston DW (2004) *Nat Biotechnol* **22,** 445-449.
33. Lelimousin M, *et al.* (2009) *Biochemistry* **48,** 10038-10046.
34. van Dongen EM, *et al.* (2007) *J. Am. Chem. Soc.* **129,** 3494-3495.
35. Evers TH, *et al.* (2007) *J Mol Biol* **374,** 411-425.

36. You X, *et al.* (2006) *Proc Natl Acad Sci U S A* **103,** 18458-18463.
37. Uhlenheuer DA, *et al.* (2009) *Chemistry* **15,** 8779-8790.
38. Boal AK & Rosenzweig AC (2009) *J Am Chem Soc* **131,** 14196-14197.
39. Banci L, *et al.* (2008) *Biochemistry* **47,** 7423-7429.
40. Zacharias DA, Violin JD, Newton AC, & Tsien RY (2002) *Science* **296,** 913-916.
41. Nagai T, *et al.* (2004) *Proc Natl Acad Sci U S A* **101,** 10554-10559.
42. Markwardt ML, *et al.* (2011) *PLoS One* **6,** e17896.
43. Erard M, *et al.* (2013) *Mol Biosyst* **9,** 258-267.
44. Alford SC, Ding Y, Simmen T, & Campbell RE (2012) *ACS Synth Biol* **1,** 569-575.
45. Grünberg R, *et al.* (2013) *Nat Methods* **10,** 1021-1027.
46. Jalink K (2013) *Nat Methods* **10,** 947-948.
47. Shaner NC, *et al.* (2013) *Nat Methods* **10,** 407-409.
48. Evers TH, Appelhof MA, Meijer EW, & Merkx M (2008) *Protein Eng Des Sel* **21,** 529-536.

Chapter 5

A red-shifted bile acid sensor for multicolor imaging

Abstract. Bile acids (BAs) are important steroid molecules for the digestion and absorption of lipids and the catabolism of cholesterol. BA synthesis is tightly regulated by the nuclear receptor FXR. BAs are also important signaling molecules and have been found to be ligands of the G protein-coupled receptor (GPCR) TGR5, which mediates downstream effects such as increased energy expenditure, using cAMP as a second messenger. Our group recently reported a FRET probe based on the ligand binding domain (LBD) of FXR, BAS-1, which allowed imaging of BA concentrations at subcellular resolution, leading to important insights on various BA membrane transporters and deleterious mutations thereof. Simultaneous imaging of BAs and the second messenger cAMP would help elucidate the intricate signaling pathways induced by BAs. To generate a red-shifted BAS sensor compatible with existing CFP/YFP-based cAMP reporters, the original Cerulean and Citrine FPs were exchanged for self-associating variants of mOrange and mCherry. A variant with the R125I mutation on both fluorescent domains was found to be optimal. RedBAS-1 bound the primary BAs cholic acid (CA, K_d = 60 μM) and chenodeoxycholic acid (CDCA, K_d = 1 μM) with affinities that were similar to those of BAS-1 and with a 66% change in emission ratio. When synthetic FXR ligand was added to HEK293 cells that had been transfected with a nucleus-targeted redBAS-1, the sensor responded with an ~18% drop in emission ratio. Finally, multicolor imaging was demonstrated by targeting redBAS-1 and BAS-1 to the same nuclei. A robust response from both sensors could be detected.

Introduction

BAs are cholesterol-derived steroid molecules that carry out several essential functions in the digestive system. Their amphiphilic properties allow them to form micelles that aid in the solubilization of cholesterol and fat-soluble vitamins, helping in the absorption and transport of these important dietary lipids. Synthesis of primary BAs, such as cholic acid (CA) and chenodeoxycholic acid (CDCA) from cholesterol is thought to be tightly regulated in order to prevent BAs from reaching toxic concentrations and to keep metabolism under control. An important protein in the regulation of BA synthesis is the nuclear receptor farnesoid X receptor (FXR), discovered and named (1) before the identity of its main ligand, the BA, was established (2-4). Like all nuclear receptors, FXR acts as a transcription factor whose activity can be modulated by its ligands, with ligand binding inducing interactions with co-activator proteins, *via* the canonical LXXLL motif.

The understanding of intracellular BA homeostasis has remained underdeveloped due to a lack of suitable probes for these molecules. Radiolabeled BAs are difficult to come by, while transcriptional (typically luciferase-based) assays are indirect and offer poor spatial and temporal resolution (5). Recently, our group reported a genetically encoded FRET sensor (BAS-1) that exploits FXR and its interactions with BAs and co-activator peptides (6). The sensor consists of FXR's ligand binding domain (LBD), fused at its N-terminus to Cerulean and at its C-terminus to a long flexible linker connecting the LBD to Citrine. A peptide containing the LXXLL co-activator motif is fused to the Citrine C-terminus. In the absence of BA, the fluorescent domains, which both carry the hydrophobic surface mutation Q204F, form an intramolecular dimer, resulting in a high level of FRET when the donor Cerulean is excited. Upon binding of BA in a pocket formed by 5 different LBD α-helices, a rearrangement of these helices occurs that allow the co-activator peptide's leucine side chains to interact with a hydrophobic groove on the LBD surface (7). In the latter state, the interaction between the fluorescent domains is disrupted, resulting in a large reduction in FRET efficiency. BAS-1 also functioned in cultured mammalian cells, albeit with an increase in emission ratio in response to BA addition, rather than a decrease. The sensor was used

to conduct a series of experiments probing the transmembrane transport and subcellular localization of several different BA species. The hydrophilic cholic acid as well as all of the conjugated BAs required active transport to cross the cell membrane. Furthermore, the functional consequences of several known mutations in NTCP, a BA transporter protein, could be directly monitored (6).

A second important player in BA signaling, membrane receptor TGR5, was discovered a few years after FXR (8). TGR5 is a member of the G protein-coupled receptor (GPCR) family of proteins that activate intracellular signaling pathways in response to extracellular changes in small molecule concentrations. Binding of extracellular BAs to TGR5 stimulates diverse downstream pathways via the second messenger cAMP. Disturbances in BA signaling may lead to overstimulation of TGR5, which has been linked to weight loss due to excess energy expenditure (9). Another highly unpleasant effect of BA misregulation was found to be pruritis (itch) and analgesia (pain), mediated by BAs' stimulation of TGR5 receptor in spinal cord neurons (10). The treatment of certain diseases would benefit from the discovery of agonists that stimulate either FXR alone, TGR5 alone or both at the same time. While the BA cholic acid (CA) is known to prevent weight gain in mice fed a high-fat diet, administration of FXR-specific synthetic ligand GW4064 to such mice induced a spectacular increase in weight (11). As an FXR-specific agonist, GW4064 inhibits BA synthesis, leading to less stimulation of TGR5. The ability to monitor cAMP levels and FXR activation simultaneously is crucial if more specific ligands are to be discovered. One could envision high throughput screens of small molecules capable of modulating the downstream effects of bile acid signaling. FRET sensors for cAMP are based on CFP and YFP derivatives, which precludes their application in the same cellular compartment with BAS-1 (12). Therefore, it is important to develop a BA sensor that is spectrally compatible with CFP/YFP-based sensors.

Here, a red-shifted BA sensor is developed by replacing the Cerulean and Citrine domains with mOrange2 and mCherry (13, 14). Previous efforts to exchange fluorescent domains often resulted in a loss of sensor functionality (15), requiring extensive re-optimization of the sensor. This is likely a consequence of sensors often

relying on poorly understood physical properties of FPs for their mechanism of action. BAS-1 was designed to exploit two mutually exclusive interactions, so that exchange of the original fluorescent domains with domains undergoing a similar interaction resulted in a sensor that worked without further optimization.

Results

Design and characterization of a red-shifted bile acid sensor

To create a red-shifted version of BAS-1 (redBAS), molecular cloning was used to replace DNA encoding the Cerulean and Citrine fluorescent domains with mOrange2 and mCherry respectively (Figure 5.1A, Figure 5.5). To ensure that co-factor peptide binding to the FXR domain would be allosterically coupled to disruption of the fluorescent domain interaction, the 9 C-terminal residues of both mOrange2 and mCherry were deleted during cloning. In the absence of BA, the sensor mechanism requires a hydrophobic interaction to occur between the fluorescent domains, yet the ideal stability of that interaction was unknown. Therefore, the effects of various combinations of mutations R125I and T127V in both mOrange2 and mCherry, were tested (Figure 5.1B). To characterize the redBAS constructs *in vitro*, the sensor proteins were expressed in *E. coli* BL21(DE3) and purified by Ni-NTA chromatography, followed by Streptactin chromatography, selecting for the presence of an N-terminal His-tag and C-terminal Strep-tag II, respectively. Protein was obtained at sufficient purity and yield (typically 0.75 mg/L bacterial culture). The primary bile acid CDCA was titrated to each of the four constructs (Figure 5.1C). For most constructs, a decrease in emission ratio was observed at increasing concentration of CDCA, consistent with the hypothesis that ligand binding induced disruption of the mOrange2-mCherry interaction. The variant with R125I at both donor and acceptor fluorescent domain (redBAS-1) clearly appeared to be the most sensitive, displaying the largest ratiometric response to CDCA addition. We therefore decided to characterize the sensor properties of this variant further.

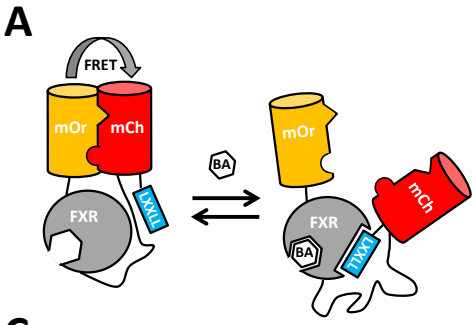

B

Construct	mOrange2 mutations	mCherry mutations
redBAS-0	R125/T127	R125/T127
redBAS-1	I125/T127	I125/T127
redBAS-2	I125/V127	I125/T127
redBAS-3	I125/T127	I125/V127
redBAS-4	I125/V127	I125/V127

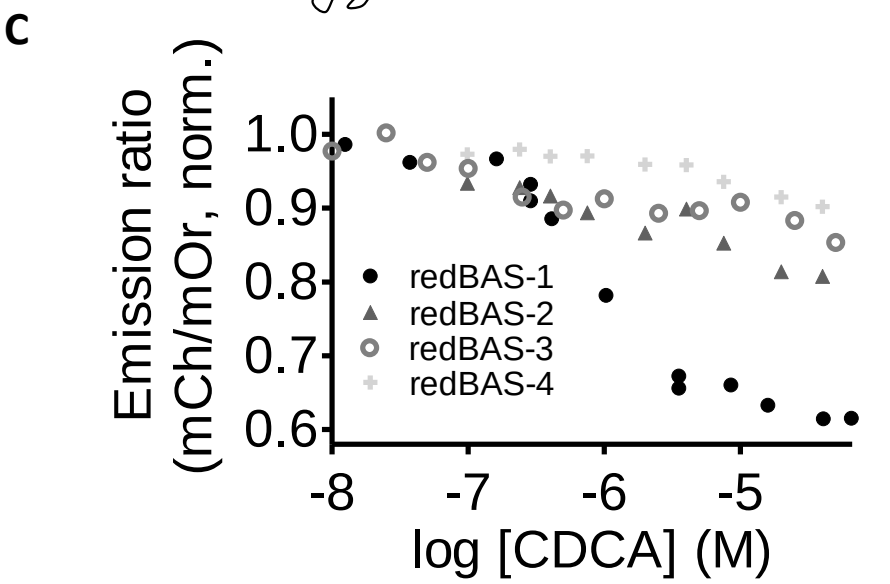

Figure 5.1: Design and initial characterization of various red-shifted bile acid sensors. *(A) Schematic representation of redBAS mechanism of action. In the absence of bile acid (BA), mOrange2 and mCherry form an intramolecular dimer. When bile acid binds to the ligand binding pocket of the FXR-LBD domain, the LXXLL motif directly fused to the mCherry C-terminus binds to the co-activator binding site on FXR-LBD, disrupting the intramolecular mOrange2-mCherry complex. (B) Overview of the mutations tested at the mOrange2-mCherry interface. (C) The fluorescence emission ratio (610/562 nm, normalized to ratio in absence of BA) was monitored as a function of CDCA concentration. Measurements were performed in 50 mM Tris-HCl (pH 8), 100 mM NaCl and 1 mM DTT at 25 °C, at a protein concentration of 0.2 µM.*

In the absence of ligand, the emission ratio (mCherry/mOrange2) of redBAS-1 was 1.6 (Figure 5.2A), which is similar to that of the redCALWY-1 Zn^{2+} sensor (Chapter 4). When CDCA was titrated to the redBAS-1 sensor, the emission ratio decreased to

0.9 (Figure 5.2A). Strikingly, at higher CDCA concentrations the emission ratio actually increased again (Figure 5.2B). A possible explanation for this observation is provided by the fact that some nuclear receptor ligands are known to directly compete for binding to the co-factor binding site with co-factor at high ligand concentrations (16). Values measured at concentrations above 65 µM, at which this effect became

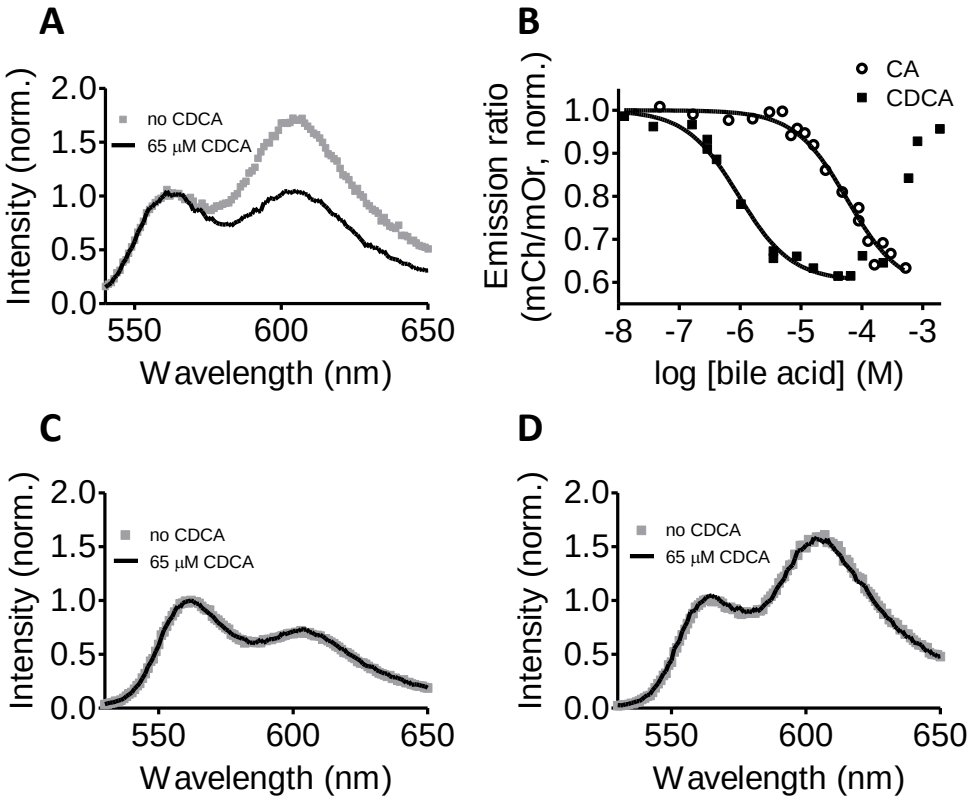

Figure 5.2: *In vitro* characterization of redBAS-1. *(A) Fluorescence emission spectra of redBAS-1 in the absence and presence of 65 µM CDCA after excitation at 520 nm. Spectra were normalized to the emission at 562 nm. (B) The redBAS-1 fluorescence emission ratio was monitored as a function of CDCA or CA concentration. The emission ratio was normalized to the value obtained in the absence of bile acid (BA) and fit to equation 5.1 (Methods). (C) Fluorescence emission spectra of redBAS-0 in the absence and presence of 65 µM CDCA after excitation at 520 nm. (D) Fluorescence emission spectra of redBAS-1-LXXAA, a variant of redBAS-1 carrying two leucine to alanine mutations in its cofactor binding motif, in the absence and presence of 65 µM CDCA after excitation at 520 nm. Measurements were performed in 50 mM Tris-HCl (pH 8), 100 mM NaCl and 1 mM DTT at 25 °C, at a protein concentration of 0.2 µM.*

apparent, were therefore excluded from the fit, which revealed a K_d of the sensor of 0.9 ± 0.1 µM CDCA. This value is similar to the K_d of 1.5 µM reported for BAS-1 (6). Titration with cholic acid (CA) led to a similar ratiometric response but without any increase in ratio at higher concentrations (Figure 5.2B). A weaker affinity (K_d = 58 ± 10 µM) was observed for CA, consistent with measurements with BAS-1 (6). When the R125I mutation on mOrange and mCherry was reverted (redBAS-0), the sensor showed a low starting emission ratio (0.6) and no longer responded to CDCA addition (Figure 5.2C), confirming the crucial role played by the R125I mutations. Further confirmation of the sensor's mechanism of action was provided by a control in which the canonical LXXLL motif of the sensor's co-activator peptide was replaced with LXXAA, preventing the peptide from interacting with the FXR LBD. As expected, this sensor variant (redBAS-1-LXXAA) displayed a high starting emission ratio of 1.5 and was unresponsive towards CDCA addition (Figure 5.2D).

Performance of redBAS-1 in cultured HEK293 cells

Since redBAS-1 displayed a robust ratiometric response to BAs *in vitro* (DR = 66%), its performance was next tested in mammalian HEK293 cells. Cells were transiently transfected with a redBAS-1 mammalian expression vector and imaged by confocal fluorescence microscopy. Using a 520 nm laser line, mOrange2 was excited, while the mOrange2 (560-590 nm) and mCherry (590-630 nm) emission was monitored. The construct carried a C-terminal NLS signal, so that redBAS-1 was exclusively localized in the nucleus. Upon addition of 5 µM of the potent, non-steroidal FXR ligand GW4064 (17), a clear decrease of ~18% was observed in the redBAS-1 emission ratio (Figure 5.3A). This decrease was consistent with redBAS-1 behavior *in vitro*, where a decrease in emission ratio was also observed upon addition of ligand. To demonstrate the importance of using self-associating FPs, we also tested the performance of redBAS-0 *in situ*. Addition of 5 µM GW4064 led only to a small, temporary increase in redBAS-0 emission ratio that soon returned to the basal level (Figure 5.3B).

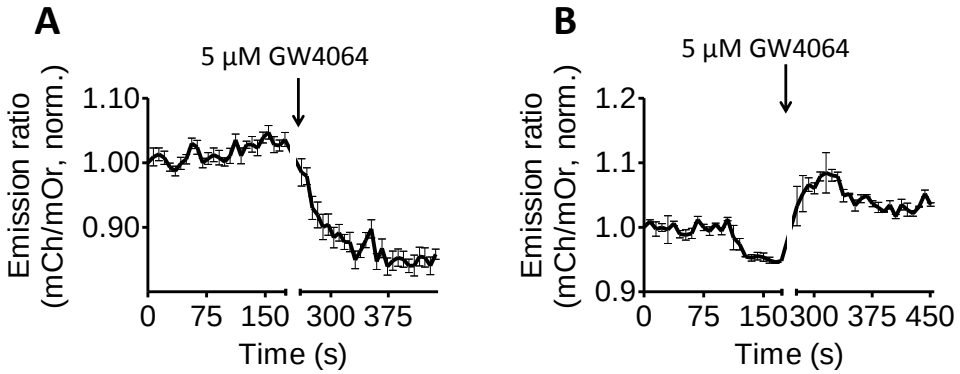

Figure 5.3: Ratiometric response of redBAS to synthetic FXR agonist GW4064 in HEK293 cells. *The redBAS-1 (A) and redBAS-0 (B) fluorescence emission ratio was monitored over time, before and after addition of 5 µM GW4064. The break in the X-axis indicates a pause in imaging to allow ligand addition to cells. Traces represent the averages of 9 (A) or 2 (B) cells, after normalization of the emission ratio to the value at t = 0. Error bars represent SEM.*

To prove that redBAS-1 was suitable for co-imaging with a CFP/YFP-based FRET sensor, HEK293 cells were co-transfected with BAS-1 and redBAS-1, both targeted to the nucleus. BAS-1 was excited with a 405 nm laser line, while redBAS-1 was excited using a 550 nm laser line, avoiding cross-excitation of Citrine. Four separate emission channels, 460-490 nm, 510-550 nm, 565-600 and 600-630 nm, allowed detection of Cerulean, Citrine, mOrange2 and mCherry emission, respectively. Upon addition of 5 µM GW4064, redBAS-1 displayed a 67% reduction in ratio, while at the same time BAS-1 displayed an increase of 26% (Figure 5.4A, B). The opposite ratiometric responses of the sensors were consistent with measurements of both sensors in isolation in the cell, where redBAS-1 also decreased its emission upon ligand addition (Figure 5.3A), while BAS-1 consistently responded with an increase (6). Interestingly, BAS-1's response appeared to be slightly delayed relative to redBAS-1, an observation we are currently unable to explain. The steady decrease in BAS-1 emission seen both before GW4064 addition and following maximal response to the ligand's addition is most likely indicative of acceptor bleaching caused by the high intensity of the 405 nm laser.

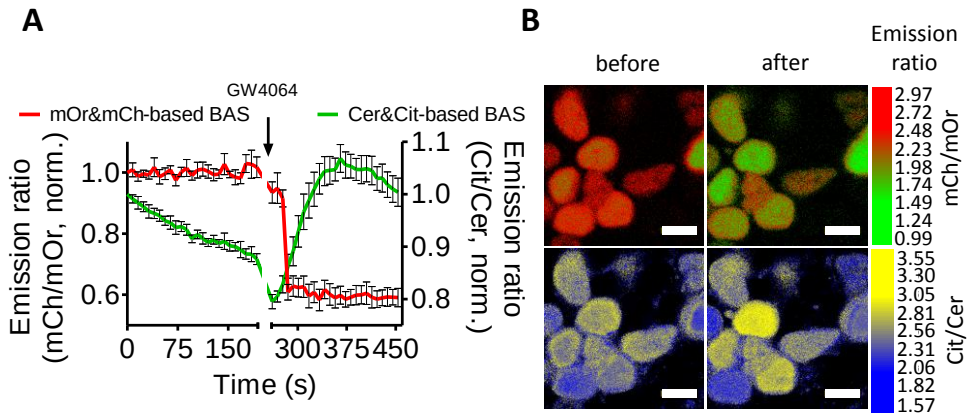

Figure 5.4: Simultaneous imaging of redBAS-1 and nucleoBAS-1 in the nuclei of co-transfected HEK293 cells. *(A) Emission ratios for both sensors were monitored over time, before and after addition of 5 µM GW4064. The break in the X-axis indicates a pause in imaging to allow ligand addition to cells. Traces represent the averages of 7 cells, after normalization of the emission ratio to the value at t = 0. Error bars represent SEM. (B) Pseudocolored ratiometric images of cells measured in (A), before and after GW4064 addition. The width of the white scale bar represents 10 µm.*

Discussion

A red-shifted FRET sensor for BA was successfully developed by replacing the Cerulean and Citrine domains of BAS-1 with mOrange2 and mCherry. By testing different interaction strengths between mOrange2 and mCherry it was found that the presence of the R125I mutation on both fluorescent domains mediated an optimal stability as it resulted in a sensor with the highest ratiometric response. Similar to what was found in the redCALWY-1 Zn^{2+} sensors (Chapter 4), further increases in FP-FP interaction strength worsened the sensors' DR. The affinity of redBAS-1 for CA and CDCA was similar to those recently established for BAS-1 and its DR of 66% allowed its robust response to a synthetic FXR ligand when the sensor was targeted to the HEK293 nucleus. Preliminary application of the sensor in HEK293 cells delivered promising results, with the sensor responding robustly to addition of a synthetic FXR ligand. The feasibility of multicolor imaging was also demonstrated, as the response

for BAS-1 and redBAS-1, targeted to the same nucleus, could be distinguished. However, more robust controls (e.g. mutations of the sensor's FXR LBD domain that prevent it from binding BA) are required and the redBAS-1 *in situ* response to natural BAs, rather than its response to synthetic FXR ligand GW4064, remains to be established.

The redBAS sensor exploits mutually exclusive interactions between mOrange and mCherry and between the FXR LBD and the co-factor peptide. A key aspect to this switch-like sensor is the strength of the intramolecular interaction between the fluorescent domains. Introduction of different combinations of the R125I and T127V mutations into redBAS, resulting in redBAS-2, -3 and -4, should increase the strength of the interaction relative to that found in redBAS-1. Increasing that strength had been expected to weaken the sensor's affinity for bile acid and to increase the DR. However, the ratiometric responses of redBAS-2, -3 and -4 were all much smaller than the response seen for redBAS-1. This result is similar to what was seen with the redCALWY Zn^{2+} sensor and like the WD4 domain in redCALWY, the FXR-LBD has a number of surface-exposed hydrophobic patches that might interact non-specifically with the fluorescent proteins (7).

It is interesting to note that in contrast to BAS-1, redBAS-1 displayed the same directionality in terms of ratiometric response *in vitro* as it did in the cell. This prompted us to reconsider the puzzling opposite directionality recently reported by our group for BAS-1 (6). It had been hypothesized that the increase in emission ratio seen in BAS-1 in the cell is caused by interference by an endogenous co-activator (6); addition of ligand might induce an interaction between the sensor LBD and this endogenous co-activator, competing out the sensor's own co-factor peptide. Consequently, at higher ligand concentrations, an ever larger fraction of BAS-1 would have intramolecularly dimerized fluorescent domains undergoing efficient FRET. This hypothesis thus predicts that there is in fact an LBD-cofactor interaction in the *absence* of ligand. In fact, *in vitro*, in absence of ligand, the BAS-1 emission ratio (~3.5) was significantly lower than the BAS-1-LXXAA ratio (~9), suggesting that a fraction of BAS-1 was in the co-factor-LBD interacting state in absence of ligand *in vitro* too (6).

It is tempting to speculate that increasing the stability of the Cerulean-Citrine interface through mutagenesis of Cerulean (A145Y/D148H, see Chapter 4) would help "lock" the fluorescent domain interaction in place in absence of ligand, potentially quadrupling the DR. Based on previous measurements (Chapter 4), the strength of the mOrange-mCherry interaction was expected to be similar to the Cerulean-Citrine interaction. It therefore remains unclear why redBAS-1 did not display the same *in vitro*/*in situ* opposite directionality behavior as BAS-1.

Once redBAS-1's utility as intracellular sensor has been established unequivocally, its application in further multiparameter experiments may be considered. It would be interesting to continue the investigations of Auwerkx and coworkers on the effect of BAs and synthetic FXR ligands on energy expenditure (9, 11). Upon stimulation of cells with a conjugated BA, how fast are cAMP levels increased, relative to active BA uptake? Co-imaging redBAS-1 with the recently developed, sensitive cAMP sensor $^{T}Epac^{VV}$ (12) would be a logical first step. Next, high throughput screening of small molecule libraries could be used to discover downstream modulators of bile acid signaling. While two sensors employing the same FRET pair could be imaged simultaneously by targeting one to the cytosol and the other to the nucleus, in high throughput screening it might be difficult to automatically recognize two different cell compartments. Furthermore, to better characterize temporal relationships between signaling events, up to four sensors could be combined: two spectrally distinct sensors in the cytosol and two in the nucleus.

It would be very interesting to be able to study bile acid homeostasis at the single cell level but in the context of a whole animal, an approach that has been shown to be feasible in the Ca^{2+} imaging field (18). Red fluorescent proteins are in principle better suited for whole animal imaging as red light penetrates tissue far better (19). For example, one could investigate the effect of a high fat diet on the intracellular concentration of bile acids in a mouse tissue of interest, with or without administration of an FXR agonist. Although redBAS-1's red-shifted emission should penetrate tissue more easily, its overall fluorescence remains too dim to be of use in an intact animal.

The sensor would therefore benefit from a brighter variant of mCherry, both in terms of dynamic range (see Chapter 1) and of signal to noise ratio.

To the best of our knowledge, this is the first red-shifted FRET sensor employing a nuclear receptor LBD domain. Previously, several FRET sensors were reported that, like BAS-1 and redBAS-1, exploit the nuclear receptor-co-factor peptide interaction. These included sensors for estradiol (20), phytoestradiol (21), glucocorticoids (22) and testosterone (23). However, these sensors did not use self-associating fluorescent domains, nor was their architecture designed to benefit from such an interaction (see Figure 1.5C in Chapter 1). The results reported in this chapter suggest that these sensors could be converted to sensitive red-shifted versions simply by replacing the LBD in redBAS with an LBD from one of these other NRs.

Methods

Cloning. To construct the pCMV-redBAS-1 mammalian expression vector (Figure 5.5), DNA from a synthetically constructed plasmid, pGen2.1-mOrange2(R125I)-linker-mCherry(R125I) and from pCMV-BAS-1 (6), was recombined using the previously described Circular Polymerase Extension Cloning (CPEC) method (Chapter 3, (*24*)). Briefly, primers 1M_Vec_iOr2_F and 10M-9_iOr_FXR_R were used to amplify an mOrange2-encoding fragment, primers 9M-9_iOr2_FXR_F and 6M_FXR_iCher_R were used to amplify a linker plus FXR LBD-encoding fragment, primers 5M_FXR_iCher_F and 12M-9_iChe_VecR were used to amplify an mCherry-encoding fragment and primers 11M-9_iChe_VecF and 2M_Vec_iOr2_R were used to amplify the vector backbone of pCVM-BAS-1 (Table 5.1). Primers were designed to introduce sequence homology between adjacent fragments, allowing their subsequent recombination by CPEC. To create a bacterial expression construct, first, pCVM-redBAS-1 was digested with restriction enzymes NheI and XhoI and the resulting insert fragment was ligated to a pET28a plasmid treated with the same restriction enzymes. Second, a C-terminal Strep-tag was introduced by site-directed mutagenesis,

Table 5.1: Primers used in cloning of redBAS constructs.

Name	Sequence
1M_Vec_iOr2_F	CAGATCCGCTAGCATGGTTTCTAAAGGCGAGGAGAATAATATGG
2M_Vec_iOr2_R	CCTTTAGAAACCATGCTAGCGGATCTGACGGTTCAC
5M_FXR_iCher_F	GGCGAAGAAGACAACATGGCCATTATTAAAGAATTCATGC
6M_FXR_iCher_R	GGCCATGTTGTCTTCTTCGCCTTTGCTCACCATACC
9M-9_iOr2_FXR_F	CGCCACAGTACTAGTGAACTCACCCCAGATCAACAGACTCTT
10M-9_iOr_FXR_R	GGGGTGAGTTCACTAGTACTGTGGCGACCTTCAGCA
11M-9_iChe_VecF	GCATTCCGCGGCCGCCGAGAA
12M-9_iChe_VecR	CGGCCGCGGAATGCCTTCCTTCGGCTC
FXR_Strep_F	TGGTCCCATCCTCAGTTTGAAAAATAACTCGAGCACCACCACCACC
FXR_Strep_R	TTTTTCAAACTGAGGATGGGACCAGGTACCCGCGTCTTCTACCTTTCTCTTCT
NID2LXXAA	ACCGCCGCTGTCCTGCGCGGCTCTGTGCAA
NID2LXXAA_R	TTGCACAGAGCCGCGCAGGACAGCGGCGGT
RCS_mOr2_I125R_F	CTATAAAGTAAAACTGCGTGGTACGAATTTTCCCTCAGATGGACC
RCS_mOr2_I125R_R	CGTACCACGCAGTTTTACTTTATAGATGAACTCCCCATCCTG
RCS_mCh_I125R_F	CAAGGTGAAGCTTAGAGGCACAAACTTTCCAAGCGACG
RCS_mCh_I125R_R	GTGCCTCTAAGCTTCACCTTGTATATAAACTCGCCG
RCS_mCh_T127V_F	GAAGCTTATCGGCGTAAACTTTCCAAGCGACGGCC
RCS_mCh_T127V_R	GGCCGTCGCTTGGAAAGTTTACGCCGATAAGCTTC
RCS_mO_T127V_F	GTAAAACTGATTGGTGTGAATTTTCCCTCAGATGGACCTGTCATGC
RCS_mO_T127V_R	GCATGACAGGTCCATCTGAGGGAAAATTCACACCAATCAGTTTTAC

with primers FXR_Strep_F and FXR_Strep_R, resulting in pET28a-redBAS-1. At this point, the T127V mutations were introduced by CPEC too. PCR fragments were generated with various combinations of the primers RCS_mCh_T127V_F, RCS_mCh_T127V_R, RCS_mO_T127V_F and RCS_mO_T127V_R, together with FXR_Strep_F and FXR_Strep_R. CPEC was also used to introduce the I125R mutations in mOrange and mCherry, in both pET28a-redBAS-1 and pCMV-redBAS-1. Primers RCS_mOr2_I125R_F and RCS_mCh_I125R_R were used in a PCR reaction to create a fragment spanning the two 125 positions of both fluorescent domains. Primers RCS_mOr2_I125R_R and RCS_mCh_I125R_F allowed amplification of the vector backbone and sequence to the 5'-side of position 125 in mOrange2 and to the 3'-side of the 125 position in mCherry. These two fragments, whose ends were homologous, were then recombined by CPEC. The redBAS-1 co-factor peptide sequence was mutated to LXXAA, using the QuickChange II Site-Directed Mutagenesis Kit (Stratagene), with primers NID2LXXAA and NID2LXXAA_R. All constructs were confirmed by sequencing (Baseclear, Netherlands) prior to use.

MGSS*HHHHHH*SSGLVPRGSHMASMVSKGEENNMAIIKEFMRFKVRMEGSVNGHEFEIEGE 60
GEGRPYEGFQTAKLKVTKGGPLPFAWDILSPHFTYGSKAYVKHPADIPDYFKLSFPEGFK 120
WERVMNYEDGGVVTVTQDSSLQDGEFIYKVKLIGTNFPSDGPVMQKKTMGWEASSERMYP 180
EDGALKGKIKMRLKLKDGGHYTSEVKTTYKAKKPVQLPGAYIVDIKLDITSHNEDYTIVE 240
QYERAEGRHSTSELTPDQQTLLHFIMDSYNKQRMPQEITNKILKEEFSAEENFLILTEMA 300
TNHVQVLVEFTKKLPGFQTLDHEDQIALLKGSAVEAMFLRSAEIFNKKLPSGHSDLLEER 360
IRNSGISDEYITPMFSFYKSIGELKMTQEEYALLTAIVILSPDRQYIKDREAVEKLQEPL 420
LDVLQKLCKIHQPENPQHFACLLGRLTELRTFNHHHAEMLMSWRVNDHKFTPLLCEIWDV 480
QGELGGSGGSGGSGGSGGSGGSGGSGGSGGSGGSGGSGGSGGSGGSGGSGGSGPRGM 540
VSKGEEDNMAIIKEFMRFKVHMEGSVNGHEFEIEGEGEGRPYEGTQTAKLKVTKGGPLPF 600
AWDILSPQFMYGSKAYVKHPADIPDYLKLSFPEGFKWERVMNFEDGGVVTVTQDSSLQDG 660
EFIYKVKLIGTNFPSDGPVMQKKTMGWEASSERMYPEDGALKGEIKQRLKLKDGGHYDAE 720
VKTTYKAKKPVQLPGAYNVNIKLDITSHNEDYTIVEQYERAEGRHSAAAEKHKILHRLLQ 800
DSGGT**PKKKRKVEDA**GT*WSHPQFEK* 825

Figure 5.5: Amino acid sequence of the pET28a-redBAS-1 expression construct. *The sequence shows an N-terminal polyHis tag (italicized), mOrange2 (highlighted in grey), FXR LBD (highlighted in black), a flexible linker, mCherry (highlighted in grey), co-factor peptide (underlined), NLS (in bold) and a C-terminal Strep-tag II (italicized). The mammalian expression construct was identical, except that it lacked purification tags.*

Protein expression and purification. *Escherichia coli* BL21(DE3) was transformed with the pET28a expression plasmids and plated on LB-agar containing 30 µg/mL kanamycin. A single colony was used to inoculate 5 mL LB, which was cultured overnight at 37 °C, 250 rpm. This culture was used to inoculate 2 L of LB, which was incubated at 37 °C, 250 rpm, until an OD_{600} of 0.6 was reached. At that point, 0.1 mM IPTG was added to induce expression, and the temperature was reduced to 25 °C. Following overnight expression, cells were harvested by centrifugation and lysed with BugBuster (Novagen). The soluble fraction, recovered by a second centrifugation step at 40,000xg, was applied to a Ni-NTA affinity chromatography column (HisBind resin, Novagen). Immobilized protein was extensively washed with a buffer (20 mM Tris-HCl (pH 8), 500 mM NaCl) containing 40 mM imidazole and eluted with the same buffer containing 250 mM imidazole. Next, the Ni-NTA eluate was applied to a Streptactin column (IBA) and washed with buffer W (100 mM Tris-HCl (pH 8), 1 mM EDTA, 150 mM NaCl). Protein was eluted using buffer W with 2.5 mM desthiobiotin. SDS-PAGE analysis indicated all proteins to be of sufficient purity, except redBAS-0, which was additionally purified by size exclusion chromatography

(Sephacryl S200, GE Healthcare) with the column equilibrated in SEC buffer (50 mM Tris-HCl (pH 8), 100 mM NaCl). The entire purification procedure (except cell lysis) was done in the presence 0.5 mM TCEP to keep the proteins reduced.

***In vitro* characterization.** Fluorescence measurements were done using 0.2 µM protein concentration, in measurement buffer (50 mM Tris-HCl (pH 8), 100 mM NaCl, 1 mM DTT) using a 1x1 cm cuvette, at 25 °C. A fluorescence spectrophotometer (Varian Eclipse) was set to excite samples at 520 nm and to record emission between 530 and 650 nm. Stock solutions of CA (5 mM) and CDCA (25 mM) were prepared in measurement buffer and used to increase the BA concentration stepwise. To determine the redBAS-1 dissociation constants (K_{d}) for BA, the emission ratio (R, 610 nm/562 nm) was fit as a function of BA concentration ([BA]) using equation 5.1.

$$R = \frac{P_1[BA]}{\mathrm{K}_d + [BA]} + P_2 \tag{5.1}$$

Here P_1 is the difference in ratio between the BA-saturated and BA-depleted states and P_2 is the ratio in the BA-depleted state of the sensor.

Mammalian cell culture, transfection and imaging. All mammalian cell culturing procedures were essentially identical to those described in the Methods of Chapter 3, except that HEK293 rather than HeLa cells were used here. Chambered borosilicate cover glass wells (4.2 cm^2 each, Lab-Tek, Nunc) were seeded with 200,000 cells one day before transfection. Transfection was carried out with GenJet Transfection Reagent Ver. II (SignaGen Laboratories) according to manufacturer's instructions, using 1 µg plasmid DNA. For co-transfection of pCMV-redBAS-1 and pCMV-BAS-1, 0.25 µg of the latter was used with 0.75 µg of the former. Cells were imaged two days after transfection. Imaging was performed with a confocal microscope (Leica, TCS SP5X) equipped with a 40x water immersion objective and acousto-optical beamsplitters (AOBS). To excite mOrange2, a white light laser set to 520 nm (15% of full power) was used while mOrange2 (560-590 nm) and mCherry (590-630 nm) emission was monitored using the AOBS and avalanche photo diode/photomultiplier tubes hybrid detectors (HyD, Leica). When redBAS-1 and nucleoBAS were imaged simultaneously, a 405 nm laser was used to excite Cerulean while the white light laser was set to 550

nm to excite mOrange2, avoiding excitation of Citrine. Emission windows were: 460-490 nm (Cerulean), 510-550 nm (Citrine), 565-600 nm (mOrange2) and 600-630 nm (mCherry). Imaging was performed every 8.21 seconds, in Dulbecco's Modified Eagle Medium (DMEM) without phenol red. After a few minutes, DMEM containing GW4064 was added to a final GW4064 concentration of 5 µM. To generate the pseudocolored ratiometric images presented in Figure 5.4B, an average image was calculated for each channel, both before (t = 0 to t = 192) and after (t = 261 to t = 453) GW4064 addition. Acceptor channel averaged images were divided by donor channel averaged images and thresholded, before a look up table (LUT) was applied.

Acknowledgements

Many of the experiments described in this chapter were designed, carried out and analyzed by Lisanne van Oppen. Anne Hessels' help with confocal microscopy is gratefully acknowledged. Sjors Wijnands greatly contributed to the molecular cloning effort. Stan van de Graaf (formerly at UMCU, now at AMC) provided many useful suggestions and encouraged the development of a red-shifted bile acid sensor.

References

1. Forman BM, *et al.* (1995) *Cell* **81,** 687-693.
2. Makishima M, *et al.* (1999) *Science* **284,** 1362-1365.
3. Parks DJ, *et al.* (1999) *Science* **284,** 1365-1368.
4. Wang H, *et al.* (1999) *Mol Cell* **3,** 543-553.
5. Merk D, Steinhilber D, & Schubert-Zsilavecz M (2014) *Expert Opin Drug Discov* **9,** 27-37.
6. van der Velden LM, *et al.* (2013) *Hepatology* **57,** 740-752.
7. Mi LZ, *et al.* (2003) *Mol Cell* **11,** 1093-1100.
8. Kawamata Y, *et al.* (2003) *J Biol Chem* **278,** 9435-9440.
9. Watanabe M, *et al.* (2006) *Nature* **439,** 484-489.
10. Alemi F, *et al.* (2013) *J Clin Invest* **123,** 1513-1530.
11. Watanabe M, *et al.* (2011) *J Biol Chem* **286,** 26913-26920.
12. Klarenbeek JB, *et al.* (2011) *PLoS One* **6,** e19170.
13. Shaner NC, *et al.* (2004) *Nat Biotechnol* **22,** 1567-1572.
14. Shaner NC, *et al.* (2008) *Nat Methods* **5,** 545-551.
15. Jost CA, Reither G, Hoffmann C, & Schultz C (2008) *ChemBioChem* **9,** 1379-1384.
16. Wang Y, *et al.* (2006) *Proc Natl Acad Sci U S A* **103,** 9908-9911.
17. Maloney PR, *et al.* (2000) *J Med Chem* **43,** 2971-2974.

18. Thestrup T, *et al.* (2014) *Nat Methods*.
19. Lin MZ, *et al.* (2009) *Chem. Biol.* **16,** 1169-1179.
20. Awais M, Sato M, Sasaki K, & Umezawa Y (2004) *Anal Chem* **76,** 2181-2186.
21. Dumbrepatil AB, *et al.* (2010) *Analyst* **135,** 2879-2886.
22. Awais M, Sato M, & Umezawa Y (2007) *Steroids* **72,** 949-954.
23. Awais M, Sato M, Lee X, & Umezawa Y (2006) *Angew Chem Int Ed Engl* **45,** 2707-2712.
24. Quan J & Tian J (2009) *PLoS One* **4,** e6441.

Chapter 6

A library of fluorescent antibody sensors for efficient epitope mapping

Abstract. The availability of short linear mimotope (synthetic epitope) peptide sequences that bind antibodies with high affinity is important in diagnostic tests, for the development of vaccines and in therapeutic applications. Here a library of genetically encoded FRET-based antibody sensors is developed to discover novel epitope sequences in a solution-based assay. First, a technique was developed that allowed creation of a DNA library encoding a randomly varied, yet perfectly repeated epitope sequence at two separate sites on the FRET sensor. This was achieved by using rolling circle amplification to create a tandem repeat of a circularized template. As a first demonstration of this technique, a library was created in which each 7-residue epitope was mutated at single position. This library was validated through sequencing and expression of single clones in a 96-well plate scale. One way to screen large libraries of this FRET sensor would be to express clones in microdroplets and use microfluidic manipulations. Here, optimization is reported of several steps in the *in vitro* transcription/translation (IVTT) of the sensor, required for expression in microdroplets. Expression of monoclonal protein in each droplet would require each microdroplet to initially contain a single copy of DNA template. It is shown here that multiple displacement amplification allowed generation of sufficient DNA for IVTT. By placing the FRET acceptor at the N-terminus, the dynamic range (DR) of IVTT-expressed sensor protein was improved 2-fold. The presence of DTT in the IVTT reaction was found to affect the conformation of the antibody. This effect could be countered by inactivating DTT with iodoacetamide. This important preliminary work paves the way for the high throughput screening of sensors with improved epitopes.

Introduction

Antibodies bind antigens at relatively short (typically 6 residue) recognition sites that are either "continuous", i.e. consisting of a short antigen primary structure or non-continuous, i.e. a particular fold in the antigen's tertiary structure. These recognition sites are known as epitopes. There is much interest in methods that can establish the identity of epitopes ("epitope mapping") for applications such as antibody detection, vaccine development and the use of antibodies as drugs. Furthermore, identification of the epitope allows further development, such as establishing the shortest antigenic version of the epitope and development of synthetic higher affinity versions of the epitope, or mimotopes, in a process known as "analoging". Mimotopes could also be used as convenient, genetically encodable alternatives to carbohydrate-based antigens. The availability of high affinity epitope sequences is essential for the construction of sensitive probes that can detect the presence of antibodies for diagnostic purposes (1-3). For example, in the diagnosis of blood group types, mimotopes might one day replace the expensive, purified red blood cells in current use (4). For vaccine development, it is very important that the precise epitope sequences are known. For example, the recent discovery that a so-called broadly neutralizing antibody recognized a short stretch of highly conserved hydrophobic amino acids on an HIV envelope protein (gp41) allowed animal immunization studies to focus on this particular antigen as a promising means to develop an HIV vaccine (5, 6). Mimotopes based on tumor-derived epitopes recognized by T cell receptors (TCRs) may also be exploited therapeutically, in order to stimulate anti-tumor T cells, generating tumor protective activities (7). Antibodies are increasingly used as cancer treatment but binding of the antibody at sites other than the tumor may cause severe side effects. To improve the therapeutic index of such antibody treatments, a masking strategy was recently devised. This masking is achieved through use of mimotopes that bind the antibody's paratopes with high affinity until such time as some other, site-specific event (e.g. protease activity), causes the mimotopes to be released and the antibody to become available for binding (8). A sufficiently high affinity of the synthetic mimotopes is critical for the success of this latter strategy.

Current epitope discovery strategies can be broadly grouped into one of two categories. In the first, large, completely randomized libraries of potential epitope sequences are screened for binding to a surface-immobilized antibody, using techniques such as phage display and ribosome display. The second strategy involves screening partially overlapping, 6 to 20-mer synthetic peptides covering a known antigenic protein. In this case, the peptides are each immobilized in a separate well of a well-plate or on beads on a chip and tested for antibody binding in an ELISA-like format. Although often yielding useful results, the need to individually synthesize and purify each peptide is both labor-intensive and expensive. Avidity effects likely aid in the recovery of useful binders in both phage display and peptide fragment mapping. In the latter, this increase in affinity is caused by the increased effective concentration of the second paratope for a mimotope once the first paratope has bound, an effect that can be modeled and is well-understood (9). In phage display, the avidity effect results from the fact that each M13 phage particle displays 5 copies of variable mimotope, allowing each phage to bind multiple paratopes, as long as target antibody is sufficiently densely coated on the well surface (10). However, the tendency for a subset of parasitic phages to outgrow useful binders complicates phage display (11). Furthermore, complicated strategies are typically required to allow correct surface immobilization of antibodies (12). Also, ELISA-like screening assays tend to be highly laborious due to multiple wash steps and limited throughput. A solution-based, bivalent screening assay for novel genetically encoded epitopes would be highly desirable.

Our group previously developed CerAbsCit (previously referred to as Absense3), a single-chain fluorescent protein-based sensor that detects antibodies (3). This sensor consists of two epitopes connected by a semi-rigid peptide linker and flanked by fluorescent proteins Citrine and Cerulean, both bearing hydrophobic surface mutations Q204F and V224L. In the absence of antibody, the fluorescent domains form an intramolecular dimeric complex and consequently undergo a high degree of Förster Resonance Energy Transfer (FRET). Binding of antibody to both epitopes disrupts that complex, resulting in a readily detectable decrease in FRET efficiency (Figure 6.1A).

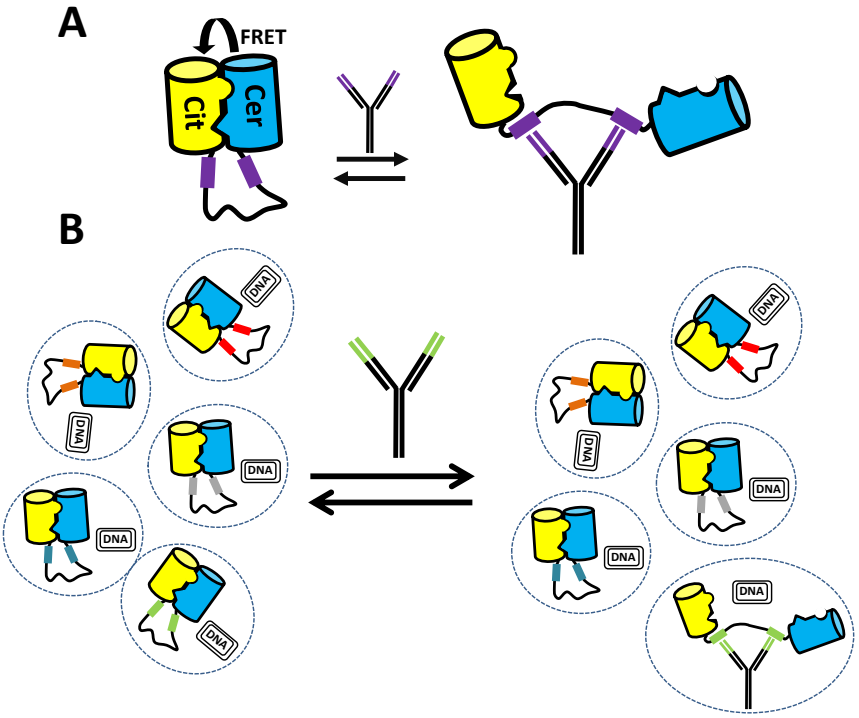

Figure 6.1: Schematic representation of the CerAbsCit mechanism of action and proposed further development. *(A) In the absence of antibody, the Cerulean and Citrine fluorescent domains form an intramolecular complex and undergo a high degree of FRET. Binding of an anti-HIV-P17 antibody to the P17-based epitopes forces the two fluorescent domains to separate, resulting in a decrease in FRET. (B) A library of CerAbsCit variants may be screened for binding to an antibody of interest. Dashed lines indicate "clonal units" comprised of sensor protein and encoding DNA. Phenotype-genotype linkage may be achieved by using individual bacterial cells or may be artificially maintained through use of aqueous droplets in oil.*

Introduction of epitopes with sequence WEKIRLR resulted in a sensor that could detect an antibody against HIV's P17 protein. The modularity of the sensor's design allowed straightforward exchange of both the reporter domains and epitopes, as recently demonstrated when the fluorescent proteins were replaced with an enzyme/inhibitor complex and P17 epitopes were exchanged for hemagglutinin and Dengue fever related epitopes (2).

As a genetically encoded sensor, CerAbsCit is amenable to directed evolution and screening sensor variants for a ratiometric response would offer a direct method to develop antibody sensors for any antibody for which high affinity, specific epitopes are not yet available (Figure 6.1B). Here the use of *in vitro* compartmentalization using a microfluidics device as a technique to select CerAbsCit variants is proposed. In this selection platform, pL aqueous droplets in oil are guided through photolithographically created channels on a PDMS microchip, where they can be incubated, fused, measured and selected (13). This technique has been successfully used to evolve enzymes with improved activity (14-18). By carrying out *in vitro* transcription/translation (IVTT) from a monoclonal DNA template encoding a CerAbsCit variant in each droplet and fusing such droplets with antibody bearing droplets, it should be possible to create a cheap and straightforward method to detect improved epitopes. Preliminary work identifying the optimal conditions for IVTT-generation of antibody FRET sensors is presented.

There are well-established techniques to introduce variation in DNA sequence, including approaches such as error prone PCR or use of NNK codons, making the construction of DNA libraries straightforward in most cases. However, the bivalent nature of the CerAbsCit-antibody interaction represents a unique challenge in DNA library construction: the variation is to be identical at both epitopes within the single-chain sensor. A new cloning technique is presented that allows the introduction of identical variation at the two separate epitope sites of the DNA encoding the antibody sensor. The resulting library was validated through sequencing and by screening library members for antibody binding in a 96-well plate based assay.

Results

Creation of DNA library

To allow directed evolution of the epitope binding sites in the CerAbsCit FRET sensor of anti-P17 antibody, it was essential to find a technique capable of introducing *identical* random mutations at both epitopes within one molecule. An extensive search

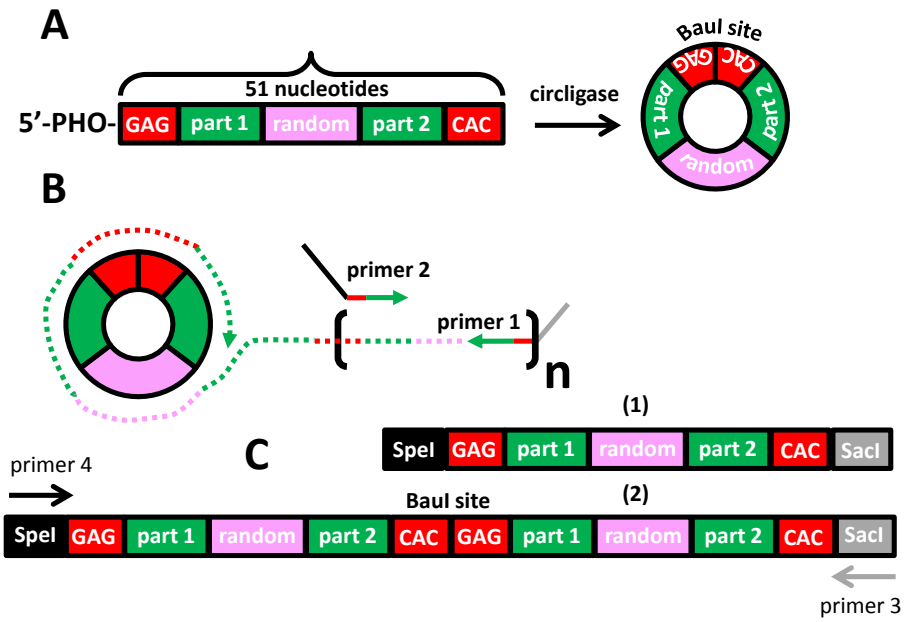

Figure 6.2: Rolling circle amplification of circularized DNA allows the generation of tandem repeats of the encoded randomized epitope sequence. *(A) Synthetic 51 nucleotide oligos bearing a random stretch of sequence are rendered circular by circligase. (B) Primer 1 is reverse complementary to Part 2 of the oligo and primes DNA polymerase-catalyzed rolling circle amplification (RCA), while oligo 2 is of identical sequence to part 1 and primes the synthesis of a strand complementary to the RCA product, resulting in different products bearing n repeats of the template oligo. (C) Discrete products such as (1) and (2) are formed, flanked by restriction sites SpeI and SacI and with a BauI site between each repeat. Following purification of desired product (2), primers 3 and 4 allow amplification by binding to non-repeated, flanking sequences.*

of the literature did not reveal a method allowing creation of DNA libraries that are varied at multiple sites yet in such a way that the sites themselves are identical. Therefore, a novel technique was devised, based on rolling circle amplification (RCA), which allows the creation of tandem repeats of short, circular, partly randomized DNA templates (19, 20). First, 51-nt "template" oligos were designed such that an epitope-encoding, partially NNK-randomized sequence was flanked by two invariant stretches of sequence called "part 1" and "part 2" (Figure 6.2A). Seven different template oligos were designed, with NNK (where N represents A, T, G or C and K represents G or T) replacing either the W, E, K, I, R, L or R-encoding codons of the epitope sequence,

with all template oligos carrying a 5'-phosphorylation. The template oligos were intramolecularly circularized using an RNA ligase (Figure 6.2A) (21). At the point of circularization, a restriction site was formed, BauI (CACGAG), that was not present in the linear template oligo. This site served as the point at which a linker was later to be introduced within a tandem epitope repeat (see below). To create a tandem repeat of the randomized epitope sequence, rolling circle-mediated amplification was carried out using the circularized DNA molecules as templates. In this reaction, carried out using a high-fidelity thermostable DNA polymerase, a reverse primer 1, reverse complementary to Part 2, initially created tandem repeats of the circular template (Figure 6.2B). A forward primer 2, present in the same reaction and of the same sequence as Part 1, together with primer 1, resulted in amplification of products, whose sizes were discrete and variable, depending on the position where primers 2 and 1 bound. Primers 1 and 2 also carried sequences at their 5'-ends that were non-complementary to the template sequence, and served to introduce restriction sites SpeI and SacI at either end of the tandem repeat (Figure 6.2C). As expected, gel electrophoretic analysis of this reaction revealed discretely sized products whose sizes correlated to multiples of 51 bp (the length of the template oligos) plus a constant 58 bp (the total length of the non-template-complementary sequence introduced by the 5'-tails of primers 1 and 2) (Figure 6.4A). The 160 bp fragment carried the desired single tandem repeat of the epitope sequence and so was excised from the gel and purified (Figure 6.4B, lane 1). Next, primers 3 and 4, complementary to the 5'-arms of primers 1 and 2 only, were used to amplify this 160 bp product (Figure 6.4B, lane 2). An acceptor vector, pET28a-Citrine(SpeI)-L9-(SacI)Cerulean (Figure 6.3A), was restricted with SpeI and SacI, allowing ligation of a similarly treated single tandem repeat (Figure 6.4B, lane 3) in between the Citrine and Cerulean sequences (Figure 6.3 B, E). Since in this construct Citrine is at the N-terminus, while Cerulean is at the C-terminus, resulting constructs will be referred to as Cit*Abs*Cer (asterisks represent variability in epitope sequence, please note that this construct is distinct from CitAbsCer introduced in the section on IVTT optimization below). The ligation mixture was

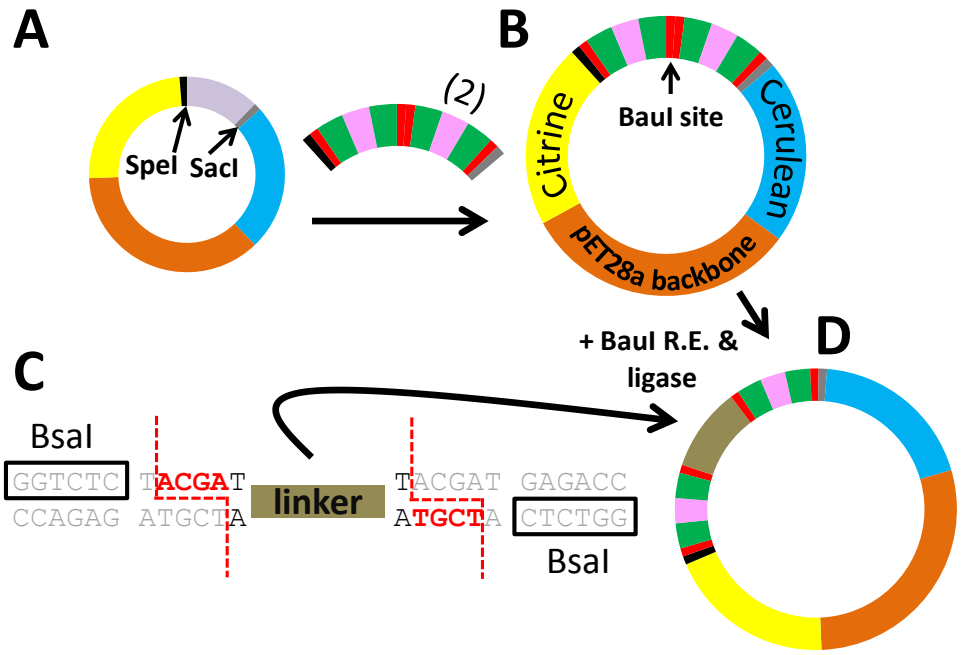

E

```
…Citrine><SpeI><----part 1---><------epitope------><---part
ttatataaaactagtgagactggagcaacgtgggaaaagataaggttgaggggcaccgca 60
 L  Y  K  T  S  E  T  G  A  T  W  E  K  I  R  L  R  G  T  A

2----><----part 1---><------epitope------><----part 2--->
actcacgagactggagcaacgtgggaaaagataaggttgaggggcaccgcaactcacggt 120
 T  H  E  T  G  A  T  W  E  K  I  R  L  R  G  T  A  T  H  G

<SacI><Cerulean…
gagctcatggtttct                                             135
 E  L  M  V  S
```

Figure 6.3: Insertion of repeated epitope-encoding sequence into acceptor vector is followed by insertion of a linker between epitope sequences. *(A) The acceptor vector encodes Citrine and Cerulean, between which SpeI and SacI sites are located. Digestion with these restriction enzymes removes a stuffer sequence. (B) SpeI & SacI restricted product (2) (see Figure 6.2C) is ligated into the acceptor vector. (C) Linker PCR product is flanked by non-palindromic BsaI restriction sites (5'-GGTCTC, boxed). BsaI digestion results in single-stranded overhangs compatible with BauI-generated overhangs. (D) BsaI-restricted linker and the BauI-digested construct from (B) are incubated in the presence of T4 DNA ligase and BauI restriction enzyme, resulting in the irreversible ligation of linker at the BauI site. (E) Annotated sequence of construct depicted in (B) with DNA in lowercase and single-letter amino acid code in uppercase. The BauI site (CACGAG) formed between Part 2 and Part 1 is shown in bold. Sequence is shown from the last three residues of Citrine to the first three residues of Cerulean.*

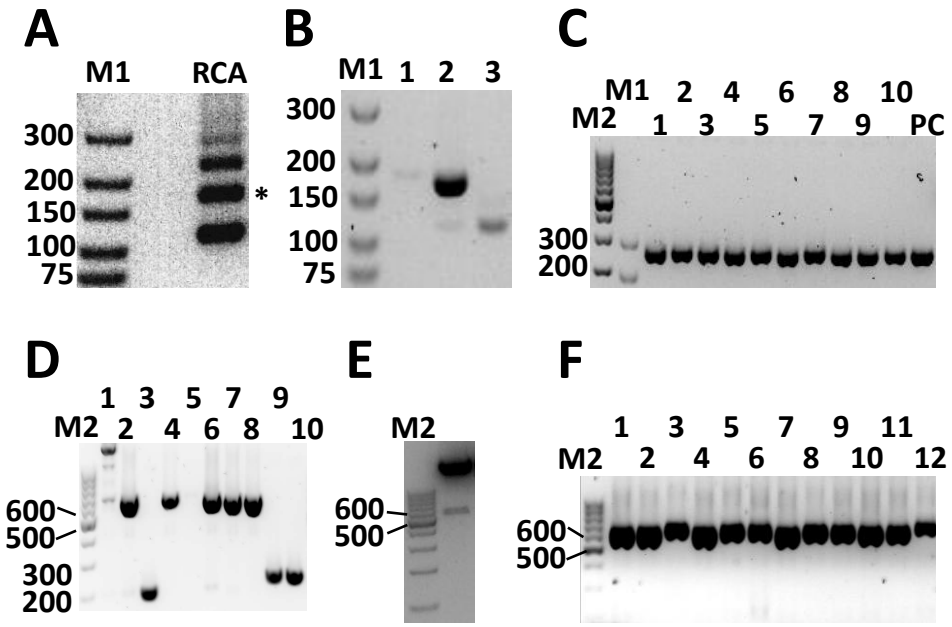

Figure 6.4: Gel electrophoretic analysis of steps involved in preparation of an identical random repeat DNA library. *(A) Rolling circle amplification results in discrete products with sizes corresponding to multiples of 51 nucleotides, together with a constant 58 nucleotides (originating from the RCA primer pair's non-annealing 5'-tails). The 160 bp product (*) represents the desired single repeat fragment. (B) Product (*) from gel A was gel extracted (lane 1), amplified with primers that bind to the unique ends of the RCA products (lane 2) and restricted with SpeI and SacI, generating a 115 bp product (lane 3). (C) Colonies (1-10) resulting from transformation of the ligation of SpeI & SacI-restricted single repeat fragment with similarly treated acceptor vector were probed by colony PCR for an expected 251 bp product, as seen for a sequenced control (lane PC). (D) Colonies (1-10) resulting from transformation of the ligation of linker at the BauI site of the single repeat-bearing acceptor vector library were analyzed by colony PCR for an expected 641 bp product. (E) Library DNA probed in (D) was treated with SpeI and SacI, allowing separation on gel of desired 506 bp restriction fragment from undesired 115 bp and 64 bp fragments. (F) Part of 96-well-scale colony PCR on colonies resulting from ligation of 506 bp restriction fragment in (E) to a SpeI/SacI-cut acceptor vector, for an expected fragment size of 641 bp. Lanes labeled M1 and M2 contained DNA ladders.*

transformed to 20 µL chemically competent *Escherichia coli* NovaBlue cells which were cultured in 5 mL LB medium. To determine the size of the library at this stage, part of the transformation reaction was plated on selective agar. The transformation yielded a total of 4000 colony forming units (cfu), with 10 out of 10 colonies analyzed

bearing the correctly sized insert (Figure 6.4C). At this stage, the epitopes' sequences were still located in tandem to one another, yet the Cit*Abs*Cer sensor mechanism dictates that they be separated by a semi-flexible 127 amino acid residue linker (3). A miniprep of the single repeat bearing vector library was treated with BauI to digest the vector at this point. Meanwhile, the semi-flexible linker-encoding fragment was amplified with primers that added BsaI sites at either end of the product. The BsaI sites were designed such that following BsaI restriction they were removed (BsaI cleaves at the 3'-side of the non-palindromic recognition site GGTCTC) and a 4-bp sticky overhang compatible with BauI was created. The non-palindromic nature of the BauI restriction site ensured that the linker could be ligated in only one orientation in the vector (Figure 6.3C, D). Furthermore, this ligation was irreversible, as ligation of the BsaI-generated cohesive ends to BauI-generated cohesive ends destroyed the original BauI recognition site. Therefore, in the presence of T4 ligase and BauI restriction enzyme, the linker insertion reaction ought to be driven to completion (Figure 6.3D). However, contrary to expectations, PCR analysis of *E. coli* colonies resulting from transformation of the latter ligation revealed that a significant fraction (50%) of colonies did not yield the expected 641 bp product and were thus incorrect (Figure 6.4D). Incorrect products formed in this colony PCR analysis included fragments corresponding to acceptor plasmids bearing zero and single epitope repeats without the linker inserted indicating that an additional library purification step was called for. A library miniprep was restricted with SpeI and SacI and subsequent gel electrophoresis allowed separation of shorter undesired fragments (barely visible) from the desired 641 bp fragment (Figure 6.4E). The latter was gel extracted and ligated to a SpeI/SacI treated acceptor vector. Analysis by PCR of colonies resulting from the transformation of this ligation revealed at least 85/92 (92%) of colonies to carry plasmids with correctly sized insert (Figure 6.4F).

Validation of small library by sequencing and expression

To test the functionality of the library, a small-scale analysis of 96 clones was carried out. Bacterial expression strain *E. coli* BL21(DE3) was transformed with library DNA and plasmids of individual colonies were sequenced. Out of 95 clones submitted, 85 were successfully sequenced. Of these 85, 19 did not contain the desired exact repeat of epitope sequence but instead contained two different epitopes. Out of the 66 sequences that did contain the desired repeat, 9 contained an undesired, but exactly repeated, single bp deletion in the epitopes. This deletion is most likely a result of truncated side-products in the oligonucleotide starting material, which was only 80% pure. Mutations found in the remaining 57 sequences are summarized in Figure 6.5. The coverage provided by the 85 sequences was 39 out of a possible 148 variants or 26% of the library.

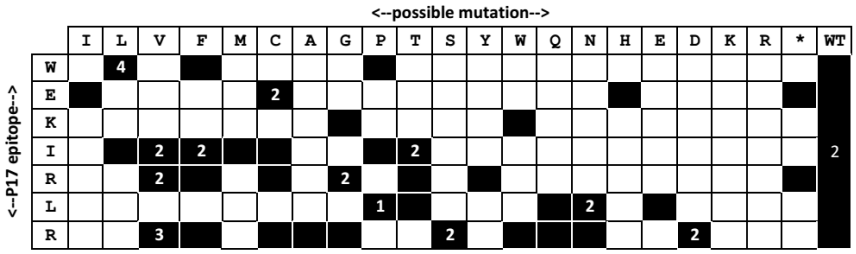

Figure 6.5: Summary of mutations found in the Cit*Abs*Cer library. *The left-hand column represents each of the 7 residues of the WEKIRLR epitope while the top row represents each of the twenty possible amino acids, in their single letter code. The Amber stop codon is represented by *. Mutations are indicated by a black box, those found more than once are indicated by an additional number.*

The isolated and sequenced clones were expressed at 2 mL scale and purified by Ni-NTA spin-columns. Fluorescence emission ratios were measured before and after addition of 200 nM anti-P17 antibody, allowing each sensor's DR to be calculated. Protein concentrations were estimated based on the fluorescence intensity of directly excited acceptor. These concentrations were found to range from less than 10 nM to around 350 nM (Figure 6.6A). When bacterially expressed CitAbsCer (see next section for details on this construct) was measured under the same conditions, a decrease in dynamic range was observed below 48 nM (Figure 6.6A). At very low concentrations

of FRET sensor protein, the larger relative contribution of background fluorescence signal likely interferes with the assay. Further analysis was therefore limited to those proteins that happened to be between 40 and 250 nM (to avoid the need to add large amounts of expensive antibody) after purification (Figure 6.6B). Promisingly, the assay appears to be reproducible, as seen by the similarity in ratiometric response obtained for the pairs of W1L, I4T, I4F and I4V mutants. Although library coverage is limited (19%), it is tempting to draw the preliminary conclusion that position I4 in the epitope is more tolerant of mutagenesis than are positions R5, L6 and R7. Position I4's apparent tolerance might be explained by this residue's position in the P17 immunogen, where it is buried in the protein core and not exposed to the surface (22). Hence, it seems likely the residue plays no role in antibody binding. Interestingly, out of 6 residues tested, proline was the only mutation of I4 that negatively affected anti-P17 binding.

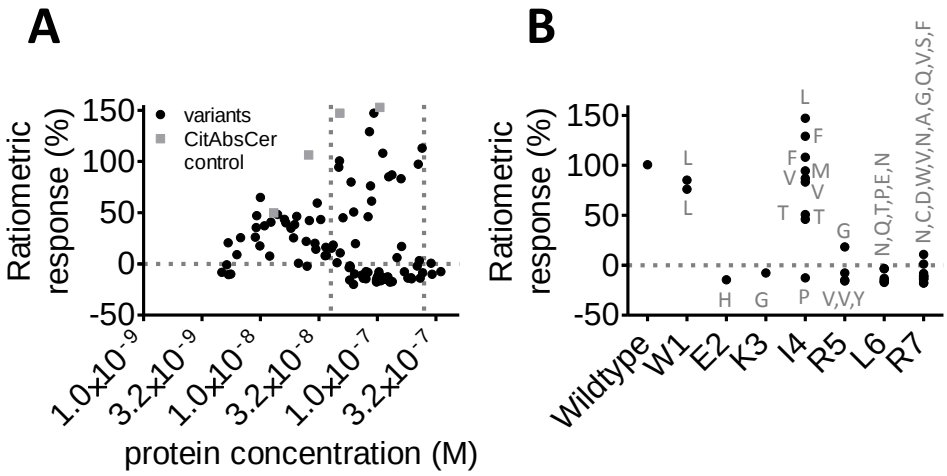

Figure 6.6: ***Cit*Abs*Cer variants' response to antibody addition.*** *(A) Variants' ratiometric response to addition of 0.2 μM anti-P17 addition is plotted as a function of their concentration measured through direct excitation of the Citrine acceptor. The ratiometric response of bacterially expressed and purified CitAbsCer (see next section for details on this construct) was also monitored at several concentrations. The upper (250 nM) and lower (40 nM) limits of detection are indicated by dashed lines. (B) Overview of the ratiometric response resulting from different mutations. Only those values measured for proteins that were between 40 and 250 nM in concentration are displayed, together with the corresponding mutation.*

Optimization of IVTT reaction conditions to allow microfluidic screening of sensor variants

After the successful construction of Cit*Abs*Cer libraries with random but identical epitope sequences, the next step was to develop a high throughput screening technique. Microfluidic screening typically requires *in vitro* transcription translation (IVTT). Here the steps involved in optimizing IVTT are described. First, a 25 µL IVTT reaction was setup with a commercially available, *E. coli*-based IVTT preparation using a saturating concentration (3.3 nM) of template DNA, encoding CerAbsCit, which displayed a DR of around 800% as purified protein (3). After incubation of the reaction at 30 °C overnight, the fluorescence emission spectrum of the IVTT mix was measured (Figure 6.7A). The emission ratio of around 2 was much lower than the ratio ~11 that was previously measured with purified CerAbsCit (3). To assess whether the IVTT-produced CerAbsCit was still functional as a FRET sensor, a titration with anti-P17 antibody was carried out on a 100-fold dilution of the IVTT reaction (Figure 6.7B). As expected, the sensor displayed a decreasing emission ratio with increasing antibody concentration, displaying an EC_{50} of ~30 nM, in the same range as measured with purified CerAbsCit (3). However, in contrast to the large response previously determined for purified CerAbsCit, a much smaller DR of 57% was measured for the IVTT-produced CerAbsCit. Such a small response to antibody would hamper the screening effort, prompting us to consider strategies to improve the DR of the IVTT-produced sensor. Premature termination of translation might lead to an excess of N-terminal truncation products, carrying the Cerulean donor, but not the Citrine acceptor, leading to a low emission ratio and thus a poor DR. We reasoned that by switching the acceptor to the N-terminus and the donor to the C-terminus, the premature truncation of translation should no longer interfere with the apparent sensor response, as Citrine-bearing fragments would not produce fluorescence in response to the ~420 nm excitation light. Using the previously described CPEC cloning technique (Chapter 3), a sensor was constructed in which Citrine was at the N-terminus and Cerulean at the C-terminus. The sensor also had an extended version of P17-derived epitopes (ELDWEKIRLP) (*2*), and is referred to as CitAbsCer (for sequence, see Figure 6.10 in

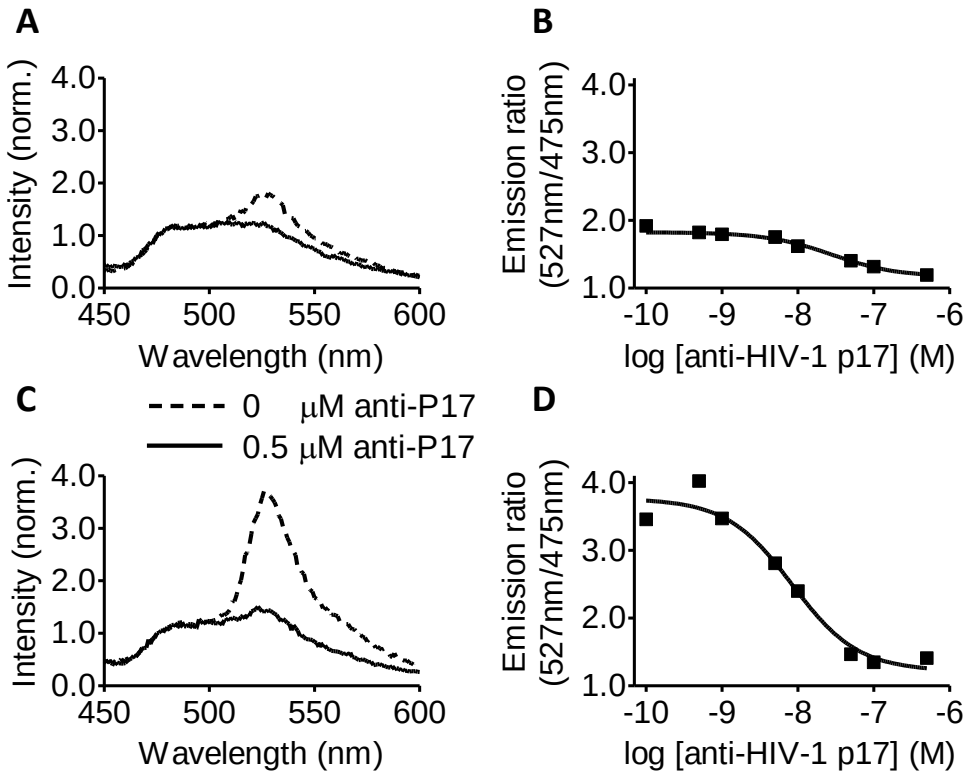

Figure 6.7: Placement of acceptor at N-terminus improves the dynamic range of an IVTT-produced FRET sensor for the anti-P17 antibody. *(A, C) Fluorescence emission spectra for IVTT-produced CerAbsCit (A) or CitAbsCer (C) were measured before and after addition of 0.5 μM anti-P17 antibody. (B, D) The fluorescence emission ratio of CerAbsCit (B) or CitAbsCer (D) was followed as a function of anti-P17 antibody concentration. Measurements were performed on 50 μL of a 100-fold dilution of overnight IVTT reactions in 50 mM Tris-HCl (pH 8), 100 mM NaCl, using a Tecan fluorescence plate reader. Excitation wavelength was set to 420 nm.*

Methods section, note that this construct is distinct from Cit*Abs*Cer discussed in section on DNA library preparation above). Promisingly, CitAbsCer displayed a 2-fold increase in emission ratio to ~4 (Figure 6.7C). Furthermore, titration with anti-P17 antibody resulted in a large reduction of emission ratio, corresponding to a DR of 209% (Figure 6.7D).

To maintain clonality, it is critical that each droplet in an IVC experiment contain no more than a single DNA plasmid. A typical 1 pL droplet formed in an IVC experiment that contains a single plasmid, would have a plasmid concentration of ~2

pM (23), about three orders of magnitude lower that what had been tested in bulk IVTT reactions with CitAbsCer so far. When 2 pM DNA template was used in an IVTT reaction, almost no fluorescence was detected above background levels (Figure 6.8A). It is known that *E. coli* lysate-based IVTT in batch mode expires after 2-3 hours, independent of template concentration (24), so that supplying the reaction with such a low concentration of DNA would lead to essentially no detectable fluorescence. PCR has been reported to be a suitable technique to increase the DNA concentration in the droplet prior to IVTT (25). However, despite extensive testing of different primer combinations, thermostable DNA polymerases and cycling conditions, emission ratios measured for IVTT programmed with PCR-amplified CitAbsCer template were consistently low, indicating that the protein that was expressed was of poor quality (Figure 6.8A). This was most likely caused by the poor quality of the DNA template produced by the PCR rather than inhibition of IVTT by PCR reagents; spiking of IVTT reactions programmed with high concentration plasmid DNA with up to 16% (v/v) of 4 different PCR buffers did not significantly affect the reactions in terms of fluorescence emission spectra (not shown). An alternative approach to DNA amplification is the use of hyperbranched rolling circle amplification (HBRCA). In this isothermal DNA amplification technique, the DNA polymerase phi29 extends random hexameric RNA primers that bind at random sites on the original template as well on newly synthesized strands, resulting in a hyperbranched DNA strand structure (26). Importantly, phi29 has a low error rate and is hyperprocessive, capable of extending for up to 70,000 nucleotides (27). Furthermore, it was shown that the technique is compatible with the microfluidics platform (28). Promisingly, amplification of 2.5 pM CitAbsCer plasmid DNA using a commercially available HBRCA kit resulted in a smear of high molecular weight DNA that migrated at a much slower rate than a 10 kbp marker in gel electrophoretic analysis (Figure 6.7B, lane 1). Treatment of this DNA with Bpu10I, a restriction enzyme that recognizes a site occuring twice per plasmid, resulted in the expected 2113 bp and 5146 bp fragments (Figure 6.8B, lane 2), confirming the high molecular weight DNA mainly consisted of concatemerized plasmid. When raw

HBRCA-amplified CitAbsCer DNA was used as a template in IVTT, FRET sensor protein was produced that displayed the same emission ratio as seen when IVTT was

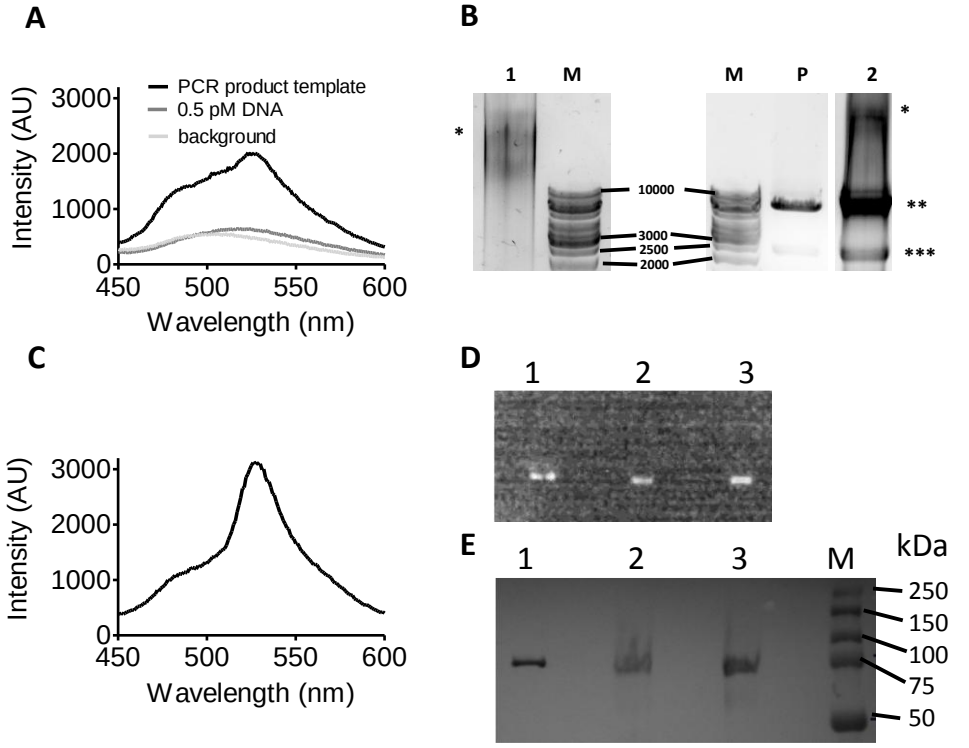

Figure 6.8: Optimization of IVTT for low starting concentration of DNA template. *(A) Fluorescence emission spectra of 25 µL IVTT reactions templated with either 0.5 pM unamplified DNA or PCR amplified DNA were measured using a plate reader. The background spectrum was measured on the PCR product–templated sample before incubation. (B) Agarose gel electrophoretic analysis of DNA (starting concentration 2.5 pM) amplified by HBRCA. Amplified DNA ran as a high molecular weight smear (lane 1, marked by *) while amplified DNA treated with Bpu10I displayed the expected 5146 (**) and 2113 (***) bp fragments (lane 2). Restriction of plasmid DNA, serving as control, resulted in the same restriction fragments, together with remaining, unrestricted DNA (lane P). (C) Fluorescence emission spectrum of 25 µL IVTT reaction templated with 7 µL of the same raw HBRCA reaction analyzed in (B). (D) SDS-PAGE with unboiled samples imaged by in-gel fluorescence, with prepurified CitAbsCer protein (lane 1), CitAbsCer that was made by IVTT programmed with HBRCA-made DNA (lane 2), CitAbsCer that was made by IVTT programmed with 3 nM plasmid DNA (lane 3). (E) Anti-GFP Western blot of SDS-PAGE with the boiled equivalents of the samples in (D). Protein marker (lane M) band sizes are indicated (kDa).*

programmed with a saturating concentration of plasmid DNA (Figure 6.8C). SDS-PAGE analysis of the CitAbsCer made with IVTT that had been programmed with DNA amplified by HBRCA, confirmed the protein to be of the correct size (Figure 6.8D, E). Mixing the components for DNA amplification with those needed for IVTT would simplify the microfluidics protocol, requiring one droplet fusion step less. Unfortunately, mixing IVTT with RCA and diluted DNA did not lead to production of detectable fluorescent antibody sensor (not shown). Therefore, HBRCA should be carried out in droplets separately, prior to fusion with IVTT containing droplets. The IVTT reaction was found to be less sensitive to HBRCA, tolerating a ratio of at least 3:2 HBRCA:IVTT, the highest fraction of HBRCA tested (not shown).

In the course of establishing the optimal conditions for IVTT, it was noticed that the CitAbsCer DR was lower when the IVTT reaction was not first diluted. To further investigate this phenomenon, purified solutions of 100 nM CitAbsCer were spiked with increasing amounts of IVTT mix. In the absence of IVTT, the sensor responded to antibody addition with a switch in emission ratio from ~4 to ~1.5, representing a DR of ~170%, as expected (Figure 6.9A). However, when increasing amounts of IVTT reaction were present, antibody addition led to only a temporary lowering in emission ratio, with the emission ratio then returning to a higher level. The rate at which the ratio increased following the temporary decrease after antibody addition appeared to depend on the amount of IVTT mix present (Figure 6.9A). The reducing environment of the IVTT mix may have a destabilizing effect on the antibody, perhaps by affecting its disulfide linkages (29, 30). Indeed, addition of 1 mM DTT resulted in a similar effect, with the CitAbsCer emission ratio attaining a higher level after anti-P17 addition (Figure 6.9B). The final emission ratio reached in the presence of IVTT mix or DTT was still lower than the emission ratio in the absence of antibody. The same final emission ratio was achieved, no matter whether 0.5 or 10 mM DTT was present (not shown). This indicates that reducing agents subtly alter the conformation of the antibody rather than completely cleaving it. By adding 10 mM of the sulfhydryl-reactive alkylating agent iodoacetamide, the DTT-mediated effect could be completely

prevented (Figure 6.9B). Similarly, addition of 10 mM iodoacetamide to IVTT completely eliminated the emission-increasing effect of IVTT (Figure 6.9C).

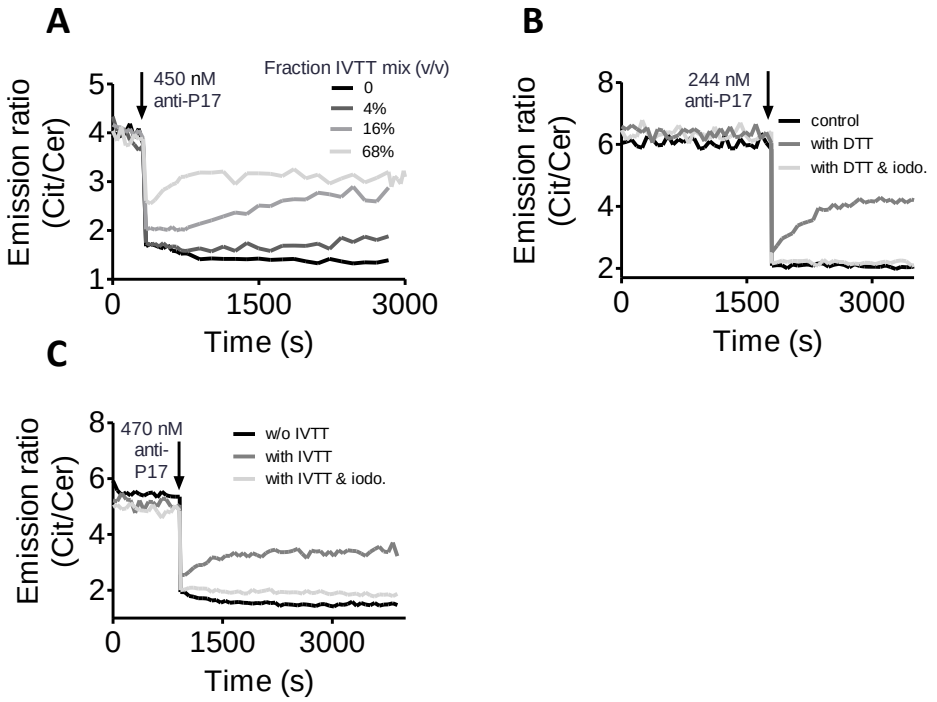

Figure 6.9: DTT in IVTT dampens the response of antibody FRET sensor. *(A) The fluorescence emission ratio of different CitAbsCer solutions (25 µL) that had been spiked with different fractions of IVTT reaction mix were monitored as a function of time. At the indicated point in time, 450 nM anti-P17 antibody was added. (B) Fluorescence emission ratio over time in absence or presence of 1 mM DTT. At the indicated point in time, either 244 nM anti-P17 or antibody in combination with 10 mM iodoacetamide was added. (C) Fluorescence emission ratio over time in absence or presence of a 20% (v/v) fraction of EasyXpress. At the indicated point in time, either 470 nM anti-P17 or antibody in combination with 10 mM iodoacetamide was added. Measurements were performed in a Tecan plate reader, using a 384-well plate. CitAbsCer protein concentration was at 100 nM. Buffer consisted of 50 mM Tris-HCl (pH 8), 100 mM NaCl, 1 mg/mL BSA.*

Discussion

Genetically encoded FRET sensor libraries provide an attractive new platform for epitope mapping and antibody sensor development based on directed evolution. The

work presented here takes two important steps towards reaching this goal, namely i) developing a novel cloning technique allowing the creation of a DNA library encoding two identical epitopes, appropriately spaced within a single protein molecule for antibody binding; ii) developing a suitable means of expressing protein variants for high throughput detection of improved epitopes.

The library cloning strategy presented here is partially based on the 1995 work by Fire & Xu (19) that showed that small DNA circles could be amplified to produce tandem repeats of the circle has so far mainly found use in the detection of clinically relevant DNA. Here it is shown that rolling circle amplification is also useful for the construction of a tandem repeat of randomized epitope sequence. A crucial feature of the design is the formation of a unique restriction site at the point of circularization. This allowed precise insertion of DNA encoding a linker necessary for the epitopes to bridge the distance between the antibody's paratopes. As a first proof of principle of the technique, a small library was created with a single mutation per epitope. Note that had the library not been specifically designed to maintain identity between both epitopes, its total theoretical size would have been 21609, 99.4% of which would have consisted of variants lacking the desired exact repeats, rendering the selection process far more arduous.

To improve library size and quality, several measures could be taken. First, oligo starting material should be prepared to the highest purity, preferably by PAGE, to prevent single nt deletions which result in frame-shifted, non-functional library members. Second, steps should be taken to ensure oligos are used in equal proportions, in order to prevent any oligo from making a dominant contribution, reducing library diversity. Third, in the course of preparing the library it was discovered that PCR amplification of repeat-bearing fragments had a detrimental effect on the number of true repeat sequences, with PCR seemingly associated with increased, undesirable "recombination" between epitopes of different molecules (not shown). Every cycle in PCR is known to result in a significant number of incompletely extended strands (31, 32). Following denaturation, incompletely extended strands might well reanneal to a noncognate complementary strand. Extension of the strand would lead to that strand –

and all subsequent copies of it- carrying two different epitopes. PCR therefore must be avoided wherever possible, although it is integral to the rolling circle amplification method. Note that the relatively short size (3 bp) of randomized DNA used in this case likely contributed to miss-annealing. Future applications will likely employ larger diversity; the longer stretches of randomized DNA would be expected to suppress recombination.

In parallel to the creation of a Cit*Abs*Cer DNA library discussed above, preliminary steps were taken to allow the library to be screened by a high throughput technique such as chip-based microdroplet screening. Here it was shown that i) it is feasible to produce sufficient sensor by IVTT to allow robust detection; ii) plasmid DNA could be amplified from a low concentration using the HBRCA technique; iii) CitAbsCer response to anti-P17 in IVTT could be monitored as long as iodoacetamide was present to prevent reduction of antibody. Unfortunately, due to time restrictions, we were unable to conduct preliminary microfluidics experiments. Screening would likely have entailed the following steps: i) mixing dilute plasmid solution with HBRCA at 4 °C, followed by emulsification; ii) incubation of emulsion at 30 °C for 1 hour; iii) injection of emulsion into microfluidic chip and fusion of droplets with IVTT-containing droplets; iv) incubation of emulsion at 30 °C overnight; v) injection of droplets into chip; vi) sorting of droplets with high FRET signal; vii) reinjection of droplets into chip and fusion with antibody containing droplets; viii) fluorescence sorting of droplets based on low FRET signal; ix) recovery and sequencing of DNA from sorted droplets. From this description of an envisioned microfluidics experiment, the complexity of the operation becomes apparent. Indeed, to the best of our knowledge, there are just a limited number of reports in the literature of successful directed evolution experiments using microfluidics IVC technology (14-18) that do not make use of the more convenient but restrictive exploitation of DNA binding, manipulation or amplification by the protein of interest (33-37). Therefore, although microfluidics holds great promise due to reduced costs, the technology is still in its infancy. As an alternative to microfluidics, fluorescence activated cell sorting (FACS) is a relatively mature technology. A recently described strategy uses microfluidics for

droplet manipulation but harnesses the power of FACS for droplet sorting (38). Before sorting, droplets are converted to double emulsions dispersed in an aqueous carrier phase, rendering the droplets compatible with the FACS machine's sheath fluid. Another strategy similarly exploits the power of flow cytometry for the selection of binders by first immobilizing both encoding DNA and protein of interest on beads in droplets (39). Either of these strategies would simplify the final screening and sorting step of large antibody sensor libraries produced using the procedures outlined in this chapter.

Methods

Cloning of individual constructs. To create a version of CerAbsCit in which the order of the donor and acceptor fluorescent domain was reversed (CitAbsCer), a CPEC-based (40) strategy was used. Four different PCR fragments, citrine, linker, cerulean and opened pET28a vector were produced with primers designed to introduce mutual overlap in sequence, each with a melting temperature of ~70 °C. The sequences of the primers used to generate these PCR fragments are summarized in Table 6.1. The linker fragment, which included two copies of the HIV-1 anti-P17 epitopes (ELDRWEKIRLRP), was obtained by using a plasmid template ("Split-beta lactamase" used in an unrelated project in our group), while the fluorescent domain sequences were produced using another plasmid from an unrelated project. Note that in this latter template, the DNA sequences for both fluorescent domains were designed to be as divergent as possible, allowing design of primers that bind with maximal specificity and that both fluorescent domains contained both the S208F and V224L hydrophobic surface mutations. PCR fragments were purified by silica spin column (Qiaquick PCR Purification Kit, Qiagen) and then combined in a standard Phusion polymerase reaction (without primers), with 200 ng of the vector fragment and equimolar amounts of the other fragments. The reaction was subjected to thermocycling, with 30 seconds at 98 °C followed by 30 cycles of [98 °C for 10 seconds, 72 °C for 3 minutes], 72 °C for 10 minutes. Finally, any remaining circular,

Table 6.1: Sequences for primers used in both site-directed mutagenesis (SDM) and CPEC-based cloning strategies in this Chapter.

Primer	Sequence (5'->3')
7CitCer_Vec_F	GACGAACTGTACAAGGGTACCTGGAGCCATCCACAGTT
2CitCer_Vec_R	TCACCATATGGCTGCCGCGCG
1CitCer_Cit_F	GCGGCAGCCATATGGTGAGCAAGGGTGAAGAATTATTC
10CitAbsCer_CitR	CGCCACCACTAGTTTTATATAACTCATCCATGCCTAACGTGATACC
9CitAbsCer_AbsF	CATGGATGAGTTATATAAAACTAGTGGTGGCGAACTGGATCG
12CitAbsCer_AbsR	GAAACCATACCCATGGAACCGCCCG
11CitAbsCer_CerF	GCGGTTCCATGGGTATGGTTTCTAAAGGCGAGGAACTGTTTAC
8CitCer_Cer_R	CTCCAGGTACCCTTGTACAGTTCGTCCATACCCAGGG
BauI_silence_F	GAGAGCGTACGATGGAGCTTCCAGGGGGAAACG
BauI_silence_R	GCTCCATCGTACGCTCTCCTGTTCCGACCC
SacI_ins_F	GAGAAGGAGCTCATGGTTTCTAAAGGCGAGGAACTGTTTA
SacI_ins_R	AGAAACCATGAGCTCCTTCTCCCAACGATCTAACTCACCTCC

methylated plasmid templates were removed by incubating the reaction mixture with DpnI (FastDigest, Fermentas) for 10 minutes at 37 °C. The final sequence for the ORF is shown is Figure 6.10. For the identical random repeat cloning strategy, a CitAbsCer-based acceptor vector was required in which to insert the SpeI/SacI-flanked single repeat. SpeI was already present between Citrine and the linker fragment. A SacI recognition site was introduced by site directed mutagenesis behind the second epitope and just before Cerulean, using primers Sac_ins_F and Sac_ins_R using a previously described technique (43). An undesired BauI (a.k.a. BssSI) site in the pET28a backbone was then destroyed using the same technique and primers BauI_silence_F and BauI_silence_R

MGSSHHHHHHSSGLVPRGSH**MVSKGEELFTGVVPILVELDGDVNGHKFSVSGEGEGDATY** 60
GKLTLKFICTTGKLPVPWPTLVTTFGYGLMCFARYPDHMKQHDFFKSAMPEGYVQERTIF 120
FKDDGNYKTRAEVKFEGDTLVNRIELKGIDFKEDGNILGHKLEYNYNSHNVYIMADKQKN 180
GIKVNFKIRHNIEDGSVQLADHYQQNTPIGDGPVLLPDNHYLSYQSALFKDPNEKRDHMV 240
LLEFLTAAGITLGMDELYKTSGGELDRWEKIRLRPGGSGGSGGGSGGSGAEAAAKEAAAK 300
EAAAKEAAAKEAAAKEAAAKAGSGGSGGSGGPQGILGQGSGGSGGSGGSGAEAAAKEAAA 360
KEAAAKEAAAKEAAAKEAAAKAGSGGSGGSGGSGGSGGSGGELDRWEKIRLRPGGSMG**MV** 420
SKGEELFTGVVPILVELDGDVNGHKFSVSGEGEGDATYGKLTLKFICTTGKLPVPWPTLV 480
TTLTWGVQCFARYPDHMKQHDFFKSAMPEGYVQERTIFFKDDGNYKTRAEVKFEGDTLVN 540
RIELKGIDFKEDGNILGHKLEYNAISDNVYITADKQKNGIKANFKIRHNIEDGSVQLADH 600
YQQNTPIGDGPVLLPDNHYLSTQSALFKDPNEKRDHMVLLEFLTAAGITLGMDELYKGTW 660
SHPQFEK- 720

Figure 6.10: Amino acid sequence of CitAbsCer. *The N-terminal poly-His tag is followed by Citrine (S208F/V224L) (in bold), the linker, including the p17 –derived epitopes (underlined) and Cerulean (S208F/V224L) (in bold), followed by a C-terminal Strep tag II.*

Cit*Abs*Cer library cloning. To circularize oligos (listed in Table 6.2), a Circligase II (Epibio, USA) reaction was carried out following the manufacturer's standard reaction conditions (71 nM of each of the 7 different input oligos, 1x Circligase II reaction buffer, 2.5 mM $MnCl_2$, 100 units Circligase II, in a 20 µL reaction volume). The reaction was incubated for 1 hour at 60 °C, followed by inactivation of the enzyme by heating to 80 °C for 10 minutes. All rolling circle and PCR reactions were carried out using Phusion DNA polymerase. Rolling circle amplification reactions consisted of 10 pmol of both primers, 1 µL of the unpurified Circligase reaction, 2 units Phusion DNA polymerase, 200 µM of each dNTP, in a total volume of 50 µL. Cycling conditions were 98 °C for 30 seconds, 30 cycles of [98 °C for 10 seconds, 60 °C for 10 seconds, 72 °C for 15 seconds], 72 °C for 5 minutes. Prior to loading DNA on agarose gel, the rolling circle amplification products were heated to 95 °C for 5 minutes, then slowly cooled to room temperature at a rate of 0.5 °C every 20 seconds. This latter step was found to be essential in ensuring correct hybridization of strands of identical length. To purify DNA from agarose gels, the Qiaquick Gel Extraction Kit (Qiagen) was used. To increase the quantity of available single repeat fragment, it was amplified with primers 3 and 4 using a thermocycle programme consisting of incubation at 98 °C for 30 seconds, followed by 30 cycles of 98 °C for 10 seconds and 72 °C for 10 seconds, followed by incubation at 72 °C for 5 minutes. The resulting PCR fragment was purified by silica spin column (Qiaquick, Qiagen). Acceptor vector and purified single repeat insert were restricted with 20 units SpeI-HF and SacI at 37 °C in NEB buffer 4 with 0.1 mg/mL BSA. Cleaved acceptor vector DNA was purified by agarose gel electrophoresis followed by gel extraction. Cleaved single insert DNA was purified by silica spin column. DNA ligation was carried out with 400 units of T4 ligase (NEB), 50 ng vector DNA, at 1:5 vector:insert molar ratio, in 1x concentrated T4 ligase buffer, in 20 µL volume. The ligation was transformed to *E. coli* NovaBlue and directly grown up as 5 mL liquid LB culture. To prepare single repeat-bearing plasmids for ligation with linker, 4.3 µg single repeat-bearing plasmid library was first treated with 40 units of BauI (Thermo) for 16 hours at 37 °C in a 100 µL volume. Linearized plasmid was separated from remaining circular plasmid by gel

electrophoresis. Meanwhile, BsaI-flanked linker DNA was prepared by PCR using primers linker_BsaI_F and linker_BsaI_R with pET28a-CitAbsCer as template. The resulting PCR product (2.4 µg) was restricted using 40 units of BsaI at 37 °C for 8 hours in a 30 µL volume. Next a 5 µL ligation was carried out with 100 units of T4 ligase, 55 ng linear vector and 12 ng insert (i.e. a 1:4 vector:insert molar ratio), in BauI restriction buffer with 1 mM of added ATP. BauI (2.5 units) was also present in this reaction to restrict self-ligated vector. The reaction was cycled between 30 minutes at 37 °C (for maximal BauI activity, restricting self-ligated vector) and 30 minutes at 16 °C (for maximal ligase activity) for approx. 16 hours and then used to transform *E. coli* DH5G by electroporation. All colony PCR reactions were carried out using Kapa2G DNA polymerase (Kapa Biosystems, USA), using primers Cit_F208S_F and Oppa_Vec_R, with cycling conditions 95 °C for 30 seconds, followed by 30 cycles of [95 °C for 10 seconds, 60 °C for 10 seconds, 72 °C for 30 seconds].

Table 6.2: Oligonucleotides used in the creation of the identical random repeat library.

Oligo	Sequence (5'-->3')
NNK_W1_Bau1	PHO-GAGACTGGAGCAACGNNKGAAAAGATAAGGTTGAGGGGCACCGCAACTCAC
NNK_E2_BauI	PHO-GAGACTGGAGCAACGTGGNNKAAGATAAGGTTGAGGGGCACCGCAACTCAC
NNK_K3_BauI	PHO-GAGACTGGAGCAACGTGGGAANNKATAAGGTTGAGGGGCACCGCAACTCAC
NNK_I4_BauI	PHO-GAGACTGGAGCAACGTGGGAAAAGNNKAGGTTGAGGGGCACCGCAACTCAC
NNK_R5_BauI	PHO-GAGACTGGAGCAACGTGGGAAAAGATANNKTTGAGGGGCACCGCAACTCAC
NNK_L6_BauI	PHO-GAGACTGGAGCAACGTGGGAAAAGATAAGGNNKAGGGGCACCGCAACTCAC
NNK_R7_BauI	PHO-GAGACTGGAGCAACGTGGGAAAAGATAAGGTTGNNKGGCACCGCAACTCAC
Primer 1	GTTCCTCGCCTTTGGACACCATGAGCTCACCGTGAGTTGCGGTGCC
Primer 2	GGCATGGACGAGCTGTACAAGACTAGTGAGACTGGAGCAACG
Primer 3	GGCATGGACGAGCTGTACAAGACTAGT
Primer 4	GTTCCTCGCCTTTGGACACCAT
linker_BsaI_F	ATATAATAGGTCTCTACGATGGTGGAAGTGGGGGCAG
linker_BsaI_R	ATTTAAGGTCTCATCGTATAACTCACCTCCGGAACCG
Cit_F208S_F	CAGAGTGCGTTAAGTAAGGATCCTAATGAAAAGCGTGACC
Oppa_Vec_R	GTAAACAGTTCCTCGCCTTTAGAAAC

At positions indicated with NNK, the wild-type codon (coding for W, E, K, I, R, L or R) was replaced with a random incorporation of A, C, G or T ("N") in the first two positions of the codon and a random incorporation of G or T only ("K") at the third position of the codon. The 5'-phosphorylation of the Circligase templates, essential for the intramolecular ligation, is indicated with "PHO".

96-well scale Cit*Abs*Cer protein expression and characterization. *E. coli* BL21(DE3) was transformed with the DNA library and plated on LB agar medium containing 30 µg/mL kanamycin. Individual colonies were picked and transferred to 15 µL water in a 96-well plate. Colony PCR reactions were performed in a 96-well PCR

plate using 1 µL of the colony suspension. The colony PCR reactions were subsequently treated with a cocktail of Exonuclease III and alkaline phosphatase (ExosapIT) to remove primers and unincorporated dNTPs. These enzymes were heat inactivated (10 minutes at 80 °C) and the 96-well plate was submitted for sequencing (Baseclear, Netherlands). The same colony suspensions used for colony PCR were used to inoculate cultures in a 96-deep well plate containing 2 mL LB with 30 µg/mL kanamycin and 0.1 mM IPTG. The plate was sealed with foil and incubated with shaking at 37 °C overnight. Cells were harvested by centrifugation of the plate at 3000 RPM for 10 minutes and the supernatant was discarded. Next 100 µL Bugbuster (Novagen) and 1 µL Benzonase (Novagen) were added to each well and the plate was incubated at room temperature for 20 minutes, with shaking. The unclarified cell lysate was mixed with 100 µL binding buffer (0.5 M NaCl, 40 mM Tris-HCl (pH 8), 5 mM imidazole) and transferred to a 96-well plate containing Ni-NTA resin (HisPur, Thermo Scientific). After centrifugation, 250 µL of 1x binding buffer was loaded on the wells and the plate was spun again. Subsequently, 250 µL of washing buffer (0.5 M NaCl, 20 mM Tris-HCl (pH 8), 40 mM imidazole) was applied to the wells, a step that was repeated twice. Finally, protein was eluted with 250 µL elution buffer (0.5 M NaCl, 20 mM Tris-HCl (pH 8), 0.4 M imidazole). 50 µL of the Ni-NTA eluate was transferred to a 384-well plate for fluorescence measurements.

Fluorescence spectroscopy. Measurements were performed using a Tecan fluorescence plate reader, with 384-well plates. Unless mentioned otherwise, measurement buffer consisted of 50 mM Tris-HCl (pH 8), 100 mM NaCl and 1 mg/mL BSA. Fluorescence emission ratios were then determined by exciting at 420 nm and measuring either full emission spectra or the emission at 475 nm (Cerulean) and 527 nm (Citrine) only. To detect Citrine directly, it was excited at 490 nm and its emission was measured at 530 nm. Comparing measured values to values determined for a serial dilution of CitAbsCer of known concentration gave a good indication of protein concentration.

***In vitro* transcription/translation.** *In vitro* transcription/translation was carried out with an *E coli* lysate-based commercial preparation (EasyXpress, Qiagen), following

the manufacturer's instructions at either 50 or 25 μL scale. Care was taken to avoid RNase contamination of reactions. Expression was carried out in 384-well plates, covered with transparent adhesive film, overnight at 30 °C. Reactions were typically monitored continuously using a Tecan fluorescence plate reader.

Amplification of DNA prior to IVTT. Initial attempts to use PCR to amplify templates for IVTT all failed. Attempts included use of a commercially available kit specifically designed to allow amplification of DNA prior to IVTT (EasyXpress Linear Template Kit Plus, Qiagen). To amplify DNA using HBRCA, a commercial kit was used (Illustra GenomiPhi v2, GE) and the manufacturer's instructions were followed.

Acknowledgements

I am grateful to prof.dr. Wilhelm Huck (Radboud University Nijmegen) for many useful suggestions and comments concerning this project prof. Huck's colleagues at RU were also most helpful, in particular dr. Aigars Piruska and Kate Sokolova. Martijn van Rosmalen first suggested the use of CerAbsCit as a target for directed evolution.

References

1. Brennan CA, Christianson K, La Fleur MA, & Mandecki W (1995) *Proc Natl Acad Sci U S A* **92,** 5783-5787.
2. Banala S AS, Schalk W, Merkx M (2013) *ACS Chem Biol* **8,** 2127-2132.
3. Golynskiy MV, Rurup WF, & Merkx M (2010) *ChemBioChem* **11,** 2264-2267.
4. Tang ZM, *et al.* (2013) *Transpl Immunol* **29,** 39-42.
5. Huang J, *et al.* (2012) *Nature* **491,** 406-412.
6. McCoy LE & Weiss RA (2013) *J Exp Med* **210,** 209-223.
7. Buhrman JD, *et al.* (2013) *J Biol Chem* **288,** 33213-33225.
8. Janssen BMG, *et al.* (2013) *Chem Sci* **4,** 1442-1450.
9. Schumaker VN, Green G, & Wilder RL (1973) *Immunochemistry* **10,** 521-528.
10. Bastings MM, *et al.* (2011) *J Am Chem Soc* **133,** 6636-6641.
11. Matochko WL, Cory Li S, Tang SK, & Derda R (2013) *Nucleic Acids Res* **10.1093/nar/gkt1104**.
12. Seo JS, Lee S, & Poulter CD (2013) *J Am Chem Soc* **135,** 8973-8980.
13. Theberge AB, *et al.* (2010) *Angew Chem Int Ed Engl* **49,** 5846-5868.
14. Mastrobattista E, *et al.* (2005) *Chem Biol* **12,** 1291-1300.
15. Kintses B, *et al.* (2012) *Chem Biol* **19,** 1001-1009.
16. Agresti JJ, *et al.* (2010) *Proc Natl Acad Sci U S A* **107,** 4004-4009.
17. Griffiths AD & Tawfik DS (2003) *EMBO J* **22,** 24-35.

18. Aharoni A, *et al.* (2005) *Chem Biol* **12,** 1281-1289.
19. Fire A & Xu SQ (1995) *Proc Natl Acad Sci U S A* **92,** 4641-4645.
20. Amiram M, Quiroz FG, Callahan DJ, & Chilkoti A (2011) *Nat Mater* **10,** 141-148.
21. Blondal T, *et al.* (2005) *Nucleic Acids Res* **33,** 135-142.
22. Matthews S, *et al.* (1995) *Biochem Soc Trans* **23,** 725-729.
23. Courtois F, *et al.* (2008) *ChemBioChem* **9,** 439-446.
24. Stogbauer T, Windhager L, Zimmer R, & Radler JO (2012) *Integr Biol (Camb)* **4,** 494-501.
25. Fallah-Araghi A, Baret JC, Ryckelynck M, & Griffiths AD (2012) *Lab Chip* **12,** 882-891.
26. Dean FB, Nelson JR, Giesler TL, & Lasken RS (2001) *Genome Res* **11,** 1095-1099.
27. Blanco L, *et al.* (1989) *J Biol Chem* **264,** 8935-8940.
28. Mazutis L, *et al.* (2009) *Anal Chem* **81,** 4813-4821.
29. Liu H & May K (2012) *MAbs* **4,** 17-23.
30. Okuno T & Kondelis N (1978) *J Clin Pathol* **31,** 1152-1155.
31. Klock HE, Koesema EJ, Knuth MW, & Lesley SA (2008) *Proteins* **71,** 982-994.
32. Li MZ & Elledge SJ (2007) *Nat Methods* **4,** 251-256.
33. Skirgaila R, *et al.* (2013) *Protein Eng Des Sel* **26,** 453-461.
34. Ellefson JW, *et al.* (2014) *Nat Biotechnol* **32,** 97-101.
35. Tay Y, Ho C, Droge P, & Ghadessy FJ (2010) *Nucleic Acids Res* **38,** e25.
36. Fen CX, Coomber DW, Lane DP, & Ghadessy FJ (2007) *J Mol Biol* **371,** 1238-1248.
37. Levy M & Ellington AD (2008) *Chem Biol* **15,** 979-989.
38. Lim SW & Abate AR (2013) *Lab Chip* **13,** 4563-4572.
39. Diamante L, Gatti-Lafranconi P, Schaerli Y, & Hollfelder F (2013) *Protein Eng Des Sel* **26,** 713-724.
40. Quan J & Tian J (2009) *PLoS One* **4,** e6441.

Appendix: Effect of bleedthrough, emission spectrum width and acceptor quantum yield on FRET sensors' dynamic range

What makes for a good FRET pair? This depends partly on the method of detection of changes in FRET. Absolute changes in FRET efficiency (E) can be determined by monitoring the donor's fluorescence life time. However, a more common approach is to indirectly observe changes in E through changes in donor to acceptor emission ratio, a method also known as Sensitized Emission (SE). In the absence of bleedthrough, such an emission ratio (R) may be defined using equation A.1,

$$R_x = \frac{I_{A_A} * E_x}{I_{D_D} * (1 - E_x)} \tag{A.1}$$

where I_{A_A} is the acceptor's fluorescence intensity in the acceptor detection channel and I_{D_D} the donor's fluorescence intensity in the donor detection channel and E_x a certain level of FRET efficiency. The donor intensity is multiplied by the factor $(1 - E_x)$ to account for the attenuating effect FRET has on the donor's intensity. The dynamic range (DR) of a FRET sensor is generally (1) defined using equation A.2,

$$DR = \frac{R_2 - R_1}{R_1} \tag{A.2}$$

where the subscripts 2 and 1 represent R resulting from high and low FRET efficiency, respectively. When equations A.1 and A.2 are combined, they can be simplified to equation A.3,

$$DR = \frac{E_2 - E_1}{(1 - E_2)E_1} \tag{A.3}$$

suggesting that the factors I_{A_A} and I_{D_D} have no influence on a FRET pair's performance. However, this is misleading, as equation A.1 fails to take bleedthrough from the donor into the acceptor detection channel into account. Many of the commonly used FRET pairs exhibit such bleedthrough, with bleedthrough from the

donor's emission channel into the acceptor detection channel often much larger than vice versa, due to the typically lop-sided shape of FPs' emission spectra (Figure A.1).

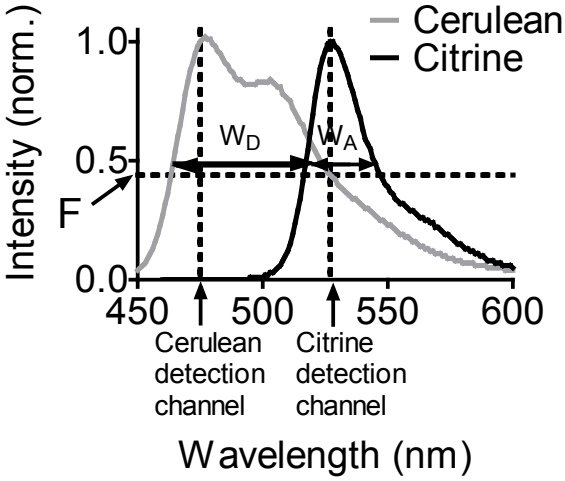

Figure A.1: Emission spectra of Cerulean and Citrine illustrate the bleedthrough that occurs in this FRET pair.

Bleedthrough's effect on emission ratio must be accounted for using equation A.4,

$$R_{x=}\frac{I_{A_A}*E_x+I_{D_A}*(1-E_x)}{I_{D_D}*(1-E_x)} \tag{A.4}$$

where I_{D_A} represents the donor's emission in the acceptor detection channel (i.e. bleedthrough). The donor's bleedthrough intensity always changes in the *opposite* direction to the acceptor's sensitized emission in response to a change in E, thereby attenuating DR. The sum in the numerator shows that increases in the acceptor's fluorescence intensity will improve DR (to a theoretical asymptotic level where bleedthrough is fully compensated for). In order to calculate the dynamic range of a FRET pair under bleedthrough conditions, equation A.4 may be combined with equation A.3, yielding equation A.5:

$$DR = \frac{I_{A_A} * (E_2 - E_1)}{(1 - E_2) * \left(E_1 I_{A_A} - E_1 I_{D_A} + I_{D_A}\right)} \tag{A.5}$$

Equation A.5 shows that in the presence of bleedthrough, the intrinsic fluorescence properties of the donor and acceptor play a role in determining DR. It is therefore

important to take a closer look at the factors making up I_{A_A} and I_{D_A}. Both the acceptor's quantum yield (Φ_A) and the shape of the acceptor's emission spectrum are important determinants for the level of change in I_{A_A} relative to the bleedthrough. A wider emission spectrum results in a relatively smaller change in emission in the detection channel upon a change in FRET. To allow comparisons across FRET acceptors, a rough but reasonable factor is full width at half maximum (FWHM) of the acceptor's emission spectrum (W_A) (equation A.6). Similarly, I_{D_A} is determined by the FWHM of the donor's emission spectrum (W_D), and by the fraction of the donor's emission in the acceptor detection channel, relative to the donor's peak intensity (F) (equation A.7).

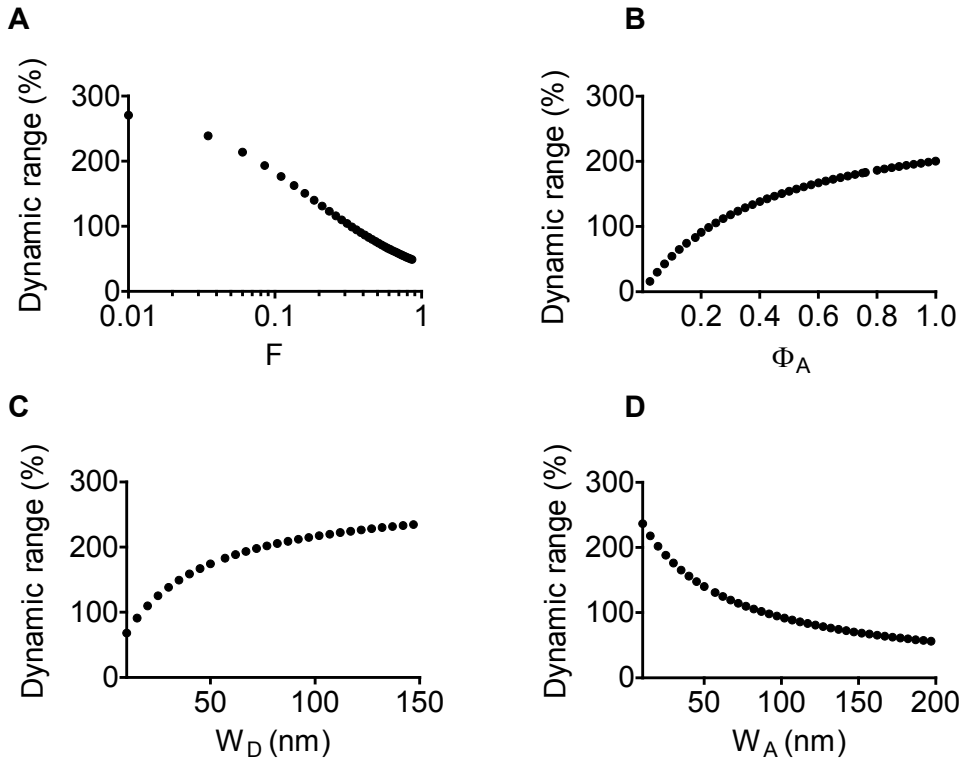

Figure A.2: Effect of varying fluorescence parameters on the theoretical DR of a simulated FRET sensor. *Assumptions were the occurrence of a change in E from 0.1 to 0.3, an F of 0.1, a W_A of 27 nm, a W_D of 57 nm and a Φ_A of 0.76, except that in (A) F was the variable, in (B) Φ_A was the variable, in (C) W_D was the variable and in (D) W_A was the variable. All data were calculated using equation A.8.*

$$I_{A_A} = \frac{\Phi_A}{W_A} \tag{A.6}$$

$$I_{D_A} = \frac{F}{W_D} \tag{A.7}$$

By combining equations A.5, A.6 and A.7, equation A.8 is generated:

$$DR = \frac{\Phi_A W_D (E_2 - E_1)}{(1 - E_2) * (\Phi_A E_1 W_D - F E_1 W_A + F W_A)} \tag{A.8}$$

The effect of varying either F, W_A, W_D or Φ_A is illustrated using plots in Figure A.2 for a simulated FRET sensor that changes in E from 0.1 to 0.3. Direct excitation of the acceptor by light intended for excitation of the donor is sometimes named as a factor negatively affecting the DR of a FRET sensor (2, 3). However, as the fluorescence intensity emitted by the acceptor remains *constant*, both at high E and low E, direct excitation does not directly affect DR and has not been accounted for in this analysis.

It is interesting to compare and contrast the commonly used FRET pairs Cerulean/Citrine and mOrange/mCherry. The mOrange/mCherry FRET pair has an R_0 of 63 Å (4), significantly larger than Cerulean/Citrine's R_0 of 54 Å (5). It is difficult to predict whether the larger R_0 in mOrange/mCherry will lead to larger changes in E as that depends on the absolute change in distance. Indeed, if changes are centered closer to 54 Å, then the Cerulean/Citrine pair will provide a larger change in E than the same absolute change in distance in the mOrange/mCherry pair. Due to the emission bleedthrough in both FRET pairs, several intrinsic properties of the FPs determine to a large extent the maximum achievable DR. Cerulean's bleedthrough into Citrine's emission peak is 0.44 of Cerulean's own peak, while mOrange's bleedthrough into mCherry is 0.37. Cerulean's emission spectrum is wide (W_D = 58 nm), decreasing the relative contribution of bleedthrough, while Citrine's emission spectrum is narrow (W_A = 27 nm), helping to increase changes in intensity in the detection channel upon changes in FRET. In contrast, mOrange has a narrow spectrum (W_D = 38 nm) and mCherry a wide spectrum (W_A = 57 nm), a less favorable situation. Furthermore, Citrine's QY_A of 0.76 (6) is much higher than mCherry's (0.22, (7)). To compare

different FRET pairs, it is useful to consider the theoretical DR that could be achieved if the FRET pair was to undergo a change in FRET efficiency from 0.1 to 0.3 (Table A.1). The orange-red FRET pairs mOrange-mCherry and LSSmOrange-mKate2 are predicted to have a poor dynamic range (Table A.1). This can be explained by the significant bleedthrough from the donor to the acceptor detection channel coupled to a relatively low acceptor quantum yield. FRET pairs based on green and red FPs offer an improved performance due to a reduced level of bleedthrough. The relative performance of some of these FRET pairs is also confirmed by reported experimental results for comparable sensors (protease sensors where FPs flank a short recognition sequence). The mOrange-mCherry DR (40%, (8)) was about twice as poor as the reported value for the LSSmOrange-mKate2 pair (70%, (3)) and almost 10 times worse than the reported value for TagGFP-TagRFP (384%, (9)).

The Clover-mRuby2 pair was recently described as being superior to classic Cerulean-Citrine-based pairs due to an increased R_0 (5). However, the analysis in Table A.1 suggests such improvements may be dampened by the fact that this pair shows poorer properties for sensitized emission FRET. Indeed, when Cerulean-Citrine was

Table A.1: Predicted dynamic range for FRET pairs if these were to undergo a change in E from 0.1 to 0.3.

FRET pair	W_D (nm)	W_A (nm)	Φ_A	F[1]	DR[2]	Reference[3]
mOrange-mCherry	38	57	0.22	0.37	12%	(7), (7)
LSSmOr-mKate2	41	87	0.4	0.19	28%	(3), (10)
mOrange-psmOrange2	38	63	0.38	0.10	57%	(7), (11)
Clover-mRuby2	28	76	0.38	0.06	59%	(5), (5)
mTurquiose2-SYFP2	56	29	0.68	0.37	81%	(12), (13)
Cerulean-Citrine	58	27	0.76	0.44	83%	(14), (6)
TagGFP-TagRFP	33	65	0.48	0.05	99%	(15), (16)
Sirius-LSSmOr	71	41	0.45	0.00	286%	(17), (3)

[1]For simplicity, it is assumed that the acceptor detection channel is centered at the acceptor's peak emission wavelength, although this may not always be the case in practice. [2]DR was calculated using equation A.8. [3]Values used to calculate DR for each FRET pair are obtained from literature, references are given for the donor, followed by the acceptor.

replaced with Clover-mRuby2 in two different FRET sensors, only modest improvements were seen (1.3-fold to 1.7-fold improvement, (5)). The poor QY of most far red RFPs limits their utility as FRET acceptors in SE FRET. A recently reported photoswitchable variant of mOrange, psmOrange2, might make an excellent acceptor – in its far red photoswitched form- to an mOrange as acceptor (11). Not only does this pair have a reasonable R_0 (50 Å), its emission peaks are well-separated, suggesting it would be an outstanding partner to a Cerulean/Citrine pair (Table A.1). Perhaps the highest DR might be achieved by using one of the LSS variants as acceptor to a highly blue-shifted donor FP. For example, a pair comprised of Sirius (ex/em peaks 355 nm/424 nm, (17)) and LSSmOrange (ex/em peaks 437/572 nm) would have an R_0 of 42 Å, and would show no emission bleedthrough whatsoever, rendering it in theory one of the most sensitive FRET pairs of all (Table A.1).

References

1. Campbell RE (2009) *Anal Chem* **81,** 5972-5979.
2. Carlson HJ & Campbell RE (2009) *Curr Opin Biotechnol* **20,** 19-27.
3. Shcherbakova DM*, et al.* (2012) *J Am Chem Soc* **134,** 7913-7923.
4. Goedhart J*, et al.* (2007) *PLoS One* **2,** e1011.
5. Lam AJ*, et al.* (2012) *Nat Methods* **9,** 1005-1012.
6. Griesbeck O*, et al.* (2001) *J Biol Chem* **276,** 29188-29194.
7. Shaner NC*, et al.* (2004) *Nat Biotechnol* **22,** 1567-1572.
8. Ouyang M*, et al.* (2010) *Cancer Res* **70,** 2204-2212.
9. Shcherbo D*, et al.* (2009) *BMC Biotechnol* **9,** 24.
10. Shcherbo D*, et al.* (2009) *Biochem J* **418,** 567-574.
11. Subach OM, Entenberg D, Condeelis JS, & Verkhusha VV (2012) *J Am Chem Soc* **134,** 14789-14799.
12. Goedhart J*, et al.* (2012) *Nat Commun* **3,** 751.
13. Kremers GJ, Goedhart J, van Munster EB, & Gadella TW, Jr. (2006) *Biochemistry* **45,** 6570-6580.
14. Rizzo MA, Springer GH, Granada B, & Piston DW (2004) *Nat Biotechnol* **22,** 445-449.
15. Merzlyak EM*, et al.* (2007) *Nat Methods* **4,** 555-557.
16. Subach OM*, et al.* (2008) *Chem Biol* **15,** 1116-1124.
17. Tomosugi W*, et al.* (2009) *Nat Methods* **6,** 351-353.

Summary

Intracellular genetically encoded fluorescent sensors allow non-invasive imaging of single cells with high spatiotemporal resolution. Many sensors have been developed based on Förster Resonance Energy Transfer (FRET) between two fluorescent proteins (FPs) fused to a recognition domain, where FRET is modulated by a change in the recognition domain's conformation in response to ligand binding. This thesis not only describes the development of new FRET sensors, but also reports generally applicable strategies towards their design.

Chapter 1 of this thesis presents an overview of the intracellular FRET sensors developed so far. FRET sensors employ different architectures and include designs based on single recognition domains or on multiple, intramolecularly interacting domains. Two remaining problems in FRET sensor design are the efficient development of sensors with high dynamic range and of sensors suitable for multiparameter imaging. Strategies such as the modular design of FRET sensors to allow easy exchange of parts, as well as the high throughput screening of many variants are potential solutions to this problem.

In **Chapter 2** the first genetically encoded FRET sensor for Mg^{2+} is reported. The Mg^{2+} ion has important structural, catalytic and regulatory roles in the cell. MagFRET was based on the protein HsCen3, which binds Mg^{2+} with almost the same affinity as it does Ca^{2+}, unlike most EF-hand containing proteins, which typically bind Ca^{2+} much more strongly than they do Mg^{2+}. Importantly, HsCen3 transitions from an extended molten globule to a compact EF-hand-like state upon binding Mg^{2+}. Mutations in the EF-hands of this recognition domain extended the range of concentrations over which Mg^{2+} could be measured. Importantly, in HEK293 cells, MagFRET did not display a ratiometric response to stimuli known to elicit large increases in cytosolic Ca^{2+} concentration. The sensor responded to changes in Mg^{2+} concentration when expressed in the cytosol of cultured mammalian cells that had been rendered permeable by treatment with digitonin. However, in intact cells, MagFRET failed to respond to procedures previously reported to perturb the free Mg^{2+} concentration in the cytosol.

Further research will be required to establish MagFRET's suitability for intracellular measurements of Mg^{2+} homeostasis.

In **Chapter 3** improved red-shifted FRET sensors are reported. A 10-fold improvement in the dynamic range of red-shifted mOrange and mCherry-based protease sensors could be achieved through the manipulation of these FPs' tendency to form dimers. The reversion of certain hydrophobic to hydrophilic mutations originally carried out to convert DsRed, the tetrameric ancestor to mOrange and mCherry, into a monomer was sufficient to generate a self-associating red FRET pair. The strategy could also be applied to other monomeric DsRed derivatives such as LSSmOrange, a long Stokes-shifted variant with a blue-shifted excitation peak. Using fluorescence polarization to monitor homodimerization of mCherry as a function of protein concentration, the K_d for dimerization of two mCherry variants was established. The self-associating red fluorescent domains proved essential for the functioning of a FRET sensor for Zn^{2+}. The large dynamic range afforded by the new red FRET pair allowed simultaneous use of differently colored FRET sensors to image Zn^{2+} over a broad concentration range in the same cellular compartment.

In **Chapter 4**, a comprehensive thermodynamic characterization of the stability of a range of self-associating FRET pairs is reported, both in mOrange/mCherry mutants and in previously report CFP/YFP variants. Urea titrations were used to induce dissociation of the intramolecular complex formed by the fluorescent domains, allowing quantification of its interaction strength. It was found that mutation S208F provided an interactional stability of around 1.6 kCal/mol for the intramolecular dimer formed by the ECFP/EYFP FRET pair, while in the more recently developed Cerulean/Citrine pair it appeared to be significantly weaker (ΔG^0_{o-c} = 0.2 kCal/mol). The technique was also used to determine the stability of mOrange-mCherry intramolecular complexes, including a series of new variants with a range of interaction strengths. The relative stabilities found with the urea-based analysis for mOrange-mCherry were supported by an assay that determined the K_d for mCherry homodimerization by monitoring the amount of homoFRET using fluorescence anisotropy. The effect of the stability of the intramolecular dimer on sensor properties

was tested in a red-shifted FRET sensor for Zn^{2+}. Weaker, subtle interactions seemed to be optimal. Together these findings allow for a better understanding of the subtle effects that determine the performance of existing FRET sensors and help guide the rational design of sensors using modular design strategies.

In **Chapter 5** the newly found self-associating mOrange-mCherry FRET pairs were used to rapidly convert another sensor based on mutually exclusive interactions to a red-shifted probe. The Cerulean and Citrine fluorescent domains in the original FXR-based bile acid sensor BAS-1 were replaced by several different self-associating variants of mOrange and mCherry. It was found that a relatively weak mOrange-mCherry interaction was optimal for the sensor. The sensor bound primary bile acids cholic acid and chenodeoxycholic acid with a 66% change in emission ratio. Multicolor intracellular imaging was demonstrated by measuring FRET from the red-shifted sensor and the original sensor targeted to the same cellular compartment.

In **Chapter 6** a library of genetically encoded FRET-based antibody sensors for the discovery of novel epitope sequences for antibodies of interest is developed. To allow bivalent binding of the antibody to members of the FRET sensor library, a technique was developed that allowed the cloning of a randomly varied, yet exactly repeated epitope sequence at two separate sites on the DNA encoding the FRET sensor. As a proof of principle, a small library of FRET sensors carrying variants of epitopes recognized by an anti-HIV antibody was screened for antibody binding. Furthermore, the first steps required for much higher throughput screening of the library using newly developed microfluidics technology are reported. The latter required *in vitro* transcription and translation (IVTT) of the FRET sensor variants. It was shown that placement of the FRET acceptor at the N-terminus helped increase the dynamic range 2-fold, while iodoacetamide was used to counter the effect of reducing agents in the IVTT on antibody conformation. Multiple displacement amplification was shown to be the optimal technique for the generation of a sufficient quantity of DNA for IVTT in a microfluidics droplet.

Samenvatting

Om de cel beter te begrijpen is het belangrijk de concentraties van de vele metaalionen, metabolieten en andere kleine moleculen die erin voorkomen te kunnen bepalen. Tot ongeveer twee decennia geleden was het heel lastig om in een enkele, levende cel, door de tijd heen, zulke concentraties te volgen. De ontdekking van het groene fluorescente eiwit (GFP) in de kwal *Aequorea victoria*, begin jaren '60, heeft binnen de moleculaire biologie een revolutie ontketend. GFP maakt het namelijk mogelijk andere eiwitten zichtbaar te maken, simpelweg door het GFP DNA aan het DNA van het andere eiwit te koppelen. Ook de binding van een eiwit aan een klein molecuul kan met fluorescente eiwitten zichtbaar gemaakt worden: door een herkenningsdomein te koppelen aan een cyaankleurig en aan een geelkleurig fluorescent eiwit (resp. CFP en YFP) verkrijgt men een fluorescent sensor eiwit voor dat kleine molecuul. De werking van zo'n sensor berust op het feit dat als CFP en YFP elkaar op korte (<10 nm) afstand naderen, er energie overdracht (FRET) plaatsvindt tussen de CFP donor, die zijn fluorescentie ziet afnemen en de YFP acceptor, die zijn fluorescentie juist ziet toenemen. Als het herkenningsdomein een ligand bindt, verandert het van conformatie, wat een verandering in de onderlinge afstand van CFP en YFP ten gevolge heeft. De daaraan gepaard gaande verandering in FRET kan eenvoudig gevolgd worden met een fluorescentiemicroscoop.

Hoofdstuk 1 beschrijft de verschillende strategieën die tot nu toe gevolgd zijn in de ontwikkeling van FRET sensoren. Het ontwerp van FRET sensoren met een groot dynamisch bereik blijkt nog altijd een grote uitdaging te vormen. De conformatieveranderingen van ligand bindende eiwitten zijn vaak zo klein en subtiel dat ze maar lastig te vertalen zijn naar een verandering in de onderlinge afstand van de FRET donor en acceptor. Een oplossing voor dit probleem is het gebruik van meerdere eiwit domeinen die samen interacties ondergaan, onder invloed van de ligand, waardoor veel grotere veranderingen van de CFP-YFP afstand mogelijk worden. Een andere strategie is het systematisch testen van vele FRET sensor varianten omdat daarmee de kans op het vinden van een verbeterde variant vergroot wordt. Een andere

uitdaging is de ontwikkeling van FRET paren met andere kleuren, om zo verschillende kleine moleculen tegelijk in dezelfde cel te kunnen volgen.

Hoofdstuk 2 beschrijft de ontwikkeling van de eerste genetisch gecodeerde FRET sensor voor magnesium (Mg^{2+}), een metaal met belangrijke katalytische, structurele en regulerende rollen binnen de cel. Als ligand bindend domein werd HsCen3 gebruikt, omdat dit eiwit Mg^{2+} en Ca^{2+} met bijna dezelfde hoge affiniteit bindt. De grote Mg^{2+}-afhankelijke verandering in conformatie van HsCen3 zorgde voor een grote verandering van de Cerulean/Citrine (varianten op CFP en YFP) emissie ratio, van zo'n 50%, met een K_d voor Mg^{2+} van 148 μM. Door mutaties aan te brengen in HsCen3 werd de affiniteit van de sensor voor Mg^{2+} verzwakt, waardoor in een breder concentratie regime gemeten kon worden. In gekweekte humane cellen vertoonde de sensor duidelijke veranderingen in emissie ratio ten gevolge van veranderingen van de Mg^{2+} concentratie. Deze veranderingen in emissie ratio werden alleen gezien als de cellen eerst met digitonine gepermeabiliseerd werden, waardoor de Mg^{2+} concentratie in het cytosol van buitenaf makkelijker beïnvloed kon worden. In intacte cellen vertoonde de sensor geen reactie op behandelingen waarvan uit de vakliteratuur bekend is dat ze zouden leiden tot veranderingen in de vrije Mg^{2+} concentratie binnen de cel. Vervolgonderzoek zal moeten uitwijzen of de sensor niet goed functioneert in de intacte cel, of dat juist de bekende behandelingen de Mg^{2+} concentratie binnen de cel onvoldoende doen veranderen. De sensor, die we MagFRET hebben genoemd, zou een waardevolle bijdrage kunnen leveren aan onderzoek naar de Mg^{2+} homeostase binnen de cel.

In **hoofdstuk 3** wordt de ontwikkeling van een verbeterd roodverschoven FRET paar beschreven. De meeste FRET paren worden gedetecteerd in het blauw-gele gebied van het spectrum en kunnen niet tegelijk in dezelfde cel gevolgd worden. Er is echter een grote behoefte aan zgn. multiparameter metingen omdat hierdoor correlaties tussen cellulaire processen nauwkeuriger bepaald kunnen worden. FRET sensoren die op basis van roodverschoven fluorescente eiwitten zoals mOrange en mCherry worden gemaakt vertonen doorgaans een matig dynamisch bereik. Om de efficiëntie van FRET energie overdracht tussen mOrange en mCherry te vergroten, werd er gezocht naar

mutaties die een hydrofobe interactie tussen beiden teweeg kon brengen. De tetrameer DsRed is de voorouder van mOrange en mCherry en bevat een hydrofobe interactie tussen twee interfaces. De residuen die in DsRed verantwoordelijk geacht werden voor deze hydrofobe interactie werden in mOrange en mCherry gemuteerd naar de oorspronkelijke aminozuren zoals die in DsRed voorkwamen. Dit zelfassociërende ("plakkerige") rode FRET paar werd gebruikt om een Cerulean/Citrine FRET paar te vervangen in eerder ontwikkelde FRET sensoren. De intramoleculaire interactie tussen mOrange en mCherry was dermate zwak dat deze verbroken kon worden wanneer binnen het zelfde eiwit alternatieve eiwit-eiwit interacties optraden ten gevolge van ligand binding. Hierdoor vond er een veel grotere verandering in FRET plaats dan zonder de interactie tussen mOrange en mCherry het geval was. Door nog een andere mutatie te gebruiken kon de interactie nog eens 300x sterker gemaakt worden. De interactie tussen mOrange en mCherry was van essentieel belang in de ontwikkeling van een roodverschoven zink (Zn^{2+}) sensor. Deze nieuwe roodverschoven Zn^{2+} sensor kon in de cel gevolgd worden, samen met een eerder ontwikkelde Zn^{2+} sensor die op Cerulean en Citrine gebaseerd was.

In **hoofdstuk 4** staat een uitgebreide thermodynamische analyse van de stabiliteit van een reeks zelfassociërende FRET paren, zowel van de mOrange/mCherry mutanten als CFP/YFP varianten die eerder in onze groep beschreven werden. Ureum titraties werden gebruikt om dissociatie teweeg te brengen van het intramoleculaire eiwit-eiwit complex, waardoor kwantificering van de sterkte van het complex mogelijk was. De relatieve sterktes die met de ureum titraties gevonden werden, werden ondersteund door een meting die de K_d voor mCherry homodimerisatie bepaalde met fluorescentie polarisatie. Tezamen zorgen deze bevindingen voor een beter begrip van de subtiele effecten die de prestaties van de bestaande FRET sensoren bepalen en helpen ze bij het rationele ontwerp van nieuwe sensoren.

Hoofdstuk 5 beschrijft nog een tweede rode FRET sensor die gebruik maakte van het zelfassociërende mOrange-mCherry FRET paar. Galzuren, gevormd door de oxidatie van cholesterol, spelen een belangrijke rol in de vertering van vetten en in de regulatie van de stofwisseling. Op basis van de nucleaire receptor voor galzuren (FXR),

het “plakkerige” mOrange en mCherry FRET paar en een co-activator peptide werd een galzuur sensor ontwikkeld. De sensor is ontworpen om tussen twee toestanden te schakelen. In de rusttoestand, in afwezigheid van galzuren, is er veel FRET wegens de interactie tussen mOrange en mCherry. Binden galzuren aan FXR, dan vindt er een nieuwe interactie plaats, tussen FXR en het co-activator peptide, waardoor de interactie tussen de fluorescente domeinen verbroken wordt. Een van de zwakkere interacties bleek optimaal voor de werking van de sensor. De binding van de sensor aan de primaire galzuren cholzuur en chenodeoxycholzuur bracht een verandering van 66% in de mOrange/mCherry emissie-ratio teweeg. Er werd eerder in onze groep al een soortgelijke sensor ontwikkeld op basis van Cerulean en Citrine. De roodverschoven sensor kon samen met de op Cerulean/Citrine gebaseerde galzuur sensor in hetzelfde cellulaire compartiment worden gevolgd.

Hoofdstuk 6 beschrijft de ontwikkeling van een bibliotheek van genetisch gecodeerde FRET sensoren waarmee nieuwe epitopen ontdekt kunnen worden. Epitopen zijn de korte eiwit fragmenten van een antigeen die door een antilichaam herkend worden. Er is grote vraag naar technieken waarmee de aminozuur volgorde van epitopen efficiënt vastgesteld kan worden. De antilichaam FRET sensor CerAbsCit, die al eerder in onze groep ontwikkeld is, bestaat uit het zelfassociërende Cerulean-Citrine FRET paar dat onderling verbonden wordt door een lange, flexibele peptide keten. Aan weerszijden van de flexibele keten, tussen de keten en beide fluorescente domeinen, bevindt zich een epitoop sequentie. De intramoleculaire interactie tussen Cerulean en Citrine veroorzaakt in eerste instantie een hoge mate van FRET tot dat binding van het antilichaam aan beide epitopen een verbreking van de interactie tussen Cerulean en Citrine veroorzaakt. Om voor een willekeurig antilichaam de epitopen vast te stellen zullen vele CerAbsCit varianten gescreend moeten worden op afname van FRET. Omdat de binding van het antilichaam aan de FRET sensor bivalent is, moest er bij de ontwikkeling van de bibliotheek rekening mee worden gehouden dat dezelfde epitoop sequentie gevarieerd moest worden op twee verschillende plaatsten van het DNA. Bovendien moesten beiden kopieën van het epitoop per DNA molecuul identiek aan elkaar zijn. Met “rolling circle” PCR was het

mogelijk om twee dezelfde epitoop sequentie varianten op een DNA molecuul te krijgen. Als “proof of principle” werd een kleine bibliotheek van FRET sensoren gekloneerd en gescreend op binding aan een anti-HIV-antilichaam, op 96-well plaat schaal. Om veel meer varianten tegelijk te screenen zijn technieken als microfluidics vereist. De eerste stappen richting deze techniek, namelijk het geschikt maken van de sensor voor *in vitro* transcriptie en translatie (IVTT) worden hier beschreven. Door de Citrine acceptor aan de N-terminus van het eiwit te plaatsen werd het dynamisch bereik van de antilichaam FRET sensor vergroot wanneer deze met IVTT tot expressie gebracht werd. Het antilichaam was niet stabiel in de IVTT mix, vermoedelijk door de hoge concentratie DTT. Door de DTT te inactiveren met joodaceetamide werd de werking van DTT tegengegaan en werd ook in de IVTT mix een hoog dynamisch bereik gehaald.

Curriculum Vitae

Laurens Lindenburg werd op 21 januari 1985 geboren in Groningen. Na het behalen van het Europese Baccalaureaat aan de Europese School in Luxemburg is hij in 2003 aan een B.Sc. studie microbiologie aan de Universiteit van Cardiff (Verenigd Koninkrijk) begonnen. Deze studie rondde hij in 2007 af, mede met onderzoek naar het effect van oxidatieve stress op de verspringing van insertie sequenties in het genoom van een pathogene bacterie. Vervolgens heeft hij een M.Sc. biomoleculaire wetenschappen gehaald aan de VU. Tijdens deze studie heeft hij onderzoek verricht naar de evolutie van genetische regulatie, onder begeleiding van prof.dr. S. Tans in AMOLF en naar de bacteriële eiwit translocatie, onder begeleiding van dr. Y. Bollen aan de VU. In december 2009 is hij begonnen aan zijn promotie onderzoek in het Laboratorium voor Chemische Biologie van de TU/e, onder leiding van prof.dr.ir. L. Brunsveld en dr. M. Merkx. De belangrijkste resultaten van zijn promotie onderzoek staan beschreven in dit proefschrift.

Laurens Lindenburg was born on January 21st, 1985 in Groningen, the Netherlands. After completing a European Baccalaureate in 2003 at the European School in Luxembourg, he studied at Cardiff University in the UK, receiving a B.Sc. degree in Microbiology in 2007. As part of his studies, he investigated the effect of oxidative stress on insertion sequence-mediated genomic rearrangements in a pathogenic bacterium. In 2009 he obtained an M.Sc. degree in Biomolecular Sciences at the Vrije Universiteit (VU, Amsterdam). During his Master studies, he performed research both at AMOLF in the group of prof.dr. S. Tans, on the evolution of genetic regulation, as well as at the VU, on bacterial protein translocation, under the supervision of dr. Y. Bollen. In december 2009 he started a PhD project at the Eindhoven University of Technology in the Laboratory for Chemical Biology under the supervision of prof.dr.ir. L. Brunsveld and dr. M. Merkx. The main results of his PhD work are described in this dissertation.

List of publications

Drevinek P., Baldwin A., Lindenburg L., Joshi L.T., Marchbank A., Vosahlikova S., Dowson C.G., Mahenthiralingam E. (2010) **Oxidative stress of *Burkholderia cenocepacia* induces insertion sequence-mediated genomic rearrangements that interfere with macrorestriction-based genotyping.** *J Clin Microbiol* 48, 34-40 (2010).

Lindenburg, L. & Merkx, M. (2012) **Colorful calcium sensors**. *ChemBioChem* 13, 349-51 (2012).

Lindenburg, L.H., Hessels, A.M., Ebberink, E.H., Arts, R. & Merkx, M. (2013) **Robust red FRET sensors using self-associating fluorescent domains.** *ACS Chem Biol* 8, 2133–2139.

Merkx, M., Golynskiy, M.V., Lindenburg, L.H. & Vinkenborg, J.L. (2013) **Rational design of FRET sensor proteins based on mutually exclusive domain interactions**. *Biochem Soc Trans* 41, 1201-5.

Lindenburg, L.H., Vinkenborg, J.L., Oortwijn, J., Aper, S.J. & Merkx, M. (2013) **MagFRET: The first genetically encoded fluorescent Mg^{2+} sensor.** *PLoS One* 8, e82009.

Lindenburg, L.H., Sips, T., Malisauskas, M., Merkx, M. (2014) **Quantifying stickiness; thermodynamic characterization of intramolecular interactions between fluorescent domains to guide the design of FRET sensors.** *To be submitted*.

Dankwoord

Ik ben blij dat ik in Eindhoven op een aio plek heb gesolliciteerd want toen ik op de TU/e op gesprek kwam was ik meteen onder de indruk van de organisatie en prettige werksfeer bij MST en Chemische Biologie. Nu, 4½ jaar later, kan ik een promotie hier warm aanbevelen, vooral door de samenwerking met de mensen die ik hier wil bedanken.

Aller eerst **Maarten**. Bedankt dat je het hebt aangedurfd mij aan te nemen. Ik had het voorrecht in je groep terecht te komen op een punt dat je al veel succes geboekt had, dat er een paar mooie systemen lagen om aan te werken, ook voorbereid door de aios en postdocs die voor mij kwamen. Jij combineert een zeer solide kennis van de biochemie en de biologie met een haast speelse manier van denken over het ontwikkelen van moleculaire sensoren. Je pragmatische instelling zorgde ervoor dat resultaten behaald konden worden en je zorgde dat ik richting bleef geven aan het onderzoek als ik af en toe dreigde te verzanden. Tijdens mijn promotie heb je me ook de kans geboden trainingen te volgen en congressen te bezoeken. Je open manier van communiceren en het regelmatige werkoverleg zorgde voor een prettig werkklimaat. Ik ben je erg dankbaar dat je mij de afgelopen maanden telkens motiveerde om dit proefschrift naar een hoger niveau te tillen. **Luc**, ik wil je bedanken voor je kritische commentaar op mijn proefschrift als promotor. Ook je leiderschapkwaliteiten kan ik waarderen; zo worden we door jou erg actief aangemoedigd om lezingen bij te wonen, waardoor we bij ons eigen praatje ook verzekerd zijn van een volle zaal. In een aantal lastige kwesties heb je door goede communicatie duidelijkheid geboden aan de mensen van de chemische biologie groep. Overige leden van de promotiecommissie, **prof. Huck**, **prof. Gadella**, **dr. Borst**, **dr. Ottmann**, bedankt voor het kritisch lezen van dit proefschrift en dat u mij tot de verdediging ervan hebt toegelaten. **Prof. Hilbers**, dank voor uw voorzitterschap en **prof. Nicolay**, dank voor het optreden als plaatsvervanger van Prof. Hilbers tijdens mijn verdediging.

Jan, ik ben blij dat ik vlak voor je promotie nog een paar maanden met je heb mogen samenwerken. Ik heb meteen veel van je geleerd, o.a. de belangrijkste eiwitzuiveringsprotocollen. Het MagFRET project wat je voor mij achterliet toen je naar Bonn vertrok was veelbelovend en ik ben je zeer dankbaar voor al het werk wat je tijdens en na je promotie gedaan hebt om er uiteindelijk samen een artikel van te kunnen publiceren. Voor het onderhoud van de nieuwe Leica confocale microscoop bij Tissue Engineering, waarmee de celmetingen in hoofdstuk 3 en 5 gedaan zijn, ben ik **Marcel Wijlaars** en **Mark van Turnhout** zeer dankbaar. Dit mooie apparaat werd in 2011 precies op het juiste moment in mijn onderzoek aangeschaft! **Dr. Stan van de Graaf** (UMC), bedankt voor je input en het idee om een rode versie van de bestaande galzuursensor te maken. Dank ook aan jou en **dr. Lieke van der Velden** voor de hulp bij metingen van MagFRET en voor het gebruik van jullie confocale microscoop in Utrecht. I'd like to thank **prof. Wilhelm Huck** and **dr. Aigars Piruska** at RU for their help and ideas concerning the directed evolution of FRET sensors using microfluidics. I enjoyed visiting you in Nijmegen and would always leave buzzing with new ideas. I wish I had had more time to do the first experiments in actual droplets!

De vaste stafleden van SMO wil ik ook bedanken voor hun hulp tijdens mijn promotie. **Bert**, bedankt voor het gebruik van de uitstekende SMO infrastructuur, de meetapparatuur, ook buiten het biolab (zoals de massaspectrometers), de kans om voordrachten over uiteenlopend onderzoek (van eiwitten tot zonnecellen) te mogen aanhoren, de jaarlijkse uitjes en het jaarlijkse Nolte-Meijer voetbalspektakel. **Joke**, bedankt voor al je werkzaamheden (administratief, verzorging kwartaalverslagen, organisatie uitjes en nog veel meer) binnen de groep. Excuses dat ik niet altijd helemaal op tijd mijn kwartaalverslag inleverde. Ik hoop dat je al volop aan het genieten bent van je pensioen en misschien tot binnenkort! **Hans**, heel erg bedankt voor het bestellen van al die gekoelde biologische reagentia en voor het uitzoeken als er een weer eens iets mis ging in de bestelketen. Henk, je heerlijke koffie heeft mij door menig maandagochtend geholpen! **Peggy** dank voor de strakke organisatie van het biolab, ik kan alleen maar hopen ook in de toekomst in zo'n schoon en veilig lab te mogen werken.

Ik heb het grote geluk gehad veel studenten als dagelijkse begeleider te mogen bijstaan in hun onderzoek en dat heeft een enorme bijdrage geleverd aan mijn proefschrift. **Eduard**, het was een

voorrecht je te mogen begeleiden tijdens je afstuderen. Je ontdekking van de mutaties in mOrange en mCherry die ze "sticky" maakten hebben me drie hoofdstukken opgeleverd. De vertraging die ik je oplegde door fluorofoorloze niet-fluorescerende eiwitten voor je te ontwerpen, heb je door slim en hard te werken al snel weten weg te werken. Ik hoop dat jouw voorstel om in de vakliteratuur een plek te bieden aan het mislukte experiment ooit gerealiseerd kan worden. Ik wens je het allerbeste toe in je promotie bij Sanquin en hopelijk blijven we contact houden. **Mark**, bedankt voor je systematische karakterisatie van het effect van de verschillende mutaties in mOrange en mCherry op hun intrinsieke fluorescente eigenschappen. Door je scherpe blik kwam je er al snel achter dat we in het begin de verkeerde threonine (positie 179 i.p.v. 180) in mOrange gemuteerd hadden. **Eric**, na keihard gewerkt te hebben aan CPEC en GoldenGate kloneringen (herinner je je nog die ene BsaI site in pET16b die niet voorkwam in het door mij verkeerd samengestelde sequentiebestand?) wilden die eiwitten toch niet "FRET-driepuntnullen". Heel erg bedankt voor je werk aan dat project en veel succes bij je promotie bij de DTU in Denemarken. **Parinaz**, je was als eerste student begonnen aan het rode zink sensor project en hebt de eerste positieve resultaten kunnen laten zien. Dit tijdens een hele zware tijd voor jou en je familie, veel dank daarvoor. **Sjors**, voor de extra tijd die je in je stage hebt gestoken om de niet eenvoudige klonering van de rode galzuursensor rond te krijgen ben ik je zeer dankbaar. **Remco**, behalve je gouden handjes op het lab, bleken je schrijfkunsten van bijzondere kwaliteit. Ik heb je ook van prille maar veel belovende OGO student zien groeien tot zelfververzekerde afstudeerder en ten slotte zelfs tot gewaardeerde collega aio. Ik ben je dankbaar voor je werk met de rode zink sensoren, zowel met zuiver eiwit als in cellen. **Lisanne**, ik ben je dankbaar voor je werk met de rode galzuursensor. Dit eiwit bleek lastig maar door te blijven proberen is het toch gelukt om mooie reproduceerbare metingen ermee te doen. Jouw metingen in HEK cellen zagen er veelbelovend uit. Hopelijk wordt dit verhaal nog vervolgd. **Tari**, bedankt voor je werk met de rode fluorescente eiwitten en de karakterisatie van nieuwe mutaties die nieuwe interacties sterktes teweeg brachten. Veel van jouw werk staat nu in hoofdstuk 4 beschreven en verschijnt binnenkort hopelijk ook als artikel. Het was mooi om je afstudeervoordracht in Heerlen mee te mogen maken.

Mijn directe collega aios in de Protein Engineering groep, **Remco**, **Stijn**, **Martijn**, **Brian** en **Anne**: bedankt voor de fijne uitstapjes (ook met oud-groepsgenoten **Eduard** en **Ilmar**). **Brian,** het was altijd gezellig je op zaterdagochtend in het lab tegen te komen en te pipetteren onder het genot van leuke muziek. Ook je geduld tijdens de dinsdagochtendmeetings als ik weer eens uitvoerig verslag uitbracht van mijn kloneringen ging bij mij niet onopgemerkt. **Anne**, ik ben je heel dankbaar voor onze samenwerking met het rode zink sensor project. Zonder jouw ervaring met confocale fluorescentie microscopie en gevoel voor celwerk waren de celmetingen in hoofdstuk 3 niet gelukt. Ik weet maar al te goed hoe lastig het werken met cellen vaak kan zijn, en wens je heel veel succes bij je ER zink project. **Stijn** en **Martijn**, ik ben dankbaar dat jullie bereid waren als paranimf op te treden tijdens mijn verdediging. Het was heel fijn met jullie samen te werken en altijd het onderzoek te kunnen bespreken. Stijn, dank ook voor je hulp bij het MagFRET manuscript en natuurlijk voor het werk (celmetingen MagFRET) wat je destijds bij Jan verricht hebt. Martijn, je had altijd goede ideeën over het directed evolution werk. Stijn, Martijn en Remco, ik heb erg genoten van ons verblijf in het mooie Liverpool na het protein engineering congres in Chester. Remco, ook als aio is het fijn je in de groep te hebben, bedankt voor de gezellige koffiepauzes en lunches. Veel succes met de BRET!

Iedereen in het biolab, ontzettend bedankt voor de fijne samenwerking. **Katja**, you were the social hub of the group during your time in Eindhoven, making life more pleasant for everyone. **Lech** en **Katja**, het was prachtig om bij jullie huwelijk in Dortmund te mogen zijn. Door de jaren heen heb ik STO 3.24 met een aantal fijne kamergenoten mogen delen. **Sascha "**de Vos", you were another "socialite", thanks for all the great parties at your place. It was always fun to watch football games with you. I still miss the passionate German Skype calls! **Loes**, met jouw komst op de oude werkplek van Sascha keerde de rust in het kantoor terug, ik wens je veel succes met je promotie en het dansen. **Parisa**, je hebt je sterk gehouden onder zware omstandigheden. Het was goed om te zien hoe je de laatste paar maanden weer de draad op hebt kunnen pakken en je bent ook altijd een goede koffiegenoot. **Ingrid**, leuk dat ik nadat ik je kort had leren kennen tijdens je promotie in de afdeling Structuurbiologie aan de VU (dankzij Luc weet je nu dat sonde en zonde homoniemen van elkaar zijn), nog een keer als kamergenoot kreeg in Eindhoven. **Luc S.,** al begreep ik maar weinig

van je vakgebied, toch wist je er altijd op een boeiende manier over te vertellen. Heel veel succes met Surfix! **Chan Vinh**, in de ~9 maanden dat we bij elkaar op STO3.24 zaten heb ik je beter leren kennen. Je "realistische" blik op de samenleving was altijd goed voor gespreksstof, dank voor al je advies over het opbouwen van professionele netwerken! Jouw inzichten over nucleaire receptoren kwam goed van pas bij mijn werk met de FXR sensor. Ik wens je een zeer spoedig herstel toe.

Buiten het werk op de universiteit heb ik de afgelopen 4 seizoenen genoten van het spelen bij RC Eindhoven, een bijzonder hechte vereniging waar je je als nieuwkomer al heel snel helemaal thuis voelt. Na de zoveelste mislukte klonering was de training toch altijd het moment om frustraties weg te werken (en soms maakte een gelukte klonering een verloren wedstrijd weer goed). Mocht ik in verband met werk uit Eindhoven vertrekken zal ik RCE en de mensen daar erg missen! Mijn andere sportieve prestatie mocht ik op zwoele zomerse woensdagavonden langs de Dommel leveren: de SMO voetbal training. Alle mede-spelers door de jaren heen, te veel om op te noemen maar o.a. **Dung**, **Luuk**, **Henk**, **Ralph**, **Sascha**, **Eduard**, **Samba**, **Micha**, **Marcel K.**, **Marcel S.**, **Remco**, **Lech**, **Brian**, **Geert** en **Seppe** ontzettend bedankt voor al die wedstrijdjes en excuses voor de ongelukkige planning van mijn verdediging op een woensdagmiddag. Enkele herinneringen: **Micha** die het altijd presteerde de bal keihard op de vrouwelijke spelers (vooral Fanny) af te vuren, **Remco** met zijn pingel acties en **Samba**, your bird-like whistle never failed to fool the opposition when in attack and in defense your raised feet could be quite lethal. I hope you are doing well at Janelia Farm. Van **Ralph** en **Remco** werd pas laat vorig seizoen ontdekt werd dat ze een dodelijk spitsen duo vormen. **Lech**, je bent niet alleen een uitstekende (vleugel)middenvelder, maar je leverde ook uitputtende analyses van ons spel.

Mijn ouders wil ik bedanken voor de steun tijdens mijn studie en voor het op pijl houden van mijn Nederlands toen we in Dublin woonden zodat ik dit dankwoord kon schrijven. Als laatste **Targol**, voor je begrip en je motiverende en relativerende woorden als het even niet meezat, dank! Ik hoop dat je dit ook in de toekomst voor mij kan blijven doen.

Laurens